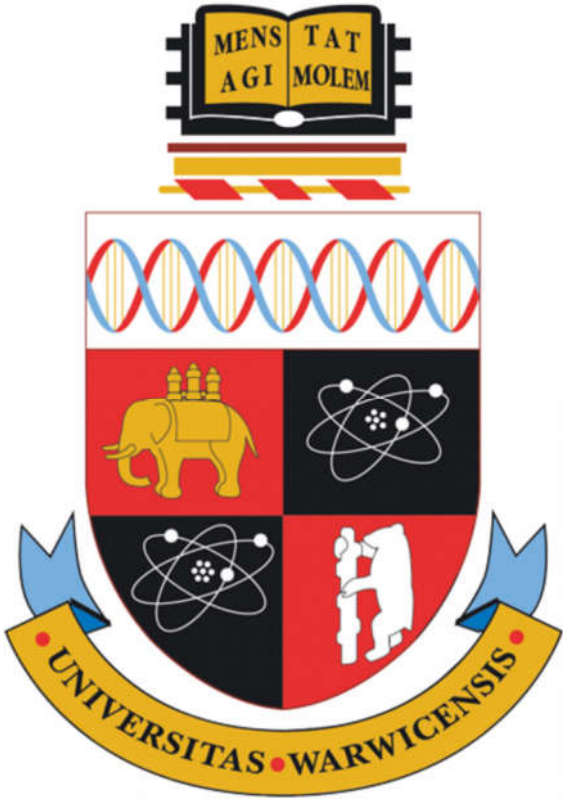

Synthetic nucleobase-containing acrylamide polymers and their applications in aqueous solutions

Zan Hua

Submitted for the degree of Doctor of Philosophy

University of Warwick

Department of Chemistry

February 2018

Table of contents

Table of contents 2

List of figures, schemes and tables 10

List of figures 10

List of schemes 26

List of tables 28

Acknowledgements 30

Declaration of authorship 32

Publications 33

Summary of thesis 34

Abbreviations 35

Chapter 1. Introduction 40

1.1. Mimicking biological functionality with synthetic polymers 41

1.2. Block copolymer (BCP) synthesis and self-assembly 42

1.2.1. Ring-opening metathesis polymerization (ROMP) 42

1.2.2. Controlled radical polymerization 43

1.2.2.1. Nitroxide-mediated polymerization (NMP) 45

1.2.2.2. Transition metal-catalyzed polymerizations 46

1.2.2.3. Reversible addition-fragmentation chain transfer polymerization (RAFT) 47

1.2.3. BCP Self-Assembly 51

1.3. H-bonding in BCP self-assembly in water 57

1.4. Syntheses of nucleobase-containing synthetic polymers 60

1.5. Novel properties of nucleobase-containing synthetic polymers and their applications 68

1.5.1. Template polymerization 69

1.5.2. Novel self-assembly properties of nucleobase-containing synthetic polymers 73

1.5.3. Applications of synthetic nucleobase-containing materials 76

1.6. Conclusions 81

1.7. Aims of the thesis 82

1.8. References 83

Chapter 2. Micellar nanoparticles with tuneable morphologies through interactions between nucleobase-containing synthetic polymers in aqueous solutions 91

2.1. Declaration of authorship 92

2.2. Abstract 93

2.3. Introduction 94

2.4. Results and discussion 97

2.4.1. Syntheses of nucleobase-containing acrylamide monomers 97

2.4.2. Synthesis and characterization of nucleobase-containing synthetic diblock copolymers 101

2.4.3. Self-assembly of PNAM-*b*-PTAm diblock copolymers 103

2.4.4. Tuning spherical micelle sizes using complementary nucleobase interactions 107

2.4.5. The mechanism of morphological transition from large spheres to smaller ones 113

2.4.6. Tuning micelle morphologies through complementary nucleobase interactions 120

2.5. Conclusions 131

2.6. Experimental section 132

2.6.1. Materials 132

2.6.2. Instrumentation 132

2.6.3. Synthesis of *N*-(3-bromopropyl) acrylamide 135

2.6.4. Synthesis of 3-(adenine-9-yl)propyl acrylamide (AAm) 135

2.6.5. Synthesis of 3-benzoylthymine 136

2.6.6. Synthesis of 3-(3-benzoylthymin-1-yl)propyl acrylamide 137

2.6.7. Synthesis of 3-(thymin-1-yl)propyl acrylamide (TAm) 138

2.6.8. Synthesis of 2-(((butylthio)carbonothiolyl)thio)propanoic acid (CTA) 138

2.6.9. Synthesis of poly(4-acryloylmorpholine) (PNAM) macro-CTA *via* RAFT polymerization 141

2.6.10. Synthesis of $PNAM_{96}$-*b*-$PTAm_n$ and $PNAM_{96}$-*b*-$PAAm_m$ diblock copolymers 141

2.6.11. Self-assembly of PNAM-*b*-PTAm diblock copolymer in water 141

2.6.12. Addition of complementary copolymer PNAM-*b*-PAAm (P2.8) into PNAM-*b*-PTAm micellar solution 142

2.6.13. Calculation of the molar ratios of complementary copolymers 142

2.7. References 144

Chapter 3. Nanoparticles with a nucleobase-containing core showing pathway dependent and complementary chain selective morphological transitions 149

3.1. Declaration of authorship 150

3.2. Abstract 151

3.3. Introduction 152

3.4. Results and discussion 154

3.4.1. Morphological transitions induced by complementary nucleobase interactions 154

3.4.2. No morphological transitions induced by only hydrophobic effects 159

3.4.3. The mechanism of the morphological transitions 166

3.4.4. Pathway-dependent morphological transitions 170

3.4.5. The effect of chain length on morphological transitions 174

3.4.6. Controlled “living” growth mediated by complementary H-bonding interactions 183

3.5. Conclusions 185

3.6. Experimental section 186

3.6.1. Materials 186

3.6.2. Instrumentation 186

3.6.3. Synthesis of 3-(*N*6, *N*6-dimethyladenine-9-yl)propyl acrylamide (MAAm) 187

3.6.4. Synthesis of 3-(3-methylthymin-1-yl)propyl acrylamide (MTAm) 190

3.6.5. Synthesis of Poly(4-acryloylmorpholine) ($PNAM_{39}$ and $PNAM_{295}$) macro-CTA *via* RAFT polymerization. 192

3.6.6. Synthesis of $PNAM_{39}$-*b*-$PTAm_n$, $PNAM_{39}$-*b*-$PMTAm_{300}$, $PNAM_x$-*b*-$PAAm_m$, $PNAM_{39}$-*b*-$PMAAm_{20}$ and $PNAM_{39}$-*b*-PSt_{20} diblock copolymers. 192

3.6.7. Self-Assembly of $PNAM_{39}$-*b*-$PTAm_{300}$ PT1, $PNAM_{39}$-*b*-$PMTAm_{300}$ PT^{Me} diblock copolymer in water 193

3.6.8. Addition of copolymers $PNAM_x$-*b*-$PAAm_y$, $PNAM_{39}$-*b*-PSt_{20}, $PNAM_{39}$-*b*-$PTAm_{20}$ or $PNAM_{39}$-*b*-$PMAAm_{20}$ into $PNAM_{39}$-*b*-$PTAm_{300}$ MT1 or $PNAM_{39}$-*b*-$PMTAm_{300}$ MT^{Me} micellar solution. 193

3.7. References 194

Chapter 4. Reversibly manipulating the surface chemistry of polymeric nanostructures *via* a 'grafting to' approach mediated by nucleobase interactions 197

4.1. Declaration of authorship 198

4.2. Abstract 199

4.3. Introduction 200

4.4. Results and discussion 203

4.4.1. Synthesis of mixed-corona micelles through a supramolecular 'grafting to' approach 203

4.4.2. Reversible alteration of the sizes of mixed-corona nanoparticles 212

4.4.3. Altering the coronas and surfaces of mixed-corona nanoparticles 215

4.4.4. Controlling the ligand display by altering the surface of mixed-corona nanoparticle 223

4.5. Conclusions 228

4.6. Experimental section 229

4.6.1 Materials 229

4.6.2 Instrumentation 229

4.6.3 Synthesis of 2-cyano-5-hydroxypentan-2-yl ethyl carbonotrithioate (CPET) 231

4.6.4. Synthesis of 2-cyano-5-(3,4-dibromo-2,5-dioxo-2,5-dihydro-1H-pyrrol-1-yl)pentan-2-yl ethyl carbonotrithioate (CPET-DBM) 233

4.6.5. Synthesis of 5-(3-bromo-4-(isopropylamino)-2,5-dioxo-2,5-dihydro-1H-pyrrol-1-yl)-2-cyanopentan-2-yl ethyl carbonotrithioate (CPET-ABM) 235

4.6.6. Synthesis of D-mannose containing RAFT CTA 235

4.6.7. Synthesis of poly(*N*-isopropylacrylamide) (PNIPAM) macro-CTA *via* RAFT polymerization 236

4.6.8. Synthesis of $PNIPAM_x$-*b*-$PAAm_y$ diblock copolymers 236

4.6.9. Self-assembly of $PNAM_{98}$-*b*-$PTAm_{302}$ P4.10 diblock copolymer in water 237

4.6.10. Preparation of mixed-corona micelles containing PNIPAM-*b*-PAAm and PNAM-*b*-PTAm 237

4.7. References 238

Chapter 5. Entrapment and rigidification of adenine by a photocrosslinked thymine network leads to fluorescent polymer nanoparticles 242

5.1. Declaration of authorship 243

5.2. Abstract 244

5.3. Introduction 245

5.4. Results and discussion 247

5.4.1. Synthesis of nucleobase-containing fluorescent nanoparticles 247

5.4.2. Effect of H-bonding on the fluorescence behavior 254

5.4.3. Importance of crosslinking on the fluorescence property 258

5.4.4. Requirement for polymer immobilization to the observed fluorescence 260

5.4.5. Probing the crosslinking process 261

5.4.6. Characterization of fluorescence pathways 265

5.4.7. Degradation studies of the fluorescent nanoparticles 267

5.4.8. Robustness of fluorescent properties to changes in temperature, solvent and pH 270

5.5. Conclusions 274

5.6. Experimental section 276

5.6.1. Materials 276

5.6.2 Instrumentation 276

5.6.3. Synthesis of 3-(adenine-9-yl)propyl acrylate (AAc) 278

5.6.4. Synthesis of 3-(3-benzoylthymin-1-yl)propyl acrylate 281

5.6.5. Synthesis of 3-(thymin-1-yl)propyl acrylate (TAc) 281

5.6.6. Synthesis of $PNAM_{96}$-*b*-$PMTAm_{19}$ ($PT^{Me'}$), $PNAM_{96}$-*b*-$PAAc_{20}$ (PA*') and $PNAM_{96}$-*b*-$PTAc_{19}$ (PT*') diblock copolymers 284

5.6.7. End group removal of $PNAM_{96}$-*b*-$PAAm_{19}$ (PA'), $PNAM_{96}$-*b*-$PTAm_{18}$ (PT'), $PNAM_{96}$-*b*-$PMTAm_{19}$ ($PT^{Me'}$), $PNAM_{96}$-*b*-$PAAc_{20}$ (PA*') and $PNAM_{96}$-*b*-$PTAc_{19}$ (PT*') diblock copolymers 284

5.6.8. Self-assembly and UV irradiation of micelles MA, MT, M(A:T), M($A+T^{Me}$), M(A*:T*) and M (9-hexylA:T) 284

5.6.9. Hydrolysis of micelles Mi(A:T) and Mi(A*:T*) 285

5.7. References 286

Chapter 6. Conclusions and outlook 289

6.1. Conclusions 290

6.2. Outlook 292

List of figures, schemes and tables

List of figures

Figure 1.1. General guidelines for the selection of the Z- and R-group of RAFT agents for various polymerizations. Figure reproduced from ref.[43] 50

Figure 1.2. Macromolecular architectural guide. The three main aspects of polymer architecture – composition, topology, and function – are shown separately in (**A**) and in combination in (**B**). Figure reproduced from ref.[48] 52

Figure 1.3. Transmission electron microscopy (TEM) micrographs and corresponding schematic diagrams of various morphologies formed from amphiphilic PSm-*b*-PAAn copolymers (note: m and n denote the degrees of polymerization of PS and PAA, respectively). In the schematic diagrams, red represents hydrophobic PS parts, while blue denotes hydrophilic PAA segments. HHHs: hexagonally packed hollow hoops; LCMs: large compound micelles, in which inverse micelles consist of a PAA core surrounded by PS coronal chains. Figure adapted from ref.[50] 53

Figure 1.4. The different morphologies obtained by targeting different packing parameters, *p*. Figure reproduced from ref.[53] 54

Figure 1.5. Schematics representations and cryo-TEM images of BCP assemblies with varying solvophilic (light blue block) weight-fractions (*f*), which form (left-to-right) vesicles, worms, and spherical micelles. Figure adapted from ref.[56] 55

Figure 1.6. Structures of compounds **1**-**4**. This figure shows the monofunctional ureidotriazines **1** and **3** and their mode of association *via* quadruple hydrogen bonds. Structures of bifunctional derivatives **2** and **4** are also shown. Figure reproduced from ref.[71] 57

Figure 1.7. Schematic representation of possible supramolecular structures of (a) PEG-*b*-PLLA and (b) PEG-TU (or U)-*b*-PLLA assemblies in water (R = S or O). Figure reproduced from ref.[67] 58

Figure 1.8. Cartoon illustration of the formation of stereocomplex spherical micelles from PLLA-*b*-PTHPA and PDLA-*b*-PTHPA. Figure reproduced from ref.[73] 59

Figure 1.9. Synthesis of nucleobase-containing diblock copolymers by ATRP and schematic structure of self-assemblies. Figure reproduced from ref.[84, 101] 62

Figure 1.10. Thiol-Michael coupling of the thymine–adenine dimer and adenine monomers (5 mol% DBU in CH_2Cl_2,1 h), yielding a thymine–adenine–adenine trimer that was photopolymerized by irradiation with 365 nm light) for 10 min in the presence of 1 mol% DMPA (DMPA=2,2-dimethoxy-2-phenylacetophenone). Inset: MALDI spectrum of this polymer, showing the 867 Da spacing associated with the TAA trimer. Figure reproduced from ref.[115] 64

Figure 1.11. Polymerization of 3',5'-cyclic 3-(3-butenyl) thymidine ethylphosphate (**5**) with 4-methoxybenzyl alcohol as the initiator and 1,5,7-triazabicyclo[4.4.0]dec-5-ene (TBD) as the catalyst. Figure reproduced from ref.[117] 65

Figure 1.12. Synthesis and self-assembly of the nucleobase-containing diblock copolymers using RAFT polymerization. Figure reproduced from ref.[87, 101] 66

Figure 1.13. Synthesis of adenine and thymine-functionalized acrylic ABA triblock copolymers using RAFT polymerization. Figure adapted from ref.[107] 67

Figure 1.14. DNA origami shapes. Figure reproduced from ref.[126] 69

Figure 1.15. Solution-based template polymerization through ROMP. Figure reproduced from ref.[100]. 70

Figure 1.16. Nucleobase-templated polymerization from well-defined template obtained through ROMP. Figure reproduced from ref.[98] 71

Figure 1.17. Dynamic exchange and cooperative assembly of templates for biomimetic radical polymerization. Figure reproduced from ref.[109] 72

Figure 1.18. Proposed mechanism of template polymerization for monomers with complementary nucleobases by Marsh and coworkers. Figure reproduced from ref.[104, 120] 73

Figure 1.19. Schematic depiction of vesicle formation between diaminopyridine-based polymer **1** and thymine-based polymer **2**. (a) Illustration showing molecular recognition within vesicle wall. (b) The corresponding recognition groups. Figure reproduced from ref.[127] 74

Figure 1.20. Schematic presentation of moderately alternated and random nucleobase-containing copolymers and their TEM images on graphene oxide. TEM images of self-assemblies of diblock copolymers containing (a, c) moderately alternated nucleobase-containing copolymers and (b, d) random nucleobase-containing copolymers. Figure adapted from ref.[85] 75

Figure 1.21. (top) Melamine (M)-driven triplex hybridization of bifacial polymer nucleic acid (bPoNA) with T/U tracts in DNA and RNA. (bottom) Structures of bPoNA studied as DNA and RNA folding and delivery agents. PEG = 5 kDa. The melamine (M) part is highlighted as a red triangle. Figure reproduced from ref.[132] 77

Figure 1.22. Tapping mode AFM phase image of (a) solution-cast poly(AdA-*b*-nBA-*b*-AdA), (b) solution-cast poly(ThA-*b*-nBA-*b*-ThA), (c) melt-pressed poly(AdA-*b*-nBA-*b*-AdA), (d) melt-pressed poly(ThA-*b*-nBA-*b*-ThA), and (e) solution-cast supramolecular blend. Figure reproduced from ref.[107] 79

Figure 2.1. ^{1}H NMR and ^{13}C NMR spectra of 3-(adenine-9-yl)propyl acrylamide (AAm) in DMSO-d_6. 98

Figure 2.2. ^{1}H NMR and ^{13}C NMR spectra of 3-(thymin-1-yl)propyl acrylamide (TAm) in DMSO-d_6. 100

Figure 2.3. Representative ^{1}H NMR spectra of macro-CTA **P2.1** and nucleobase-containing diblock copolymers **P2.4** and **P2.5** in DMSO-d_6..... 102

Figure 2.4. SEC traces (DMF + 5 mM NH_4BF_4 as eluent) of macro-CTA **P2.1** and nucleobase-containing diblock copolymers **P2.2-2.8**. 103

Figure 2.5. (a, c) DLS analyses and (b, d) TEM images of self-assembled micelles **M2.4** (with a small thymine core) and **M2.5** (with a large thymine core) from $PNAM_{96}$-*b*-$PTAm_{114}$ **P2.4** and $PNAM_{96}$-*b*-$PTAm_{301}$ **P2.5** on graphene oxide without staining, respectively. 104

Figure 2.6. Histograms of the diameters of PNAM-*b*-PTAm spherical micelles **M2.4-2.7** as determined by TEM analyses. 105

Figure 2.7. DLS analysis and TEM image of $PNAM_{96}$-*b*-$PTAm_{301}$ (**P2.5**) solution by direct dissolution in water at 70 °C, under overnight stirring. 106

Figure 2.8. SLS plot of the Rayleigh ratio *vs* q^2 for (a) $PNAM_{96}$-*b*-$PTAm_{114}$ (**M2.4**) and (b) $PNAM_{96}$-*b*-$PTAm_{301}$ (**M2.5**) micelles in water with 10% error bars. This plot gave $M_w = 1.97 \times 10^4$ kg mol^{-1}, N_{agg} = 390 for **M2.4** (with a small thymine core) and $M_w = 4.7 \times 10^4$ kg mol^{-1}, N_{agg} = 431 for **M2.5** (with a large thymine core), respectively..... 107

Figure 2.9. The characterization of the copolymer **P2.8** (with an adenine block) in H_2O by SLS and SAXS analyses. (a). SLS plot of the Rayleigh ratio *vs* q^2 for **P2.8** (with an adenine block) gave M_w = 262 kg mol^{-1}, N_{agg} = 13; (b) SAXS analysis gave R_g = 6.9 nm for **P2.8** (with an adenine block). 108

Figure 2.10. Interactions between **P2.8** (with an adenine block) and micelle **M2.4** (with a small thymine core) result in a change in nanoparticle sizes. (a) Schematic of the micellar size decrease through hydrogen-bonding interactions between **P2.8** (with an adenine block) and micelle **M2.4** (with a small thymine core); (b) DLS hydrodynamic diameters (D_h) of micellar solutions of **M2.4** (with a small

thymine core) with increasing molar ratios of **P2.8** (with an adenine block); (c, d) TEM images of micellar solutions of **M2.4** (with a small thymine core) upon addition of 1 molar eq. and 5 molar eq. of **P2.8** (with an adenine block). 109

Figure 2.11. (a) DLS data of $PNAM_{96}$-*b*-$PTAm_{63}$ (**M2.6**) or $PNAM_{96}$-*b*-$PTAm_{160}$ (**M2.7**) micelle solutions mixed with different molar ratios of $PNAM_{96}$-*b*-$PAAm_{19}$ (**P2.8**); (b) DLS data of $PNAM_{96}$-*b*-$PTAm_{114}$ micelle **M2.4** solutions mixed with different molar ratios of the non-complementary copolymer $PNAM_{96}$-*b*-$PTAm_{17}$ (**P2.2**). 110

Figure 2.12. DLS analyses and TEM images of $PNAM_{96}$-*b*-$PTAm_{63}$ **M2.6** micelle solution mixed with different molar ratios of $PNAM_{96}$-*b*-$PAAm_{19}$ (**P2.8**). (a, e) 0 molar eq., (b, f) 1 molar eq., (c, g) 3 molar eq., (d, h) 5 molar eq. of $PNAM_{96}$-*b*-$PAAm_{19}$ (**P2.8**)..... 111

Figure 2.13. DLS analyses and TEM images of $PNAM_{96}$-*b*-$PTAm_{160}$ **M2.7** micelle solutions mixed with different molar ratios of $PNAM_{96}$-*b*-$PAAm_{19}$ (**P2.8**). (a, e) 0 molar eq., (b, f) 1 molar eq., (c, g) 3 molar eq., (d, h) 5 molar eq. of $PNAM_{96}$-*b*-$PAAm_{19}$ (**P2.8**). 112

Figure 2.14. ^1H NMR spectra of $PNAM_{96}$-*b*-$PAAm_{19}$ **P2.8**, $PNAM_{96}$-*b*-$PTAm_{114}$ **M2.4** micelle solution and their mixtures at different molar ratios in D_2O. 114

Figure 2.15. (a) Representative UV measurements of the mixture of $PNAM_{96}$-*b*-$PTAm_{114}$ **M2.4** (with a small thymine core) micelle solutions mixed with 5 molar eq. $PNAM_{96}$-*b*-$PAAm_{19}$ **P2.8** at different times. (b) The peak absorbance (262 nm) of UV-vis measurements of the mixture of $PNAM_{96}$-*b*-$PTAm_{114}$ **M2.4** micelle solutions mixed with 1, 3, and 5 molar eq. of $PNAM_{96}$-*b*-$PAAm_{19}$ **P2.8** at different times. 115

Figure 2.16. (a) SAXS experimental profiles of micellar solutions of **M2.4** (with a small thymine core) with 0, 1, 3 and 5 molar eq. of **P2.8** (with an adenine block). (b) Mean particle diameters determined for micellar solutions of **M2.4** (with a small thymine core) with 0, 1, 3 and 5 molar eq. of **P2.8** (with an

adenine block) by SAXS (D_g), DLS (D_h), and TEM (D_n). (c) Mean aggregation number (N_{agg}) determined for micelle solutions of **M2.4** (with a small thymine core) with 0, 1, 3 and 5 molar eq. of **P2.8** (with an adenine block) by SLS and SAXS and the theoretical aggregation number for a non-interacting mixture as calculated from Equation 2.1. 116

Figure 2.17. SAXS raw profiles, Guinier-Porod fits (left) and Guinier fits (right) for micellar solutions of **M2.4** (with a small thymine core) mixed with different molar ratios of **P2.8** (with an adenine block). (a) 0 molar eq., (b) 1 molar eq., (c) 3 molar eq., (d) 5 molar eq. of **P2.8** (with an adenine block). 118

Figure 2.18. Morphological transitions induced by the interactions between **P2.8** (with an adenine block) and micelles of **M2.5** (with a large thymine core). (a) Schematic of the morphological transition through hydrogen-bonding interactions between **P2.8** (with an adenine block) and micelles of **M2.5** (with a large thymine core); (b) DLS hydrodynamic diameters (D_h) of micelles of **M2.5** (with a large thymine core) with increasing molar ratios of **P2.8** (with an adenine block); (c-g) TEM images of micelles of **M2.5** (with a large thymine core) with 1, 3, 5, 10 and 20 molar eq. of **P2.8** (with an adenine block). 121

Figure 2.19. DLS analyses of $PNAM_{96}$-*b*-$PTAm_{301}$ **M2.5** micelle solutions mixed with different molar ratios of $PNAM_{96}$-*b*-$PAAm_{19}$ (**P2.8**). (a) 0 molar eq., (b) 1 molar eq., (c) 3 molar eq., (d) 5 molar eq., (e) 20 molar eq. of $PNAM_{96}$-*b*-$PAAm_{19}$ (**P2.8**). 122

Figure 2.20. DLS hydrodynamic diameters (D_h) of micellar solutions of **M2.4** (with a small thymine core) and **M2.5** (with a large thymine core) with increasing quantity of **P2.8 (with an adenine block)**. (a, b) D_h of micellar solutions of **M2.4** (with a small thymine core) with increasing quantity of **P2.8** (with an adenine block) using copolymer molar ratio and A:T ratio, respectively; (c, d) D_h of micellar solutions of **M2.5** (with a large thymine core) with increasing quantity of **P2.8** (with an adenine block) using copolymer molar ratio and A:T ratio, respectively**.** 123

Figure 2.21. ^{1}H NMR spectra of PNAM$_{96}$-*b*-PAAm$_{19}$ (**P2.8**), PNAM$_{96}$-*b*-PTAm$_{301}$ **M2.5** micelle solution and their mixtures at different molar ratios in D_2O. 124

Figure 2.22. The peak absorbance of UV-vis measurements of the mixture of PNAM$_{96}$-*b*-PTAm$_{301}$ **M2.5** micelle solutions mixed with 1, 3, 5 and 20 molar eq. of PNAM$_{96}$-*b*-PAAm$_{19}$ **P2.8** at different times..... 125

Figure 2.23. SAXS experimental profiles and fittings of micellar solutions of **M2.5** (with a large thymine core) with 0, 1, 5 and 20 molar eq. of **P2.8** (with an adenine block). 126

Figure 2.24. SAXS raw profiles, Guinier-Porod fits (left) and Guinier fits (right) for micellar solutions of **M2.5** (with a large thymine core) mixed with different molar ratios of **P2.8** (with an adenine block). (a) 0 molar eq., (b) 1 molar eq., (c) 3 molar eq., (d) 5 molar eq., (e) 10 molar eq., (f) 15 molar eq., (g) 20 molar eq. of **P2.8** (with an adenine block)..... 129

Figure 2.25. ^{1}H NMR and ^{13}C NMR spectra of 2-(((butylthio)carbonothiolyl)thio)propanoic acid (CTA) in $CDCl_3$. 140

Figure 3.1. ^{1}H NMR spectra of PNAM$_{39}$, **PA1** (PNAM$_{39}$-*b*-PAAm$_{20}$) and **PT1** (PNAM$_{39}$-*b*-PTAm$_{300}$) by ^{1}H NMR spectroscopy (400 MHz) in DMSO-d_6..... 155

Figure 3.2. SEC traces of PNAM$_{39}$, **PA1** (PNAM$_{39}$-*b*-PAAm$_{20}$) and **PT1** (PNAM$_{39}$-*b*-PTAm$_{300}$) by DMF SEC, with poly(methyl methacrylate) (PMMA) standards..... 156

Figure 3.3. Micelles with different morphologies were prepared through mixing complementary **PA1** solution into the initial spherical micelle **MT1** under stirring at room temperature. Dry-state TEM images on graphene oxide of micelle **MT1** after adding **PA1** with variable molar ratios of **A:T**. (a) 0, (b) 0.07, (c) 0.20, (d) 0.33, (e) 0.67, (f) 1.00, (g) 1.33; scale bars = 200 nm. 158

Figure 3.4. DLS analysis of self-assemblies **MT1** of PNAM$_{39}$-*b*-PTAm$_{300}$ **PT1** in water..... 158

Figure 3.5. ^{1}H NMR spectra of **PS** (PNAM$_{39}$-*b*-PSt$_{20}$), **PT2** (PNAM$_{39}$-*b*-PTAm$_{20}$) and **PA^{Me}** (PNAM$_{39}$-*b*-PMAAm$_{20}$) by ^{1}H NMR spectroscopy (400 MHz) in deuterated DMSO. 160

Figure 3.6. SEC traces of **PS** (PNAM$_{39}$-*b*-PSt$_{20}$), **PT2** (PNAM$_{39}$-*b*-PTAm$_{20}$) and **PA^{Me}** (PNAM$_{39}$-*b*-PMAAm$_{20}$) by DMF SEC, with poly(methyl methacrylate) (PMMA) standards. 160

Figure 3.7. Variation of hydrodynamic diameter of the mixture of micelle with non-complementary copolymers as determined by DLS analyses. (a) Micelle **MT1** with **PS**; (b) micelle **MT1** with **PT2**; (c) micelle **MT1** with **PA^{Me}**. 161

Figure 3.8. DLS analyses of small aggregated formed in water by (a) **PS**; (b) **PT2**; (c) **PA^{Me}**. 162

Figure 3.9. No morphological transitions were induced by non-complementary diblock copolymers through hydrophobic effects. Dry-state TEM images on graphene oxide of micelles **MT1** after adding **PS**, **PT2** and **PA^{Me}** with molar ratios of (a) **St:T** = 1.00; (b) **T:T** = 1.00; (c) **A^{Me}:T** = 1.00; scale bars = 200 nm. 163

Figure 3.10. TEM images of **PS** aggregates formed in water; scale bar = 200 nm. 163

Figure 3.11. (a) ^{1}H NMR spectra of **PT^{Me}** (PNAM$_{39}$-*b*-PMTAm$_{300}$) by ^{1}H NMR spectroscopy (400 MHz) in deuterated DMSO; (b) SEC traces of **PT^{Me}** (PNAM$_{39}$-*b*-PMTAm$_{300}$) by DMF SEC, with poly(methyl methacrylate) (PMMA) standards. 164

Figure 3.12. (a) DLS analysis of micelle **MT^{Me}** in water; (b) TEM images of micelle **MT^{Me}**; scale bar = 200 nm. 164

Figure 3.13. No morphological transitions were induced by non-complementary diblock copolymers through hydrophobic effects. (a) Variation of hydrodynamic diameter of the mixture of micelle **MT^{Me}** with non-complementary copolymers **PA1** as determined by DLS analyses; (b) dry-state TEM images of micelles **MT^{Me}** after adding **PA1** with molar ratios of **A:T^{Me}** = 1.00; scale bar = 200 nm. 165

Figure 3.14. AFM analyses of **MT1** micelle after adding **PA1** with different molar ratios of **A:T**. (a) 0, (b) 0.07, (c) 0.20. Micelles with different morphologies were prepared through mixing complementary **PA1** solution into the initial spherical micelle **MT1** under stirring at room temperature. The micelle solutions (0.1 mg mL^{-1}) were drop cast on silicon surface for AFM imaging. The average height was obtained from the measurement of at least 10 micelles. 167

Figure 3.15. DLS analysis of **MT** micelles after adding **PA1** with the molar ratios of **A:T** = 0.20. 169

Figure 3.16. Morphological change from (a) spheres **MT1** to (b) dumbbells (**A:T** = 0.20) then to (c) worms (**A:T** = 0.33) by adding complementary copolymers validated by cryo-TEM imaging; scale bars = 100 nm. 170

Figure 3.17. TEM images of micelles consisting of **PA1** and **PT1** prepared through a solvent switch method with different molar ratios of **A:T**. (a) 0.33; (b) 0.67; (c) 1.00; scale bars = 200 nm. 171

Figure 3.18. Variation of the hydrodynamic diameter of the micelle consisting of **PA1** and **PT1** (**A:T** = 1.00) with temperature as determined by DLS. 171

Figure 3.19. TEM images and DLS analyses of micelle **MT1** after stepwise addition of **PA1** with different molar ratios of **A:T**. Dry-state TEM images on graphene oxide of micelle **MT1** after adding **PA1** with different **A:T** molar ratios: (a) 0.33; (b) 0.67; (c) 1.00; scale bars = 200 nm. (d) Variation of hydrodynamic diameters of the mixtures of micelle **MT1** with complementary copolymers **PA1** by adding stepwise as determined by DLS analyses 173

Figure 3.20. (a) DLS analyses of small aggregated formed in water by **PA1**; (b) A plot of the scattered light intensity obtained for various concentrations of **PA1** in water. The intersection of the two lines at *ca.* 0.09 mg mL^{-1} corresponds to the critical micelle concentration (CMC). 174

Figure 3.21. ^{1}H NMR spectra of **PA1** ($PNAM_{39}$-*b*-$PAAm_{20}$), **PA2** ($PNAM_{39}$-*b*-$PAAm_{10}$) and **PA3** ($PNAM_{39}$-*b*-$PAAm_{30}$) with different lengths of the hydrophobic block by ^{1}H NMR spectroscopy (400 MHz) in deuterated DMSO. 175

Figure 3.22. SEC traces of **PA1** ($PNAM_{39}$-*b*-$PAAm_{20}$), **PA2** ($PNAM_{39}$-*b*-$PAAm_{10}$) and **PA3** ($PNAM_{39}$-*b*-$PAAm_{30}$) with different lengths of the hydrophobic block by DMF SEC, with poly(methyl methacrylate) (PMMA) standards. 175

Figure 3.23. DLS analyses and TEM images of micelle **MT1** after adding complementary copolymers **PA2** and **PA3** with different hydrophobic chain lengths at different molar ratios of **A:T**. (a) Variation of hydrodynamic diameters of the mixtures of micelle **MT1** with complementary copolymers **PA1-3** as determined by DLS analyses. Dry-state TEM images on graphene oxide of micelle **MT1** after adding (b-d) **PA2** and (e-g) **PA3** with different **A:T** molar ratios: (b, e) 0.33; (c, f) 0.67; (d, g) 1.00; scale bars = 200 nm. 176

Figure 3.24. ^{1}H NMR spectra of **PA1** ($PNAM_{39}$-*b*-$PAAm_{20}$), **PA4** ($PNAM_{96}$-*b*-$PAAm_{20}$) and **PA5** ($PNAM_{295}$-*b*-$PTAm_{20}$) with different lengths of the hydrophobic block by ^{1}H NMR spectroscopy (400 MHz) in deuterated DMSO. 178

Figure 3.25. SEC traces of $PNAM_{295}$ and **PA5** ($PNAM_{295}$-*b*-$PAAm_{20}$) analyzed by DMF SEC, with poly(methyl methacrylate) (PMMA) standards. 178

Figure 3.26. DLS analyses and TEM images of micelle **MT1** after adding complementary copolymers **PA4** and **PA5** with different hydrophilic chain lengths at different molar ratios of **A:T**. (a) Variation of hydrodynamic diameters of the mixtures of micelle **MT1** with complementary copolymers **PA4-5** as determined by DLS analyses. DLS analyses of **PA1** was also shown for comparison. Dry-state TEM images on graphene oxide of micelle **MT1** after adding (b-d) **PA4** and (e-g) **PA5** with different **A:T** molar ratios: (b, e) 0.33; (c, f) 0.67; (d, g) 1.00; scale bars = 200 nm. 180

Figure 3.27. TEM images and DLS analyses of micelle **MT1** after stepwise adding (a-c) **PA2** and (d-f) **PA3** with different molar ratios of **A:T**: (a, d) 0.33; (b, e) 0.67; (c, f) 1.00; scale bars = 200 nm. 181

Figure 3.28. TEM images and DLS analyses of micelle **MT1** after stepwise adding (a-c) **PA4** and (d-f) **PA5** with different molar ratios of **A:T**: (a, d) 0.33; (b, e) 0.67; (c, f) 1.00; scale bars = 200 nm. 181

Figure 3.29. TEM images of micelle **MT1** after adding (a-b) **PA4** and (c-d) **PA5** consisting of different hydrophilic chain lengths with different **A:T** molar ratios: (a, c) 0.07; (b, d) 0.20; scale bar = 200 nm. 182

Figure 3.30. (a-d) Dry-state TEM images on graphene oxide of micelles after stepwise addition of **PA1** into the seeded micelle solution consisting of **MT1** micelle with **PA1** having **A:T** molar ratio of 0.33. **A:T** molar ratios in total: (a) 0.33; (b) 0.40; (c) 0.53; (d) 0.67; scale bars = 500 nm. (e) Analyses of contour lengths and widths of the worms in Figure 3.30a-d. 184

Figure 3.31. ^{1}H, ^{13}C NMR spectra of 3-(*N*6, *N*6-dimethyladenine-9-yl)propyl acrylamide (MAAm). 189

Figure 3.32. ^{1}H, ^{13}C NMR spectra of 3-(3-methylthymin-1-yl)propyl acrylamide (MTAm). 191

Figure 4.1. SEC traces (DMF + 5 mM NH_4BF_4 as eluent) of nucleobase-containing diblock copolymers **P4.2**-**P4.5**. 204

Figure 4.2. ^{1}H NMR (400 MHz) spectra of nucleobase-containing diblock copolymers **P4.2**-**4.5** in DMSO-d_6. 205

Figure 4.3. DLS analysis of the mixed-corona micelles in water (0.5 mg mL^{-1}). (a) **M4.2**; (b) **M4.3**; (c) **M4.4**; (d) **M4.5** at 15 °C and (e) **M4.2**; (f) **M4.3**; (g) **M4.4**; (h) **M4.5** at 60 °C..... 207

Figure 4.4. Variation of the hydrodynamic diameter (D_h) of the mixed-corona micelles **M4.4** (0.5 mg mL^{-1}) with temperature, as determined by DLS analysis. 208

Figure 4.5. TEM images (stained with uranyl acetate) and histograms of number-average diameter distribution of **M4.4** at (a, b) 20 °C and (c, d) 60 °C; scale bar: 200 nm. 209

Figure 4.6. Variation of the hydrodynamic diameter (D_h) of the micelle **M4.6** (0.5 mg mL^{-1}) (which consisted of micelle **M4.1** and $PNIPAM_{262}$ **P4.6**). 210

Figure 4.7. Plot of Kc/R_θ *vs* q^2 for the mixed-corona micelle **M4.4** (0.5 mg mL^{-1}) at 15, 35 and 50 °C with 10% error bars. Static light scattering (SLS) measurements were conducted from 50° to 150° with an interval of 10° against a toluene standard. 211

Figure 4.8. Variation of the hydrodynamic diameter (D_h) of **M4.7** (which consisted of micelle **M4.1** and $PNAM_{295}$-*b*-$PAAm_{20}$ **P4.7**) (0.5 mg mL^{-1}). 212

Figure 4.9. DLS analysis of the mixed-corona micelles **M4.2**-**4.5** (0.5 mg mL^{-1}) with different PNIPAM chain lengths heated from 15 to 60 °C. 213

Figure 4.10. Reversible size change (D_h) of mixed-corona micelles **M4.2**-**4.5** (0.5 mg mL^{-1}) at both 15 and 60 °C. Error bars show size dispersity (PD). 215

Figure 4.11. ^1H and ^{13}C NMR spectra of 5-(3-bromo-4-(isopropylamino)-2,5-dioxo-2,5-dihydro-1H-pyrrol-1-yl)-2-cyanopentan-2-yl ethyl carbonotrithioate (CPET-ABM) in $CDCl_3$. 217

Figure 4.12. Demonstration of a reversible fluorescence ON/OFF switch using ABM-tagged mixed-corona nanoparticles and fluorescence spectra (λ_{ex} = 350 nm) of a mixed-corona micelle **M4.8** at 25 (black) and 40 °C (red). 219

Figure 4.13. Fluorescence spectra of (a) micelle **M4.4** which does not contain the aminobromomalemide (ABM) probe; (b) the mixed-corona micelle **M4.9** which consisted of micelle **M4.1** and ABM-attached $PNAM_{244}$-*b*-$PAAm_{20}$ **P4.9** and (c) mixed micelle which consisted of micelle **M4.1** and ABM-attached $PNIPAM_{40}$-*b*-$PAAm_{20}$ at 25 and 40 °C. 221

Figure 4.14. Reversible fluorescence emission intensity of **M4.8** at 488 nm at 25 °C and 40 °C for five consecutive heating and cooling cycles, λ_{ex} = 350 nm. 222

Figure 4.15. ^{1}H NMR and ^{13}C NMR spectra of D-mannose containing RAFT CTA in DMSO-d_6. 224

Figure 4.16. DLS analysis of (a) micelle **M4.10** and (b) mixed-corona micelle **M4.11** (0.5 mg mL^{-1}) in water at 15 °C. 226

Figure 4.17. Controlled ligand display on the mixed-corona micelle surface. (a) Agglutination assay of mixed-corona micelle **M4.11** with Con A at 25 and 40 °C; Con A without M4.11 at 40 °C showing no agglutination; (b) Fluorescence spectra of **M4.11** at 25 and 40 °C, λ_{ex} = 350 nm. 227

Figure 4.18. ^{1}H and ^{13}C NMR spectra of 2-cyano-5-hydroxypentan-2-yl ethyl carbonotrithioate (CPET) in $CDCl_3$. 232

Figure 4.19. ^{1}H and ^{13}C NMR spectra of 2-cyano-5-(3,4-dibromo-2,5-dioxo-2,5-dihydro-1H-pyrrol-1-yl)pentan-2-yl ethyl carbonotrithioate (CPET-DBM) in $CDCl_3$. 234

Figure 5.1. ^{1}H NMR spectra of PNAM$_{96}$-*b*-PAAm$_{19}$ (**PA**) (a) before and (b) after end group removal and DMF SEC traces of PNAM$_{96}$-*b*-PAAm$_{19}$ (**PA**) before and after end group removal (c) RI and (d) UV response at 309 nm. 249

Figure 5.2. ^{1}H NMR spectra of PNAM$_{96}$-*b*-PTAm$_{18}$ (**PT**) (a) before and (b) after end group removal and DMF SEC traces of PNAM$_{96}$-*b*-PTAm$_{18}$ (**PT**) before and after end group removal (c) RI and (d) UV response at 309 nm. 250

Figure 5.3. DLS analyses of (a) noncrosslinked micelle **M(A:T)** and (b) crosslinked micelle **Mi(A:T)** containing a complementary nucleobase core of A and T. 251

Figure 5.4. SLS plot of the Rayleigh ratio *vs* q^2 for (a) noncrosslinked micelle **M(A:T)** and (b) crosslinked micelle **Mi(A:T)** in water with 10% error bars. This plot gave $M_w = 3.03 \times 10^5$ g mol^{-1} and an average aggregation number $N_{agg} = 15$ for **M(A:T)** and $M_w = 3.18 \times 10^5$ g mol^{-1} and $N_{agg} = 16$ for **Mi(A:T)**. 252

Figure 5.5. Characterization of the crosslinked nanoparticles **Mi(A:T)**: a) TEM on graphene oxide[27] (scale bar = 50 nm); b) DLS analyses by scattered light intensity (blue), particle volume (red) and particle number (black); c) Fluorescence excitation ($\lambda_{em} = 415$ nm) and emission ($\lambda_{ex} = 365$ nm) spectra (inset **Mi(A:T)** solution under UV lamp (365 nm) with a red laser flux in the horizontal direction).... 253

Figure 5.6. SAXS raw profiles, Guinier-Porod fits (left) and Guinier fits (right) for mixed micelles (a) **M(A:T)** and (b) **Mi(A:T)**. 253

Figure 5.7. AFM image and the corresponding height profile of **Mi(A:T)** along the line labelled 1. .. 254

Figure 5.8. DLS analyses for nucleobase-containing nanoparticles (a) **M(A)**, (b) **Mi(A)**, (c) **M(T)** and (d) **Mi(T)**. 255

Figure 5.9. Cartoons showing the core compositions of irradiated micelles **Mi(A:T)**, **MiA**, **MiT**, **Mi(A+T^{Me})** and **Mi(9-hexylA:T)**, and (right) fluorescence emission spectra ($\lambda_{ex} = 365$ nm) for these particles, showing that no significant fluorescence was observed as a result of the absence or interruption of H-bonding, or detachment of A from the polymer backbone. 256

Figure 5.10. (a) Fluorescence spectra ($\lambda_{ex} = 365$ nm) of solutions (0.5 mg mL^{-1}) of **Mi(A:T)** and **Mi(A+T^{Me})**; the insets show the photos of **Mi(A:T)** and **Mi(A+T^{Me})** solutions under UV lamp (365 nm); (b) Illustration of the interruption of H-bonding in the core of micelle **Mi(A+T^{Me})** due to thymine methylation. 257

Figure 5.11. DLS and DMF SEC analyses of noncrosslinked micelle **M(A+T^{Me})** and crosslinked micelle **Mi(A+T^{Me})** containing nucleobase core which is incapable of H-bonding consisting of adenine (A) and methylated thymine (T^{Me}). DLS analyses of (a) **M(A+T^{Me})** and (b) **Mi(A+T^{Me})**; DMF SEC analyses of (c) **M(A+T^{Me})** and **Mi(A+T^{Me})**; (d) UV-vis spectra of solutions of **M(A+T^{Me})** and **Mi(A+T^{Me})** (0.1 mg mL^{-1}) and **MiA** (0.05 mg mL^{1}) after 12 h irradiation at 302 nm, illustrating high photodimerization (over 80%) of T^{Me}..... 258

Figure 5.12. SEC traces using DMF as solvent of (a) **MA** and **MiA**; (b) **MT** and **MiT**; (c) **M(A:T)** and **Mi(A:T)**. In cases where T was present in the core, a new peak at around 250 kDa appeared, attributed to the crosslinked nanoparticles, which could not disassemble even in a good solvent..... 259

Figure 5.13. The crosslinked micelle **Mi(9-hexylA:T)** from micelle **M(9-hexyl-A:T)** consisting of **PT** and small molecule 9-hexyladenine (9-hexylA). (a) Fluorescence spectra of **M(9-hexyl-A:T)** and **Mi(9-hexyl-A:T)**; (b) DMF SEC analyses of **M(9-hexyl-A:T)** and **Mi(9-hexyl-A:T)**..... 260

Figure 5.14. DLS analyses for nucleobase-containing nanoparticles **M(9-hexylA:T)** and **Mi(9-hexylA:T)**..... 261

Figure 5.15. UV-vis absorption (a) and fluorescence emission (b, λ_{ex} = 365 nm) spectra of **M(A:T)** after different irradiation times to form **Mi(A:T)**, showing the decrease in absorbance at 272 nm due to crosslinking of the T groups and the appearance of the characteristic fluorescence peak for the crosslinked nanoparticles..... 261

Figure 5.16. UV-vis spectra of micelles (a, b) **MiA**; (c, d) **MiT** containing an individual nucleobase core A or T at different concentrations ((a, c) 0.1 mg mL^{-1} and (b, d) 9.5 mg mL^{-1}) with different irradiation times..... 262

Figure 5.17. Calculated photodimerization degree of thymine in micelles **MiT** and **Mi(A:T)** using the drop in absorbance at 272 nm in UV-vis analyses with different irradiation times..... 263

Figure 5.18. Plot of fluorescence intensity of Mi(A:T) at 415 nm versus photodimerization degree showing the non-linear relationship. Error bars are the standard deviation from three experimental replicates. 263

Figure 5.19. UV-vis absorption spectrum of **M(A:T)** after different irradiation times to form **Mi(A:T)** at a higher concentration of 9.5 mg mL^{-1} showing the appearance of vibronic features with a principal peak at 362 nm. 264

Figure 5.20. Analysis of the observed fluorescence of **Mi(A:T)**. (a) Fluorescence spectra (λ_{ex} = 305 nm) of solutions (0.5 mg mL^{-1}) of **M(A:T)** and **Mi(A:T)**; (b) variation of the UV absorbance (at 362 nm) of **Mi(A:T)** (9.5 mg mL^{-1}) with the photodimerization degree of thymine as determined by UV-vis analyses; the inset shows UV-vis spectra of solutions of **Mi(A:T)** after different irradiation times. 265

Figure 5.21. Normalized TCSPC fluorescence lifetime decay spectra with residuals for **MiA**, **MiT**, **M(A:T)** and **Mi(A:T)** in water at 0.5 mg mL^{-1}, showing the similarity between the adenine-containing samples. The instrument response function (IRF, black) is also shown for comparison. 266

Figure 5.22. Synthesis and characterization of the hydrolyzable nanoparticle **Mi(A*:T*):** a) cartoon illustrating the crosslinking and subsequent disassembly of **Mi(A*:T*)** by hydrolysis to give **MiH(A*:T*)**; b) DMF SEC analysis of **Mi(A*:T*)** showing the persistent high molecular weight peak attributed to the crosslinked nanoparticle (orange trace) – following hydrolysis to produce **MiH(A*:T*)** (black trace) this peak disappeared and the trace indicated only the presence of free polymer; c) Fluorescence emission spectra (λ_{ex} = 365 nm) of **Mi(A*:T*)** and **MiH(A*:T*)** showing the loss of fluorescence upon hydrolysis; d) HPLC chromatogram showing the two low molecular weight species isolated upon hydrolysis of **Mi(A*:T*)** – MS analyses (shown above each peak) confirmed these to be the expected products. 268

Figure 5.23. ^{1}H NMR spectra of **Mi(A*:T*)** and separated $PNAM_{96}$-*b*-PAA_{19} from **MiH(A*:T*)**.... 269

Figure 5.24. The hydrolysis of micelle **Mi(A:T)** into **MiH(A:T)** showed no obvious change under the same conditions as **Mi(A*:T*)**. (a) SEC traces of **MiH(A:T)** using DMF as solvent; (b) fluorescence spectra (λ_{ex} = 365 nm) of **MiH(A:T)** (0.5 mg mL^{-1}). 270

Figure 5.25. Fluorescence spectra (λ_{ex} = 365 nm) of micelles **M(A:T)** and **Mi(A:T)** after heating at 60 °C overnight. 271

Figure 5.26. Effect of solvent conditions on **Mi(A:T)** fluorescence: a) Fluorescence emission spectra (λ_{ex} =365 nm) for **Mi(A:T)** dispersed in different solvents; b) Dependence of fluorescence emission intensity at 415 nm (λ_{ex} =365 nm) on aqueous solution pH for **Mi(A:T)** – data were scaled so that the emission intensity at pH 10 was 100 AU. 273

Figure 5.27. Dependence of fluorescence emission intensity at 415 nm (λ_{ex} = 365 nm) on different solvents for **Mi(A:T)** with irradiation times, *i.e.* different crosslink densities – data were scaled so that the emission intensity in water was 100 AU. 273

Figure 5.28. Dependence of fluorescence emission intensity at 415 nm (λ_{ex} = 365 nm) on aqueous solution with different NaCl concentrations for **Mi(A:T)**. 273

Figure 5.29. ^{1}H NMR and ^{13}C NMR spectra of 3-(adenine-9-yl)propyl acrylate (AAc) in DMSO-d_6. 280

Figure 5.30. ^{1}H NMR and ^{13}C NMR spectra of 3-(thymin-1-yl)propyl acrylate (TAc) in DMSO-d_6. . 283

List of schemes

Scheme 1.1. Mechanism of ROMP. 43

Scheme 1.2. A schematic representation of the steps of initiation, propagation, termination and transfer. I is the initiator and M is the monomer.[24] 44

Scheme 1.3. Schematic representation of the equilibrium in NMP. 45

Scheme 1.4. Chemical structures of commonly used nitroxides in NMP. 46

Scheme 1.5. Reaction mechanism of ATRP. 46

Scheme 1.6. Proposed mechanism of RAFT polymerization. Figure reproduced from ref.[43] 48

Scheme 1.7. Typical structures of RAFT chain transfer agent (CTA).[44] 49

Scheme 2.1. Syntheses of adenine and thymine acrylamide monomers (AAm and TAm). 97

Scheme 2.2. Synthetic routes for the preparation of $PNAM_{96}$ **P2.1** and the nucleobase-containing block copolymers, **P2.2-P2.8**. 101

Scheme 2.3. Synthesis of 2-(((butylthio)carbonothiolyl)thio)propanoic acid (CTA). 139

Scheme 3.1. Synthetic routes for $PNAM_{39}$, **PA1** ($PNAM_{39}$-*b*-$PAAm_{20}$) and **PT1** ($PNAM_{39}$-*b*-$PTAm_{300}$). 154

Scheme 3.2. Fabrication of thymine-containing core-functionalized micelles **MT1** and morphological transitions induced by adding distinct complementary nucleobase diblock copolymers **PA1-5**. 157

Scheme 3.3. The synthesis of 3-(*N*6, *N*6-dimethyladenine-9-yl)propyl acrylamide (MAAm)..... 188

Scheme 3.4. Synthesis of 3-(3-methylthymin-1-yl)propyl acrylamide (MTAm). 190

Scheme 4.1. Synthesis of $PNIPAM_x$-*b*-$PAAm_{20}$ **P4.2-4.5** with different DPs of PNIPAM. 203

Scheme 4.2. Synthesis of mixed-corona polymeric nanostructures **M4.2**–**4.7** through a supramolecular 'grafting to' approach mediated by complementary nucleobase interactions. 206

Scheme 4.3. Synthesis of an ABM functionalized RAFT agent (CPET-ABM). 216

Scheme 4.4. Synthesis of ABM functionalized PNIPAM$_{237}$-*b*-PAAm$_{20}$ **P4.8** and subsequent addition to **M4.1** to afford mixed micelles **M4.8** and D-mannose functionalized PNAM$_{98}$-*b*-PTAm$_{302}$ **P4.10** and subsequent assembly to afford micelles **M4.10** and mixed micelles **M4.11**..... 220

Scheme 4.5. Synthesis of the D-mannose containing RAFT CTA..... 248

Scheme 5.1. End group removal of PNAM$_{96}$-*b*-PAAm$_{19}$ (**PA'**) and PNAM$_{96}$-*b*-PTAm$_{18}$ (**PT'**). 248

Scheme 5.2. Synthesis of fluorescent nanoparticles by self-assembly and photocrosslinking of nucleobase-containing polymers. **PA** and **PT** were mixed in a 1:1 molar ratio and dissolved in water, to give micelles **M(A:T)** with complementary A:T base pairing in the core. Irradiation with UV light for 12 hours induced photodimerization of T and yielded fluorescent nanoparticles **Mi(A:T)**..... 251

Scheme 5.3. Synthesis of 3-(adenine-9-yl)propyl acrylate (AAc). 279

Scheme 5.4. Synthesis of 3-(thymin-1-yl)propyl acrylate (TAc)..... 282

List of tables

Table 1.1. Summary of polymerization methods, monomers, nucleobases and obtained DP of relevant nucleobase-containing polymers. Table adapted from ref.[101]..... 61

Table 2.1. Characterization data of macro-CTA and nucleobase-containing diblock copolymers. 102

Table 2.2. Comparison of the diameters and average-aggregation number, N_{agg} for micelles of **M2.4** (with a small thymine core) and **M2.5** (with a large thymine core). 107

Table 2.3. Different parameters of the fitted SAXS profiles given in Figure 2.17 using the Guinier fit and the Guinier-Porod fit. 117

Table 2.4. Different parameters of the fitted SAXS profiles given in Figure 2.24 using Guinier fit and Guinier-Porod fit..... 129

Table 3.1. Characterization of macroCTA and nucleobase-containing diblock copolymers. 155

Table 3.2. Summary of SLS characterization of **MT1** and **MT1** with **PA1** (**A:T** = 0.20). 169

Table 4.1. Characterization data of polymers **P4.1-4.10**. 204

Table 5.1. Summary of the SEC data (using DMF as an eluent) of nucleobase-containing diblock copolymers (**PA**, **PT**, **PT^{Me}**, **PA*** and **PT***) after end group removal. 247

Table 5.2. Emission lifetime for **MiA**, **MiT**, **M(A:T)** and **Mi(A:T)** solutions (λ_{ex} = 369 nm, λ_{em} = 415 nm). 266

Table 5.3. Relative quantum yields for **MA**, **MiA**, **MT**, **MiT**, **M(A:T)** and **Mi(A:T)** solutions with respect to quinine sulfate dihydrate.[31] 267

Acknowledgements

Firstly, I would like to thank my supervisor Prof. Rachel O'Reilly for her mentorship, invaluable advice, constant encouragements and helpful guidance throughout my PhD. Thank you for giving me the great opportunity to study and work in the group. I have been very grateful for her eagerness to help and support me in my future career. I also want to thank the University of Warwick and China Scholarship Council for offering me the scholarship, which has provided me enough support for both study and life here.

A massive thank-you must also go to all members of the O'Reilly group, past and present. All your help and advice make the past three and a half year good fun. Besides, I would like to thank Dr. Yan Kang for providing patient help and discussion in the beginning of my PhD, which made my project progress smoothly. I would acknowledge Dr. Tom Wilks and Mr. Rob Keogh, who offered invaluable help and advice for my projects and manuscripts. I thank Dr. Dafni Moatsou for helpful discussion about thymine photodimerization. I also thank Wei, Bo, Yujie, Jin and Gordon (All friends at 'the Chinese corner') for bringing me more fun and happiness and relieving my tiredness in the lab. Extra acknowledgements are given to those of you who have proof-read Chapters of this thesis: Jin, Lucy, Zac, Tom, Gordon, Jeff and Ben. Your advice and discussion from the reader's perspective have really improved my thesis.

In addition, I want to say thank-you to my great collaborators. Prof. Vasilios Stavros at Warwick is acknowledged for the helpful discussion and advice on fluorescent nucleobase nanoparticles project. Prof. Guosong Chen and Mr. Zhen Li are thanked for the help in the Sugar-ConA study and your hospitality during my visit to Fudan University made me happy in Shanghai. Prof. Alex Adronov and Mr. Darryl Fong at McMaster University are acknowledged for the help in the project of dispersing nanotubes using my polymers.

Finally, I want to thank my wife Yuan for her strong supports and kind encouragements. Without your constant love and help, I could not have finished my PhD. I want to say 'I love you and I will use my

whole life to prove it'. I also want to acknowledge my parents Mr. Zhongchao Hua and Mrs. Jiexiang Chen for their encouragements through my whole study life.

Declaration of authorship

This thesis is submitted to the University of Warwick in support of my application for the degree of Doctor of Philosophy. It has been composed by myself and has not been submitted in any previous application for any degree. The work presented (including data generated and data analysis) was carried out by the author except in the cases outlined below:

1. The SAXS data in Chapter 2 was collected and analyzed by Dr. Anaïs Pitto-Barry (University of Warwick).
2. The SLS data in Chapter 3 was analyzed by Dr. Joe Jones (University of Warwick).
3. The cryo-TEM images in Chapter 3 were obtained by Dr. Saskia Bakker (University of Warwick);
4. The syntheses of (2-aminoethyl)-α-D-mannopyranoside and 5-(3-bromo-4-(isopropylamino)-2,5-dioxo-2,5-dihydro-1H-pyrrol-1-yl)-2-cyanopentan-2-yl ethyl carbonotrithioate (CPET-ABM) in Chapter 4 were performed by Mr. Zhen Li (Fudan University, China) and Mr. Robert Keogh (University of Warwick), respectively.
5. The SAXS data in Chapter 5 was collected by Dr. Steven Huband (University of Warwick) and analyzed by Mr. Robert Keogh (University of Warwick).
6. HR Mass Spectra in Chapters 2-5 was analyzed by mass spectrometry group (University of Warwick).

Publications

1. Hua, Z.; Pitto-Barry, A.; Kang, Y.; Kirby, N.; Wilks, T. R.; O'Reilly, R. K. Micellar Nanoparticles with Tuneable Morphologies through Interactions between Nucleobase-Containing Synthetic Polymers in Aqueous Solution. *Polym. Chem.* **2016**, *7*, 4254-4262.

2. Kang, Y.; Pitto-Barry, A.; S. Rolph, M.; Hua, Z.; Hands-Portman, I.; Kirby, N.; O'Reilly, R. K. Use of Complementary Nucleobase-Containing Synthetic Polymers to Prepare Complex Self-Assembled Morphologies in Water. *Polym. Chem.* **2016**, *7*, 2836-2846.

3. Hua, Z.; Keogh, R.; Li, Z.; Wilks, T. R.; Chen, G.; O'Reilly, R. K. Reversibly Manipulating the Surface Chemistry of Polymeric Nanostructures *via* a "Grafting To" Approach Mediated by Nucleobase Interactions. *Macromolecules* **2017**, *50*, 3662-3670.

4. Fong, D.; Hua, Z.; Wilks, T. R.; O'Reilly, R. K.; Adronov, A. Dispersion of Single-Walled Carbon Nanotubes Using Nucleobase-Containing Poly(acrylamide) Polymers. *J. Polym. Sci., Part A: Polym. Chem.* **2017**, *55*, 2611-2617.

5. Hua, Z.; Wilks, T. R.; Keogh, R.; Herwig, G.; Stavros, V. G.; O'Reilly, R. K. Entrapment and Rigidification of Adenine by a Photo-Cross-Linked Thymine Network Leads to Fluorescent Polymer Nanoparticles. *Chem. Mater.* **2018**, *30*, 1408-1416.

Summary of thesis

This thesis explores the synthesis and self-assembly of nucleobase-containing acrylamide amphiphiles and investigates their self-assembly behaviors and potential applications in aqueous solutions.

In Chapter 1, the synthesis and self-assembly of block copolymers are briefly introduced. Then the effect of H-bonding interactions on self-assembly behaviours is highlighted. Finally, an overview of the synthesis, self-assembly and applications of synthetic nucleobase-containing polymers is presented.

Chapter 2 investigates the effect of complementary nucleobase interactions within micellar cores on the morphologies of self-assemblies in aqueous solutions. Self-assemblies with different core sizes of thymine are fabricated and their morphological transitions with introducing complementary copolymers are studied as well.

Chapter 3 systematically explores the pathway-dependent and complementary chain-selective morphological transitions of micelles with a thymine core. In addition, the complementary H-bonding within micellar cores is utilized to prepare a series of worms with different lengths and widths in aqueous media.

Chapter 4 builds on the knowledge obtained in the previous Chapters. A series of mixed corona micelles are fabricated through a simple supramolecular 'grafting-to' approach. By introducing protein ligands and environment-sensitive fluorophores at the end of corona, the reveal and concealment of functional groups on the micelle surface through heating and cooling are investigated.

Chapter 5 reveals the synergetic H-bonding and thymine photodimerization give a novel polymer fluorescent dots. A number of factors are investigated on the observed fluorescent properties, including the effect of blocking H-bonding interactions and changing the degree of core-crosslinking.

Finally, Chapter 6 summarizes the conclusions of Chapters 2-5 and provides some insights and outlines for the future work.

Abbreviations

A	adenine/adenosine/5'-acryloyladenine
$A^{Me}Am$	3-(*N*6, *N*6-dimethyladenine-9-yl)propyl acrylamide
AA	acrylic acid
AAc	3-(adenine-9-yl)propyl acrylate
AAm	3-(adenine-9-yl)propyl acrylamide
AFM	atomic force microscopy
AIBN	azobisisobutylonitrile
ATRP	atom transfer radical polymerization
BCPs	block copolymers
br	broad (^{1}H NMR)
c	concentration
CAC	critical aggregation concentration
$CDCl_3$	deuterated chloroform
$CHCl_3$	chloroform
CMC	critical micelle concentration
COSY	correlated spectroscopy
CRP	controlled radical polymerization
cryo-TEM	cryogenic transmission electron microscopy
CTA	chain transfer agent
d	days/doublet
DCM	dichloromethane
D_h	hydrodynamic diameters
DLS	dynamic light scattering

$Đ_M$	dispersity
DMF	dimethylformamide
DMF-d_7	deuterated dimethylformamide
DMSO	dimethyl sulfoxide
DMSO-d_6	deuterated dimethyl sulfoxide
d*n*/d*c*	the refractive index increment
DP	degree of polymerization
DSC	differential scanning calorimetry
D_t	translational diffusion coefficient
eq.	equivalents
FRP	free radical polymerization
GO	graphene oxide
HMBC	heteronuclear multiple-bond correlation
HMQC	heteronuclear multiple-quantum coherence
HR-MS	high resolution mass spectrometry
I(q)	scattering intensity
J	coupling constant
K_B	Boltzmann's constant
k_p	propagation rate constant
LCST	lower critical solution temperature
m	multiple (^{1}H NMR)
m/z	mass-to-charge ratio
macro-CTA	macromolecular chain transfer agent
MADIX	macromolecular design *via* the interchange of xanthates
M_n	number average molecular weight

M_w	weight average molecular weight
n	refractive index
N_{agg}	aggregation number
NMP	nitroxide-mediated radical polymerization/N-methyl-2-pyrrolidone
NMR	nuclear magnetic resonance
p	packing parameter
P4VP	poly(4-vinylpyridine)
PAA	poly(acrylic acid)
PAAc	poly(3-(adenine-9-yl)propyl acrylate)
PAAm	poly(3-(adenine-9-yl)propyl acrylamide)
PD	polydispersity
PDLA	poly(*D*-lactide)
PL	photoluminescence
PLA	polylactide
PLLA	poly(*L*-lactide)
PMAAm	poly(3-(*N*6, *N*6-dimethyladenine-9-yl)propyl acrylamide)
PMDETA	*N*,*N*,*N*′,*N*″,*N*″-pentamethyldiethylenetriamine
PMTAm	poly(3-(3-methylthymin-1-yl)propyl acrylamide)
PNAM	poly(4-acryloylmorpholine)
PNAM-*b*-PAAc	poly(4-acryloylmorpholine)-*b*-poly(3-(adenine-9-yl)propyl acrylate)
PNAM-*b*-PAAm	poly(4-acryloylmorpholine)-*b*-poly(3-(adenine-9-yl)propyl acrylamide)
PNAM-*b*-PS	poly(4-acryloylmorpholine)-*b*-poly(styrene)
PNAM-b-PTAc	poly(4-acryloylmorpholine)-*b*-poly(3-(thymin-1-yl)propyl acrylate)
PNAM-b-PTAm	poly(4-acryloylmorpholine)-*b*-poly(3-(thymin-1-yl)propyl acrylamide)
PNIPAM	poly(*N*-isopropylacrylamide)

PNIPAM-b-PAAm	poly(*N*-isopropylacrylamide)-*b*-poly(3-(adenine-9-yl)propyl acrylamide)
POEGMA	poly(oligo(ethylene glycol)methyl ether methacrylate)
PS	poly(styrene)
PTAc	poly(3-(thymin-1-yl)propyl acrylate)
PTAm	poly(3-(thymin-1-yl)propyl acrylamide)
PU	poly(5'-acryloyuridine)
PVBT	poly(vinylbenzylthymine)
q	quartet
q	scattering vector
r	reactivity ratio
r.t.	room temperature
RAFT	reversible addition-fragmentation chain transfer
R_g	radius of gyration
R_h	hydrodynamic radius
RI	refractive index
ROMP	ring-opening metathesis polymerization
R_θ	Rayleigh ratio
SAXS	small angle x-ray scattering
SEC	size exclusion chromatography
SEM	scanning electron microscopy
SET-LRP	single-electron transfer living radical polymerization
SLD	scattering length density
SLS	static light scattering
STEM	scanning transmission electron microscopy
$T^{Me}Am$	3-(3-methylthymin-1-yl)propyl acrylamide

T	absolute temperature
t	triplet
TEA	triethylamine
TEM	transmission electron microscopy
TEMPO	2,2,6,6-tetramethyl-1-piperidinoxyl
T_g	glass transition temperature
THF	tetrahydrofuran
TAc	3-(thymin-1-yl)propyl acrylate
TAm	3-(thymin-1-yl)propyl acrylamide
TMS	tetramethylsilane
U	uracil/5'-acryloyluridine
UV	ultraviolet
UV-vis	ultraviolet-visible
VBA	vinylbenzyladenine
VBT	vinylbenzylthymine
w	weight fraction
δ	chemical shift
η	viscosity of solvent
θ	angle
λ	wavelength
ρ-ratio	R_g /R_h

Chapter 1. Introduction

1.1. Mimicking biological functionality with synthetic polymers

Nature provides a wealth of models ranging from macroscopic to molecular levels for scientists and engineers to mimic. Aircraft are a good mimic of birds, but their wings are fixed. Many other novel properties of materials found in nature, such as the footpads of a gecko, the legs of water strider, spider silk, the adhesive secreted by mussels and to name but a few, also attract widespread interest and inspire scientists to fabricate superior materials using synthetic building blocks.

At the molecular level, biopolymers like nucleic acids and proteins consist of highly functional monomers and well-defined monomer sequences. Their outstanding properties are mainly based on the formation of unique 3-D structures upon folding their specific sequences. However, the precise synthesis of sequence-controlled polymers, which are expected to demonstrate comparable properties as biopolymer, is still in its infancy.

In the majority of natural biological systems, the major building blocks are made up of proteins, carbohydrates and nucleic acids, which are essentially polymers. These complex biopolymers are exceedingly sensitive to environment cues such as light, heat, pH and other interactive molecules. Their excellent properties enable the response of biological triggers and the modulation of the interaction between cells and tissues. Notably, it is exceedingly expensive and time-consuming to synthesize highly precise biopolymers at relatively large scales (such as in grams), even with the development of state of the art techniques. Synthetic polymers can be easily synthesized with similar structures as biopolymers and are considered as excellent building blocks for mimicking biological functionalities due to their low cost of synthesis and the ability to access multiple stimuli responses. A range of responsive polymers have been reported involving stimuli of temperature, light, salts, and pHs.[1] Meanwhile, many chemical triggers which are present *in vivo*, can also be utilized for the generation of novel polymeric nanomaterials.[2, 3]

1.2. Block copolymer (BCP) synthesis and self-assembly

Nowadays, synthetic polymers have become an indispensable part of our lives. Meanwhile, polymer science, as an independent discipline, has been widely accepted and developed, following great interest from both academic and industrial researchers. Due to their poor control over polymer structures, conventional polymerization methods might not be easily employed to synthesize polymers with novel properties. Control over polymerizations was achieved with the invention of "living" polymerization,[4] leading to the formation of a range of different polymer architectures and versatile applications. "Living" polymerizations are accepted as those that "retain their ability to propagate for a long time and grow to a desired maximum size while their degree of termination or chain transfer is still negligible".[5] The term "living" polymer was first introduced when styrene was observed to be able to further react on addition of monomer using anionic polymerization.[5] Up to now, "living" polymerizations mainly include anionic,[6] cationic,[7] group-transfer,[8] ring-opening,[9] ring-opening metathesis[10] and controlled radical polymerizations.[11-17] Block copolymers can be straightforwardly synthesized *via* "living" polymerization techniques. Many of these approaches are widely utilized for polymerization of functional monomers, so will be described further.

1.2.1. Ring-opening metathesis polymerization (ROMP)

ROMP is a type of olefin metathesis chain-growth polymerization that yields many industrially important products such as Vestenamer, Telene, Metton and Norsorex. An understanding of the mechanism of olefin metathesis is fundamental to the successful preparation of polymers using ROMP,[18-21] and was first elucidated by Nobel Prize winner Yves Chauvin and his colleagues (Scheme 1.1).[22]

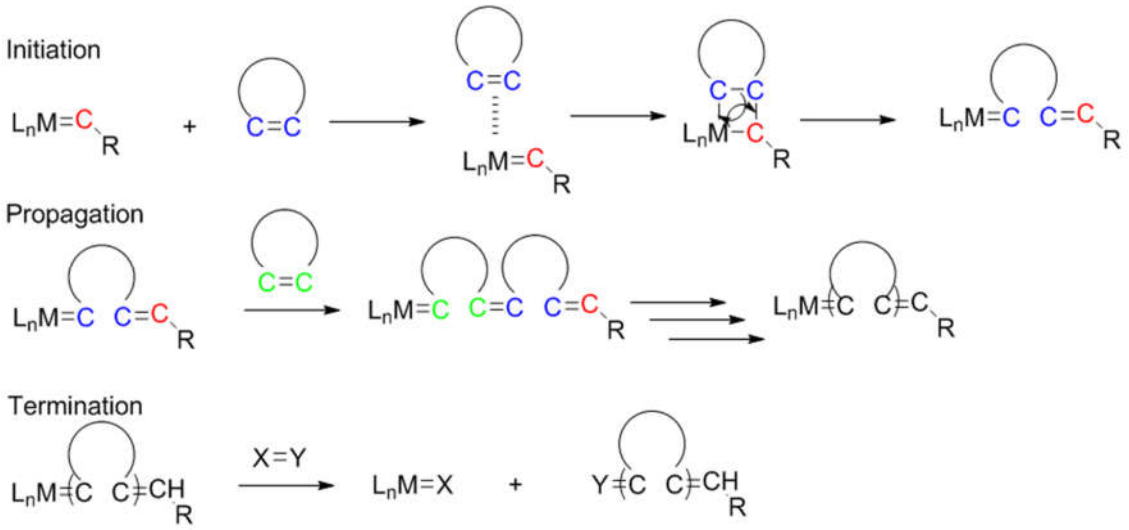

Scheme 1.1. Mechanism of ROMP.

The polymerization starts from the coordination between a metal carbene initiator and a cyclic olefin monomer (Scheme 1.1). A metallacyclobutane intermediate is formed *via* a [2+2] cycloaddition, which then undergoes a cycloreversion to incorporate the olefin monomer and generate a new metal carbene center. Repetitions of this process yield polymers with a metal carbene end group. Termination can occur when adding a quenching agent that removes and deactivates the metal from the end of the polymer chain *via* cross metathesis. The termination also provides an easy approach to achieving post-polymerization modification of the polymer.

1.2.2. Controlled radical polymerization

In the past two decades, the tremendous development of controlled radical polymerization (CRP) has enabled the facile synthesis of functional polymers/materials. Compared with other "living" polymerization methods, CRP avoids extremely stringent experimental conditions and overcomes poor functional group tolerance. Meanwhile, CRP usually does not require the use of relatively unstable catalysts, as in ROMP, which makes it one of the most widely used polymerization techniques among polymer chemists.

The term CRP was initially coined by Otsu as a result of his investigation of iniferters:[17, 23] compounds that can initiate, transfer, and terminate a radical polymerization. A generalized free radical polymerization (FRP) mechanism is shown in Scheme 1.2. The first step is initiation, in which a reactive radical is generated. The generated radical is highly reactive and tends to react with vinyl monomers. Secondly, propagation is the growth of polymer chains by addition of monomers to the chain end radical. Lastly, the reactive radical can be terminated by a combination of coupling and disproportionation of two chain end radicals to produce 'dead' polymers.

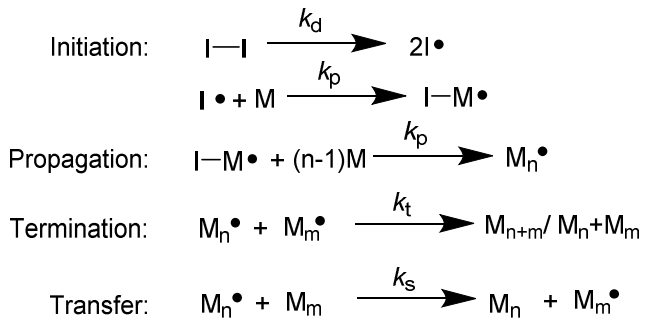

Scheme 1.2. A schematic representation of the steps of initiation, propagation, termination and transfer. I is the initiator and M is the monomer.[24]

The development of CRP was driven by the desire to avoid termination events, by controlling the concentration of polymer radicals in solution, and therefore achieving something closer to a living polymerization. The principal CRP techniques are nitroxide-mediated polymerization (NMP),[11] atom transfer radical polymerization (ATRP),[14, 16, 25, 26] single-electron transfer living radical polymerization (SET-LRP),[15, 27] reversible addition-fragmentation chain transfer (RAFT) polymerization,[13, 28] and macromolecular design *via* the interchange of xanthates (MADIX).[12, 29] The mechanisms of each are described in more detail below.

1.2.2.1. Nitroxide-mediated polymerization (NMP)

Among all CRP techniques, NMP was the first to be developed. It relies on the equilibrium between an active species that involves active radical chain ends and a dormant species whereby the polymer end is capped by combination with nitroxide radicals (Scheme 1.3).[11, 30-33]

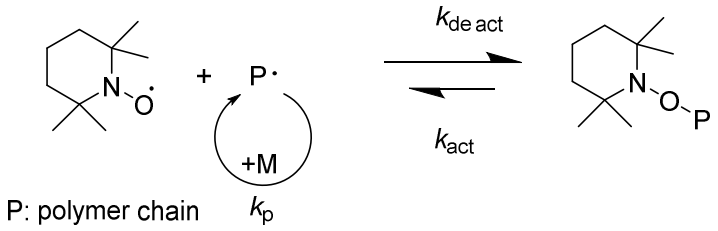

Scheme 1.3. Schematic representation of the equilibrium in NMP.

Although a range of monomer functionalities are compatible with NMP, it also suffers from some disadvantages, such as the need for high temperatures (commonly above 100 °C). This dramatically limits the successful polymerization of volatile monomers. However, new nitroxides have been prepared which significantly improve the monomer compatibility of NMP. Now, NMP can be performed at lower temperatures and is compatible with a variety of monomers including styrenes, acrylates, acrylamides, 1,3-dienes and acrylonitriles. The alkoxyamine initiators introduced in NMP commonly include 2,2,6,6-tetramethyl-1-piperidinyloxy (TEMPO), 2,2,5-trimethyl-4-phenyl-3-azahexane-*N*-oxyl (TIPNO) and *t*-butyl 1-diethylphosphono-2,2-dimethylpropyl nitroxide (DEPNO) (Scheme 1.4). Recent work also demonstrated the successful polymerization of methacrylates, which used to be difficult to polymerize using NMP.[34-36] Several inherent limitations of NMP, including slow polymerization kinetics, high polymerization temperatures and a narrow range of monomers, have led to the slightly less applications than ATRP and RAFT polymerizations in polymer synthesis.[34]

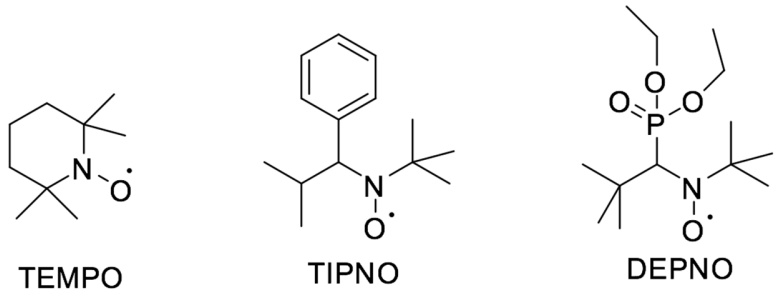

Scheme 1.4. Chemical structures of commonly used nitroxides in NMP.

1.2.2.2. Transition metal-catalyzed polymerizations

Matyjaszewski *et al.* and Sawamoto *et al.* in 1995 separately described the polymerization of styrene and methyl methacrylate, respectively, in the presence of transition metal complexes.[14, 16] Widely known as atom transfer radical polymerization (ATRP), this method relies on the equilibrium between the propagating polymers and its dormant species mediated by the metal catalyst. Since the dormant form of the polymer is dominant, side reactions are significantly suppressed, providing good control over the polymerization. Upon transfer of the (pseudo)halogen from the polymer chain end to the transition metal complex, the propagating radical is formed while the transition metal adopts a higher oxidation state (Scheme 1.5).[37]

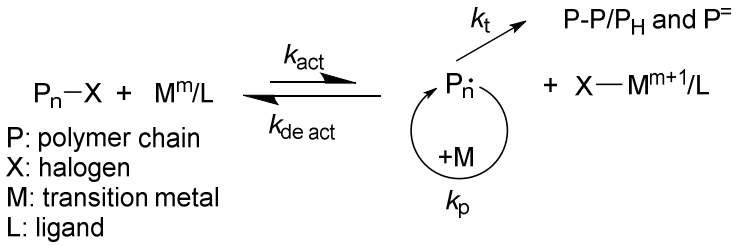

Scheme 1.5. Reaction mechanism of ATRP.

ATRP is a versatile polymerization method with the ability to polymerize a wide range of monomers under mild conditions and in a variety of solvents (as well as in bulk), thus making it attractive in many applications. An interesting development has also been the use of zero valent metals as the catalytic

species in polar solvents (DMSO and water), named as single-electron transfer living radical polymerization (SET-LRP).[38] The mechanism of SET-LRP has been extensively studied by Percec *et al*.[38] Notably, the mechanism is still under debate,[39] but it has already proved to be a powerful tool in the synthesis of well-defined polymers.[40, 41]

1.2.2.3. Reversible addition-fragmentation chain transfer polymerization (RAFT)

RAFT polymerization was first reported by Moad, Rizzardo, and Thang *et al.* in Australia.[13] A few months before that, a similar process called MADIX was reported in France.[42] The same mechanism is followed by both RAFT polymerization and MADIX and the only difference between them is the structure of the polymerization mediators. MADIX is limited to the use of xanthates as chain transfer agents (CTA). RAFT polymerization generally offers faster polymerization kinetics and lower polymerization temperatures than NMP and allows versatile monomers to be polymerized with the same initiation system. Meanwhile, it also avoids the utilization of metal catalysts which might decrease the biological toxicity in potential medical applications. For these reasons, RAFT was chosen to prepare the polymers described in this thesis, so the mechanism is discussed in greater detail below.

The mechanism of RAFT polymerization is distinct from ATRP and NMP. In RAFT polymerization, control is not achieved by equilibrium between a dormant species and its corresponding active radical chain end, but by an equilibrium between polymer chains through a reversible transfer reaction normally using a thiocarbonylthio as the chain transfer agent (CTA), giving all polymer chains equal opportunities to propagate and thus achieving a controlled polymerization. A general mechanism of RAFT polymerization is shown in Scheme 1.6, which commonly consists of the steps of a general FRP (initiation (steps I and II), propagation (steps IV and V), and termination (step VI) steps) and extra chain transfer (step III) and equilibration (step V) steps.[43]

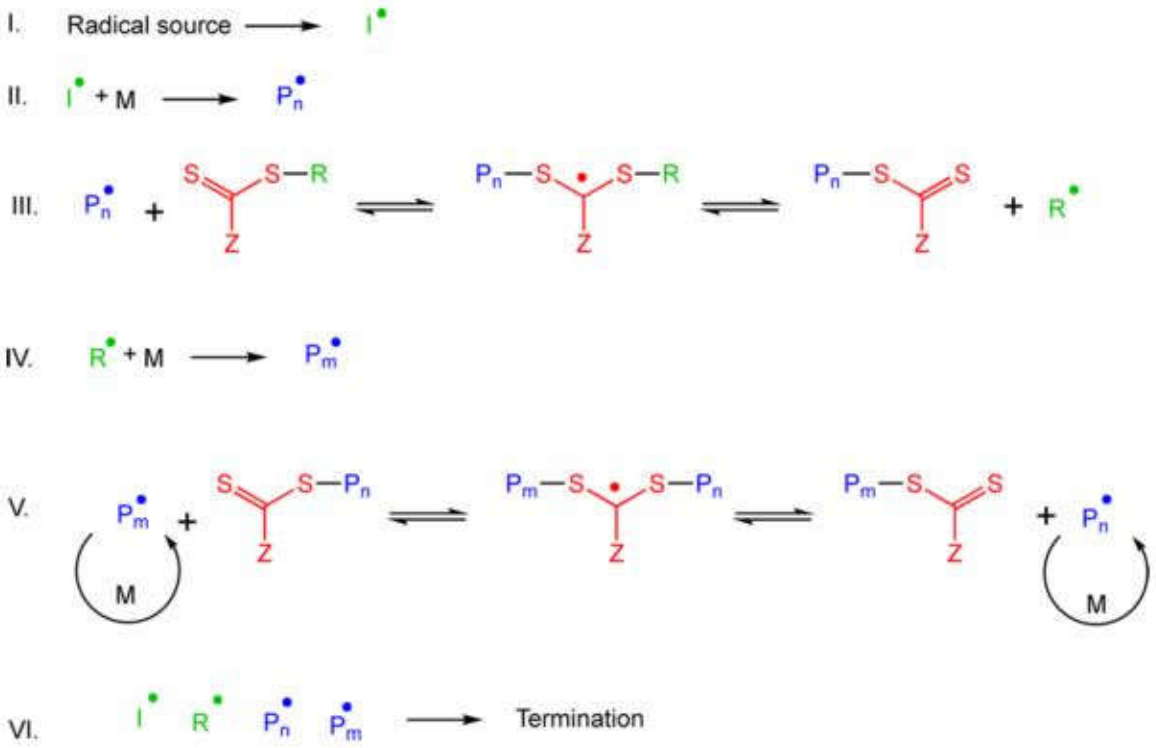

Scheme 1.6. Proposed mechanism of RAFT polymerization. Figure reproduced from ref.[43]

The amount of initiator added is usually low for RAFT polymerization. Thus, the probability of undesired chain termination or the generation of 'dead' chains is remarkably decreased. RAFT can give polymers with controlled molecular weights and narrow molecular weight distributions. In addition, as termination is dramatically decreased, the majority of polymers consist of the re-initiating R group at one end and a thiocarbonylthio group at the other end.

In RAFT, theoretical molecular weight $M_{n,th}$ at time t is given by Equation 1.1:[43]

$$M_{n,th} = \frac{[M]_0 p M_M}{[CTA]_0 + 2f[I]_0(1 - e^{-k_d t})\left(1 - \frac{f_c}{2}\right)} + M_{CTA} \qquad \text{(Equation 1.1)}$$

where $[M]_0$, $[CTA]_0$, and $[I]_0$ are the initial concentrations of monomer, CTA and initiator, respectively. The term $1 - f_c/2$ represents the number of chains produced in a radical−radical termination event with f_c the coupling factor. p, f, and k_d is the monomer conversion, the initiator efficiency and the decomposition

rate coefficient of the initiator. M_M and M_{CTA} are the molar masses of monomer and chain transfer agent, respectively.

In practice, this equation is usually simplified to Equation 1.2:[43]

$$M_{n,th} = \frac{[M]_0 p M_M}{[CTA]_0} + M_{CTA} \qquad \text{(Equation 1.2)}$$

One of the key features of RAFT polymerization is its ability to polymerize an extensive range of functional monomers. The typical structure of a CTA is shown in Scheme 1.7, where both Z and R groups affect the efficiency of the CTA.[28, 44]

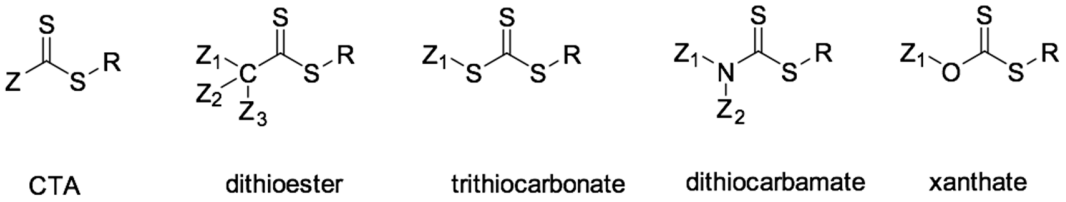

Scheme 1.7. Typical structures of RAFT chain transfer agent (CTA).[44]

By judicious choice of the CTA, successful control over the polymerization of either "more activated" monomers (MAMs) or "less activated" monomers (LAMs) (Figure 1.1) can be achieved. MAMs usually have a relatively stable vinyl group, which is conjugated to a double bond, an aromatic ring, a carbonyl group, or a nitrile (*e.g.*, butadiene, styrene, vinylpyridine, (meth)acrylates, (meth)acrylamides, maleic anhydride, maleimide and acrylonitrile). "Less activated" monomers (LAMs) contain a double bond adjacent to oxygen, nitrogen, halogen, sulfur lone pairs, or saturated carbons (*e.g.*, vinyl acetate, N-vinylpyrrolidone, vinyl chloride, 1-alkenes). The monomer compatibility in RAFT polymerization mainly arises from the reactivity of the added CTA. The key to a successful RAFT polymerization is to ensure that the C=S bond in the CTA is more reactive to radical addition than the C=C bond of the monomer, and this is achieved by careful selection of both the Z- and R-group. General guidelines for the selection of the Z- and R-group are also shown in Figure 1.1.[43]

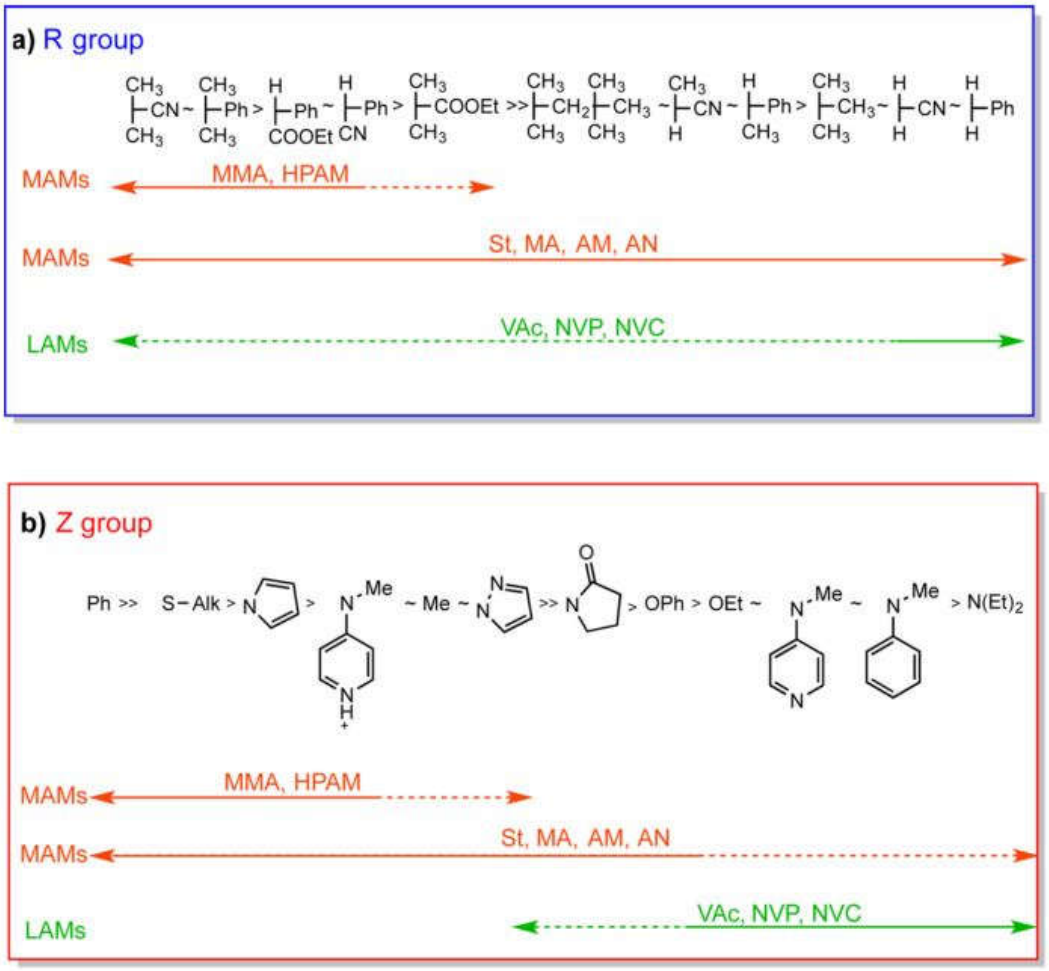

Figure 1.1. General guidelines for the selection of the Z- and R-group of RAFT agents for various polymerizations. Figure reproduced from ref.[43]

The Z-group is mostly responsible for the reactivity of the C=S bond toward the addition of the radical and effectively controls the stability of the intermediate radical (Scheme 1.6). Due to the effective electronic delocalization by the substituent, the polymerization of MAMs normally produces more stabilized radicals and therefore it is important to choose a Z-group that will help with the stabilization of the intermediate radical, to favour the addition of radical to the C=S. Therefore, trithiocarbonate (Z = *S*-alkyl) or dithiobenzoate (Z = Ph) CTAs are usually selected to achieve the polymerization of MAMs. In stark contrast, the high reactivity of LAMs makes them poor homolytic leaving groups. The controlled polymerization of LAMs requires intermediate radicals to be less stable, by using xanthates (Z = *O*-alkyl)

or dithiocarbamates (Z = *N*-alkyl), to favour the fragmentation of the propagating radical. The lone pair of electrons on oxygen (xanthates) and nitrogen (dithiocarbamates) is delocalized in the thiocarbonyl group and therefore deactivates the C=S bond toward radical addition and destabilizes the radical intermediate. This effect therefore promotes propagation and intermediate fragmentation, thus enabling control over the polymerization of LAMs.

The role of the R-group is much more subtle. The R group should be a good leaving group and also controls the re-initiation steps. It also contributes to the stabilization of the intermediates although it is less important compared to the Z group. Typically, good R-groups are groups that mimic monomer radicals or thermal initiators such as AIBN. Meanwhile, the lower sensitivity of RAFT reactivity to the choice of R group provides a feasible route to functionalize the CTA. Thus, reasonable control over polymerization and incorporation of functional handles can be easily targeted through functionalizing the R group of a CTA.

The major disadvantages of RAFT polymerization are the use of toxic and odorous starting materials such as carbon disulfide and thiol-containing alkyls to make CTAs, and the colored polymers obtained. The first disadvantage is not easy to avoid, even though synthetic improvements have been gradually achieved.[45] The second drawback sometimes can be turned into an advantage by removing or transforming the end groups into other functionalities.[46, 47] Among all CRP techniques, RAFT polymerization appears to be one of the most versatile techniques in terms of the mild reaction conditions and the compatibility with various functionalities.

1.2.3. BCP Self-Assembly

The development of "living" polymerizations, such as CRP, has allowed access to polymers with various compositions and architectures (Figure 1.2), including amphiphilic block copolymers (BCPs).[48]

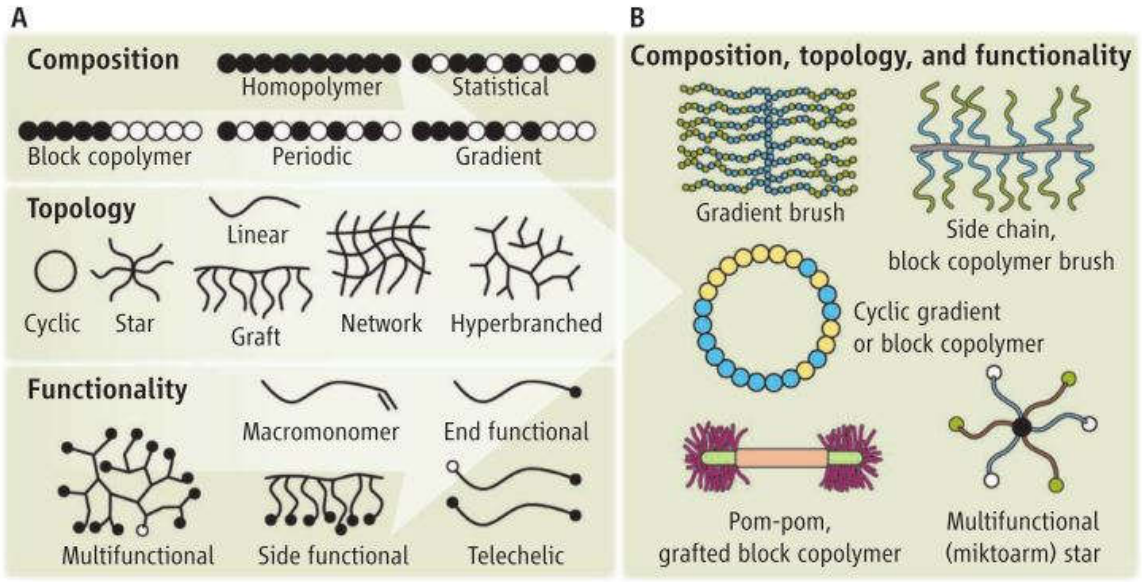

Figure 1.2. Macromolecular architectural guide. The three main aspects of polymer architecture – composition, topology, and function – are shown separately in (**A**) and in combination in (**B**). Figure reproduced from ref.[48]

Self-assembly of amphiphilic BCPs occurs in selective solvents – solvents in which (at least) one block is soluble and (at least) one block is insoluble. This self-assembly is driven by the solvophobic attractions between solvophobic blocks, which is counterbalanced by steric repulsions between solvophilic blocks.[49] A number of different solution state self-assembled microdomain morphologies have been observed, including spherical micelles, vesicles (polymersomes), cylinders/rods, lamellae, bicontinuous structures, hexagonally packed hollow hoops (HHHs), large compound micelles (LCMs) and disc-like micelles (Figure 1.3).[50] In the examples depicted in Figure 1.3, the hydrophilic poly(acrylic acid) (PAA) block stabilizes the aggregates formed in solution, behaving as the corona/shell of the structures. The hydrophobic poly(styrene) (PS) block is confined in the core of the structures to avoid energetically infavourable hydrophobe-water interactions and thus lowers the total free energy of system.

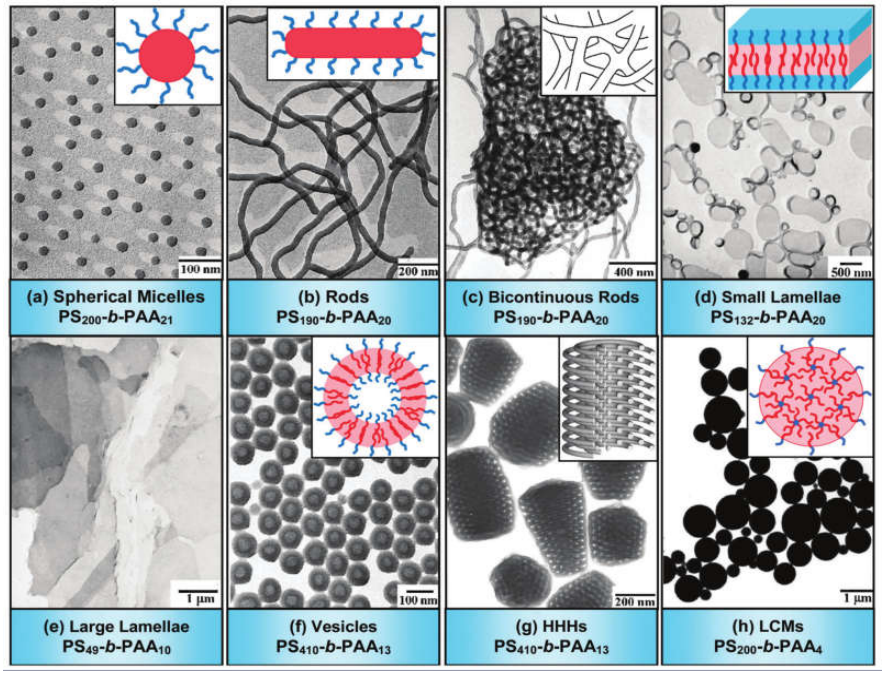

Figure 1.3. Transmission electron microscopy (TEM) micrographs and corresponding schematic diagrams of various morphologies formed from amphiphilic PS_m-*b*-PAA_n copolymers (note: m and n denote the degrees of polymerization of PS and PAA, respectively). In the schematic diagrams, red represents hydrophobic PS parts, while blue denotes hydrophilic PAA segments. HHHs: hexagonally packed hollow hoops; LCMs: large compound micelles, in which inverse micelles consist of a PAA core surrounded by PS coronal chains. Figure adapted from ref.[50]

There are many factors influencing the formation of aggregates, such as copolymer composition, preparation methods or conditions and the nature of the polymers, which makes it difficult to predict the resultant morphologies. The vast range of nanostructure morphologies formed at equilibrium is governed by the minimization of free energy between the two blocks in solution and between each block and the surrounding solvent.[51] This is strongly related to the packing parameter, *p*, which was initially investigated for surfactant micelles (Figure 1.4).[52]

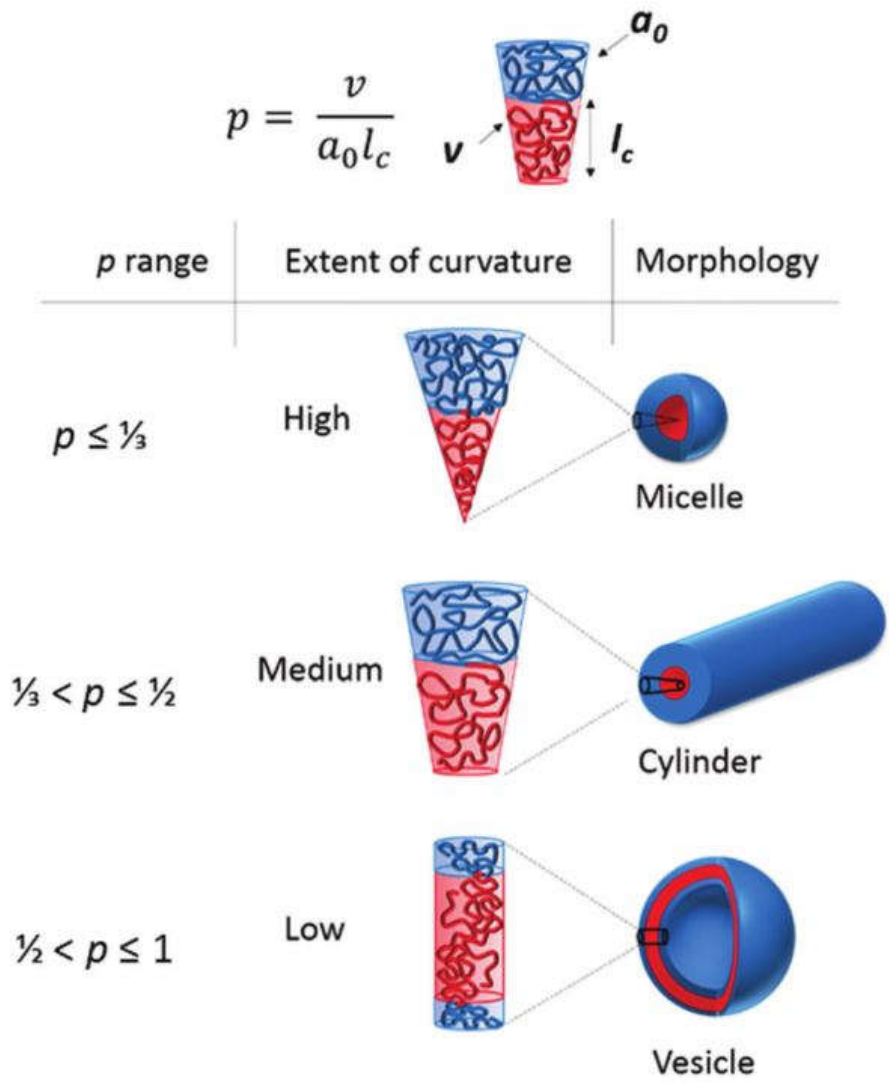

Figure 1.4. The different morphologies obtained by targeting different packing parameters, *p*. Figure reproduced from ref.[53]

Amphiphilic copolymers can be considered as mimics of small molecule surfactants, where the hydrophobic block can be regarded as the surfactant's nonpolar tail and the hydrophilic block as the polar head group.[54] Therefore, the concept of *p* can also be applied to amphiphilic copolymers, where $p = v/a_0 l_c$ (a_0, l_c and v are the head group area, hydrophobic tail length and volume of the hydrophobic segment, respectively).[53] Spheres, cylinders and vesicles are sequentially formed with the increase of *p*. In practice, *p* is difficult to calculate and therefore seldom used. Instead, the solvophobic and solvophilic weight fractions (*f*) are commonly considered. The relative weight fractions (*f*) of solvophobic and solvophilic

blocks dictate the curvature obtainable by the assembled chains (Figure 1.5), with empirical rules to determine the final equilibrium morphology expected for the aggregates.[55, 56] However, as illustrated in Figure 1.3, multiple morphologies can be prepared by self-assembly of BCPs with the same two blocks, having the same (or very similar) block weight fractions. This is due to the propensity for the formation of kinetically trapped ('frozen') structures,[57, 58] with morphology therefore dependent on the preparation pathway.

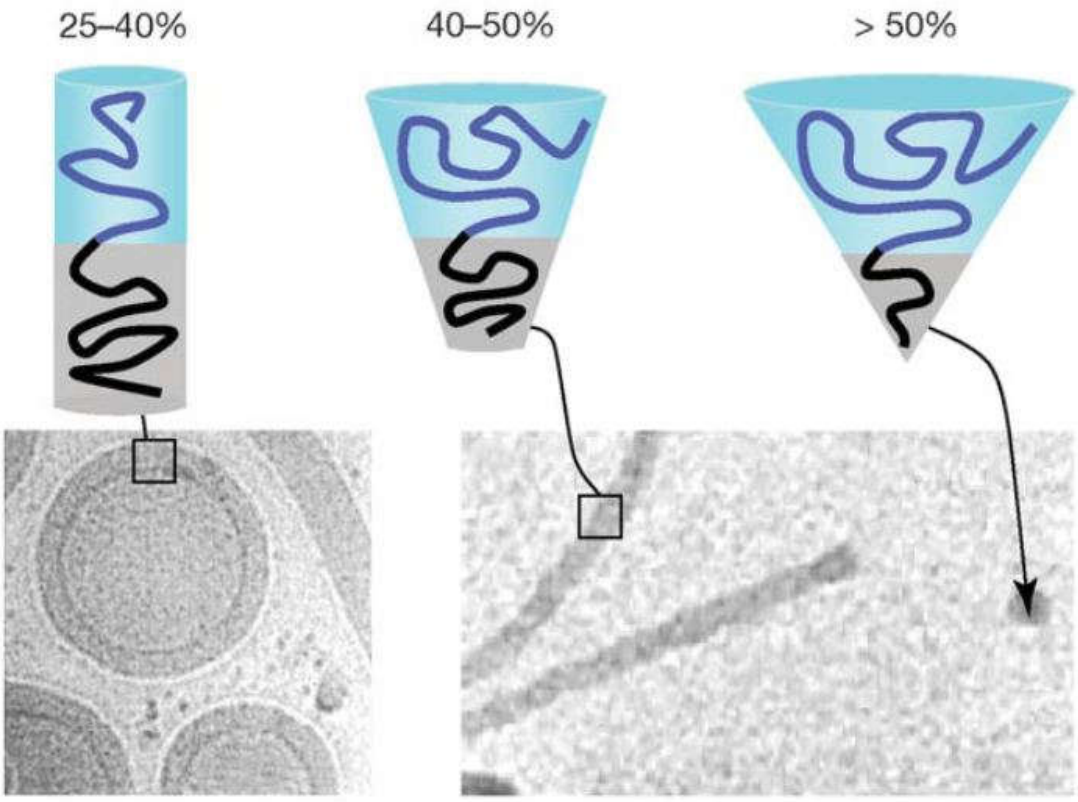

Figure 1.5. Schematics representations and cryo-TEM images of BCP assemblies with varying solvophilic (light blue block) weight-fractions (*f*), which form (left-to-right) vesicles, worms, and spherical micelles. Figure adapted from ref.[56]

Besides the weight/volume ratios of hydrophobic and hydrophilic blocks, the chemical properties of the polymers used can also affect the resultant morphologies, including copolymer composition,[50, 55, 56, 59] thermal properties of polymers (*e.g.*, glass transition temperature (T_g)[58] and crystallinity[60-64]),

polydispersities.[53, 65, 66] and the presence of specific interactions between polymers (*e.g.*, hydrogen bonding (H-bonding),[67] π-π stacking[68]).

Notably, among these, most assemblies of different morphologies in nature, such as virus capsids,[69] rely on the latter, especially H-bonding. Numerous researchers have therefore explored the effect of H-bonding on BCP self-assembly.

1.3. H-bonding in BCP self-assembly in water

H-bonding interactions have been widely employed to fabricate supramolecular polymers by the self-assembly of monomeric building blocks.[70] For example, the Meijer group have shown that helical self-assembled polymers can be prepared through cooperative stacking of hydrogen-bonded pairs (Figure 1.6).[71] They have described a general strategy for the design of functionalized monomer units and their association in either water or alkane into non-covalently linked polymeric structures with controlled helicity and chain length.

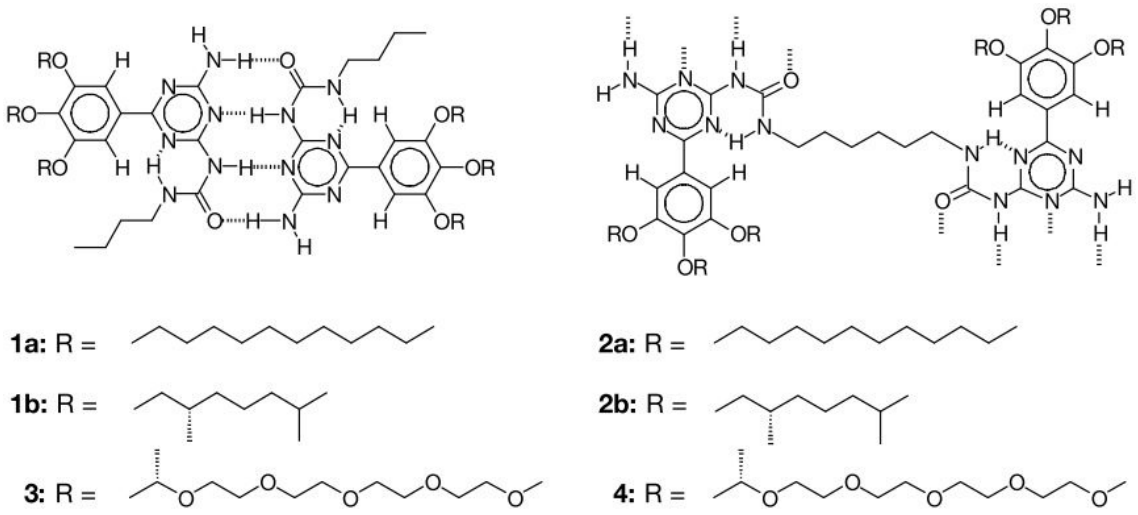

Figure 1.6. Structures of compounds **1**-**4**. This figure shows the monofunctional ureidotriazines **1** and **3** and their mode of association *via* quadruple hydrogen bonds. Structures of bifunctional derivatives **2** and **4** are also shown. Figure reproduced from ref.[71]

H-bonding interactions also play a vital role in influencing the self-assembly of amphiphilic block copolymers. Hedrick and coworkers have demonstrated the effect of H-bonding interactions on the resultant morphologies of diblock copolymer PEO_{114}-*b*-poly(*L*-lactide)$_{32}$ (PLLA) in water (Figure 1.7).[67]

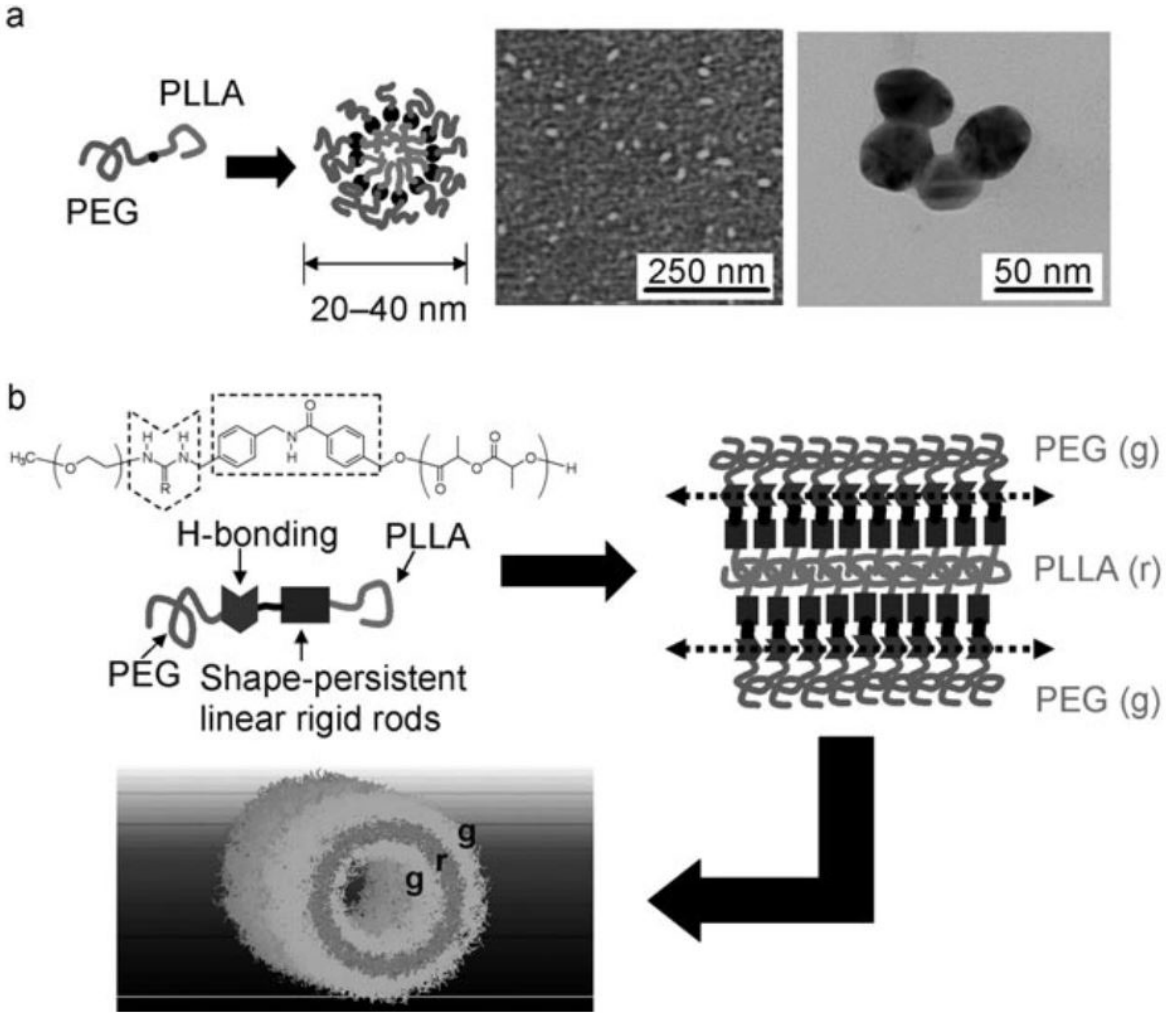

Figure 1.7. Schematic representation of possible supramolecular structures of (a) PEG-*b*-PLLA and (b) PEG-TU (or U)-*b*-PLLA assemblies in water (R = S or O). Figure reproduced from ref.[67]

Without a benzamide group at the block junction, spherical micelles were formed.[67] In contrast, by incorporating rigid small-molecule hydrogen-bonding moieties at the interface of the amphiphilic diblock copolymer (both ureabenzamide and thiourea-benzamide motifs), nanotubes were attained due to the strong anisotropic nature of H-bonding interactions. In addition, Yang and co-workers have shown that different nanostructures could be prepared by finely tuning the hydrophobic group near the H-bonding moieties.[72] Elongated, spherical and disk-like nanoparticles can be formed respectively through directional H-bonding interactions.

Recent work by the O'Reilly and Dove groups has shown that H-bonding interactions between poly(*D*-lactide) (PDLA) and PLLA can lead to the formation of stereocomplex spherical micelles (Figure 1.8).[73] Two opposite homochiral polymer chains, *i.e.* PLLA and PDLA, form a more compact conformation and a much denser polymeric packing than the homochiral crystallites. They have demonstrated that stereocomplexation by H-bonding can be used to trigger the reorganization of homochiral PLA-containing cylindrical micelles to form small stereocomplex spherical micelles.

Figure 1.8. Cartoon illustration of the formation of stereocomplex spherical micelles from PLLA-*b*-PTHPA and PDLA-*b*-PTHPA. Figure reproduced from ref.[73]

As we know, H-bonding interactions among nucleobases are the archetypal example of specific complementary H-bonding interactions. These complementary interactions have played a vital role in various areas such as DNA origami and organic catalysis. It is anticipated that complementary H-bonding among nucleobases can significantly affect the self-assembly behaviour of BCPs.

1.4. Syntheses of nucleobase-containing synthetic polymers

The H-bonding recognition interaction of nucleobases is a fundamental property of nucleic acid chemistry and determines associated transcription, translation, and replication functions, which is the origin of complex biological evolution. After Watson and Crick[74] elucidated that the structure of DNA was an intricate polymeric double helix bound together by specific H-bonding of complementary nucleobases, numerous chemists were inspired to expand their recognitive functionality to wholly synthetic chemistry or materials. Research into synthetic nucleobase polymers began with the attachment of nucleobases to preformed natural polymers such as cellulose.[75] Subsequently, the first wholly synthetic nucleic acid analogues were prepared by T'so[76] and Takemoto[77] through the conventional radical polymerization of *N*-vinyl derivatives bearing nucleobase functionalities. Following these pioneering works, a series of nucleobase polymers with different backbones were reported by Inaki and Smith *et al.*, which was also reviewed in the 1990s.[78, 79] However, as discussed above, conventional radical polymerization is uncontrolled and gives access to limited architectures, and anionic or cationic polymerization would not be compatible with nucleobase functionalities. Only homopolymers or random copolymers were reported, and their structural diversities were remarkably lacked. Thus, the very limited potential applications of these polymers were polymer complexes formed through complementary nucleobase interactions and materials including HPLC stationary phases or photoresists.[78]

For advanced applications, a high degree of control of the molecular structures of nucleobase-containing polymers is undoubtedly needed, *e.g.* for preparing tailor-made macromolecular architectures, defined nanostructures or functionalized surfaces. Both nucleobases (thymine, uracil, adenine, cytosine and guanine) and nucleosides (thymidine, uridine, adenosine, cytidine and guanosine) can achieve specific H-bonding with complementary nucleobases.[39, 80] A wide range of nucleobase- or nucleoside-containing

monomers including (meth)acrylate,[81-88] (meth)acrylamide,[79, 89] styrene,[90-94] and norbornene, [95-100] have been successfully polymerized *via* different polymerization methods (Table 1.1).

Table 1.1. Summary of polymerization methods, monomers, nucleobases and obtained DP of relevant nucleobase-containing polymers. Table adapted from ref.[101]

Polymerization method	Monomers	Nucleobases	DP (no. of nucleobases)
ATRP[81, 82, 84, 92, 102-105]	Styrenes and derivatives	A, T, C, G, U	10-100
	Acrylates		
	Methacrylates		
RAFT[85-88, 106-110]	Styrenes and derivatives	A, T, C, G	10-100
	Acrylates		
	Methacrylates		
NMP[109, 111-113]	Styrenes and derivatives	A, T, U	20-100
	Acrylates		
ROMP[95-100]	Norbornenes	A, T, C, G	10-40
Click chemistry[114-116]	Azides	A, T	10-50
	Alkynes		
	Thiols		
	Vinyls		
	Acrylamides		
	Dienes		
Ring opening polymerization[117, 118]	Cyclic monomers (*e.g.*, acetals, lactams, lactones)	T	10-40
Conventional radical polymerization[83, 91, 93, 94]	Common monomers	A, T, C, G, U	80-200

The advent of "living" polymerizations has allowed the preparation of various nucleobase-containing polymers with moderate control. The pioneering works in this area were done by Marsh, Haddleton and coworkers, who reported the controlled radical polymerization of nucleoside-substituted methacrylate monomers.[102, 103] They successfully prepared well-defined polymers containing uridine or adenosine units

using ATRP. Recently, the same group also demonstrated the synthesis of nucleobase-containing triblock and pentablock copolymers using ATRP.[119, 120] Although the distributions were not very narrow, this made it possible to prepare nucleobase-containing polymers with complex architectures. Van Hest and coworkers have also successfully polymerized adenine-, thymine-, cytosine- and guanine-functionalized methacrylates by ATRP and prepared homopolymers and block copolymers containing nucleobase moieties (Figure 1.9).[81, 82, 84] Controlled polymerization of adenine-, thymine- and guanine-monomers could be obtained and the cytosine monomer needed to be polymerized using a stronger copper binding ligand, *N*,*N*,*N*′,*N*″,*N*″-pentamethyldiethylenetriamine (PMDETA). Lutz and coworkers and Shen and coworkers investigated the ATRP of styrene derivatives bearing either thymine, adenine or uracil moieties.[92, 105] The same monomers were also successfully polymerized through NMP to give well-defined products.[109]

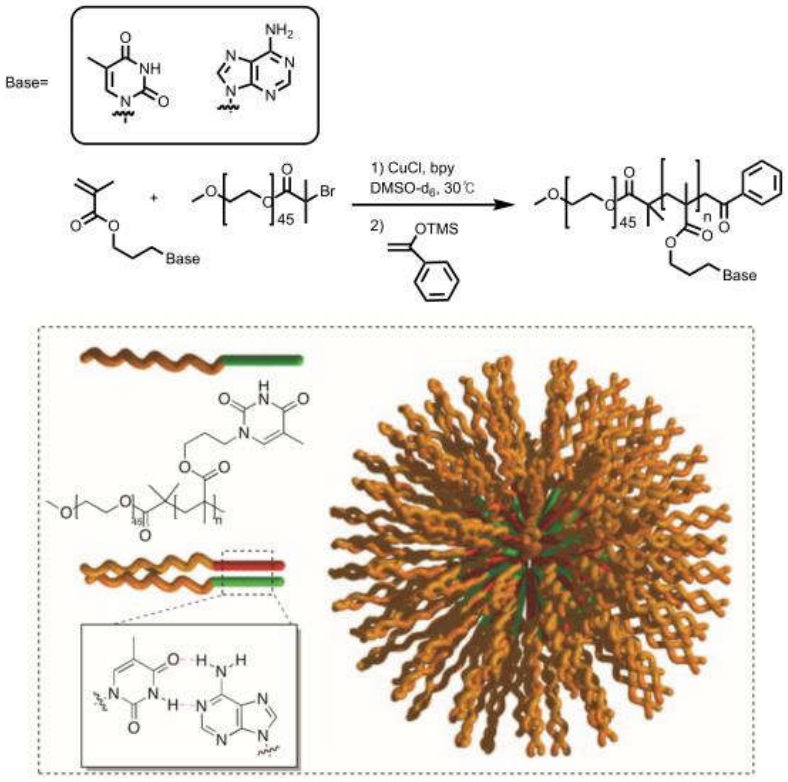

Figure 1.9. Synthesis of nucleobase-containing diblock copolymers by ATRP and schematic structure of self-assemblies. Figure reproduced from ref.[84, 101]

ROMP was also demonstrated to be a straightforward method for polymerizing nucleobase-substituted norbornenes. Gibson and coworkers described the first synthesis of norbornene derivatives bearing either thymine, adenine, cytosine or guanine moieties.[95, 96] However, the polymerization of these monomers was found to be rather difficult or, in some cases, even impossible due to solubility limitations. The authors found that the apolar spacer length of the monomer was a key factor to affect the polymerization. Subsequently, the Sleiman group[97] and the Weck group[99] reported novel generations of nucleobase-substituted norbornenes having optimized molecular structures following on from Gibson's work.

Recently, the Bowman group demonstrated the synthesis of clickable nucleic acids through thiol-ene or thiol-Michael addition reactions (Figure 1.10).[115, 116, 121] They suggested that the utilization of click chemistry could provide a feasible route to prepare sequence-controlled periodic copolymers/oligomers bearing nucleobase pendant groups. However, the step-growth polymerization methods they used hindered the preparation of well-defined polymers with narrow distributions. The possible side reactions such as Michael addition of nucleobases and photodimerization of thymine might limit control over polymerization conducted under basic conditions or photo-irradiation. They also reported that the synthetic polymers could be rendered water soluble by designing and synthesizing more hydrophilic backbones.[116]

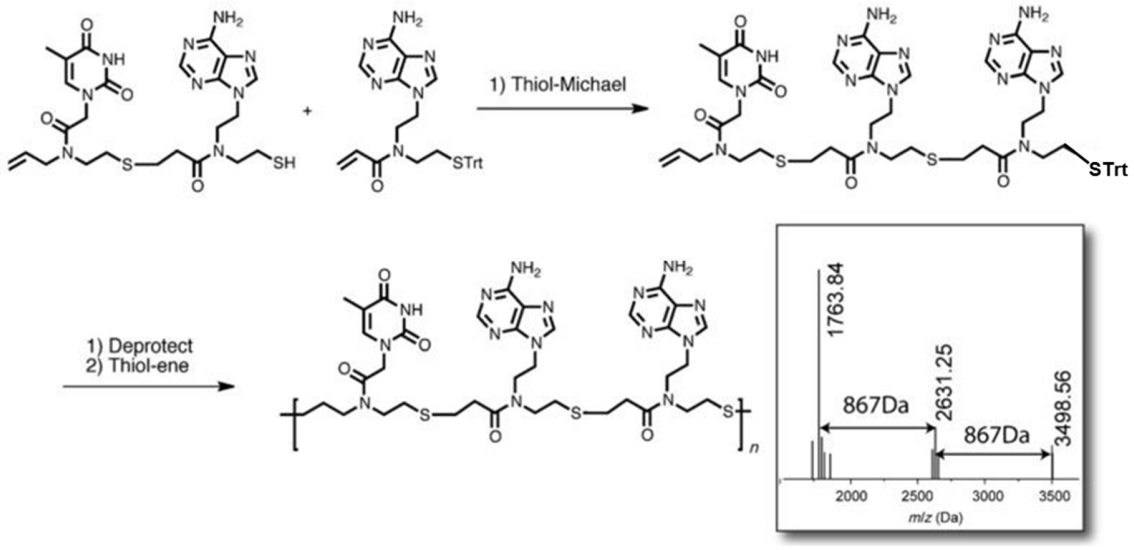

Figure 1.10. Thiol-Michael coupling of the thymine–adenine dimer and adenine monomers (5 mol% DBU in CH_2Cl_2,1 h), yielding a thymine–adenine–adenine trimer that was photopolymerized by irradiation with 365 nm light) for 10 min in the presence of 1 mol% DMPA (DMPA=2,2-dimethoxy-2-phenylacetophenone). Inset: MALDI spectrum of this polymer, showing the 867 Da spacing associated with the TAA trimer. Figure reproduced from ref.[115]

In addition, the Wooley group developed a novel approach to synthesizing thymidine-derived poly(deoxyribonucleotide) annalogues from a six-membered cyclic phosphoester (Figure 1.11).[117, 118] This ring-opening polymerization strategy enabled the facile and scalable synthesis of functional nucleobase-containing macromolecules. This new method might open a more direct route to prepare poly(deoxyribonucleotide)s. Due to the possible incompatibility of unprotected thymine with ring-opening conditions, the *N*-3 protected thymine moieties need to be deprotected in order to explore their potential applications involving complementary H-bonding interactions.

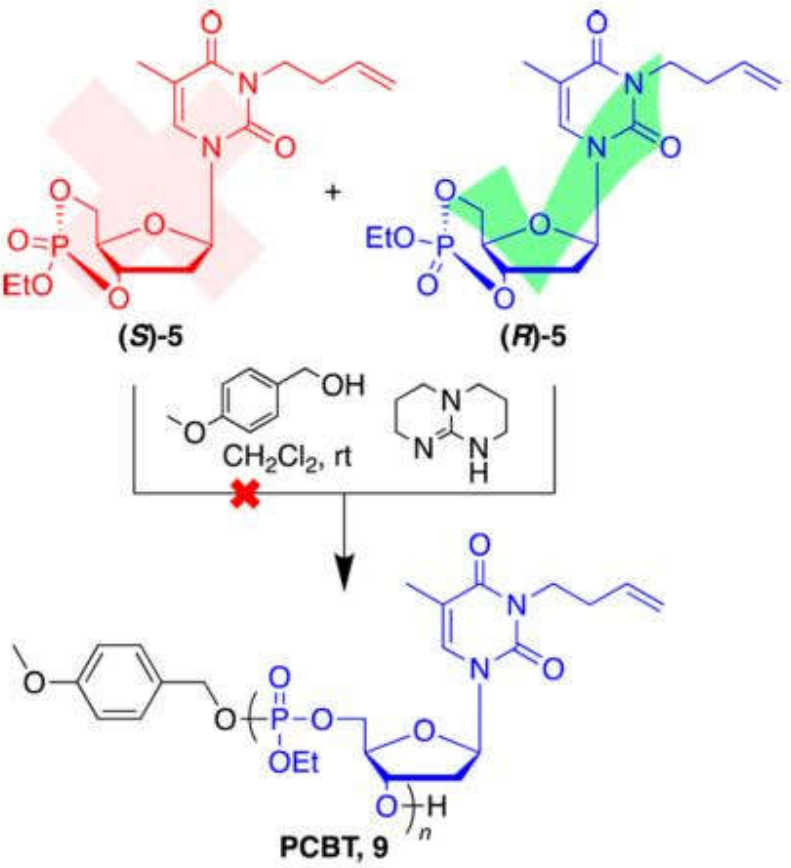

Figure 1.11. Polymerization of 3',5'-cyclic 3-(3-butenyl) thymidine ethylphosphate (**5**) with 4-methoxybenzyl alcohol as the initiator and 1,5,7-triazabicyclo[4.4.0]dec-5-ene (TBD) as the catalyst. Figure reproduced from ref.[117]

RAFT polymerization conditions are perhaps the most tolerant towards nucleobase functionalities, and make it possible to synthesize nucleobase-containing polymers with higher DPs and low dispersities (Table 1.1). The O'Reilly group systematically investigated the polymerization of nucleobase-containing methacrylate monomers in organic solvents with different H-bonding support ability using RAFT polymerization (Figure 1.12).[85-88] The polymerization of these monomers proceeded well and good end group fidelity was observed, facilitating the synthesis of well-defined diblock copolymers for self-assembly.

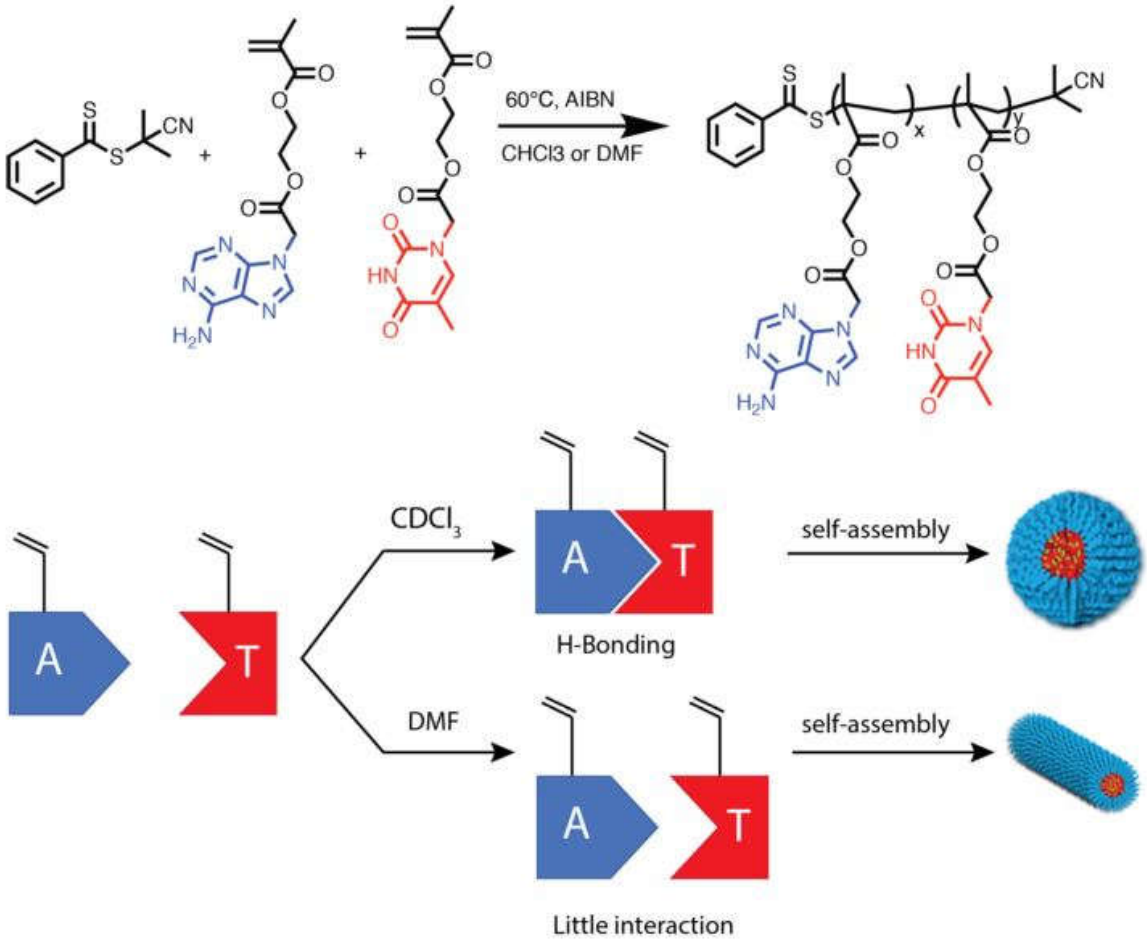

Figure 1.12. Synthesis and self-assembly of the nucleobase-containing diblock copolymers using RAFT polymerization. Figure reproduced from ref.[87, 101]

Long and coworkers reported the polymerization of nucleobase-functionalized acrylates by RAFT polymerization.[106-108] Nucleobase-containing ABA triblock copolymers have been prepared using difunctionalized RAFT CTA (Figure 1.13). Well-defined triblock copolymers were synthesized and their properties of supramolecular blends were explored by mixing copolymers with complementary nucleobases.

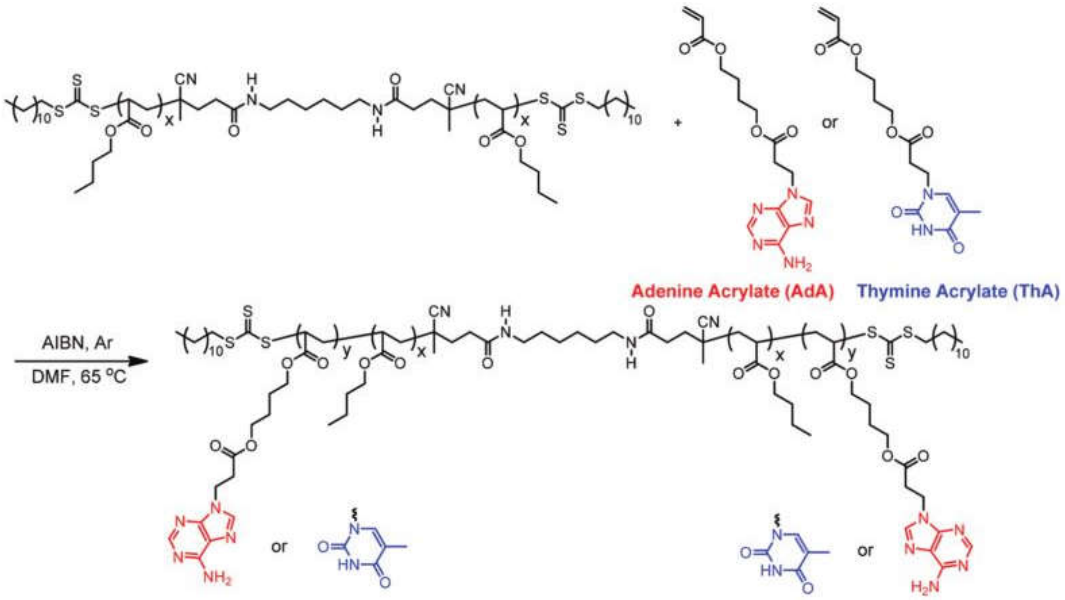

Figure 1.13. Synthesis of adenine and thymine-functionalized acrylic ABA triblock copolymers using RAFT polymerization. Figure adapted from ref.[107]

Although a series of nucleobase-containing polymers can be successfully synthesized through various polymerization methods (Table 1.1), several important aspects still need to be resolved in order to expand their impact and utility in polymer and materials science. Firstly, poor solubility of nucleobase-containing monomers and polymers in water, to some extent, prevents these nucleic acid analogues from mimicking DNAs and RNAs. Secondly, only limited DPs (less than 100) of nucleobase-containing polymers have been achieved through controlled polymerization, which might not produce materials with robust properties. More importantly, sequence-controlled nucleobase containing polymers which demonstrate specific complementary interactions are hard to prepare. Therefore, more versatile nucleobase monomers, oligomers and polymers are highly attractive, which will be, to some extent, built on the development of new methodologies in both organic syntheses and polymer syntheses.

Although the synthesis of nucleobase-containing acrylamide polymers was reported over 2 decades ago,[79] the complicated monomer synthetic routes hindered their widespread applications. In addition, no controlled polymerizations were conducted using these novel monomers. In this thesis, water-soluble acrylamide monomers were prepared and polymerized with a higher DP than previously achieved, through a facile RAFT method.

1.5. Novel properties of nucleobase-containing synthetic polymers and their applications

The self-assembly of DNA strands is partly due to the intermolecular formation of H-bonds between complementary purine (adenine and guanine) and pyrimidine (thymine and cytosine) bases of nucleic acids, which are attached to a phosphate sugar backbone. Adenine (A) bonds selectively to thymine (T), whereas guanine (G) bonds selectively to cytosine (C). An elegant example involves the selective complementary interactions between specific DNA strands, leading to higher order nanomaterials, such as DNA origami (Figure 1.14).[122-126] The major difference between nucleic acids and nucleobase polymers is the distinct backbones. Their synthetic backbones are much more robust towards degradation *in vivo*. More importantly, nucleobase-containing synthetic polymers have some advantages in contrast to DNAs, such as much cheaper synthetic costs and larger scale preparation. Synthetic polymers bearing nucleobases as pendant groups (A, T, G or C) are expected to exhibit interesting supramolecular self-assembly or self-sorting properties that is previously observed within DNAs.

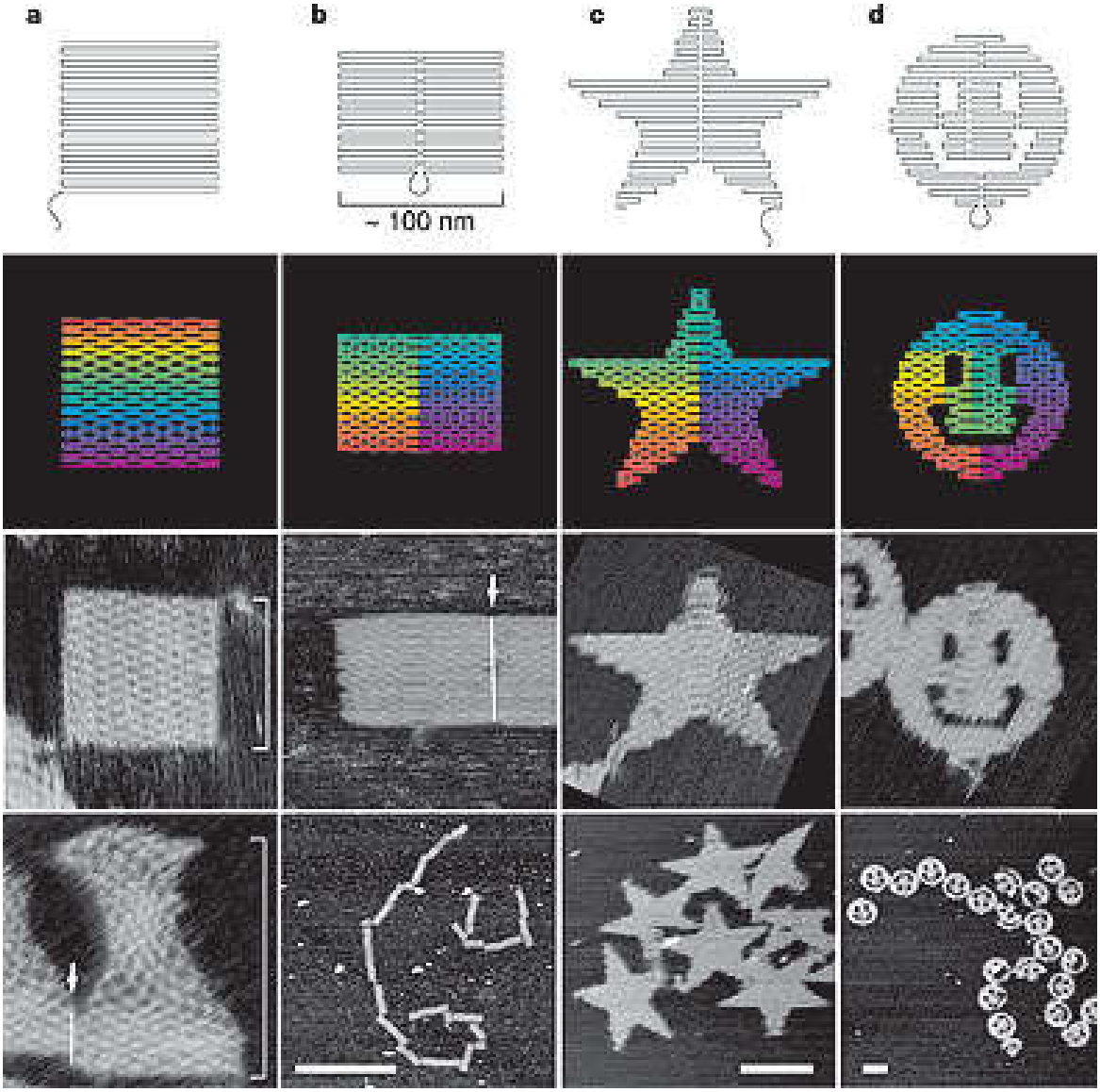

Figure 1. 14. DNA origami shapes. Figure reproduced from ref.[126]

1.5.1. Template polymerization

Specific interactions between purine and pyrimidine families are widely used in the field of organic, macromolecular and biochemical syntheses.[127] Much attention has been given to template polymerization using nucleobase-containing synthetic polymers. Pioneering works were conducted by Takemoto and Inaki *et al.* from 1970 to 1990.[78, 89] Methacrylate and methacrylamide monomers containing nucleobase functionalities were prepared and the template polymerization of nucleobase monomers was achieved using polymers containing the complementary nucleobase functionality. These seminal works in the area

of template polymerization shed some light on the feasibility of the template polymerization approach for the synthesis of polymers. However, the limited synthetic technology at that time limited the structural accuracy, characterization and chemical diversity of the materials. The conventional free radical polymerization of the template polymer inevitably makes its molecular weight distribution broad, which also leads to a large dispersity for the daughter polymers. In addition, only homopolymers or random copolymers containing nucleobase functionalities could be synthesized and used as templates, which hindered the accessibility of more complicated daughter structures or the utility of template alongside self-assembly.

Well-defined polymers prepared by ROMP polymerization methods have been utilized in template polymerizations. Weck[100] and coworkers reported that diaminopyridine functionalized norbornenes polymerized *via* ROMP could act as templates for the template polymerization of a norbornene–based thymine monomer. They found the rate of template polymerization was enhanced by the increase of local monomer concentration caused by templating. Meanwhile, the resin-supported template they used produced a well-defined daughter polymer (M_n = 8.2 kDa, $Đ_M$ = 1.19) (Figure 1.15).

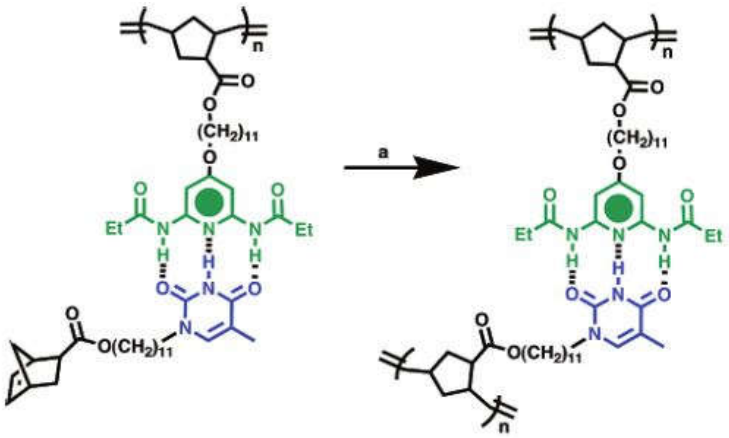

Figure 1.15. Solution-based template polymerization through ROMP. Figure reproduced from ref.[100]

Another seminal contribution to this area comes from the Sleiman group.[98] They successfully replicated the chain length and narrow molecular weight distribution of a template polymer containing thymine

functionality. The template was also synthesized by ROMP to give a polymer with a narrow M_W distribution ($Đ_M$ = 1.07), which generated a daughter adenine-functionalized conjugated polymer with a similarly narrow distribution (Figure 1.16). More importantly, the daughter polymer had a similar degree of polymerization to the initial template, indicating precisely templated polymerization.

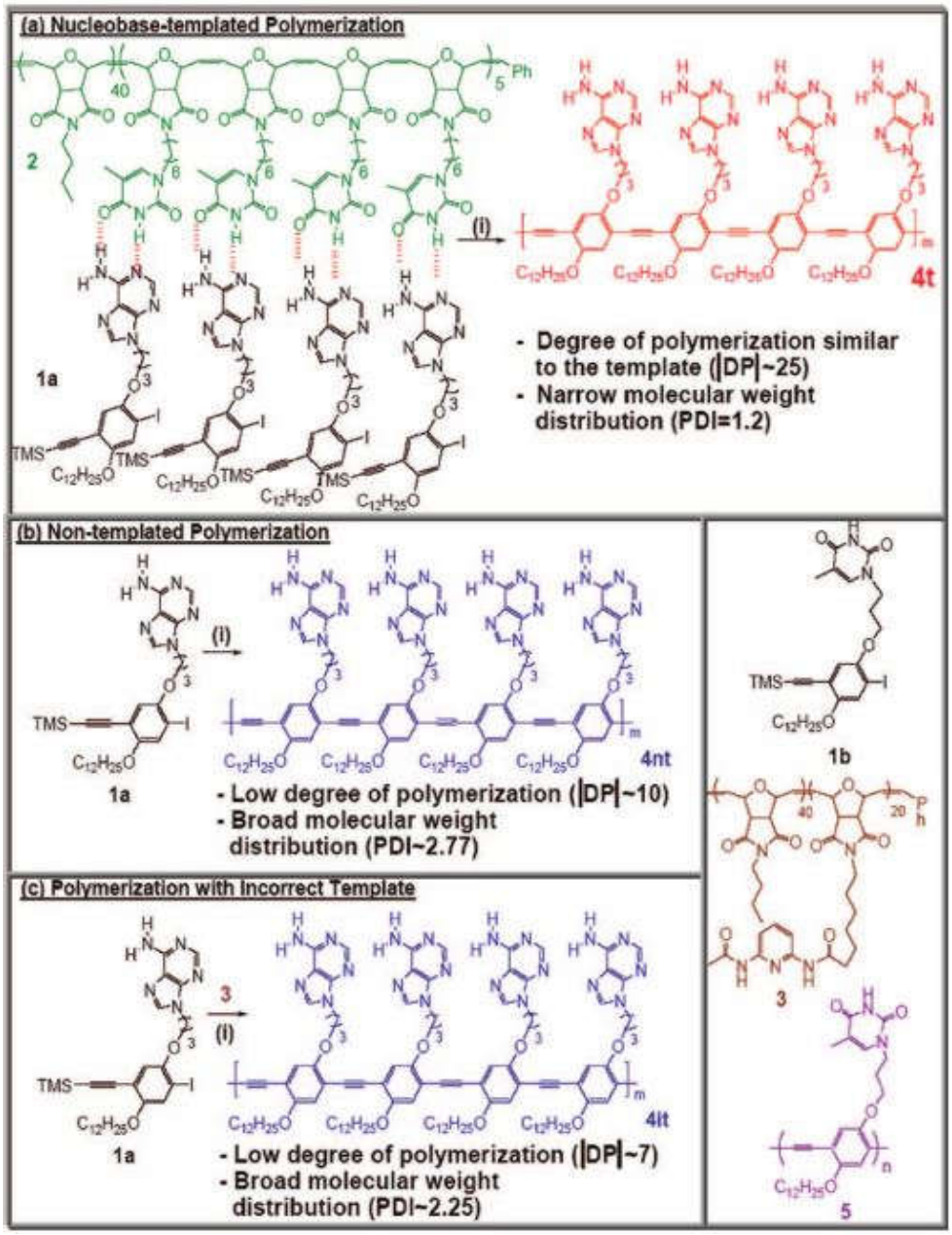

Figure 1.16. Nucleobase-templated polymerization from well-defined template obtained through ROMP. Figure reproduced from ref.[98]

Moreover, O'Reilly[109] and coworkers reported that a biomimetic segregation/templating approach using synthetic nucleobase polymers had been developed (Figure 1.17). A nucleobase polymer with low dispersity was prepared through NMP, which could self-assemble to form well-defined micelles in chloroform ($CHCl_3$). These nucleobase-functionalized micelles could then act as a template for the synthesis of a complementary daughter nucleobase polymer with high molecular weight (M_w up to ~400,000 g mol^{-1}) and low dispersity ($Đ \leq 1.08$), through conventional free radical polymerization confined in the micellar template. The confined environment in the micelles allowed for segregation of the active species and provided good polymerization control.

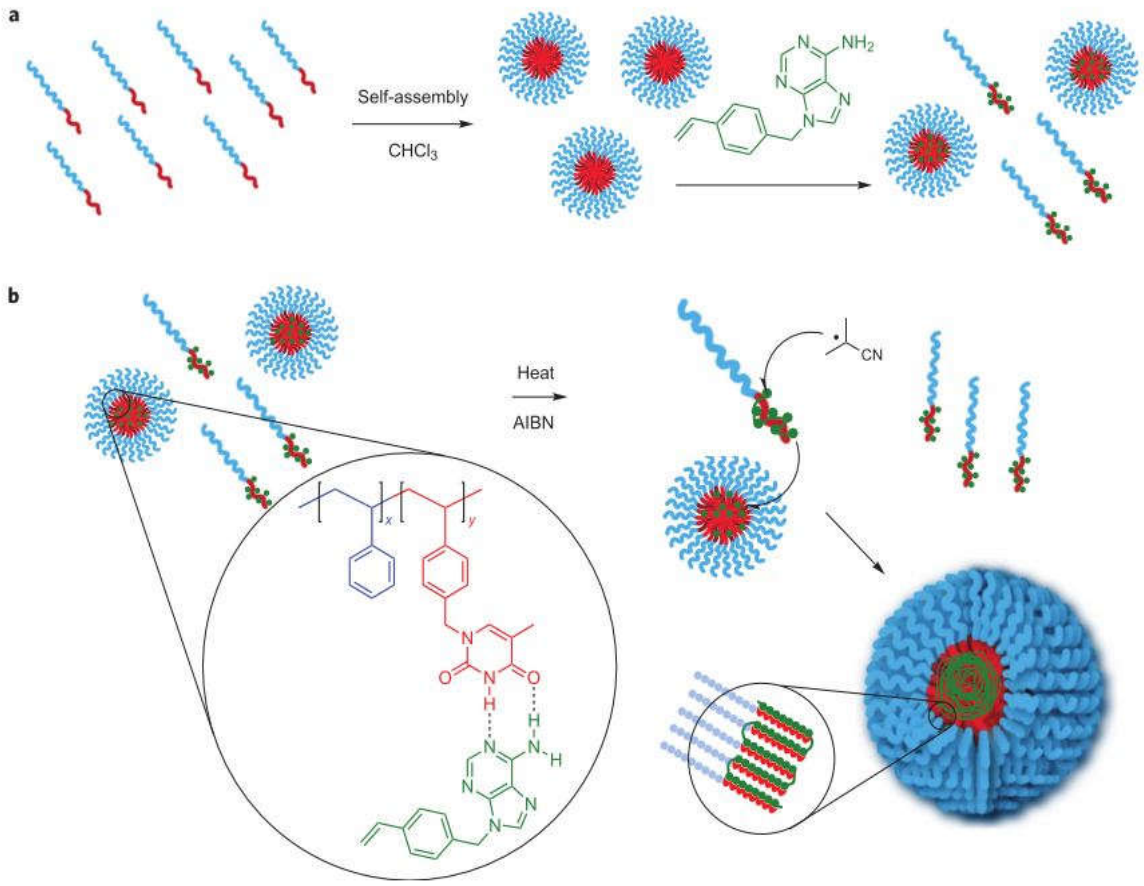

Figure 1.17. Dynamic exchange and cooperative assembly of templates for biomimetic radical polymerization. Figure reproduced from ref.[109]

Recently, Marsh, Haddleton and coworkers prepared polymer templates tethered on solid supports through copper-mediated living radical polymerization, which could efficiently control the length and dispersity of the template polymers bound to the supports.[104, 120] Uridine-derived templates achieved good fidelity of replication by incorporating mainly complementary nucleobase monomers in the daughter polymer, even using a mixture of non-complementary and complementary monomers. The daughter polymers produced were approximately half of the template length, which was attributed to the dual H-bonding interaction between the daughter and template including Watson-Crick and possibly Hoogsteen-type interactions (Figure 1.18). Moreover, templates prepared from adenosine, uridine, cytidine and guanosine substituted methacrylate monomers were also successfully prepared and utilized.

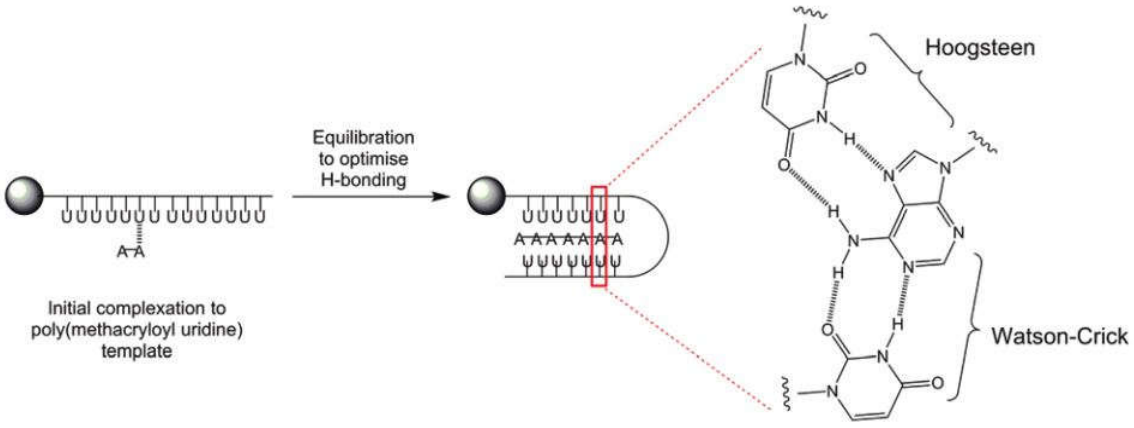

Figure 1.18. Proposed mechanism of template polymerization for monomers with complementary nucleobases by Marsh and coworkers. Figure reproduced from ref.[104, 120]

1.5.2. Novel self-assembly properties of nucleobase-containing synthetic polymers

The self-assembly of nucleobase-containing polymers is of great interest as it often involves specific nucleobase interactions besides the hydrophilic-to-hydrophobic balance. The Rotello group demonstrated the formation of giant vesicles by mixing thymine/uracil containing polystyrene or polynorbornene with diacyldiaminopyridine functionalized polymers in chloroform. The formation of giant vesicles was driven

by the complementary H-bonding interactions between thymine/uracil and the diacyldiaminopyridine functional group (Figure 1.19).[128, 129] Sleiman and coworkers observed rod-like nanoparticles upon the self-assembly of adenine-containing norbornene polymers in THF, which was unexpected considering the high ratio between solvophobic and solvophilic blocks (1:10). They hypothesized that this observation was induced by the presence of self-complementary H-bonding interactions and the aromatic π-stacking behaviour of adenine.[97]

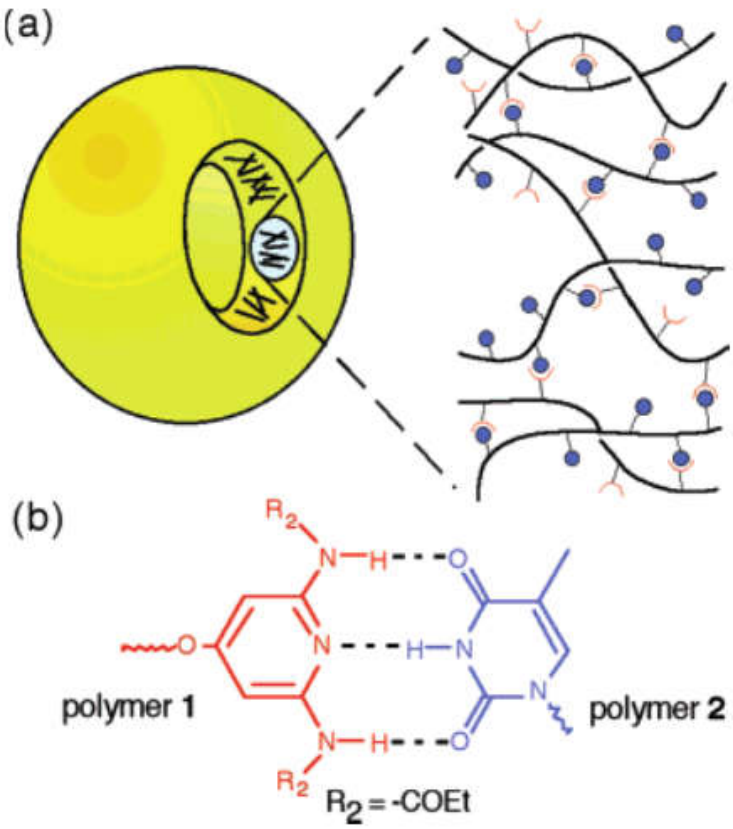

Figure 1.19. Schematic depiction of vesicle formation between diaminopyridine-based polymer **1** and thymine-based polymer **2**. (a) Illustration showing molecular recognition within vesicle wall. (b) The corresponding recognition groups. Figure reproduced from ref.[127]

The O'Reilly group found that distinct self-assembled morphologies were formed with nucleobase-containing copolymers with different sequences (Figure 1.20).[85] Strong H-bonding interactions in $CHCl_3$ gave rise to the preparation of moderately alternated copolymers, which formed spherical micelles upon

self-assembly. In contrast, elongated worm-like structures tended to form with the random copolymers of complementary nucleobase monomers. They hypothesized that the different morphologies were mainly caused by the solubility of copolymers with different monomer sequences. The same group also demonstrated that different morphological evolutions were observed in $CHCl_3$ and dioxane during the dispersion polymerization of nucleobase-functionalized monomers.[86, 130]

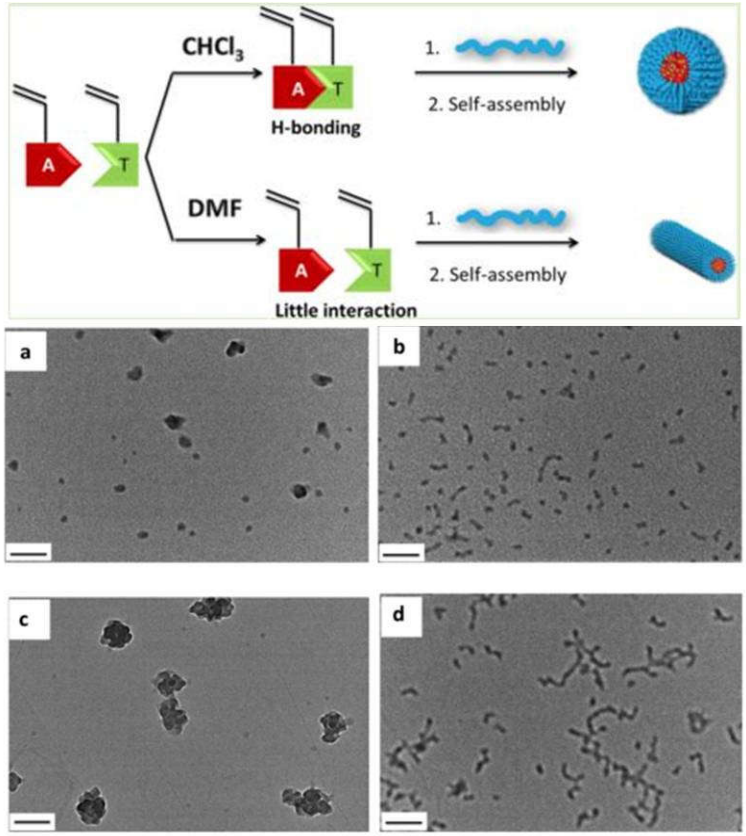

Figure 1.20. Schematic presentation of moderately alternated and random nucleobase-containing copolymers and their TEM images on graphene oxide. TEM images of self-assemblies of diblock copolymers containing (a, c) moderately alternated nucleobase-containing copolymers and (b, d) random nucleobase-containing copolymers. Figure adapted from ref.[85]

Although all the five nucleobases (adenine, thymine, cytosine, guanine and uracil) have very limited solubility in water, the hydrophilic backbone of phosphate-sugar ester make DNA and RNA highly water soluble. In contrast, most synthetic polymers containing nucleobase functionalities have poor solubility in water or aqueous solutions due to the hydrophobic carbon-carbon backbone. To our knowledge, there

is relatively little research into the self-assembly of nucleobase-containing synthetic polymers in aqueous solutions.

Van Hest[84] and coworkers reported the synthesis of poly(ethylene glycol)-*b*-poly(nucleobase) block copolymers *via* ATRP from a PEG macro-initiator and investigated the self-assembly behaviour of a series of amphiphilic block copolymers (containing single nucleobase functionality (A or T) and the mixed A/T system) in aqueous solutions. They found that self-assembly was mainly controlled by the hydrophobic-hydrophilic balance in the diblock copolymers containing only individual A or T nucleobases. However, in the A/T mixed systems the complementary nucleobase interactions played a crucial role in the block copolymer assembly through shifting the hydrophobic-to-hydrophilic balance of the blocks towards an increase of hydrophilicity, as elucidated by CAC measurements.[84]

Recently, O'Reilly and coworkers prepared nucleobase-containing diblock copolymers with poly(oligo(ethylene glycol)methyl ether methacrylate) (POEGMA) acting as the hydrophilic block.[88] The complementary H-bonding in the micellar core enabled the formation of complex polymeric morphologies in water. In this thesis, a principal goal was to further study the influence of the complementary nucleobase interactions on the morphologies of self-assembled structures in aqueous solutions. Meanwhile, the specific complementary interactions between polymers were utilized to tune and control the self-assemblies.

1.5.3. Applications of synthetic nucleobase-containing materials

Apart from the novel self-assembly properties, nucleobase-containing polymers are also attractive to be used as multi-functional materials. The initial motivation to prepare nucleic acid mimics is to replace DNAs/RNAs using cheap and scalable synthetic polymers. Takemoto and Inaki[78] reported the interaction between water-soluble polyethyleneimine derivatives of nucleobases and polynucleotides with complementary nucleobases. Later on, some of the artificial polymer mimics of DNA such as peptide

nucleic acids (PNA) were found to be quite promising.[131] However, these water-soluble nucleic acid analogues are hard to synthesize at large scales, which, to some extent, limits their further applications. Recently, Bong and coworkers reported discrete triplex hybridization of DNA and RNA with polyacrylates bearing the nucleobase analog melamine (Figure 1.21).[132] Despite stereoregio backbone heterogeneity, the triazine polymers bind T/U-rich DNA or RNA with exceedingly high affinity upon mixing. This scalable and well-defined assembly strategy highlights the integration of polymer architectures with DNA and RNA and their utilization in aptamer turn-on, delivery, and siRNA silencing.

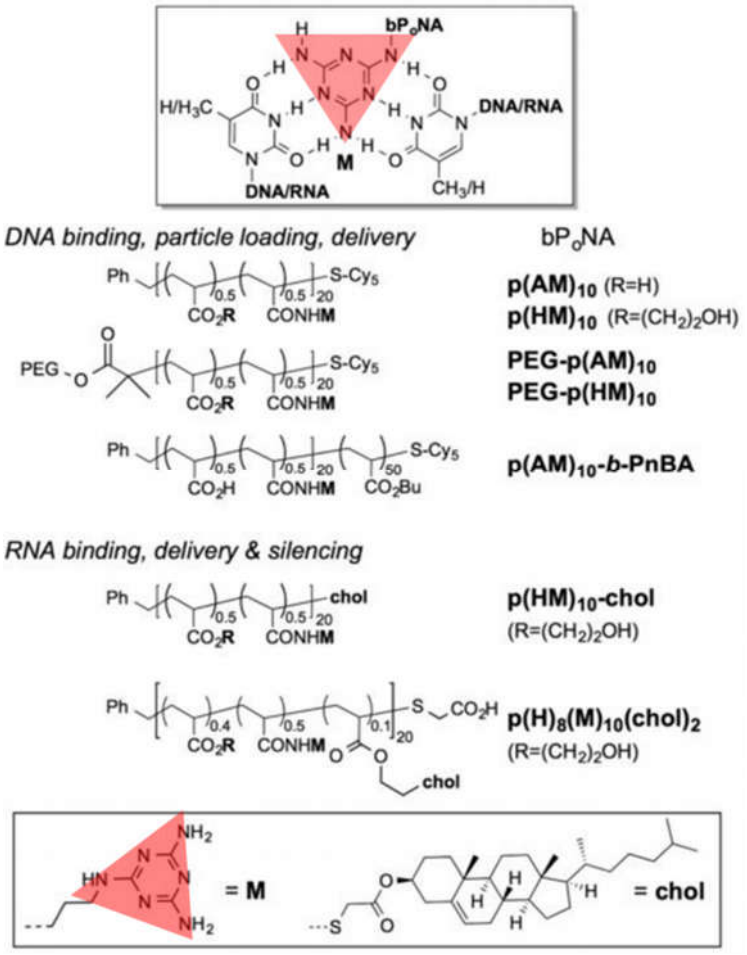

Figure 1.21. (top) Melamine (M)-driven triplex hybridization of bifacial polymer nucleic acid (bPoNA) with T/U tracts in DNA and RNA. (bottom) Structures of bPoNA studied as DNA and RNA folding and delivery agents. PEG = 5 kDa. The melamine (M) part is highlighted as a red triangle. Figure reproduced from ref.[132]

Cha and coworkers fabricated a novel kind of nanoparticle, consisting of click-nucleic-acid (CNA)-containing PEG-PLGA triblock copolymers.[121] A photoinitiated thiol-ene polymerization between CNA monomer and PEG thiol yielded PEG-CNA, following coupling to PLGA to produce the triblock copolymer. The middle block CNA (T10) could be used to efficiently encapsulate large amounts of complementary DNA. This new polymeric nanoparticle could serve as an efficient nanocarrier to co-encapsulate hydrophobic drugs and hydrophilic nucleic acid strands.

In addition to the preparation of novel nanomaterials, synthetic nucleobase-containing polymers have also been utilized to fabricate bulk materials. Long and coworkers[106-108, 112] demonstrated the formation of long-range, ordered lamellar microphase-separated morphologies on non-patterned substrates using ABA/ABC triblock copolymers bearing adenine- and thymine-functionalized external blocks. Intermolecular H-bonding between thymine and adenine promoted self-assembly into well-defined hard domains of complementary nucleobase (Figure 1.22). Meanwhile, complementary thymine and adenine interactions significantly contributed to the superior mechanical properties.

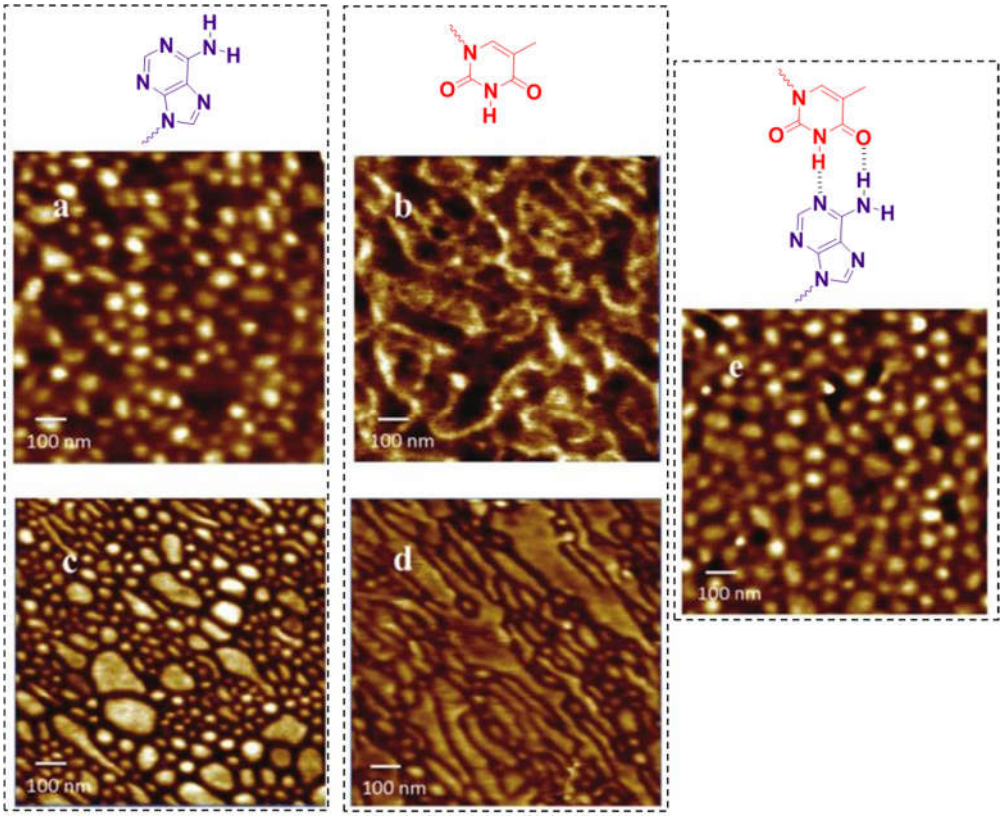

Figure 1.22. Tapping mode AFM phase image of (a) solution-cast poly(AdA-*b*-nBA-*b*-AdA), (b) solution-cast poly(ThA-*b*-nBA-*b*-ThA), (c) melt-pressed poly(AdA-*b*-nBA-*b*-AdA), (d) melt-pressed poly(ThA-*b*-nBA-*b*-ThA), and (e) solution-cast supramolecular blend. Figure reproduced from ref.[107]

Moreover, the Long group reported a type of supramolecular adhesive containing two copolymers with complementary nucleobase moieties.[83] Nucleobase-containing H-bonding polymers possessed peel and shear strengths 3-4 times higher than the carboxylic acid (AA) –and vinylpyridine (VP)-based complementary polymer analogs. Arimitsu and coworkers[133] fabricated more robust adhesive materials utilizing a thymine-adenine interaction and thymine photodimerization. The peel strength of this novel material was significantly improved by simultaneous UV irradiation.

Very recently, Gao *et. al.* showed that nucleobase-containing acrylamide hydrogels were prepared through copolymerizing acrylamide and nucleobase-bearing acrylamide monomers.[134] These novel hydrogels exhibited an excellent adhesive behaviour for not only various solid substrates (*e.g.* plastics, rubbers, glasses, metals and woods) but also biological tissues consisting of heart, liver, spleen, lung, kidney, bone and muscle. This bioinspired strategy using nucleobase-containing polymers could open a novel avenue

for fabricating soft and adhesive materials. Meanwhile, it is anticipated that the nucleobase-containing hydrogels could expand the scale of biomedical applications of hydrogels.

Inspired by these previous works, we aim to expand the potential applications of nucleobase-containing polymers/materials in this thesis. The use of complementary nucleobase interactions between polymers to tune the morphologies of nanostructures, which provides a new stimulus for responsive materials, will be described. Meanwhile, the photodimerization of thymine also offers the possibility to introduce synergetic properties, for example enhanced fluorescence, by the combination of complementary H-bonding interactions and covalent rigidification.

1.6. Conclusions

Firstly, the concept of utilizing synthetic polymers to mimic versatile functionalities in nature has been introduced in this Chapter. Secondly, efficient routes to the synthesis of block copolymers have been outlined, including the basic knowledge and mechanisms of controlled "living" polymerization techniques, among which RAFT has been chosen to prepare nucleobase-containing polymers throughout this thesis. Following this, self-assembly of block copolymers has been discussed, including some empirical rules related to the packing parameter. The effect of H-bonding on self-assembly behaviors has been highlighted. In addition, the literature on the syntheses, properties and applications of nucleobase-containing synthetic polymers has also been reviewed.

1.7. Aims of the thesis

Although some exploitation of nucleobase-containing synthetic polymers has been successful, these novel materials are still in their infancy. Meanwhile, the poor solubility and limited examples of the successful synthesis of nucleobase-containing polymers with high molecular weights represent a major limitation for their widespread application.

Based on the above knowledge and inspired by these pioneering works, this thesis will describe how the synthesis and self-assembly of nucleobase-containing materials has been expanded. The synthesis of more flexible nucleobase-containing acrylamide polymers with much higher DPs (up to around 300) through RAFT polymerization will be detailed. The novel properties of these polymers, including specific complementary interactions in aqueous solution, will be explored. This specific supramolecular interaction will provide us a facile approach to functionalizing polymeric nanoparticles. We aim to fabricate novel polymeric micelles which can respond to complementary polymers. We anticipate that these developments will breathe new life into functional nucleobase-containing materials, and generate more widespread interest using their unique properties.

1.8. References

1. P. Theato, B. S. Sumerlin, R. K. O'Reilly and T. H. Epps III, *Chem. Soc. Rev.*, **2013**, *42*, 7055-7056.

2. P. M. Kharkar, K. L. Kiick and A. M. Kloxin, *Chem. Soc. Rev.*, **2013**, *42*, 7335-7372.

3. Z. Ge and S. Liu, *Chem. Soc. Rev.*, **2013**, *42*, 7289-7325.

4. M. Szwarc, *Nature*, **1956**, *178*, 1168-1169.

5. M. Szwarc, *J. Polym. Sci., Part A: Polym. Chem.*, **1998**, *36*, IX-XV.

6. M. Szwarc, M. Levy and R. Milkovich, *J. Am. Chem. Soc.*, **1956**, *78*, 2656-2657.

7. S. Aoshima and S. Kanaoka, *Chem. Rev.*, **2009**, *109*, 5245-5287.

8. O. W. Webster, W. R. Hertler, D. Y. Sogah, W. B. Farnham and T. V. RajanBabu, *J. Am. Chem. Soc.*, **1983**, *105*, 5706-5708.

9. S. Penczek, M. Cypryk, A. Duda, P. Kubisa and S. Słomkowski, *Prog. Polym. Sci.*, **2007**, *32*, 247-282.

10. C. W. Bielawski and R. H. Grubbs, *Prog. Polym. Sci.*, **2007**, *32*, 1-29.

11. C. J. Hawker, A. W. Bosman and E. Harth, *Chem. Rev.*, **2001**, *101*, 3661-3688.

12. R. Francis and A. Ajayaghosh, *Macromolecules*, **2000**, *33*, 4699-4704.

13. J. Chiefari, Y. K. Chong, F. Ercole, J. Krstina, J. Jeffery, T. P. T. Le, R. T. A. Mayadunne, G. F. Meijs, C. L. Moad, G. Moad, E. Rizzardo and S. H. Thang, *Macromolecules*, **1998**, *31*, 5559-5562.

14. J.-S. Wang and K. Matyjaszewski, *J. Am. Chem. Soc.*, **1995**, *117*, 5614-5615.

15. V. Percec and B. Barboiu, *Macromolecules*, **1995**, *28*, 7970-7972.

16. M. Kato, M. Kamigaito, M. Sawamoto and T. Higashimura, *Macromolecules*, **1995**, *28*, 1721-1723.

17. T. Otsu and M. Yoshida, *Makromol. Chem. Rapid Commun.*, **1982**, *3*, 127-132.

18. K. Ziegler, E. Holzkamp, H. Breil and H. Martin, *Angew. Chem., Int. Ed.*, **1955**, *67*, 426-426.

19. Y. Chauvin, *Angew. Chem., Int. Ed.*, **2006**, *45*, 3740-3747.

20. R. H. Grubbs, *Angew. Chem., Int. Ed.*, **2006**, *45*, 3760-3765.

21. R. R. Schrock, *Angew. Chem., Int. Ed.*, **2006**, *45*, 3748-3759.

22. P. Jean-Louis Hérisson and Y. Chauvin, *Makromol. Chem.*, **1971**, *141*, 161-176.

23. T. Otsu, M. Yoshida and T. Tazaki, *Makromol. Chem. Rapid Commun.*, **1982**, *3*, 133-140.

24. D. Colombani, *Prog. Polym. Sci.*, **1997**, *22*, 1649-1720.

25. K. Matyjaszewski and J. Spanswick, *Mater. Today*, **2005**, *8*, 26-33.

26. K. Matyjaszewski, T. E. Patten and J. Xia, *J. Am. Chem. Soc.*, **1997**, *119*, 674-680.

27. B. M. Rosen and V. Percec, *Chem. Rev.*, **2009**, *109*, 5069-5119.

28. G. Moad, E. Rizzardo and S. H. Thang, *Aust. J. Chem.*, **2012**, *65*, 985-1076.

29. D. Charmot, P. Corpart, H. Adam, S. Z. Zard, T. Biadatti and G. Bouhadir, *Macromol. Symp.*, **2000**, *150*, 23-32.

30. M. K. Georges, R. P. N. Veregin, P. M. Kazmaier and G. K. Hamer, *Macromolecules*, **1993**, *26*, 2987-2988.

31. C. J. Hawker, *J. Am. Chem. Soc.*, **1994**, *116*, 11185-11186.

32. D. Benoit, V. Chaplinski, R. Braslau and C. J. Hawker, *J. Am. Chem. Soc.*, **1999**, *121*, 3904-3920.

33. D. Benoit, S. Grimaldi, S. Robin, J.-P. Finet, P. Tordo and Y. Gnanou, *J. Am. Chem. Soc.*, **2000**, *122*, 5929-5939.

34. R. B. Grubbs, *Polym. Rev.*, **2011**, *51*, 104-137.

35. C. Detrembleur, C. Jerome, J. De Winter, P. Gerbaux, J.-L. Clement, Y. Guillaneuf and D. Gigmes, *Polym. Chem.*, **2014**, *5*, 335-340.

36. A. C. Greene and R. B. Grubbs, *Macromolecules*, **2010**, *43*, 10320-10325.

37. W. A. Braunecker and K. Matyjaszewski, *Prog. Polym. Sci.*, **2007**, *32*, 93-146.

38. V. Percec, A. V. Popov, E. Ramirez-Castillo, M. Monteiro, B. Barboiu, O. Weichold, A. D. Asandei and C. M. Mitchell, *J. Am. Chem. Soc.*, **2002**, *124*, 4940-4941.

39. J.-F. Lutz and H. G. Börner, *Prog. Polym. Sci.*, **2008**, *33*, 1-39.

40. R. Whitfield, A. Anastasaki, V. Nikolaou, G. R. Jones, N. G. Engelis, E. H. Discekici, C. Fleischmann, J. Willenbacher, C. J. Hawker and D. M. Haddleton, *J. Am. Chem. Soc.*, **2017**, *139*, 1003-1010.

41. A. Anastasaki, C. Waldron, P. Wilson, C. Boyer, P. B. Zetterlund, M. R. Whittaker and D. Haddleton, *ACS Macro Lett.*, **2013**, *2*, 896–900.

42. P. Corpart, D. Charmot, T. Biadatti, S. Zard and D. Michelet, *Rhodia Chimie Int. Appl.*, **1997**, WO 9858974.

43. S. Perrier, *Macromolecules*, **2017**, *50*, 7433-7447.

44. S. Perrier and P. Takolpuckdee, *J. Polym. Sci., Part A: Polym. Chem.*, **2005**, *43*, 5347-5393.

45. M. R. Wood, D. J. Duncalf, S. P. Rannard and S. Perrier, *Org. Lett.*, **2006**, *8*, 553-556.

46. S. Perrier, P. Takolpuckdee and C. A. Mars, *Macromolecules*, **2005**, *38*, 2033-2036.

47. H. Willcock and R. K. O'Reilly, *Polym. Chem.*, **2010**, *1*, 149-157.

48. K. Matyjaszewski, *Science*, **2011**, *333*, 1104-1105.

49. O. V. Borisov, E. Zhulina, F. A. M. Leermakers and A. H. E. Müller, *Self Organized Nanostructures of Amphiphilic Block Copolymers I*, Springer Berlin Heidelberg, **2011**, 57-129.

50. Y. Mai and A. Eisenberg, *Chem. Soc. Rev.*, **2012**, *41*, 5969-5985.

51. I. A. Nyrkova and A. N. Semenov, *Faraday Discuss.*, **2005**, *128*, 113-127.

52. J. N. Israelachvili, D. J. Mitchell and B. W. Ninham, *Biochim. Biophys. Acta*, **1977**, *470*, 185-201.

53. K. E. B. Doncom, L. D. Blackman, D. B. Wright, M. I. Gibson and R. K. O'Reilly, *Chem. Soc. Rev.*, **2017**, *46*, 4119-4134.

54. S. Jain and F. S. Bates, *Science*, **2003**, *300*, 460-464.

55. D. E. Discher and A. Eisenberg, *Science*, **2002**, *297*, 967-973.

56. D. E. Discher and F. Ahmed, *Annu. Rev. Biomed. Eng.*, **2006**, *8*, 323-341.

57. R. C. Hayward and D. J. Pochan, *Macromolecules*, **2010**, *43*, 3577-3584.

58. T. Nicolai, O. Colombani and C. Chassenieux, *Soft Matter*, **2010**, *6*, 3111-3118.

59. B. E. McKenzie, H. Friedrich, M. J. M. Wirix, J. F. de Visser, O. R. Monaghan, P. H. H. Bomans, F. Nudelman, S. J. Holder and N. A. J. M. Sommerdijk, *Angew. Chem., Int. Ed.*, **2015**, *54*, 2457-2461.

60. N. Petzetakis, A. P. Dove and R. K. O'Reilly, *Chem. Sci.* , **2011**, *2*, 955-960.

61. J. Massey, K. N. Power, I. Manners and M. A. Winnik, *J. Am. Chem. Soc.*, **1998**, *120*, 9533-9540.

62. J. A. Massey, K. Temple, L. Cao, Y. Rharbi, J. Raez, M. A. Winnik and I. Manners, *J. Am. Chem. Soc.*, **2000**, *122*, 11577-11584.

63. N. Petzetakis, D. Walker, A. P. Dove and R. K. O'Reilly, *Soft Matter*, **2012**, *8*, 7408-7414.

64. X. Wang, G. Guerin, H. Wang, Y. Wang, I. Manners and M. A. Winnik, *Science*, **2007**, *317*, 644-647.

65. A. L. Schmitt, M. H. Repollet-Pedrosa and M. K. Mahanthappa, *ACS Macro Lett.*, **2012**, *1*, 300-304.

66. L. Luo and A. Eisenberg, *J. Am. Chem. Soc.*, **2001**, *123*, 1012-1013.

67. S. H. Kim, F. Nederberg, R. Jakobs, J. P. K. Tan, K. Fukushima, A. Nelson, E. W. Meijer, Y. Y. Yang and J. L. Hedrick, *Angew. Chem., Int. Ed.*, **2009**, *48*, 4508-4512.

68. M. He, L. Zhao, J. Wang, W. Han, Y. Yang, F. Qiu and Z. Lin, *ACS Nano*, **2010**, *4*, 3241-3247.

69. J. J. Green and J. H. Elisseeff, *Nature*, **2016**, *540*, 386-394.

70. O. Goor, S. I. S. Hendrikse, P. Y. W. Dankers and E. W. Meijer, *Chem. Soc. Rev.*, **2017**, *46*, 6621-6637.

71. J. H. K. K. Hirschberg, L. Brunsveld, A. Ramzi, J. A. J. M. Vekemans, R. P. Sijbesma and E. W. Meijer, *Nature*, **2000**, *407*, 167-170.

72. S. Venkataraman, Z. A. Chowdhury, A. L. Lee, Y. W. Tong, I. Akiba and Y. Y. Yang, *Macromol. Rapid Commun.*, **2013**, *34*, 652-658.

73. L. Sun, A. Pitto-Barry, N. Kirby, T. L. Schiller, A. M. Sanchez, M. A. Dyson, J. Sloan, N. R. Wilson, R. K. O'Reilly and A. P. Dove, *Nat. Commun.*, **2014**, *5*, 5746-5754.

74. J. D. Watson and F. H. C. Crick, *Nature*, **1953**, *171*, 737-738.

75. A. S. Jones, D. G. Parsons and D. G. Roberts, *Eur. Polym. J.*, **1967**, *3*, 187-198.

76. J. Pitha and P. O. P. Ts'o, *J. Org. Chem.*, **1968**, *33*, 1341-1344.

77. N. Ueda, K. Konda, M. Kono, K. Takemoto and M. Imoto, *Makromol. Chem.*, **1968**, *120*, 13-20.

78. Y. Inaki, *Prog. Polym. Sci.*, **1992**, *17*, 515-570.

79. W. T. Smith Jr, *Prog. Polym. Sci.*, **1996**, *21*, 209-253.

80. R. McHale and R. K. O'Reilly, *Macromolecules*, **2012**, *45*, 7665-7675.

81. H. J. Spijker, A. J. Dirks and J. C. M. van Hest, *Polymer*, **2005**, *46*, 8528-8535.

82. H. J. Spijker, F. L. van Delft and J. C. M. van Hest, *Macromolecules*, **2007**, *40*, 12-18.

83. S. Cheng, M. Zhang, N. Dixit, R. B. Moore and T. E. Long, *Macromolecules*, **2012**, *45*, 805-812.

84. H. J. Spijker, A. J. Dirks and J. C. M. van Hest, *J. Polym. Sci., Part A: Polym. Chem.*, **2006**, *44*, 4242-4250.

85. Y. Kang, A. Lu, A. Ellington, M. C. Jewett and R. K. O'Reilly, *ACS Macro Lett.*, **2013**, *2*, 581-586.

86. Y. Kang, A. Pitto-Barry, A. Maitland and R. K. O'Reilly, *Polym. Chem.*, **2015**, *6*, 4984-4992.

87. Y. Kang, A. Pitto-Barry, H. Willcock, W. D. Quan, N. Kirby, A. M. Sanchezc and R. K. O'Reilly, *Polym. Chem.*, **2015**, *6*, 106-117.

88. Y. Kang, A. Pitto-Barry, M. S. Rolph, Z. Hua, I. Hands-Portman, N. Kirby and R. K. O'Reilly, *Polym. Chem.*, **2016**, *7*, 2836-2846.

89. Y. Inaki, K. Ebisutani and K. Takemoto, *J. Polym. Sci., Polym. Chem. Ed.*, **1986**, *24*, 3249-3262.

90. M. Sedlák, P. Šimůnek and M. Antonietti, *J. Heterocycl. Chem.*, **2003**, *40*, 671-675.

91. J.-F. Lutz, A. F. Thunemann and K. Rurack, *Macromolecules*, **2005**, *38*, 8124-8126.

92. H. Tang, M. Radosz and Y. Shen, *J. Polym. Sci., Part A: Polym. Chem.*, **2006**, *44*, 6607-6615.

93. J.-F. Lutz, S. Pfeifer, M. Chanana, A. F. Thünemann and R. Bienert, *Langmuir*, **2006**, *22*, 7411-7415.

94. M. Nakahata, Y. Takashima, A. Hashidzume and A. Harada, *Chem. Eur. J.* , **2015**, *21*, 2770-2774.

95. V. C. Gibson, E. L. Marshall, M. North, D. A. Robson and P. J. Williams, *Chem. Commun.*, **1997**, 1095-1096.

96. R. Gareth Davies, V. C. Gibson, M. B. Hursthouse, M. E. Light, E. L. Marshall, M. North, D. A. Robson, I. Thompson, A. J. P. White, D. J. Williams and P. J. Williams, *J. Chem. Soc., Perkin Trans. 1*, **2001**, 3365-3381.

97. H. S. Bazzi and H. F. Sleiman, *Macromolecules*, **2002**, *35*, 9617-9620.

98. P. K. Lo and H. F. Sleiman, *J. Am. Chem. Soc.*, **2009**, *131*, 4182-4183.

99. C. Burd and M. Weck, *Macromolecules*, **2005**, *38*, 7225-7230.

100. C. R. South and M. Weck, *Macromolecules*, **2007**, *40*, 1386-1394.

101. H. Yang and W. Xi, *Polymers*, **2017**, *9*, 666-689.

102. A. Khan, D. M. Haddleton, M. J. Hannon, D. Kukulj and A. Marsh, *Macromolecules*, **1999**, *32*, 6560-6564.

103. A. Marsh, A. Khan, M. Garcia and D. M. Haddleton, *Chem. Commun.*, **2000**, 2083-2084.

104. M. Garcia, K. Kempe, D. M. Haddleton, A. Khan and A. Marsh, *Polym. Chem.*, **2015**, *6*, 1944-1951.

105. J.-F. Lutz, A. F. Thünemann and R. Nehring, *J. Polym. Sci., Part A: Polym. Chem.*, **2005**, *43*, 4805-4818.

106. K. Zhang, G. B. Fahs, M. Aiba, R. B. Moore and T. E. Long, *Chem. Commun.*, **2014**, *50*, 9145-9148.

107. K. Zhang, M. Aiba, G. B. Fahs, A. G. Hudson, W. D. Chiang, R. B. Moore, M. Ueda and T. E. Long, *Polym. Chem.*, **2015**, *6*, 2434-2444.

108. K. Zhang, S. J. Talley, Y. P. Yu, R. B. Moore, M. Murayama and T. E. Long, *Chem. Commun.*, **2016**, *52*, 7564-7567.

109. R. McHale, J. P. Patterson, P. B. Zetterlund and R. K. O'Reilly, *Nat. Chem.*, **2012**, *4*, 491-497.

110. D. Fong, Z. Hua, T. R. Wilks, R. K. O'Reilly and A. Adronov, *J. Polym. Sci., Part A: Polym. Chem.*, **2017**, *55*, 2611-2617.

111. Y.-S. Wu, Y.-C. Wu and S.-W. Kuo, *Polymers*, **2014**, *6*, 1827-1845.

112. B. D. Mather, M. B. Baker, F. L. Beyer, M. A. G. Berg, M. D. Green and T. E. Long, *Macromolecules*, **2007**, *40*, 6834-6845.

113. B. D. Mather, M. B. Baker, F. L. Beyer, M. D. Green, M. A. G. Berg and T. E. Long, *Macromolecules*, **2007**, *40*, 4396-4398.

114. J. Han, Y. Zheng, B. Zhao, S. Li, Y. Zhang and C. Gao, *Sci. Rep.*, **2014**, *4*, 4387.

115. W. Xi, S. Pattanayak, C. Wang, B. Fairbanks, T. Gong, J. Wagner, C. J. Kloxin and C. N. Bowman, *Angew. Chem., Int. Ed.*, **2015**, *54*, 14462-14467.

116. Z. Liu, B. Fairbanks, L. He, T. Liu, P. Shah, J. N. Cha, J. W. Stansbury and C. N. Bowman, *Chem. Commun.*, **2017**, *53*, 10156-10159.

117. Y. T. Tsao and K. L. Wooley, *J. Am. Chem. Soc.*, **2017**, *139*, 5467-5473.

118. Y.-Y. T. Tsao, T. H. Smith and K. L. Wooley, *ACS Macro Lett.*, **2018**, *7*, 153-158.

119. M. Garcia, M. P. Beecham, K. Kempe, D. M. Haddleton, A. Khan and A. Marsh, *Eur. Polym. J.*, **2015**, *66*, 444-451.

120. M. Garcia, *Sythesis and Template-Directed Polymerization Studies of Nucleoside Analogues*, Ph. D. Thesis, Universisty of Warwick, 2003.

121. A. Harguindey, D. W. Domaille, B. D. Fairbanks, J. Wagner, C. N. Bowman and J. N. Cha, *Adv. Mater.*, **2017**, *29*, 1700743.

122. J. J. Storhoff and C. A. Mirkin, *Chem. Rev.*, **1999**, *99*, 1849-1862.

123. Z. J. Gartner, M. W. Kanan and D. R. Liu, *J. Am. Chem. Soc.*, **2002**, *124*, 10304-10306.

124. C. T. Calderone and D. R. Liu, *Angew. Chem., Int. Ed.*, **2005**, *117*, 7549-7552.

125. G. De Bo, S. Kuschel, D. A. Leigh, B. Lewandowski, M. Papmeyer and J. W. Ward, *J. Am. Chem. Soc.*, **2014**, *136*, 5811-5814.

126. P. W. Rothemund, *Nature*, **2006**, *440*, 297-302.

127. Q. Zhou and S. E. Rokita, *Proc. Natl. Acad. Sci. U. S. A.*, **2003**, *100*, 15452-15457.

128. F. Ilhan, T. H. Galow, M. Gray, G. Clavier and V. M. Rotello, *J. Am. Chem. Soc.*, **2000**, *122*, 5895-5896.

129. U. Drechsler, R. J. Thibault and V. M. Rotello, *Macromolecules*, **2002**, *35*, 9621-9623.

130. Y. Kang, A. Pitto-Barry, H. Willcock, W. Quan, N. Kirby, A. M. Sanchez and R. K. O'Reilly, *Polym. Chem.*, **2015**, *6*, 106-117.

131. P. E. Nielsen, *Curr. Opin. Biotechnol.*, **1999**, *10*, 71-75.

132. Z. Zhou, X. Xia and D. Bong, *J. Am. Chem. Soc.*, **2015**, *137*, 8920-8923.

133. N. Ishikawa, M. Furutani and K. Arimitsu, *ACS Macro Lett.*, **2015**, *4*, 741-744.

134. X. Liu, Q. Zhang and G. Gao, *Adv. Funct. Mater.*, **2017**, *27*, 1703132.

Chapter 2. Micellar nanoparticles with tuneable morphologies through interactions between nucleobase-containing synthetic polymers in aqueous solutions

2.1. Declaration of authorship

The SAXS data in this Chapter was collected and analyzed by Dr. Anaïs Pitto-Barry (University of Warwick). HR Mass Spectra in this Chapter was analyzed by mass spectrometry group (University of Warwick).

This work has been published in *Polymer Chemistry*.

Hua, Z.; Pitto-Barry, A.; Kang, Y.; Kirby, N.; Wilks, T. R.; O'Reilly, R. K. Micellar Nanoparticles with Tuneable Morphologies through Interactions between Nucleobase-Containing Synthetic Polymers in Aqueous Solution. *Polym. Chem.* **2016**, *7*, 4254-4262.

2.2. Abstract

Herein, nucleobase-containing synthetic amphiphilic diblock copolymers were prepared using RAFT polymerization. Well-defined spherical micelles were formed in aqueous solutions through the self-assembly of amphiphilic copolymers, with the nucleobase functionality sequestered in the core of the particles. Following assembly, copolymers with the complementary nucleobase were introduced into the preformed micellar solutions. This addition induced a change in nanostructure size and morphology and this reorganization was fully characterized by DLS, TEM, SLS and SAXS analyses. The insertion of copolymers with the complementary nucleobase into formed micelles was also confirmed by ^{1}H NMR and UV-vis spectroscopy. For micelles consisting of moderately short hydrophobic blocks, upon the addition of complementary nucleobase copolymer a decrease in size was observed, but without any accompanying morphological change. For micelles formed from longer hydrophobic blocks, a morphological transition from spheres to cylinders and then to smaller spheres was observed upon increasing the amount of the complementary copolymer added. This work highlights how complementary nucleobase interactions can be used to induce nanostructure reorganizations and through a simple mixing process provide access to different nanostructure sizes and morphologies.

2.3. Introduction

The self-assembly of amphiphilic block copolymer micelles has attracted considerable attention due to the wide range of morphologies that can be formed, and the possibility to incorporate specific functional molecules, potentially leading to a number of novel applications. Different morphologies include spherical micelles,[1] cylindrical micelles,[2-5] bicontinuous structures,[6] lamellae[7, 8] and vesicles,[1, 9-12] among others. Such morphologies can be predictably accessed through changes to the hydrophobic/hydrophilic weight fraction, which influences the packing parameter.[13, 14] There is significant interest in tuning nanostructure size and morphology as these are critical parameters in desired applications. For example, nanostructures with different morphologies can show distinct properties *in vivo*. Indeed, cylindrical micelles can persist in the circulation up to ten times longer than their spherical counterparts.[15] Different morphologies can be accessed through using standard post-polymerization self-assembly methods,[16-18] or more recently polymerization-induced self-assembly (PISA).[19-22] There is also increasing interest in the utility of responsive polymers to enable reversible morphology transitions in polymeric nanostructures.[23-25]

Nucleobase-containing synthetic polymers inspired by nature have been widely exploited to mediate polymer tacticity,[26] to control polymer composition or sequence[27, 28] and to template polymerizations.[29-31] All these studies have been inspired by the sequence specificity and selective recognition of nucleobase functionalities which can be exploited to create DNA materials[32-34] and perform DNA template chemistry.[35-37]

Nucleobase interactions have also been utilized to drive self-assembly[38-43] and for achieving a biomimetic segregation/templating approach to polymer synthesis.[44] More recently, it has been shown that distinct self-assembled morphologies were formed with different nucleobase copolymer compositions and different morphological evolutions were observed in $CHCl_3$ and 1,4-dioxane during the RAFT dispersion polymerization of nucleobase-functional monomers.[28, 45, 46] The poor solubility and slow hydrolysis of the

monomers in water, however, limits their applications in aqueous solutions. To the best of our knowledge, there is relatively little research into the self-assembly of nucleobase-containing polymers in aqueous solutions.[42, 47-50] A study by the van Hest group reported the self-assembly behavior of nucleobase-containing amphiphilic copolymers in aqueous solutions and most notably an increase of overall hydrophilicity of the diblock, due to complementary (adenine:thymine) nucleobase interactions, was observed.[42]

A new family of amphiphilic block copolymers, known as DNA block copolymers (DBCs), have been described, which are composed of a hydrophobic synthetic polymer component attached to a single-stranded (ss) DNA.[51-53] The introduction of DBCs into water leads to the formation of micelles with a hydrophobic polymer core and a hydrophilic DNA corona. Precise pairings between complementary functional DNA can be used to modify the micelle at particular locations, from the hydrophobic-hydrophilic interface to the whole corona.[54, 55] However, the complementary DNA interactions can only be achieved in the corona. Pioneering work reported by the Gianneschi group demonstrated the size and shape of micelles could be controlled through complementary base pairing interactions in the corona.[56] But this approach requires expensive DNA building blocks for polymer coupling and this to date has hindered their large-scale and widespread application in self-assembly. Hence, there is significant interest in the exploration of complementary nucleobase interactions embedded within synthetic polymers to allow for access to new classes of responsive and tuneable materials and nanostructures.

Herein we report the assembly of nucleobase-containing micelles with tuneable morphologies through the introduction of complementary nucleobase interactions within the core of the micelles. The initial micellar constructs in water consist of synthetic nucleic acid cores and hydrophilic coronas (poly(4-acryloylmorpholine)-*b*-poly(3-(thymin-1-yl)propyl acrylamide) (PNAM-*b*-PTAm)). Another diblock copolymer with the complementary nucleobase (poly(4-acryloylmorpholine)-*b*-poly(3-(adenine-9-yl)propyl acrylamide) (PNAM-*b*-PAAm)) was utilized to induce a morphological change in these micelles. For micelles with TAm blocks of moderate length, a gradual decrease in the size of the spherical micelles

was observed with the introduction of increasing amounts of the complementary diblock copolymer, PNAM-*b*-PAAm. Micelles with a much longer TAm block core, demonstrated different behaviors as they showed an initial increase of hydrodynamic diameters through insertion of PNAM-*b*-PAAm into the micellar core, which was then followed by a morphological change from spheres to cylinders, and finally to smaller spheres. The utilization of unique complementary A-T interactions in the micellar cores enables us to progressively tailor nanostructure sizes and morphologies and provides a new route to access functional nanomaterials.

2.4. Results and discussion

2.4.1. Syntheses of nucleobase-containing acrylamide monomers

Although nucleobase-containing methacrylate-, styrene-, acrylate- and methacrylamide-type monomers have been reported by different groups,[28, 29, 57-59] the more reactive and water-soluble acrylamide analogs have rarely been prepared.[38, 60, 61] The synthesis of nucleobase-containing acrylamide monomers AAm and TAm was achieved using 3-bromopropylacrylamide as alkylating agent according to Scheme 2.1.

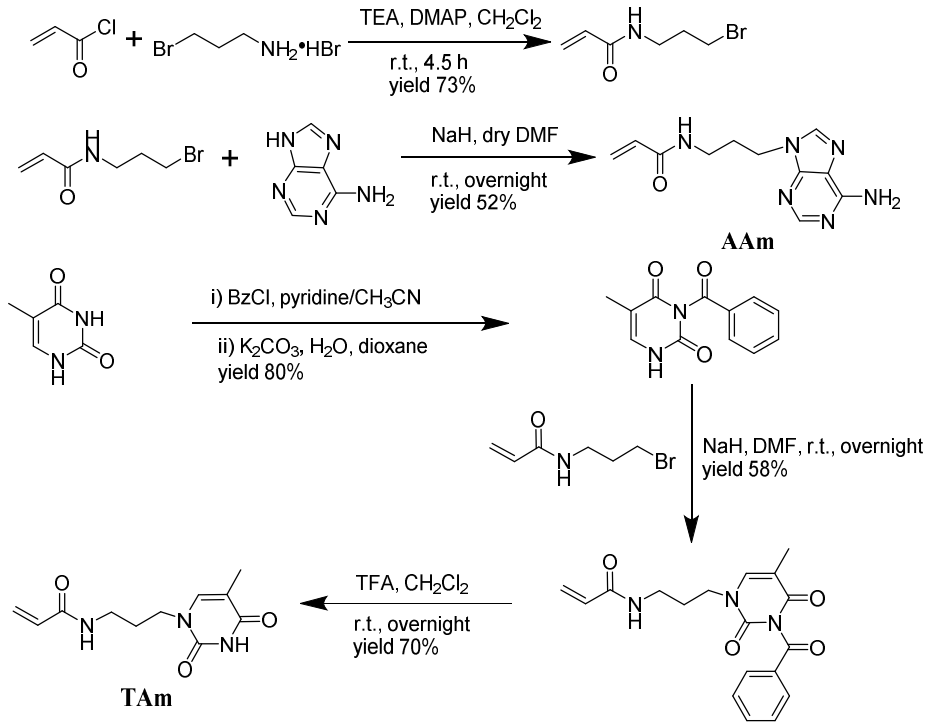

Scheme 2.1. Syntheses of adenine and thymine acrylamide monomers (AAm and TAm).

The obtained 3-bromopropylacrylamide was used immediately, as the possible substitution between the amide and bromide could not be avoided during storage. 3-(Adenine-9-yl)propyl acrylamide (AAm) of high purity were made in a relatively high yield by direct substitution (Figure 2.1).

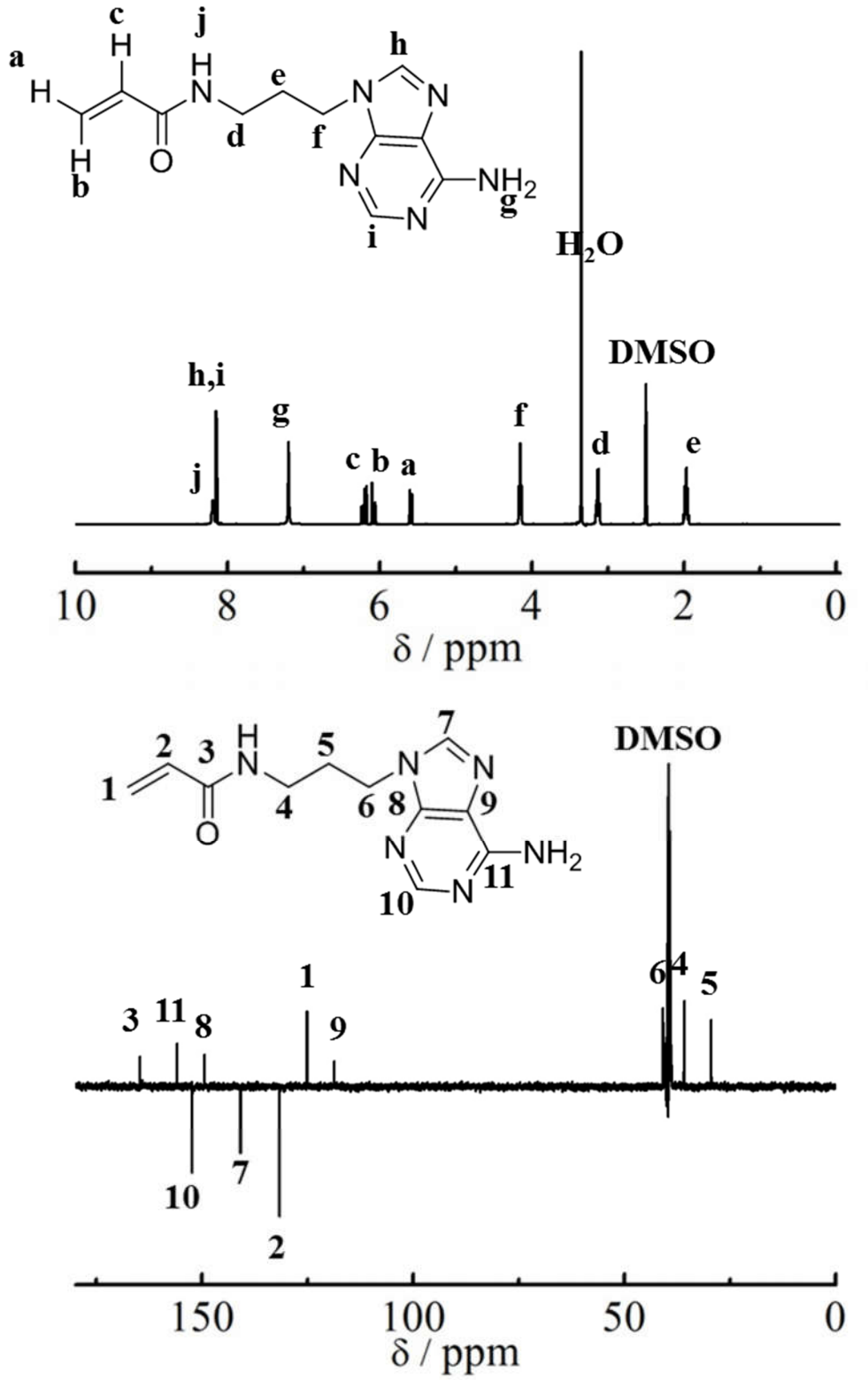

Figure 2.1. ^{1}H NMR and ^{13}C NMR spectra of 3-(adenine-9-yl)propyl acrylamide (AAm) in DMSO-d_6.

In contrast, the direct alkylation of thymine led to a mixture of many species, including the substitution and the Michael addition of both *N*1 and *N*3 position in thymine with 3-bromopropylacrylamide. Several attempts to optimize the reaction conditions by decreasing the reaction temperature and time could not increase the selectivity and yield of the targeted molecule. Therefore, the selective protection and deprotection strategies were used to make 3-(thymin-1-yl)propyl acrylamide (TAm) in a moderate yield of 33% over 3 steps (Scheme 2.1 and Figure 2.2).

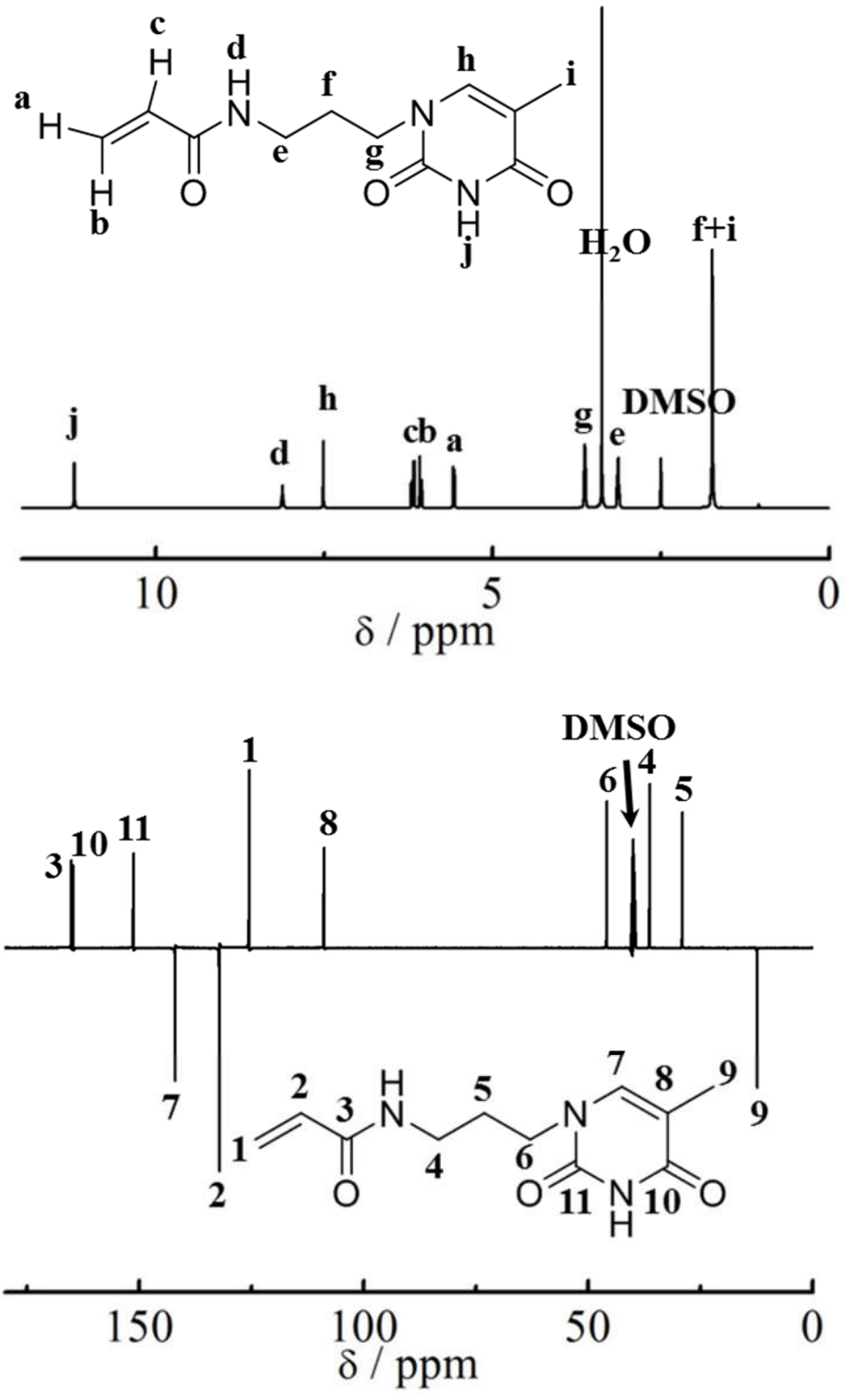

Figure 2.2. ^{1}H NMR and ^{13}C NMR spectra of 3-(thymin-1-yl)propyl acrylamide (TAm) in DMSO-d_6.

2.4.2. Synthesis and characterization of nucleobase-containing synthetic diblock copolymers

A PNAM macro-CTA was synthesized by RAFT polymerization in a mixture of water and 1,4-dioxane (Scheme 2.2).[62]

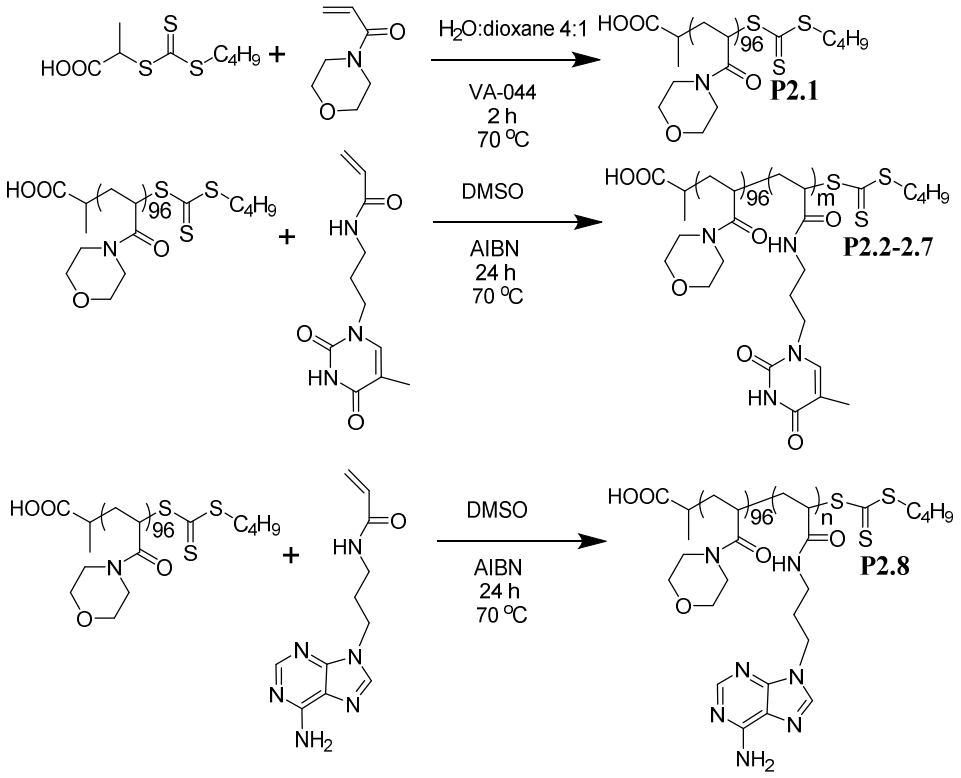

Scheme 2.2. Synthetic routes for the preparation of $PNAM_{96}$ **P2.1** and the nucleobase-containing block copolymers, **P2.2-P2.8**.

This $PNAM_{96}$ macro-CTA (**P2.1**) was then chain-extended with various amounts of TAm or AAm in DMSO to yield a series of $PNAM_{96}$-*b*-PTAm/PAAm diblock copolymers (**P2.2**–**P2.8**). Each TAm/AAm polymerization was carried out for 24 h at 70 °C prior to analysis by ^{1}H NMR spectroscopy and SEC with DMF as eluent.

The characterization data for the polymers are summarized in Table 2.1. ^{1}H NMR spectroscopy was used to calculate the DP by comparing the integrated signals corresponding to characteristic signals from the

nucleobases (δ = 11.23 ppm) with those assigned to the end group of the CTA (δ = 0.84 ppm) (Figure 2.3).

Table 2.1. Characterization data of macro-CTA and nucleobase-containing diblock copolymers.

Polymer	Structure	Micelle formed	$M_{n,NMR}$[a] (kDa)	$M_{n,SEC}$[b] (kDa)	$Đ_M$[b]
P2.1	$PNAM_{96}$	-	13.8	13.9	1.06
P2.2	$PNAM_{96}$-*b*-$PTAm_{17}$	-	17.8	19.1	1.09
P2.3	$PNAM_{96}$-*b*-$PTAm_{34}$	-	21.8	22.9	1.10
P2.4	$PNAM_{96}$-*b*-$PTAm_{114}$	**M2.4**	40.8	33.7	1.24
P2.5	$PNAM_{96}$-*b*-$PTAm_{301}$	**M2.5**	85.1	68.4	1.29
P2.6	$PNAM_{96}$-*b*-$PTAm_{63}$	**M2.6**	28.7	26.0	1.18
P2.7	$PNAM_{96}$-*b*-$PTAm_{160}$	**M2.7**	51.7	40.6	1.28
P2.8	$PNAM_{96}$-*b*-$PAAm_{19}$	-	18.5	19.9	1.08

[a]Measured by ^{1}H NMR spectroscopy (400 MHz) in deuterated DMSO. [b]Measured by DMF SEC at 50 °C with poly(methyl methacrylate) (PMMA) standards.

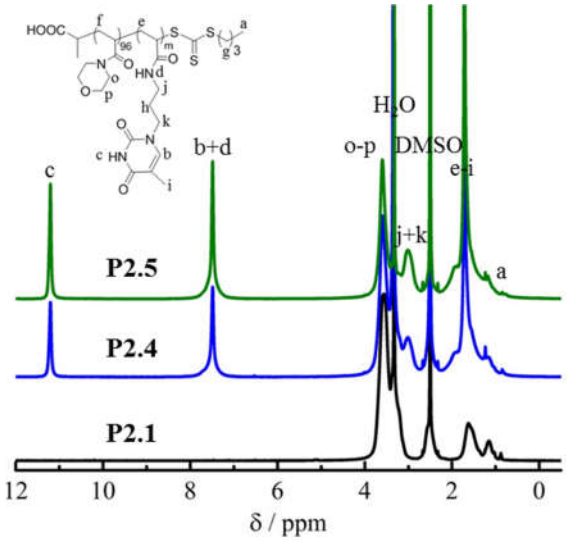

Figure 2.3. Representative ^{1}H NMR spectra of macro-CTA **P2.1** and nucleobase-containing diblock copolymers **P2.4** and **P2.5** in DMSO-d_6.

SEC traces revealed unimodal molecular weight distributions ($Đ_M$ < 1.30) and minimal contamination of unreacted $PNAM_{96}$ macro-CTA (Figure 2.4). These results indicated diblock nucleobase copolymers were obtained with relatively high blocking efficiencies through RAFT polymerization.

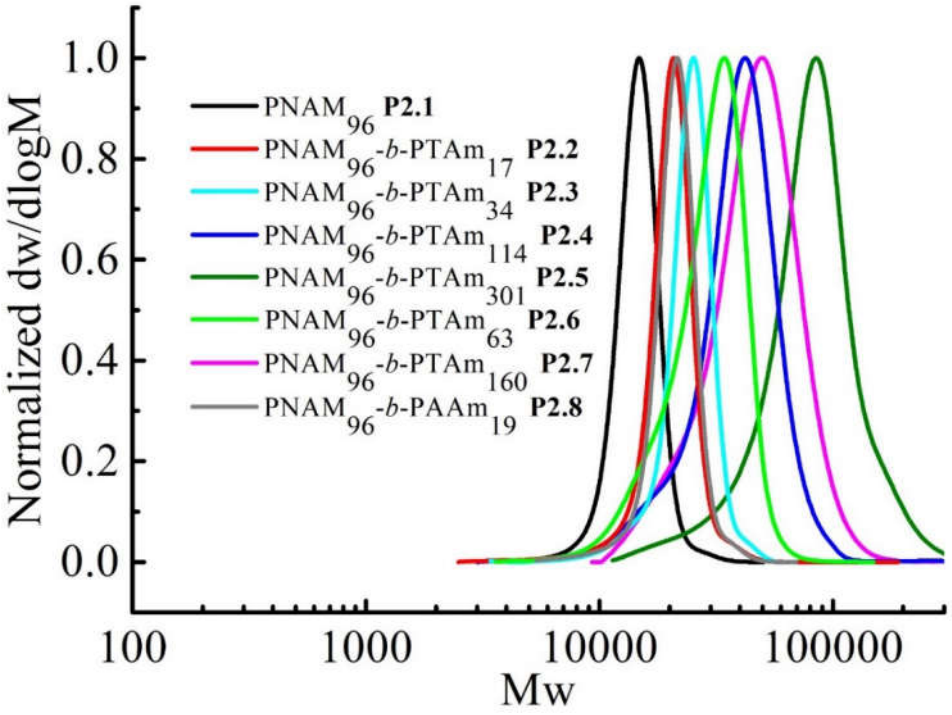

Figure 2.4. SEC traces (DMF + 5 mM NH_4BF_4 as eluent) of macro-CTA **P2.1** and nucleobase-containing diblock copolymers **P2.2**-**2.8**.

2.4.3. Self-assembly of PNAM-*b*-PTAm diblock copolymers

The self-assembly of the diblock copolymers was achieved by direct dissolution of the polymers in water at a concentration of 10 mg mL^{-1} at 70 °C, with overnight stirring. DLS analysis of the solution **M2.4** (with a small thymine core) showed that nanoparticles with a diameter of 58 nm were formed from copolymer **P2.4** (Figure 2.5a). TEM images confirmed the spherical nature of the micelles **M2.4** (with a small thymine core) from copolymer **P2.4** (Figure 2.5b).

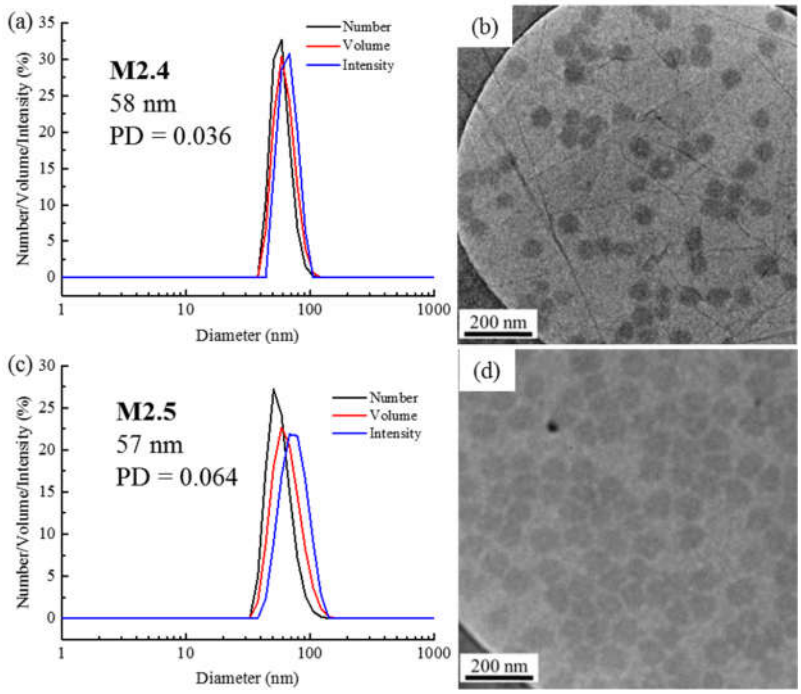

Figure 2.5. (a, c) DLS analyses and (b, d) TEM images of self-assembled micelles **M2.4** (with a small thymine core) and **M2.5** (with a large thymine core) from $PNAM_{96}$-*b*-$PTAm_{114}$ **P2.4** and $PNAM_{96}$-*b*-$PTAm_{301}$ **P2.5** on graphene oxide without staining, respectively.

The diblock copolymers **P2.4-2.7** with relatively long hydrophobic TAm blocks can efficiently self-assemble to form micelles **M2.4-2.7** (Table 2.1), respectively, as the long TAm block can provide sufficient hydrophobic effects to form a stable hydrophobic core.[63] The image analysis revealed that the diameter of the spherical micelles **M2.4-2.7** was narrowly dispersed (Figure 2.6). The diameter from TEM analysis is slightly smaller than that from DLS analyses partly due to the insensitivity of the former technique to the hydrophilic corona domain.

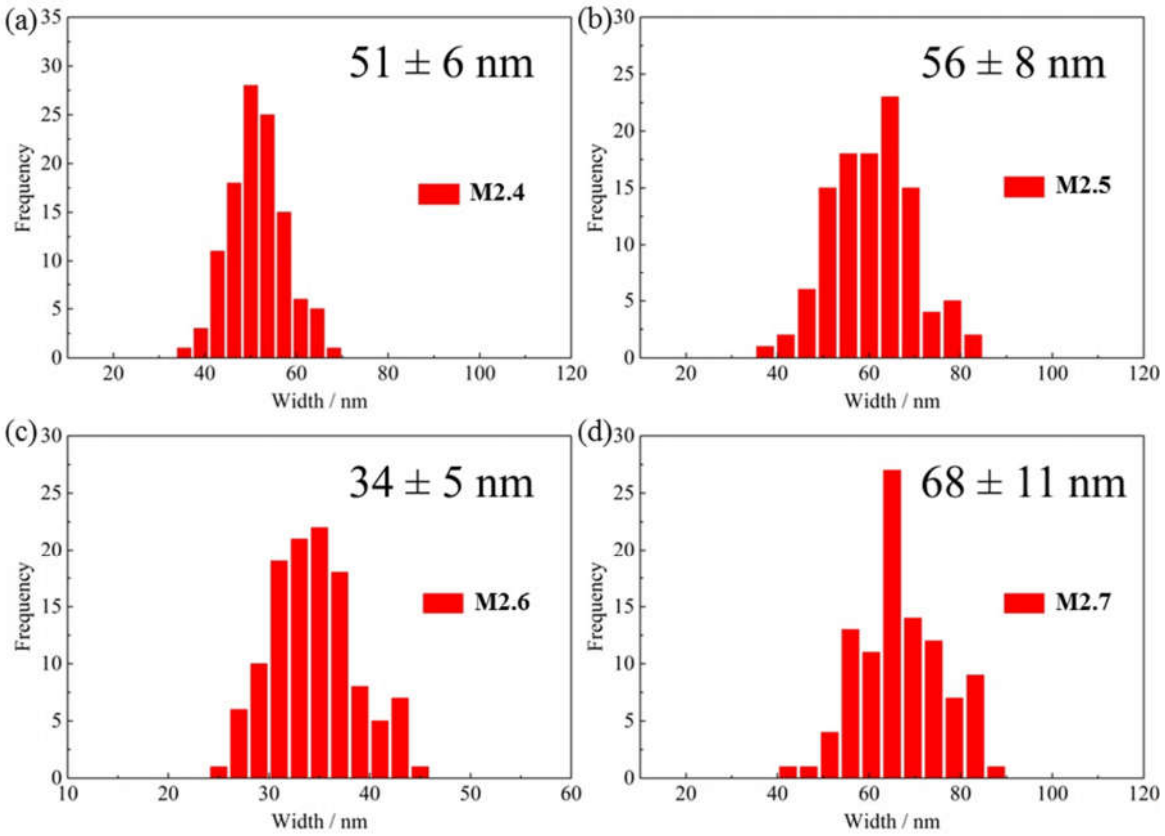

Figure 2.6. Histograms of the diameters of PNAM-*b*-PTAm spherical micelles **M2.4-2.7** as determined by TEM analyses.

For copolymer **P2.5**, which has a much longer hydrophobic block, a direct dissolution method could only form ill-defined nanostructures. DLS analysis showed a bimodal distribution and TEM images also indicated that the sample contained both worms and spheres (Figure 2.7). No morphological change was observed even after heating at 70 °C for several days. The long hydrophobic block could result in a large energy barrier for unimer exchange, leading to the formation of 'frozen' micelles.[64]

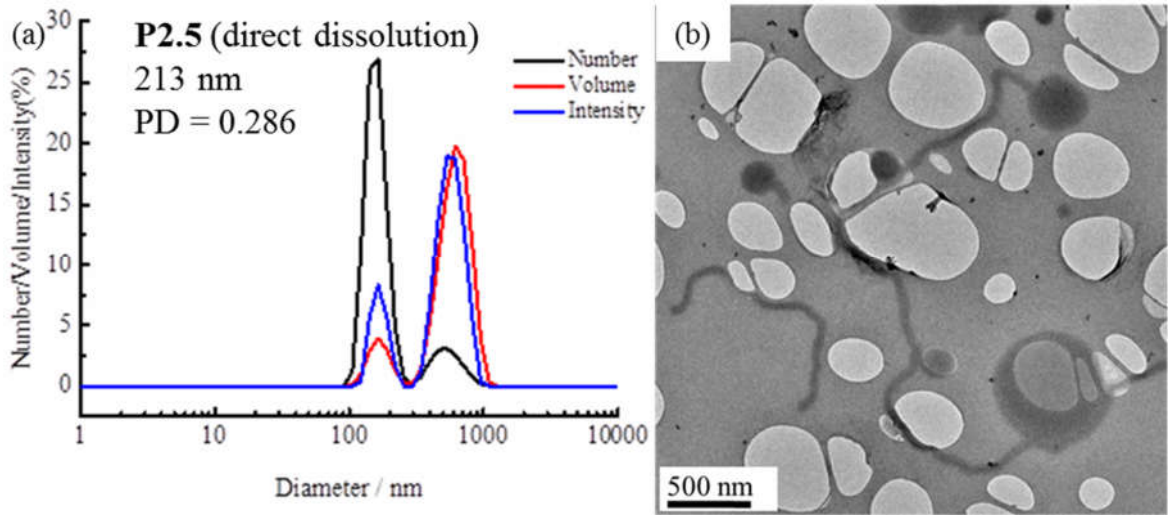

Figure 2.7. DLS analysis and TEM image of $PNAM_{96}$-*b*-$PTAm_{301}$ (**P2.5**) solution by direct dissolution in water at 70 °C, under overnight stirring.

Compared with the direct dissolution method, it was found that well-defined micelles could be easily formed through a solvent switch method, especially for the crew-cut aggregates with a long hydrophobic block like **P2.5**. Specifically, the copolymer **P2.5** was dissolved in DMF at 8 mg mL^{-1} and water was added at a very slow rate (1 mL h^{-1}) to make a final solution of *ca.* 1 mg mL^{-1}. The DMF was then removed by dialysis against water incorporating at least 6 water changes. DLS and TEM analyses indicated well-defined nanostructures **M2.5** (with a large thymine core) were formed (Figure 2.5c and d).

It is noteworthy that micelles of both **M2.4** (with a small thymine core) and **M2.5** (with a large thymine core) had a similar D_h and N_{agg} as determined by the combined DLS and SLS analyses (Figure 2.8 and Table 2.2). Therefore, a much larger hydrophobic core was formed for **M2.5** as the hydrophobic block was much longer than **M2.4**. Compared with **M2.4** (with a small thymine core), a much higher energy barrier for chain exchange in **M2.5** (with a large thymine core) was required to be overcome due to the higher interfacial tension between the hydrophobic block and the solvent.[64]

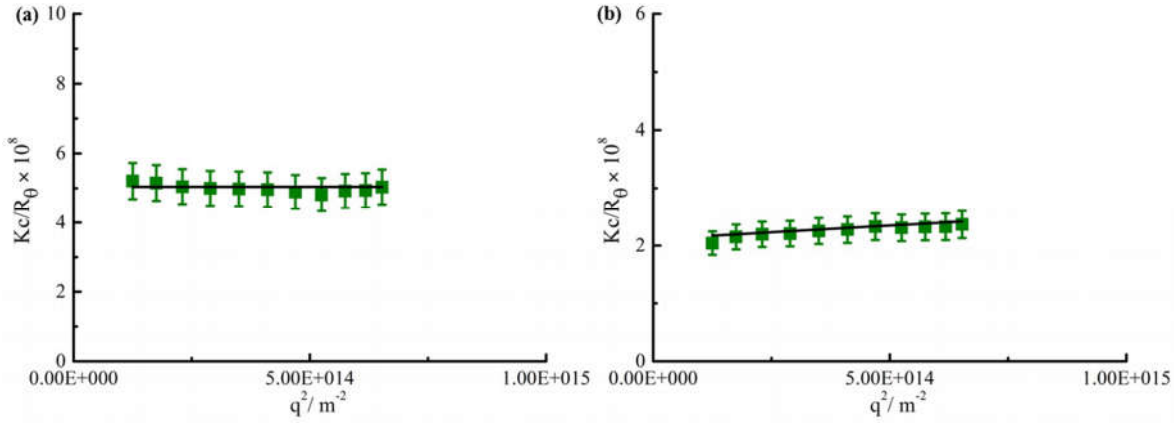

Figure 2.8. SLS plot of the Rayleigh ratio *vs* q^2 for (a) PNAM$_{96}$-*b*-PTAm$_{114}$ (**M2.4**) and (b) PNAM$_{96}$-*b*-PTAm$_{301}$ (**M2.5**) micelles in water with 10% error bars. This plot gave M_w = 1.97 × 10^4 kg mol^{-1}, N_{agg} = 390 for **M2.4** (with a small thymine core) and M_w = 4.7 × 10^4 kg mol^{-1}, N_{agg} = 431 for **M2.5** (with a large thymine core), respectively.

Table 2.2. Comparison of the diameters and average-aggregation number, N_{agg} for micelles of **M2.4** (with a small thymine core) and **M2.5** (with a large thymine core).

Sample	D_h[a] (nm)	D_n[b] (nm)	N_{agg}[c]	D_{core}[d] (nm)
M2.4	58	51	390	32
M2.5	57	56	431	47

[a]Measured by DLS. [b]Measured by TEM. [c]Measured by SLS. [d]Core sizes were calculated according to the N_{agg} from SLS.[65]

2.4.4. Tuning spherical micelle sizes using complementary nucleobase interactions

The formed self-assembled micelles contained TAm cores, which can interact with AAm through hydrogen-bonding. To explore this, copolymer **P2.8** containing the complementary nucleobase adenine was added to the micellar solutions described above with the aim of inducing a response as a result of the formation of complementary hydrogen bonds within the confined core domain. It is notable that copolymer **P2.8** (with an adenine block) was observed to form small aggregates in water with N_{agg} of *ca.* 13 as measured by SLS and SAXS analyses (Figure 2.9).

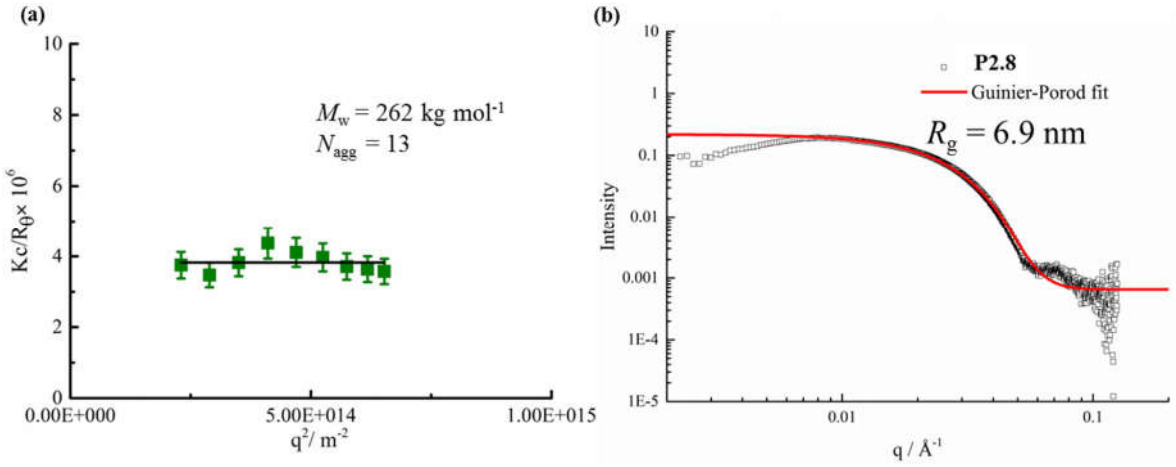

Figure 2.9. The characterization of the copolymer **P2.8** (with an adenine block) in H_2O by SLS and SAXS analyses. (a). SLS plot of the Rayleigh ratio *vs* q^2 for **P2.8** (with an adenine block) gave M_w = 262 kg mol^{-1}, N_{agg} = 13; (b) SAXS analysis gave R_g = 6.9 nm for **P2.8** (with an adenine block).

It is expected that copolymers with longer AAm blocks could form larger and more stable aggregates, which may limit their ability to induce such complementary interactions upon addition to the parent micelles. Therefore, we explored the addition of copolymer **P2.8** (with an adenine block), which had a relatively short AAm block, to micelle solutions of **M2.4** (with a small thymine core) and **M2.5** (with a large thymine core).

To explore this reorganization, different molar ratios of **P2.8** (with an adenine block) solution (10 mg mL^{-1}) were added to micelle solutions of **M2.4** (with a small thymine core) and left to stir overnight at room temperature. The solutions were then analyzed by DLS, which indicated a significant decrease in micelle sizes with an increased quantity of complementary copolymers (Figure 2.10b). The pristine micelles had a diameter of *ca.* 58 nm, which decreased to just 38 nm after the addition of 1 molar eq. of **P2.8** (with an adenine block). Further, smaller micelles with diameters of *ca.* 34 nm and 29 nm were obtained upon addition of 3 molar eq. and 5 molar eq. of **P2.8** (with an adenine block), respectively (Figure 2.10b).

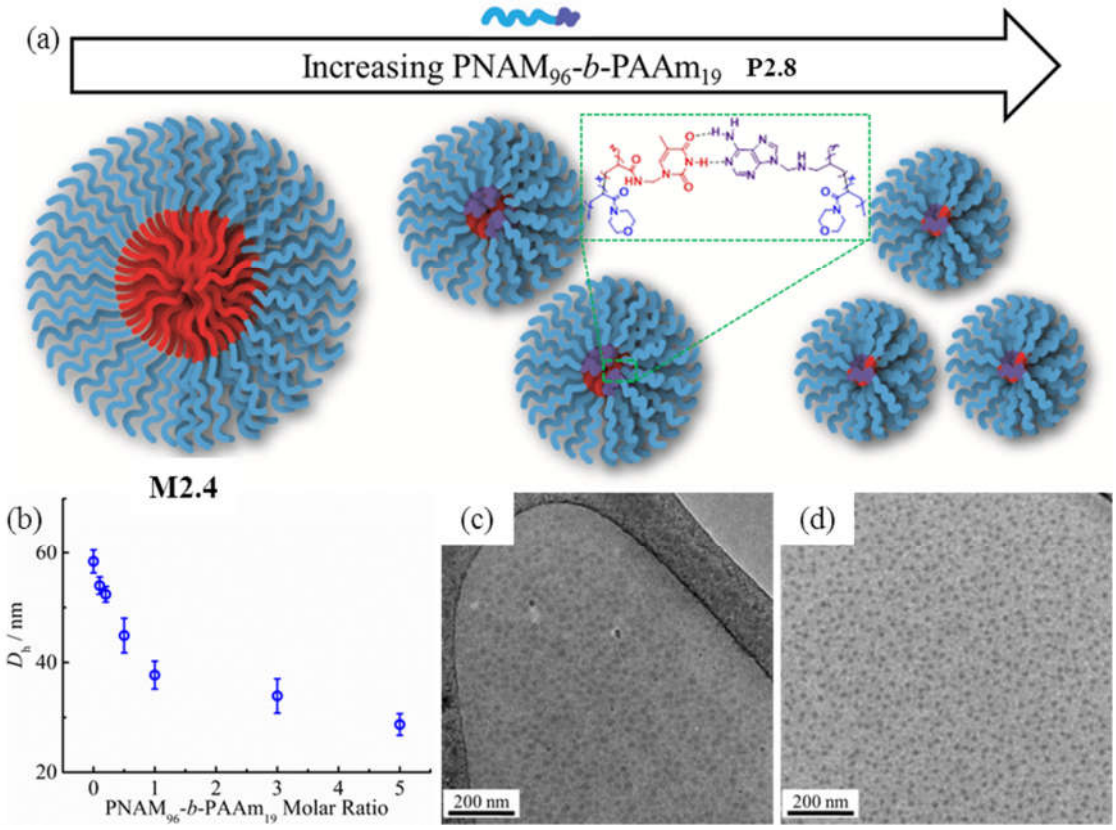

Figure 2.10. Interactions between **P2.8** (with an adenine block) and micelle **M2.4** (with a small thymine core) result in a change in nanoparticle sizes. (a) Schematic of the micellar size decrease through hydrogen-bonding interactions between **P2.8** (with an adenine block) and micelle **M2.4** (with a small thymine core); (b) DLS hydrodynamic diameters (D_h) of micellar solutions of **M2.4** (with a small thymine core) with increasing molar ratios of **P2.8** (with an adenine block); (c, d) TEM images of micellar solutions of **M2.4** (with a small thymine core) upon addition of 1 molar eq. and 5 molar eq. of **P2.8** (with an adenine block).

Further TEM images confirmed smaller spherical micelles were produced by mixing initial micelles composed of **M2.4** (with a small thymine core) and complementary copolymer **P2.8** (with an adenine block) (Figure 2.10c, d). For self-assembled spherical micelles **M2.6** or **M2.7** composed of **P2.6** or **P2.7** with a slightly shorter or longer hydrophobic block respectively, a similar change of micelle sizes was observed (Figure 2.11-2.13). Meanwhile, there were no obvious changes observed when mixing initial micelles of **M2.4** (with a small thymine core) and non-complementary copolymer **P2.2** (Figure 2.11).

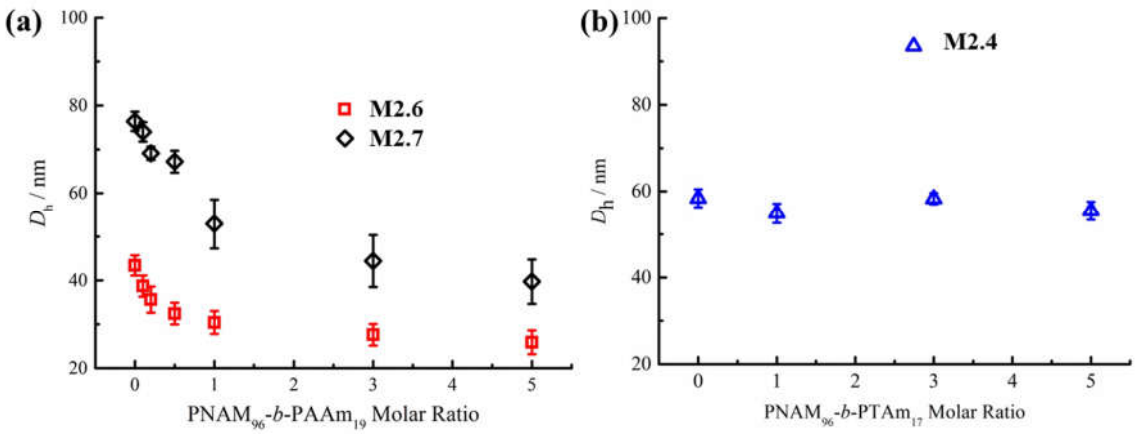

Figure 2.11. (a) DLS data of PNAM$_{96}$-*b*-PTAm$_{63}$ (**M2.6**) or PNAM$_{96}$-*b*-PTAm$_{160}$ (**M2.7**) micelle solutions mixed with different molar ratios of PNAM$_{96}$-*b*-PAAm$_{19}$ (**P2.8**); (b) DLS data of PNAM$_{96}$-*b*-PTAm$_{114}$ micelle **M2.4** solutions mixed with different molar ratios of the non-complementary copolymer PNAM$_{96}$-*b*-PTAm$_{17}$ (**P2.2**).

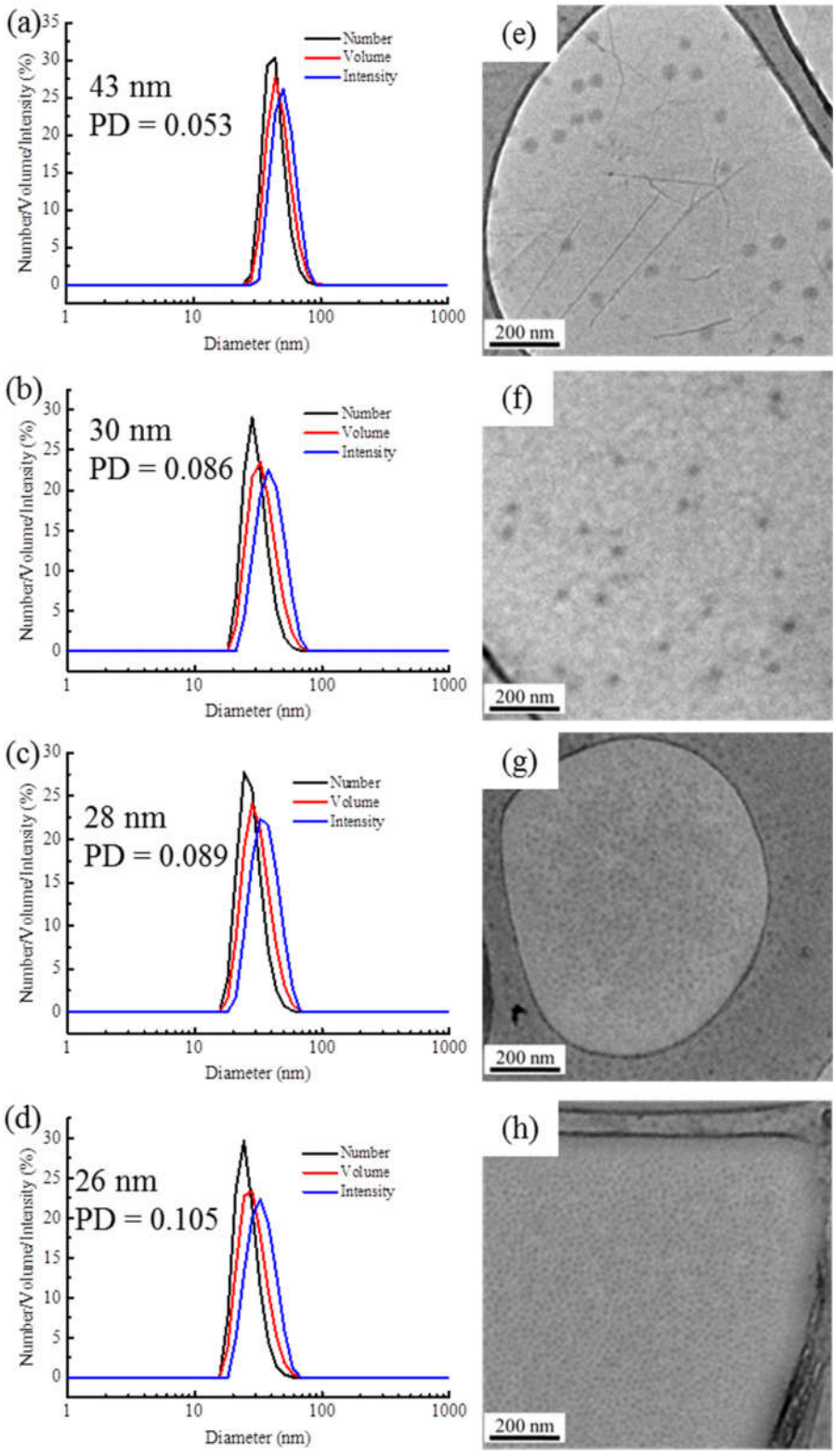

Figure 2.12. DLS analyses and TEM images of $PNAM_{96}$-*b*-$PTAm_{63}$ **M2.6** micelle solution mixed with different molar ratios of $PNAM_{96}$-*b*-$PAAm_{19}$ (**P2.8**). (a, e) 0 molar eq., (b, f) 1 molar eq., (c, g) 3 molar eq., (d, h) 5 molar eq. of $PNAM_{96}$-*b*-$PAAm_{19}$ (**P2.8**).

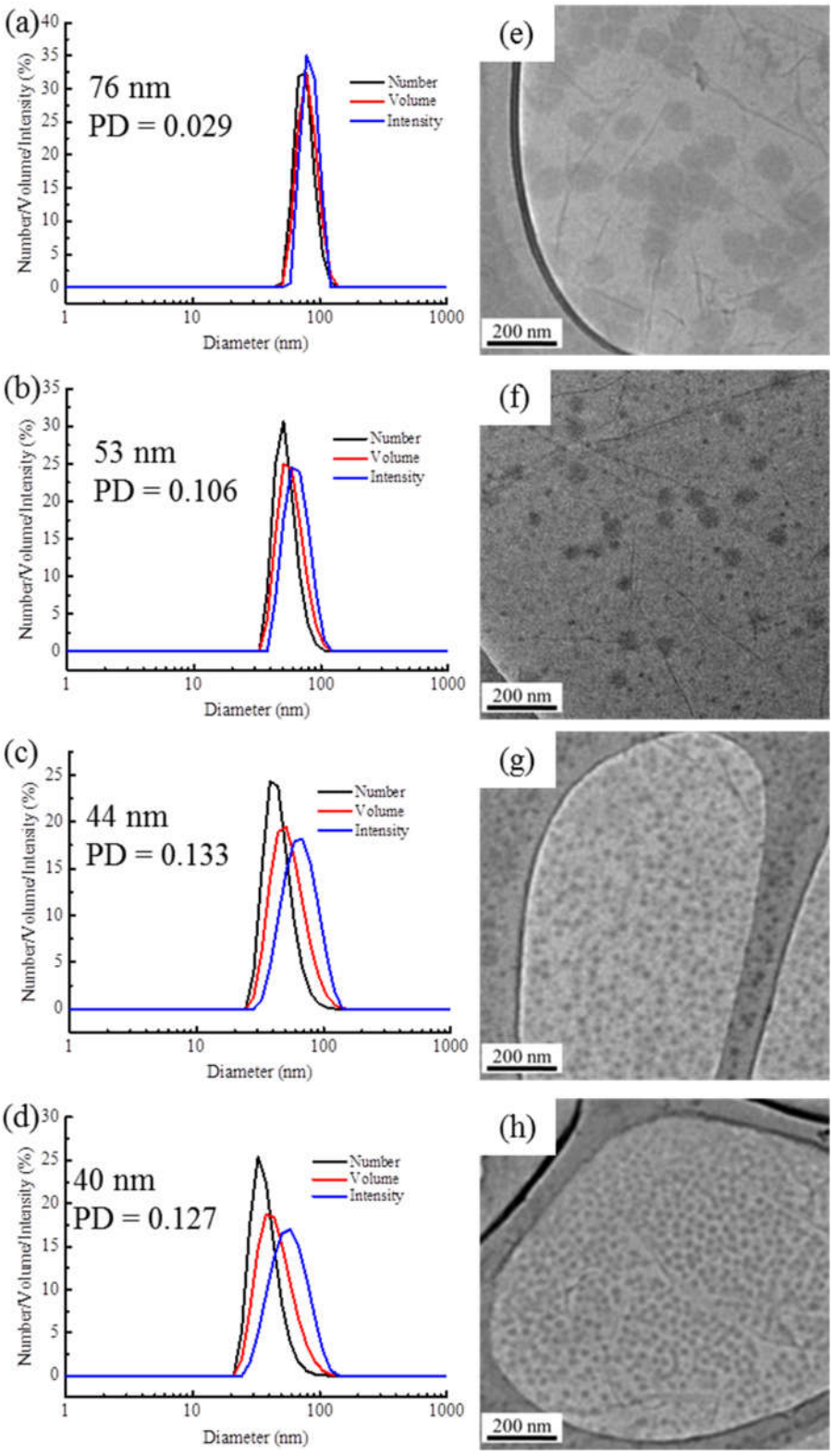

Figure 2.13. DLS analyses and TEM images of PNAM$_{96}$-*b*-PTAm$_{160}$ **M2.7** micelle solutions mixed with different molar ratios of PNAM$_{96}$-*b*-PAAm$_{19}$ (**P2.8**). (a, e) 0 molar eq., (b, f) 1 molar eq., (c, g) 3 molar eq., (d, h) 5 molar eq. of PNAM$_{96}$-*b*-PAAm$_{19}$ (**P2.8**).

2.4.5. The mechanism of morphological transition from large spheres to smaller ones

In order to further corroborate the interactions between **M2.4** (with a small thymine core) and **P2.8** (with an adenine block), ^{1}H NMR and UV-vis spectroscopy were used to characterize the micellar mixtures. The ^{1}H NMR spectrum of **P2.8** (with an adenine block) in D_2O showed the protons of adenine at 7.62 ppm (Figure 2.14). Conversely, only the peaks of the hydrophilic NAM block in micelles of **M2.4** (with a small thymine core) were observed by ^{1}H NMR analyses, which indicated the thymine block formed a hydrophobic core in D_2O. If the copolymer **P2.8** (with an adenine block) could interact with the hydrophobic thymine core of **M2.4** (with a small thymine core), the AAm block was confined into the insoluble hydrophobic core and the relaxation time increased significantly. Both factors above decreased the peak intensity of the protons attributable to the adenine functionality. Indeed, an obvious decrease or disappearance of the adenine peaks was observed in the ^{1}H NMR spectra of the mixtures of **M2.4** (with a small thymine core) and **P2.8** (with an adenine block) (Figure 2.14). Thus, it was proposed that copolymer **P2.8** (with an adenine block) could insert into the thymine core of micelles composed of **M2.4** (with a small thymine core).

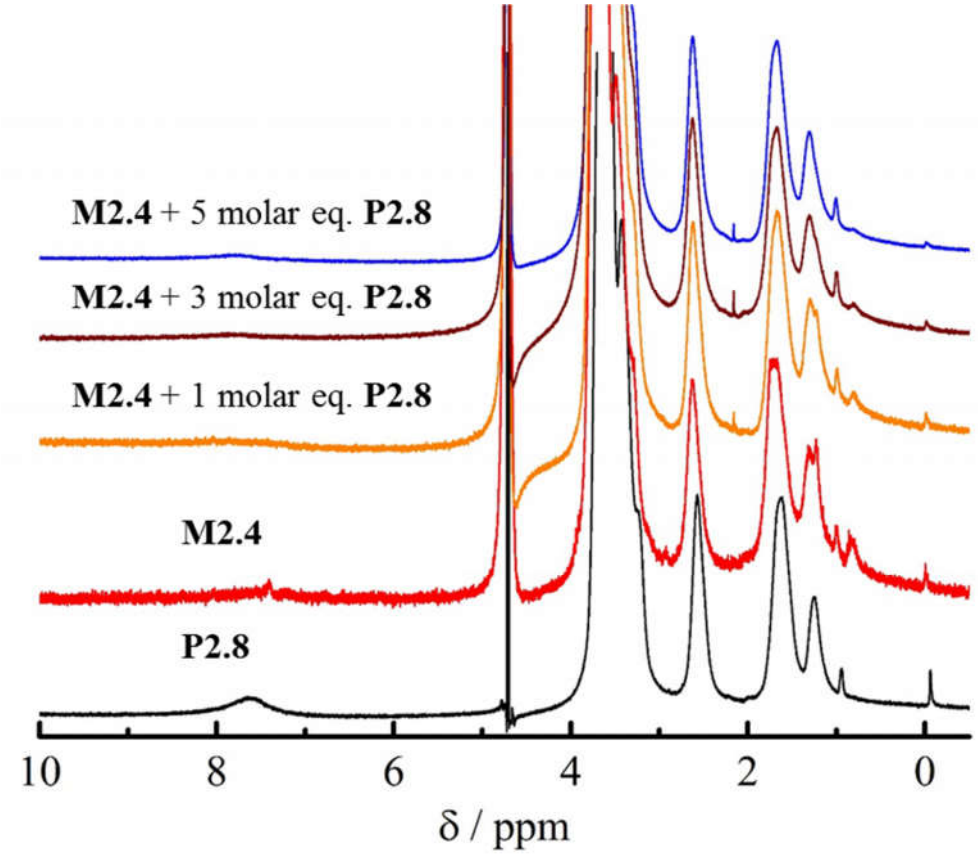

Figure 2.14. ^{1}H NMR spectra of PNAM$_{96}$-*b*-PAAm$_{19}$ **P2.8**, PNAM$_{96}$-*b*-PTAm$_{114}$ **M2.4** micelle solution and their mixtures at different molar ratios in D_2O.

The hydrogen-bonding interactions between the adenine and thymine containing amphiphiles were also examined by UV-vis spectroscopy (Figure 2.15). To explore this, 5 molar eq. of **P2.8** (with an adenine block) in water was added into a micellar solution of **M2.4** (with a small thymine core) and UV-vis measurements were performed at different times after mixing (Figure 2.15a). The maximum absorption peak was at 262 nm just after mixing and no shift of peak absorbance was detected after 10 h. However, a greater than 9% decrease in peak intensity was observed within 2 h, with no further decrease after this time (Figure 2.15b). The decrease in absorption suggested that interactions between the complementary nucleobases adenine and thymine were taking place. This decrease of absorbance is analogous to the hypochromicity for two complementary DNA.[66] Thus, we propose that the nucleobase-containing synthetic diblock copolymers **P2.4** and **P2.8** with complementary adenine and thymine residues interacted

through hydrogen bonding. Their interactions decreased the interfacial tension of the hydrophobic block with the solvent due to the increasing volume ratio of the hydrophilic block. The energy barrier for chain exchange was thus significantly lowered, leading to reorganization to generate smaller spherical micelles.

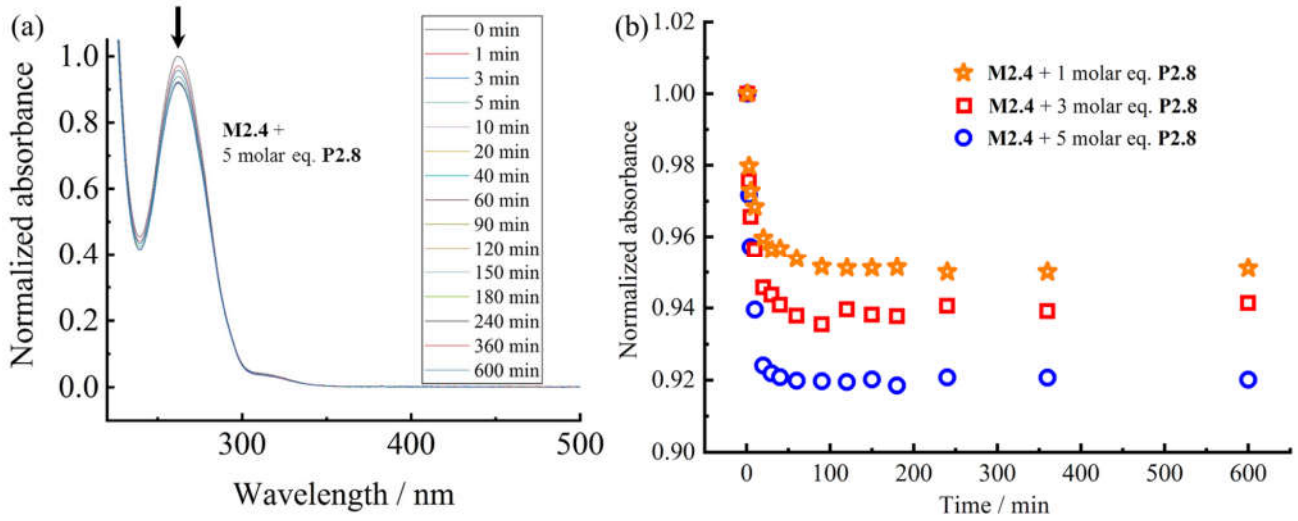

Figure 2.15. (a) Representative UV measurements of the mixture of PNAM$_{96}$-*b*-PTAm$_{114}$ **M2.4** (with a small thymine core) micelle solutions mixed with 5 molar eq. PNAM$_{96}$-*b*-PAAm$_{19}$ **P2.8** at different times. (b) The peak absorbance (262 nm) of UV-vis measurements of the mixture of PNAM$_{96}$-*b*-PTAm$_{114}$ **M2.4** micelle solutions mixed with 1, 3, and 5 molar eq. of PNAM$_{96}$-*b*-PAAm$_{19}$ **P2.8** at different times.

Another factor, as described previously is that the interactions between complementary nucleobase copolymers can increase the hydrophilicity of the core-corona interface.[42] Thus, the interfacial tension also decreased. Moreover, the insertion of the complementary copolymers could lead to the formation of a denser hydrophilic corona, increasing the core-chain stretching and the corona-chain repulsion simultaneously. In order to reduce the total free energy of the system, spherical micelles underwent reorganization into spheres with smaller diameters, whereby the corona-chain repulsion and core-chain stretching were reduced. The micellar reorganization was further facilitated by the low interfacial tension of the polymers with moderately short hydrophobic blocks.

SAXS was utilized to further characterize the change in micelle size upon addition of the complementary diblock copolymer. Scattering curves expressed as double-logarithmic plots of $I(q)$ against q were shown in Figure 2.16a.

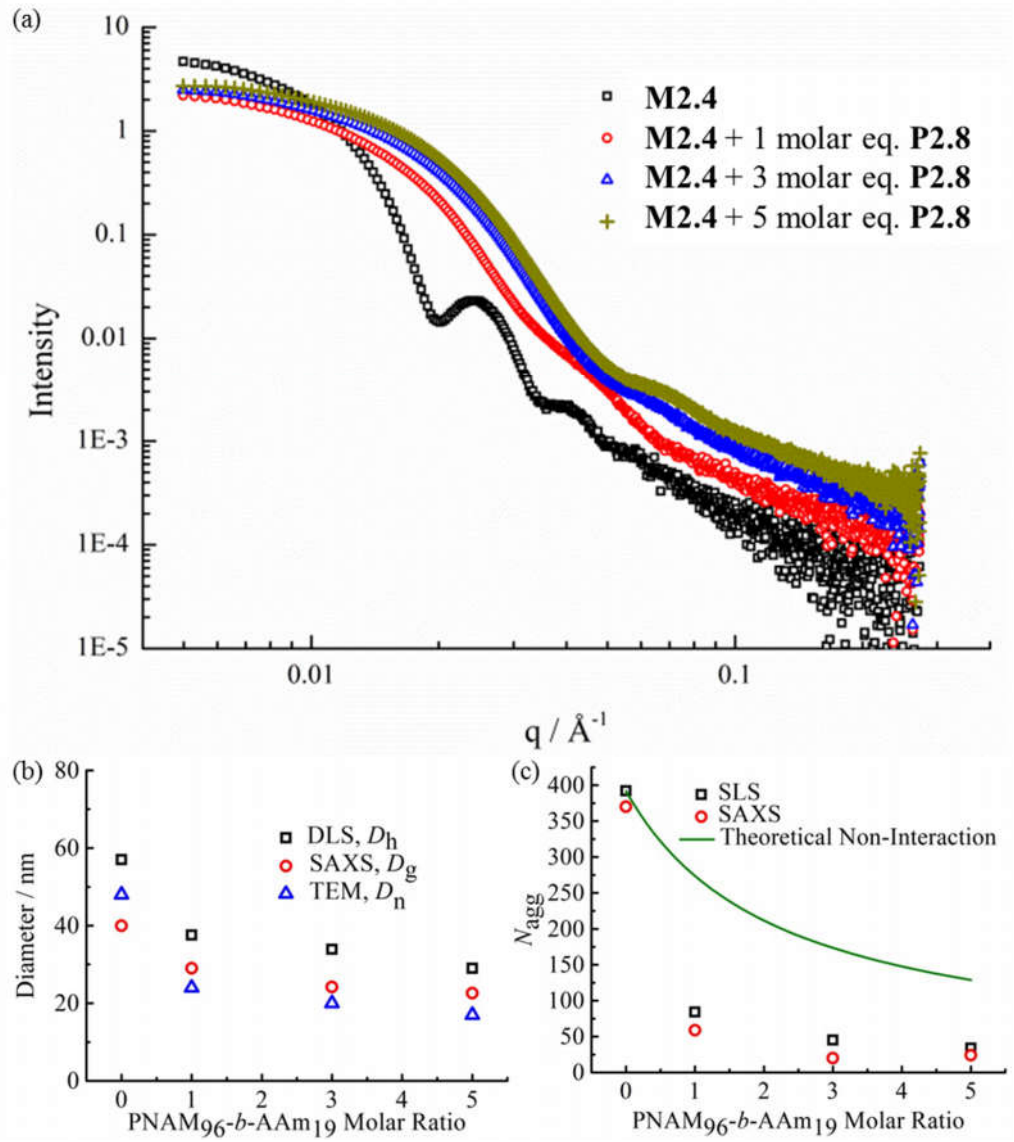

Figure 2.16. (a) SAXS experimental profiles of micellar solutions of **M2.4** (with a small thymine core) with 0, 1, 3 and 5 molar eq. of **P2.8** (with an adenine block). (b) Mean particle diameters determined for micellar solutions of **M2.4** (with a small thymine core) with 0, 1, 3 and 5 molar eq. of **P2.8** (with an adenine block) by SAXS (D_g), DLS (D_h), and TEM (D_n). (c) Mean aggregation number (N_{agg}) determined for micelle solutions of **M2.4** (with a small thymine core) with 0, 1, 3 and 5 molar eq. of **P2.8** (with an adenine block) by SLS and SAXS and the theoretical aggregation number for a non-interacting mixture as calculated from Equation 2.1.

The Guinier fit was performed to determine the R_g while the anisotropy was determined by the Gunier-Porod fit. A significant decrease in diameters of gyration D_g ($D_g = 2R_g$) was observed (Table 2.3 and Figure 2.17), which was consistent with decreasing D_h values from DLS upon increasing addition of polymer **P2.8** (with an adenine block).

Table 2.3. Different parameters of the fitted SAXS profiles given in Figure 2.17 using the Guinier fit and the Guinier-Porod fit.

Sample	R_g (nm)	s[a]	R_g/R_h[b]	R_{core} (nm)[c]
M2.4	19.9	0	0.74	15.4
M2.4 with 1 molar eq. of **P2.8**	14.5	0.38	0.77	7.0
M2.4 with 3 molar eq. of **P2.8**	12.1	0.37	0.71	4.2
M2.4 with 5 molar eq. of **P2.8**	11.3	0.24	0.78	4.2

[a]s = 0: spheres; s = 1: cylinders; s = 2: platelets.[b]R_g/R_h values related to morphology. $R_g/R_h = 0.775$: spherical micelles; $R_g/R_h = 1$: vesicles; $R_g/R_h > 1$: cylinders; R_g and R_h were determined by SAXS and DLS, respectively. [c]R_{core} values were calculated from the N_{agg} from SAXS.

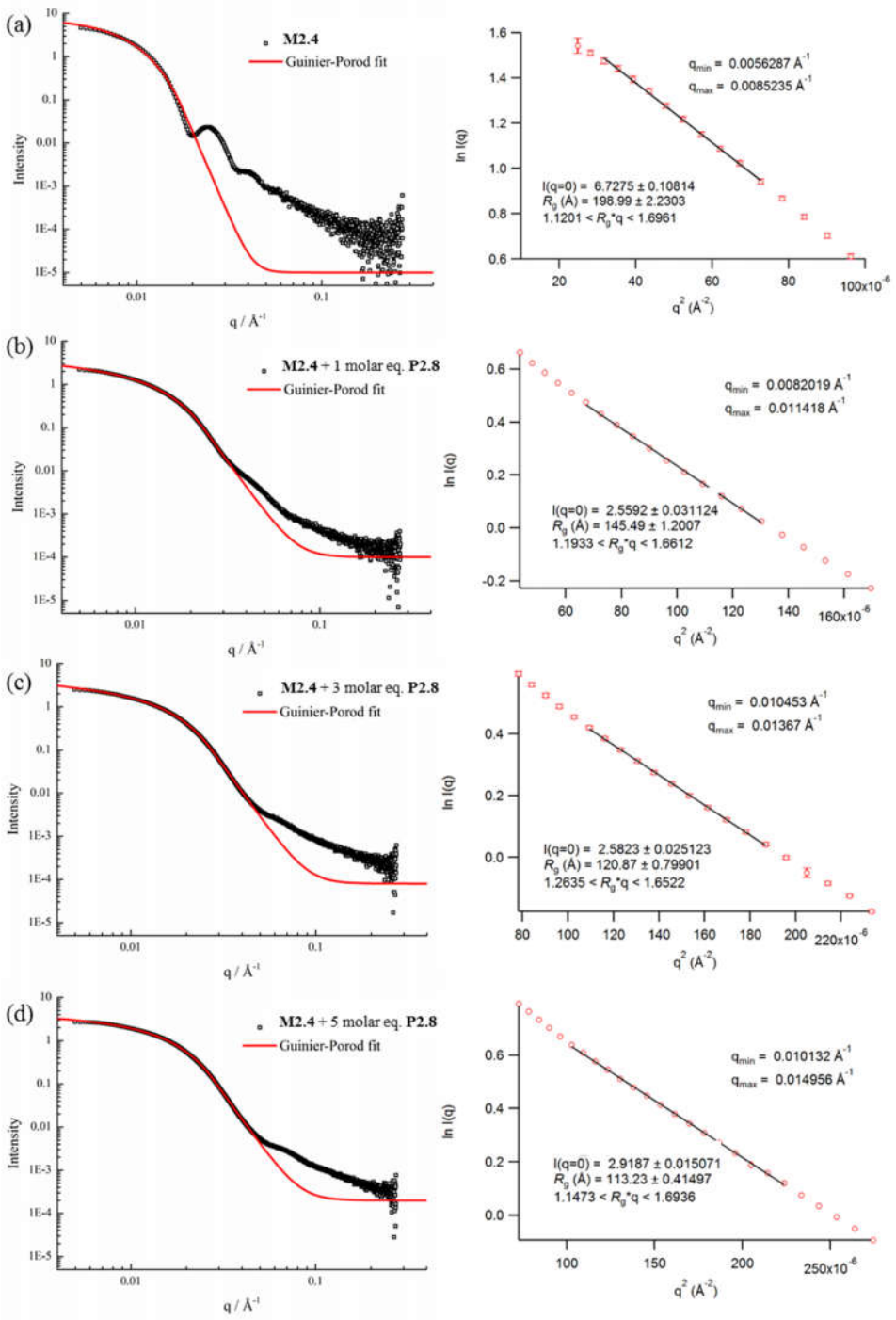

Figure 2.17. SAXS raw profiles, Guinier-Porod fits (left) and Guinier fits (right) for micellar solutions of **M2.4** (with a small thymine core) mixed with different molar ratios of **P2.8** (with an adenine block). (a) 0 molar eq., (b) 1 molar eq., (c) 3 molar eq., (d) 5 molar eq. of **P2.8** (with an adenine block).

Also, the ratios of R_g/R_h were close to 0.77 for all cases, indicating all of the micelles were spherical in nature (Table 2.3).[67] Meanwhile, the mean particle diameters as measured from TEM images also

demonstrated the same trend (Figure 2.16b). Notably, number-average diameters D_n determined by TEM analysis are somewhat smaller than those measured by DLS due to the dry state of the analysis compared to solution analysis for DLS and hence the former technique does not fully account for the loose coronal PNAM domain. Furthermore, the change of the mean aggregation number N_{agg} of the micelles, upon addition of **P2.8** (with an adenine block), was determined by SLS. The M_w values for both diblock copolymers were determined by multiplying their M_n (determined by end group analyses from ^{1}H NMR spectroscopy) by the corresponding M_w/M_n values determined by SEC analyses. The $M_{w,mix}$ values of the mixed micellar solutions were calculated according to the weighted sum of the copolymers in solutions. The mean aggregation number (N_{agg}) was then calculated by dividing the $M_{w,micelle}$ determined for the micelles by the $M_{w,mix}$ calculated for the mixed diblock copolymers. Using this method for N_{agg} determination by both SLS and SAXS analyses showed a similar decrease of N_{agg}. Specifically, N_{agg} decreased significantly from 392 to 84 after adding 1 molar eq. of **P2.8** (with an adenine block) and a slight decrease was observed with further addition of the complementary copolymer (Figure 2.16c). Also, the core sizes R_{core} of the micelles also showed the same trend (Table 2.3). We propose that the increasing hydrophilic volume ratios (upon formation of the A:T complementary interactions) lead to smaller N_{agg} values,[68] which also contributes to the reorganization to smaller micelles due to the increase of polymer curvature. Meanwhile, the average aggregation number of the micelles was significantly different from the expected value for a mixture of non-interacting micelles which could be calculated according to Equation 2.1, where c is the weight concentration of the copolymers in solution.[69]

$$N_{\mathrm{agg,mixed}} = \frac{c_{\mathbf{M2.4}} N_{\mathrm{agg},\mathbf{M2.4}} + c_{\mathbf{P2.8}} N_{\mathrm{agg},\mathbf{P2.8}}}{c_{\mathbf{M2.4}} + c_{\mathbf{P2.8}}} \qquad \text{(Equation 2.1)}$$

2.4.6. Tuning micelle morphologies through complementary nucleobase interactions

Previous studies have demonstrated that polymer chain exchange is limited by the kinetic requirements of the system, which strongly depend on the length of the hydrophobic block.[64, 70] Clearly, a longer hydrophobic block, which would have a higher interfacial tension with the solvent, maybe sufficient to freeze the aggregates and prevent chain exchange. To explore this, a second block copolymer **P2.5** with a longer hydrophobic domain was utilized. The same experiment was performed as described previously for **M2.4** (with a small thymine core). However, in this second case distinct morphological changes were observed when **P2.8** (with an adenine block) was added into the micelle **M2.5** (with a large thymine core) solution (Figure 2.18a). This transition was examined by DLS, SAXS and TEM analysis. Figure 2.18b showed the increase in hydrodynamic diameter from 57 nm to 89 nm which resulted from the addition of 5 molar eq. of **P2.8** (with an adenine block) to a micellar solution of **M2.5** (with a large thymine core).

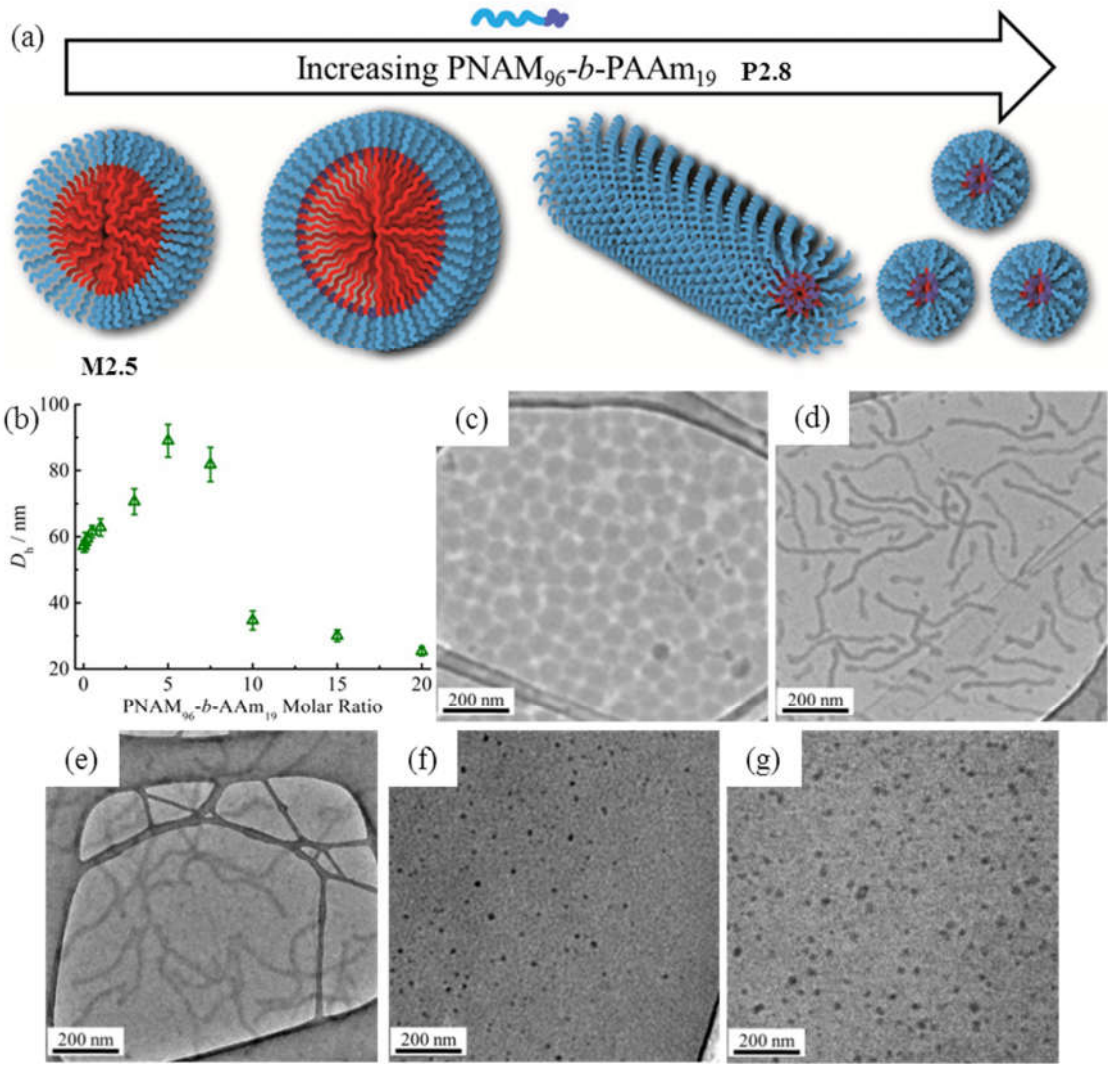

Figure 2.18. Morphological transitions induced by the interactions between **P2.8** (with an adenine block) and micelles of **M2.5** (with a large thymine core). (a) Schematic of the morphological transition through hydrogen-bonding interactions between **P2.8** (with an adenine block) and micelles of **M2.5** (with a large thymine core); (b) DLS hydrodynamic diameters (D_h) of micelles of **M2.5** (with a large thymine core) with increasing molar ratios of **P2.8** (with an adenine block); (c-g) TEM images of micelles of **M2.5** (with a large thymine core) with 1, 3, 5, 10 and 20 molar eq. of **P2.8** (with an adenine block).

Increasing the quantity of **P2.8** (with an adenine block) from 10 and then to 20 molar eq. induced a decrease in the size of the micelles (Figure 2.18b and 2.19) to 25 nm by DLS analysis. Using molar ratios of either complementary copolymers or nucleobases, the micellar size change shows the same trend (Figure 2.20).

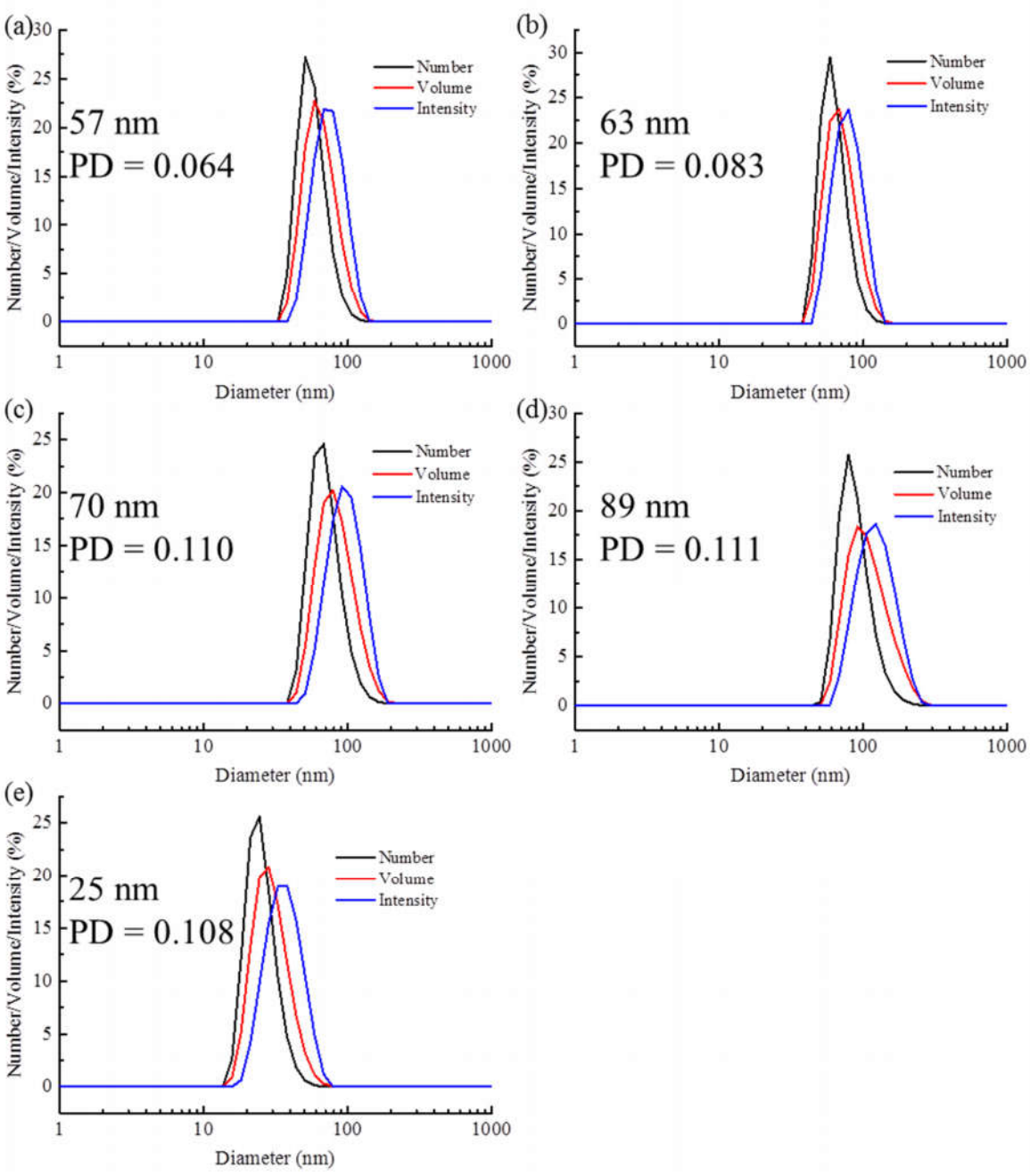

Figure 2.19. DLS analyses of $PNAM_{96}$-*b*-$PTAm_{301}$ **M2.5** micelle solutions mixed with different molar ratios of $PNAM_{96}$-*b*-$PAAm_{19}$ (**P2.8**). (a) 0 molar eq., (b) 1 molar eq., (c) 3 molar eq., (d) 5 molar eq., (e) 20 molar eq. of $PNAM_{96}$-*b*-$PAAm_{19}$ (**P2.8**).

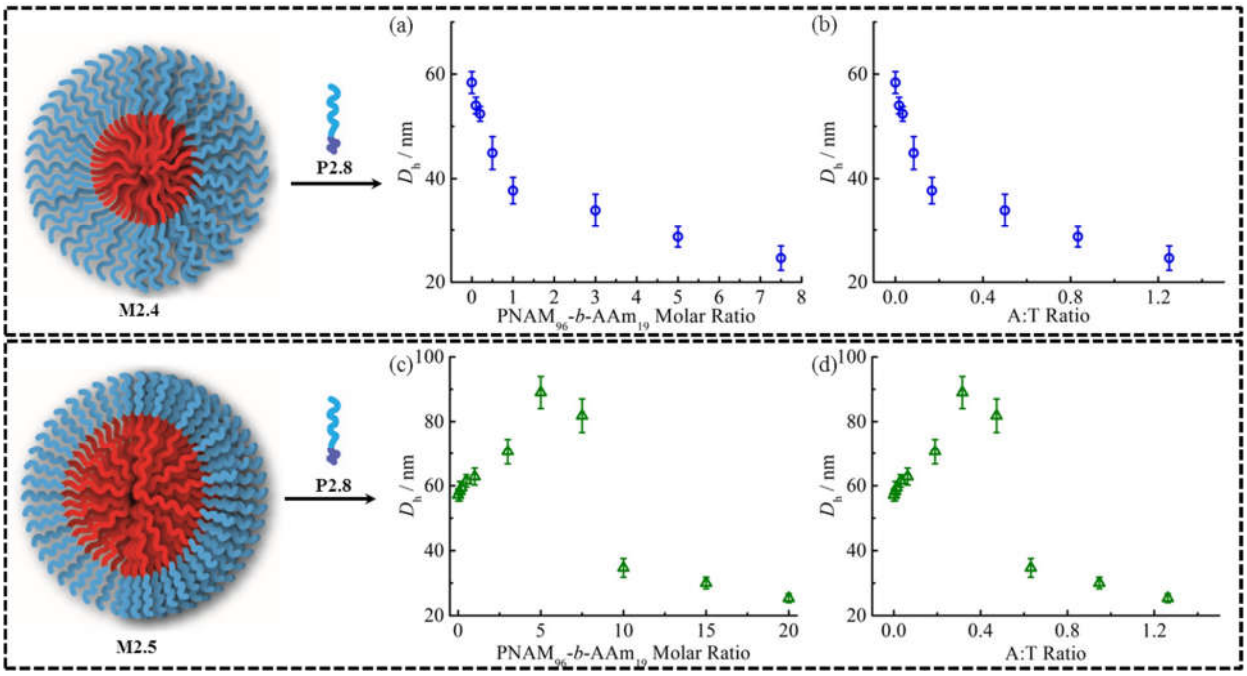

Figure 2.20. DLS hydrodynamic diameters (D_h) of micellar solutions of **M2.4** (with a small thymine core) and **M2.5** (with a large thymine core) with increasing quantity of **P2.8** (with an adenine block). (a, b) D_h of micellar solutions of **M2.4** (with a small thymine core) with increasing quantity of **P2.8** (with an adenine block) using copolymer molar ratio and A:T ratio, respectively; (c, d) D_h of micellar solutions of **M2.5** (with a large thymine core) with increasing quantity of **P2.8** (with an adenine block) using copolymer molar ratio and A:T ratio, respectively**.**

To explore these changes in size as observed by light scattering, the self-assembled micelles were also analyzed by dry-state TEM analysis. TEM images revealed that morphological transitions from spherical micelles to cylindrical micelles and then to smaller spherical micelles occurred upon increasing additions of polymer **P2.8** (with an adenine block) to the micellar solution of **M2.5** (with a large thymine core). Only spherical micelles with a slight increase in size were observed by TEM after adding 1 molar eq. of **P2.8** (with an adenine block), which is consistent with DLS analyses (Figure 2.18c). Interestingly, long cylindrical micelles of *ca.* 300 nm in length and 20 nm in width were observed with 3 molar eq. or 5 molar eq. of **P2.8** (with an adenine block), suggesting that cylindrical micelles were formed from the initially spherical micelles due to the addition of copolymer containing the complementary nucleobase functionality (Figure 2.18d and 2.18e). It is also noteworthy that much smaller spherical micelles relative to those initially observed were produced once 10 molar eq. of **P2.8** (with an adenine block) had been

added (Figure 2.18f). TEM image analysis showed the diameter was only around 24 nm. No new structures were formed when the amount of **P2.8** (with an adenine block) was increased to 20 molar eq. (Figure 2.18g).

The interactions between the polymer **P2.8** (with an adenine block) and micelles of **M2.5** (with a large thymine core) were also studied by ^{1}H NMR spectroscopy. As before, an intensity decrease and disappearance signals attributable to adenine were observed, indicating the insertion of **P2.8** (with an adenine block) into the micelles (Figure 2.21).

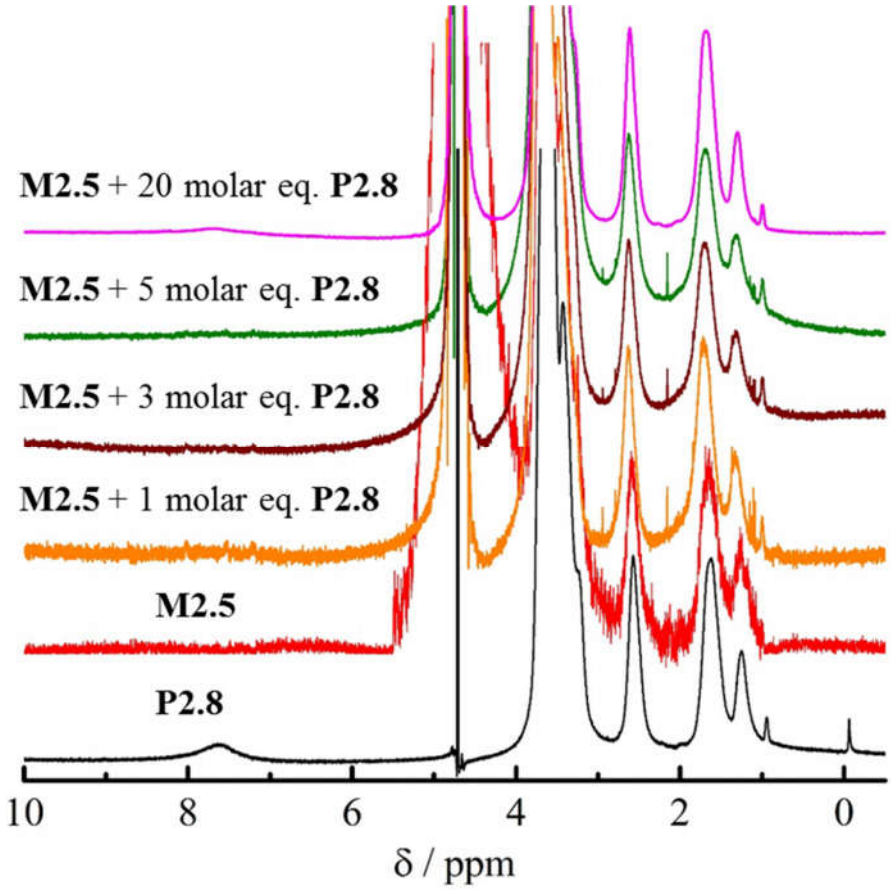

Figure 2.21. ^{1}H NMR spectra of PNAM$_{96}$-*b*-PAAm$_{19}$ (**P2.8**), PNAM$_{96}$-*b*-PTAm$_{301}$ **M2.5** micelle solution and their mixtures at different molar ratios in D_2O.

Meanwhile, UV-vis measurements also suggested that interactions between complementary nucleobases in the micellar core and added **P2.8** (with an adenine block) were taking place (Figure 2.22). This data

alongside the nanostructure characterization data suggests that micelles of differing morphologies could be generated through complementary nucleobase interactions just by changing the corresponding molar ratios added to the assemblies.

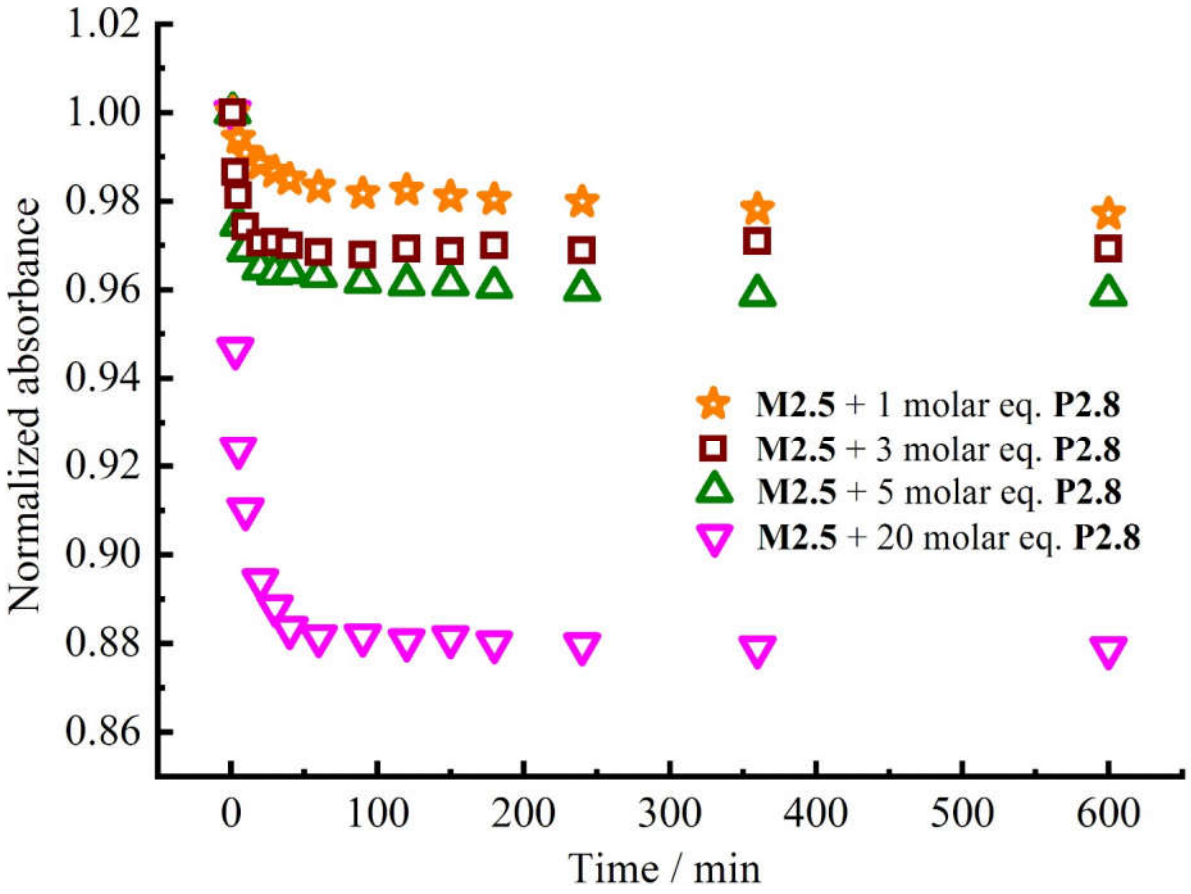

Figure 2.22. The peak absorbance of UV-vis measurements of the mixture of $PNAM_{96}$-*b*-$PTAm_{301}$ **M2.5** micelle solutions mixed with 1, 3, 5 and 20 molar eq. of $PNAM_{96}$-*b*-$PAAm_{19}$ **P2.8** at different times.

Further SAXS analyses also confirmed that transitions from spherical micelles to cylindrical micelles and then to smaller spherical micelles were taking place (Figure 2.23). A slight increase in spherical micellar size was observed, which is strongly indicative of the insertion of **P2.8** (with an adenine block) into the original micelles (Table 2.4). Interestingly, morphological changes occurred as 3 molar eq. or 5 molar eq. of **P2.8** (with an adenine block) were added. Long cylinders were formed, which was also confirmed by

increase in the s parameter from SAXS analyses and which was also consistent with TEM imaging (Table 2.4 and Figure 2.24). Compared with micelles containing moderate hydrophobic blocks, the interactions between complementary nucleobase copolymers could thermodynamically favour the formation of smaller spherical micelles due to the decreased interfacial tension and corona-chain repulsion. However, the much longer hydrophobic block, which had a higher energy barrier for chain exchange, confined the mobility of the micellar copolymer.

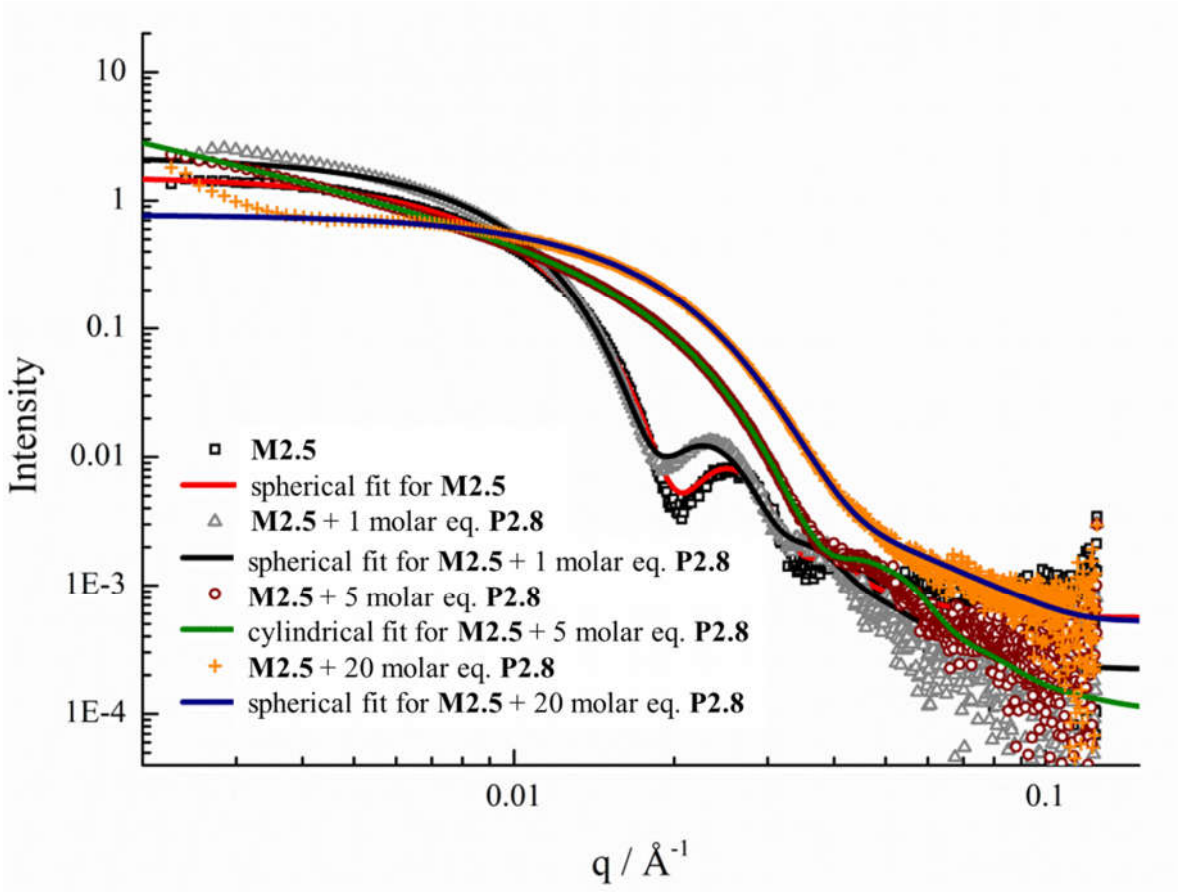

Figure 2.23. SAXS experimental profiles and fittings of micellar solutions of **M2.5** (with a large thymine core) with 0, 1, 5 and 20 molar eq. of **P2.8** (with an adenine block).

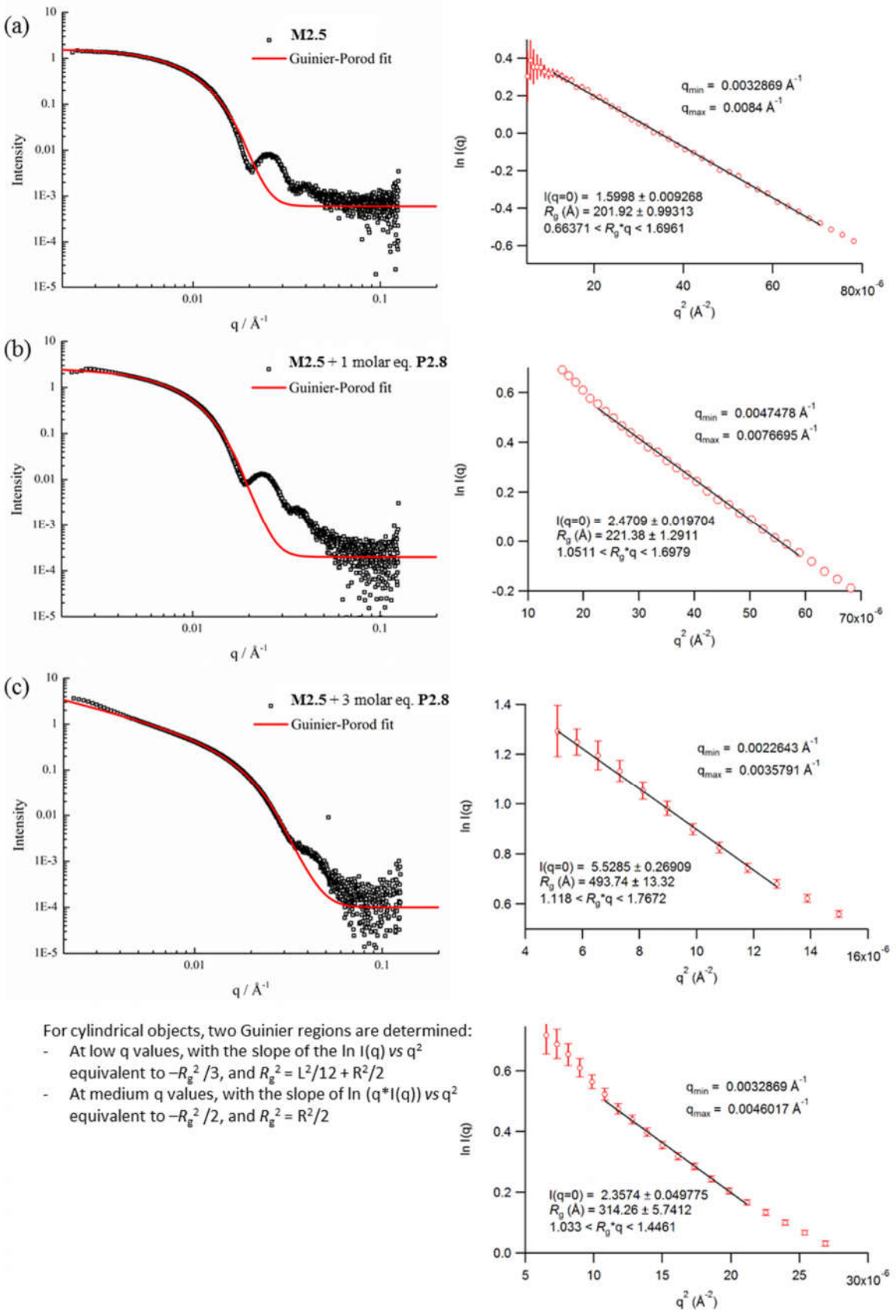

For cylindrical objects, two Guinier regions are determined:

- At low q values, with the slope of the ln I(q) *vs* q^2 equivalent to $-R_g^2/3$, and $R_g^2 = L^2/12 + R^2/2$
- At medium q values, with the slope of ln (q*I(q)) *vs* q^2 equivalent to $-R_g^2/2$, and $R_g^2 = R^2/2$

(d)

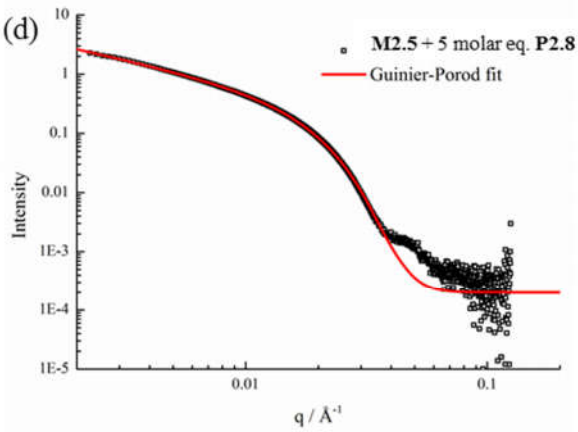

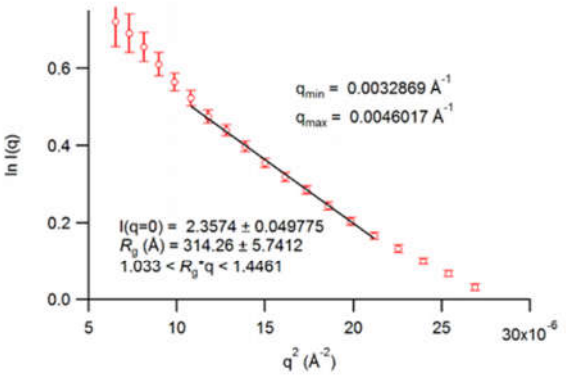

For cylindrical objects, two Guinier regions are determined:

- At low q values, with the slope of the ln I(q) *vs* q^2 equivalent to $-R_g^2/3$, and $R_g^2 = L^2/12 + R^2/2$
- At medium q values, with the slope of ln (q*I(q)) *vs* q^2 equivalent to $-R_g^2/2$, and $R_g^2 = R^2/2$

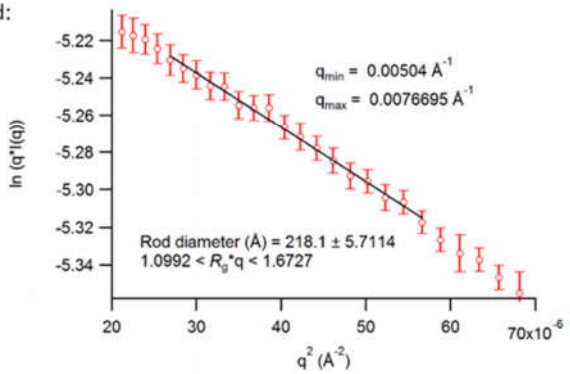

(e)

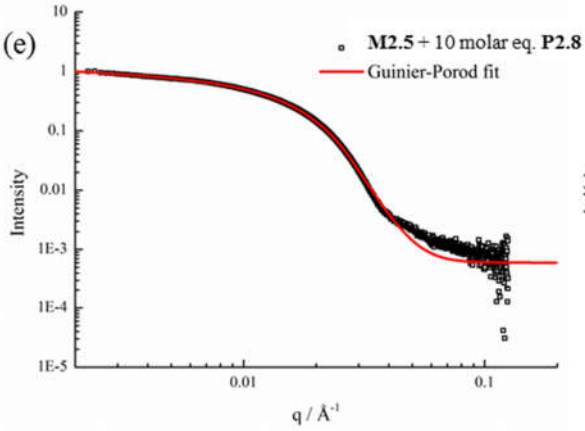

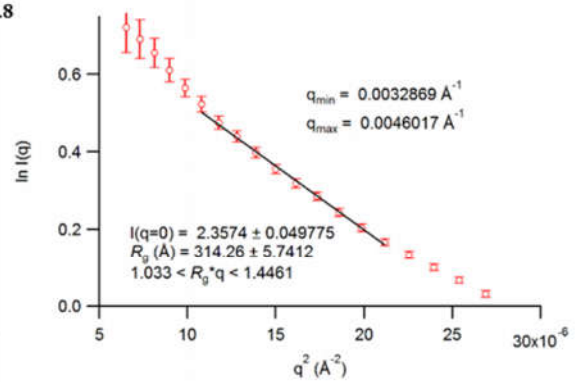

(f)

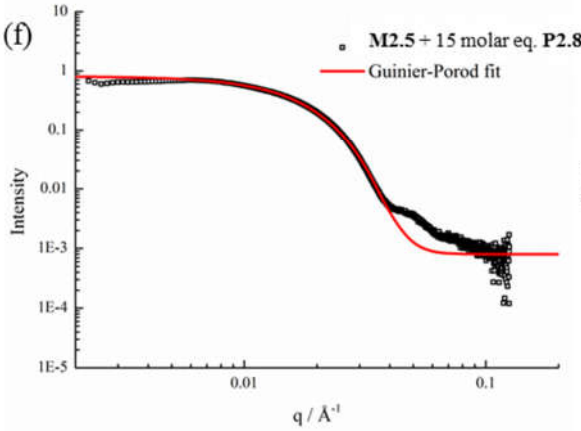

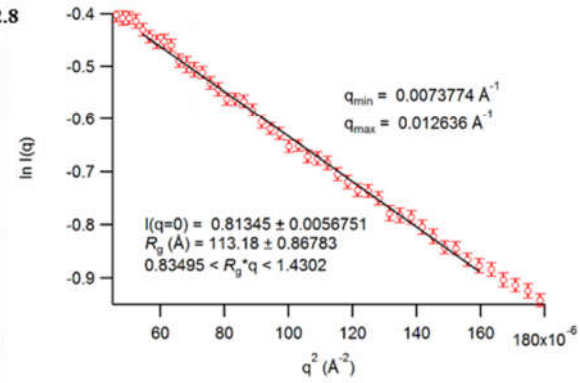

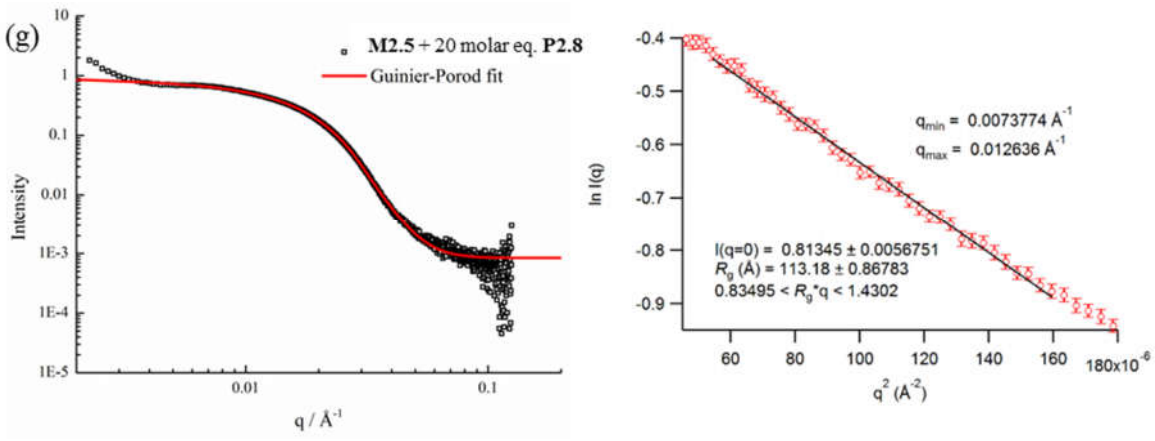

Figure 2.24. SAXS raw profiles, Guinier-Porod fits (left) and Guinier fits (right) for micellar solutions of **M2.5** (with a large thymine core) mixed with different molar ratios of **P2.8** (with an adenine block). (a) 0 molar eq., (b) 1 molar eq., (c) 3 molar eq., (d) 5 molar eq., (e) 10 molar eq., (f) 15 molar eq., (g) 20 molar eq. of **P2.8** (with an adenine block).

Table 2.4. Different parameters of the fitted SAXS profiles given in Figure 2.24 using Guinier fit and Guinier-Porod fit.

Sample	R_g (nm)	s[a]	R_g/R_h[b]
M2.5	20.2	0	0.71
M2.5 with 1 molar eq. of **P2.8**	22.1	0.07	0.70
M2.5 with 3 molar eq. of **P2.8**	L = 166.7 W = 31.4[c]	1.05	1.38
M2.5 with 5 molar eq. of **P2.8**	L = 105.5 W = 21.8[c]	0.91	1.64
M2.5 with 10 molar eq. of **P2.8**	13.0	0.21	0.75
M2.5 with 15 molar eq. of **P2.8**	10.1	0	0.67
M2.5 with 20 molar eq. of **P2.8**	11.3	0.1	0.81

[a]s = 0: spheres; s = 1: cylinders; s = 2: platelets.[b]R_g/R_h values related to morphology. R_g/R_h = 0.775: spherical micelles; R_g/R_h = 1: vesicles; R_g/R_h > 1: cylinders; R_g and R_h were determined by SAXS and DLS for spherical micelles and R_g was determined by SLS for cylinders. [c]Length and width are fitted from SAXS data using the Guinier fit.

More importantly, the micelle of **M2.5** with a larger core provided more space and surface area for the inserted copolymers compared with the nanostructure formed from **M2.4** (with a small thymine core) (Table 2.2). Hence, a slight increase in the micelle size could, to some extent, relieve the corona-chain repulsion through increasing the volume of the corona. In response to the resulting entropic penalty, and in order to reduce the total free energy of the system, a morphological transition from spheres to smaller diameter cylinders occurred after adding 3 molar eq. of **P2.8** (with an adenine block), which led to a reduction in both corona-chain repulsion and core-chain stretching. Only smaller spherical micelles were formed after adding 10 molar eq. of **P2.8** (with an adenine block). Further increasing the quantity of **P2.8** (with an adenine block) only led to smaller spherical micelles and no new nanostructures were formed. This transition was similar to the micelles formed from copolymers with moderate hydrophobic blocks. When more complementary copolymers interacted through hydrogen-bonding with the long hydrophobic core, the interfacial tension was further decreased with higher hydrophilic volume ratios, leading to a lower energy barrier for chain exchange. Smaller spherical micelles were, therefore, formed to reduce the increased corona-chain repulsion introduced through the insertion of the complementary copolymer. Compared with the morphology or size change of micellar nanostructures induced by external stimuli such as temperature, pH or salts, the unique complementarity of nucleobases (A and T) can be utilized to progressively tailor micellar sizes and shapes just by varying the relative molar ratios. Complementary nucleobase interactions between copolymers with A and T can change the dynamics and stabilities of nanostructures to afford a new method for control over nanostructure size and morphology changes.

2.5. Conclusions

In summary, a series of nucleobase-containing synthetic block copolymers were prepared *via* RAFT polymerization. Monodisperse spherical micelles were formed through direct dissolution or solvent switch methods and characterized by DLS and TEM. The interactions between these micelles and amphiphilic copolymers with complementary nucleobases were exploited to trigger size and morphology changes in the nanostructures. The insertion of the complementary copolymers into the micelles was analyzed by ^{1}H NMR spectroscopy and nucleobase interactions confirmed by UV-vis spectroscopy. For micelles with hydrophobic TAm blocks of moderate lengths, a significant decrease in micellar sizes with increased quantities of complementary copolymers was observed and characterized by DLS, TEM and SAXS. Both SAXS and SLS confirmed a significant decrease in N_{agg} upon the addition of complementary copolymer. Low interfacial tension of hydrophobic blocks with moderate length enabled micelle reorganization to smaller spherical micelles by reducing the corona-chain repulsion and core-chain stretching. Furthermore, for the micelle with a much longer hydrophobic block, morphological transitions from spheres to cylinders and then to smaller spheres could be achieved with increased quantities of the complementary copolymer. Swelling and slightly larger spherical micelles were formed with initial addition of PNAM-*b*-AAm due to a high energy barrier for chain exchange of the long hydrophobic block. Through reducing corona-chain repulsion and core-chain stretching, long cylinders were produced followed by disassembly into smaller spherical micelles with further addition of the complementary copolymer. We propose that complementary nucleobase interactions in synthetic polymers provide a new stimulus to access different nanostructure sizes and morphologies as desired for applications such as delivery vehicles or catalytic nanoreactors.

2.6. Experimental section

2.6.1. Materials

2,2'-Azo-bis(isobutyronitrile) (AIBN) was obtained from Molekula and recrystallized from methanol. 2,2'-Azobis[2-(2-imidazolin-2-yl)propane]dihydrochloride (VA-044, Wako) was used without further purification. Adenine was obtained from Sigma and thymine was bought from Acros. Sodium hydride (60% dispersion mineral oil) was purchased from Aldrich. 4-Acryloylmorpholine (NAM) was bought from Aldrich and was purified by vacuum distillation. DMF, DMSO, triethylamine and other chemicals were obtained from Fisher Chemicals and used without further purification. Dry solvents used in the experiments were obtained by passing over a column of activated alumina using an Innovative Technologies solvent purification system. Dialysis membranes (MWCO = 3.5-5 kDa) were purchased from Spectra/Por. The synthesis of 2-(((butylthio)carbonothiolyl)thio)propanoic acid (CTA) is described in the Section 2.6.8.

2.6.2. Instrumentation

^{1}H NMR and ^{13}C NMR spectra were recorded on a Bruker DPX-300, DPX-400 or HD500 spectrometer with DMSO-d_6 or $CDCl_3$ as the solvent. The chemical shifts of protons were relative to tetramethylsilane (TMS) at $\delta = 0$ ppm when using $CDCl_3$ or solvent residues (DMSO 2.50 ppm). Fourier transform infrared (FT-IR) spectra were obtained using a Perkin Elmer Spectrum 100 FT-IR. Scans from 550 to 4000 cm^{-1} were taken, and the spectra corrected for background absorbance. UV-vis spectra were recorded on a Perkin-Elmer Lambda 35 UV-vis instrument. Scans from 200 to 700 nm were taken using a quartz cuvette at different times after mixing. High resolution mass spectrometry (HR-MS) was conducted on a Bruker UHR-Q-TOF MaXis with electrospray ionization (ESI). Size exclusion chromatography (SEC) data were obtained in HPLC grade DMF containing 5 mM NH_4BF_4 at 50 °C, with a flow rate of 1.0 mL min^{-1}, on a

set of two PLgel 5 μm Mixed-D columns, and a guard column. SEC data were analyzed with Cirrus SEC software calibrated using polymethyl methacrylate (PMMA) standards.

Hydrodynamic diameters (D_h) and size distributions of the self-assemblies were determined by dynamic light scattering (DLS). The DLS instrumentation consisted of a Malvern Zetasizer NanoS instrument operating at 25 °C with a 4 mW He-Ne 633 nm laser module. Measurements were made at a detection angle of 173° (back scattering), and Malvern DTS 7.03 software was used to analyze the data. D_h was calculated by fitting the apparent diffusion coefficient in the Stokes-Einstein equation $D_h = kT/(3\pi\eta D_{app})$, where k, T and η are the Boltzmann constant, the temperature and the viscosity of the solvent, respectively. When only the measured sample is a solution of monodispersed spherical micelles, D_h coincides to the real hydrodynamic diameter as D_{app} is equal to the translational diffusion coefficient (D_t). For anisotropic nanoparticles such as cylinders, the non-negligible rotational diffusion also contributes to the D_{app}. Therefore, the measured D_h for these samples only represents a relative value and provides polydispersity information to detect multiple populations. Static light scattering (SLS) measurements were conducted with an ALV CGS3 (λ = 632 nm) at 20 °C. The data were collected from 50° to 150° with an interval of 10° against a toluene standard. The self-assembled solutions were filtered through 0.45 μm nylon filters prior to analysis. In SLS analysis, the angular dependence of the absolute excess time-average scattering intensity, the Rayleigh ratio R_θ, can lead to the weight-average molar mass M_w, the radius of gyration R_g and the second virial coefficient A_2 by:

$$\frac{Kc}{R_\theta} = \frac{1}{M_w}\left(1 + \frac{q^2 R_g^2}{3}\right) + 2A_2 c \qquad \text{(Equation 2.2)}$$

Where K is a constant and $q = (4\pi n/\lambda_0)\sin(\theta/2)$ with n and λ_0 being the solvent refractive index and the wavelength of light. The dn/dc values were determined using a Shodex RI-101 refractometer. The dn/dc values of copolymers **P2.4**, **P2.5** and **P2.8** in water are 0.169, 0.173 and 0.158 mL g^{-1}, respectively. The dn/dc values of mixed micelles were calculated using the weighted sum of the dn/dc values of mixed copolymers[5]:

$$\left(\frac{\mathrm{d}n}{\mathrm{d}c}\right)_{\text{mixed}} = \mathrm{w}_{\mathbf{P2.4}}\left(\frac{\mathrm{d}n}{\mathrm{d}c}\right)_{\mathbf{P2.4}} + \mathrm{w}_{\mathbf{P2.8}}\left(\frac{\mathrm{d}n}{\mathrm{d}c}\right)_{\mathbf{P2.8}} \qquad \text{(Equation 2.3)}$$

where $w_{\mathbf{P2.4}}$ and $w_{\mathbf{P2.8}}$ are respectively the weight fractions of copolymers **P2.4** and **P2.8**. The aggregation number of the micellar aggregates was calculated by $N_{agg} = M_{w,aggregate}/M_{w,unimers}$. The $M_{w,unimers}$ values were determined by multiplying their M_n (determined by end group analyses from ^{1}H NMR spectroscopy) by the corresponding M_w/M_n values determined by SEC analyses.

TEM observations were performed on a JEOL 2000FX electron microscope at an acceleration voltage of 200 kV. All TEM samples were prepared on graphene-oxide (GO)-coated lacey carbon grids (400 Mesh, Cu, Agar Scientific), to enable high contrast TEM images without any staining.[71] Generally, a drop of sample (10 μL) was pipetted on a grid and left for several minutes, then blotted away. TEM images were analyzed using the ImageJ software, and over 100 particles were counted for each sample to obtain number-average diameter D_n (for spherical micelles) or number-average width W_n (for cylindrical micelles).

Small-angle X-ray scattering (SAXS) experiments were performed on the SAXS/WAXS beamline at the Australian Synchrotron facility at a photon energy of 12 keV. The samples in solutions were run using 1.5 mm diameter quartz capillaries. The measurements were collected at 25 °C with a sample-to-detector distance of 3.252 or 7.160 m to give q ranges of 0.005 to 0.22 and 0.002 to 0.10 Å^{-1}, respectively, where q is the scattering vector and is related to the scattering angle (2θ) and the photon wavelength (λ) by the following equation:

$$q = \frac{4\pi\sin(\theta)}{\lambda} \qquad \text{(Equation 2.4)}$$

All patterns were normalized to a fixed transmitted flux using a quantitative beam stop detector. The two-dimensional SAXS images were converted into one-dimensional SAXS profile ($I(q)$ *versus* q) by circular averaging, where $I(q)$ is the scattering intensity. ScatterBrain, Primus and NCNR Data Analysis IGOR PRO software were used to plot and analyze SAXS data.[72, 73] The scattering length density of the solvents

and monomers were calculated using the "Scattering Length Density Calculator" provided by the NIST center for Neutron Research.

2.6.3. Synthesis of *N*-(3-bromopropyl) acrylamide

N-(3-bromopropyl) acrylamide was synthesized using procedures similar to the previous literature.[74] To a solution of 3-bromopropylamine (10.1 g, 45 mmol), triethylamine (TEA) (14 mL, 100 mmol) and 4-(dimethylamino)pyridine (DMAP) (288 mg, 2.3 mmol) in CH_2Cl_2 (150 mL), acryloyl chloride (4.2 mL, 50 mmol) was added dropwise in an ice bath and then left at room temperature for another 4.5 h. The reaction solution was washed with saturated $NaHCO_3$ aqueous solution (100 mL) and water twice sequentially (2 × 100 mL). The organic layer was collected and dried with anhydrous $MgSO_4$ and filtered. Then 2,6-bis(1,1-dimethylethyl)-4-methylphenol (6.3 mg, 1.5 mmol) was added to the filtrate followed by concentrating under vacuum to give a brown oil. The brown oil (6.3 g, 73%) was used for the following reaction immediately without further purification.

^{1}H NMR (400 MHz, $CDCl_3$) δ = 6.27 (d, *J* = 16.8 Hz, 1H, C*H*=CH_2-CO), 6.11 (d, *J* = 10.0 Hz, 1H, C*H*=CH_2-CO), 6.06 (s, 1H, N*H*CO), 5.63 (dd, *J* = 16.8 Hz, 10.0 Hz, 1H, CH_2=C*H*-CO), 3.42-3.50 (m, 4H, C*H*$_2$-CH_2-C*H*$_2$-Br), 2.08-2.15 (m, 2H, CH_2-C*H*$_2$-CH_2-Br) ppm.

^{13}C NMR (400 MHz, $CDCl_3$) δ = 166.0, 130.8, 126.7, 38.2, 32.2, 31.0 ppm.

2.6.4. Synthesis of 3-(adenine-9-yl)propyl acrylamide (AAm)

To a suspension of adenine (3.0 g, 24.2 mmol) in dry DMF (100 mL), NaH (0.85 g, 35.4 mmol) was slowly added. The mixture was stirred for 1 h until no gas was produced. The viscous mixture was immersed into an ice bath and *N*-(3-bromopropyl) acrylamide freshly synthesized (5.4 g, 28.2 mmol) was added dropwise. The yellow viscous mixture was stirred overnight and the resulting suspension was concentrated under vacuum. The solid was washed by CH_2Cl_2 several times and then concentrated. The

mixture was further purified by column chromatography using a mixture of CH_2Cl_2 and CH_3OH as eluent and a gradient from 1:0 to 9:1 to give a white solid, AAm (3.18 g, 52%).

^{1}H NMR and ^{13}C NMR spectra are shown in Figure 2.1.

^{1}H NMR (400 MHz, DMSO-d_6) δ = 8.19 (t, J = 5.2 Hz, CON*H*), 8.15 (s, 1H, purine *H*-2), 8.14 (s, 1H, purine *H*-8), 7.20 (s, 2H, NH_2), 6.21 (dd, J = 16.8 Hz, 10.0 Hz, 1H, CH_2=C*H*-CO), 6.08 (dd, J = 16.8 Hz, 2.0 Hz, 1H, C*H*=CH_2-CO), 5.59 (dd, J = 10.0 Hz, 2.0 Hz, 1H, C*H*=CH_2-CO), 4.15 (t, 2H, J =6.8 Hz, CH_2-purine) 3.13 (m, 2H, OC-NH-CH_2), 1.97 (m, 2H, OC-NH-CH_2-CH_2-CH_2-purine) ppm.

^{13}C NMR (400 MHz, DMSO-d_6) δ = 165.6, 153.3, 150.4, 148.3, 141.8, 132.6, 126.1, 119.7, 41.8, 36.8, 30.4 ppm.

FTIR (neat) ν_{max}/cm^{-1}: 3281 and 3091 (H-N Purine), 1684 and 1605 (C=N purine), 1652 (C=O amide), 1575, 1541, 1485, 1458 and 1440 (C-N purine).

HR-MS (m/z) found 269.1119, calc. 269.1127 $[M+Na]^+$.

Elemental analysis: Calculated (%) C 53.65, H 5.73, N 34.13; Found (%) C 53.83, H 5.46, N 34.05.

Melting point: 206-208 °C

2.6.5. Synthesis of 3-benzoylthymine

Following the procedures in a previous report,[75] benzoyl chloride (11.24 mL, 96.8 mmol) and thymine (3.0 g, 24.2 mmol) were suspended in a mixture of acetonitrile (30 mL) and pyridine (12 mL) under nitrogen. The reaction was stirred under a nitrogen atmosphere at room temperature overnight. The reaction solution was then concentrated under vacuum. The viscous liquid was partitioned between CH_2Cl_2 and water. The aqueous layer was extracted three times with CH_2Cl_2 and the combined organic layers were dried over anhydrous K_2CO_3. The solvent was removed under vacuum. The residue was dissolved in dioxane (30 mL) and K_2CO_3 (4.1 g) in 30 mL of water was added and the reaction mixture

was stirred for 2 h. The crude product was concentrated and colourless crystals (4.5 g, 80%) were recrystallized from the solution.

^{1}H NMR (400 MHz, DMSO-d_6) δ = 11.4 (br, 1H, pyrimidine-*H*1), 7.94 (d, *J* = 10.0 Hz, 2H, benzene-*H*1,*H*5), 7.77 (t, *J* = 10.0 Hz, 1H, benzene-*H*3), 7.59 (d, *J* = 10.0 Hz, 2H, benzene-*H*2,*H*4), 7.53 (s, 1H, pyrimidine-*H*6), 1.82 (d, 3H, *J* = 6.8 Hz, CH_3-pyrimidine) ppm.

^{13}C NMR (400 MHz, DMSO-d_6) δ = 170.7, 164.1, 150.5, 139.3, 135.8, 131.9, 130.7, 129.9, 108.4, 12.2 ppm.

2.6.6. Synthesis of 3-(3-benzoylthymin-1-yl)propyl acrylamide

To the solution of 3-benzoylthymine (2.3 g, 10.0 mmol) in dry DMF (50 mL), 60% NaH (0.42 g, 10.5 mmol) was slowly added. The mixture was stirred for 1 h until no gas was produced. The viscous mixture was immersed in an ice bath and *N*-(3-bromopropyl) acrylamide freshly synthesized (2.3 g, 12.0 mmol) was added dropwise. The yellow, viscous mixture was stirred overnight. The resulting solution was concentrated under vacuum. The residue was partitioned with EtOAc and water. The aqueous layer was extracted three times with EtOAc and the combined organic layers were dried over anhydrous $MgSO_4$. The solvent was removed under vacuum. The mixture was further purified by column chromatography using EtOAc as eluent to give a viscous liquid (2.0 g, 58%).

^{1}H NMR (400 MHz, DMSO-d_6) δ = 8.17 (t, *J* = 5.2 Hz, CON*H*), 7.96 (d, *J* = 6.0 Hz, 2H, benzene-*H*1,*H*5), 7.79 (s, 1H, pyrimidine-*H*6), 7.77 (t, *J* = 6.0 Hz, 1H, benzene-*H*3), 7.59 (d, *J* = 6.0 Hz, 2H, benzene-*H*2, *H*4), 6.20 (dd, *J* = 17.0 Hz, 10.0 Hz, 1H, CH_2=C*H*-CO), 6.10 (dd, *J* = 17.0 Hz, 2.0 Hz, 1H, C*H*=CH_2-CO), 5.58 (dd, *J* = 10.0 Hz, 2.0 Hz, 1H, C*H*=CH_2-CO), 3.73 (t, 2H, *J* = 7.0 Hz, CH_2-pyrimidine), 3.20 (m, 2H, OC-NH-CH_2), 1.84 (d, 3H, *J* = 6.8 Hz, CH_3-pyrimidine), 1.82 (m, 2H, OC-NH-CH_2-CH_2-CH_2-pyrimidine) ppm.

^{13}C NMR (400 MHz, DMSO-d_6) δ = 170.3, 165.2, 163.4, 149.9, 143.0, 135.9, 132.1, 131.7, 130.8, 130.0, 125.6, 109.0, 46.6, 36.3, 28.9, 12.3 ppm.

2.6.7. Synthesis of 3-(thymin-1-yl)propyl acrylamide (TAm)

(3-Benzoylthymin-1-yl)propyl acrylamide (2.0 g, 5.9 mmol) was dissolved in a mixture of TFA/DCM (3:1) (20 mL). The reaction solution was stirred at room temperature overnight. After completion of the reaction, solvent was removed under vacuum. The residue was purified by column chromatography with a gradient of $CHCl_3$/CH_3OH from 1:0 to 93:7 to give a viscous liquid. Ethanol (20 mL) was then added to give a white solid (1.0 g, 70%). ^{1}H NMR and ^{13}C NMR spectra are shown in Figure 2.2.

^{1}H NMR (500 MHz, DMSO-d_6) δ = 11.23 (s, 1H, pyrimidine-*H*3), 8.12 (t, *J* = 5.2 Hz, CON*H*), 7.51 (s, 1H, pyrimidine-*H*6), 6.18 (dd, *J* = 16.8 Hz, 10.0 Hz, 1H, CH_2=C*H*-CO), 6.07 (dd, *J* = 16.8 Hz, 2.0 Hz, 1H, C*H*=CH_2-CO), 5.58 (dd, *J* = 10.0 Hz, 2.0 Hz, 1H, C*H*=CH_2-CO), 3.63 (t, 2H, *J* = 6.8 Hz, CH_2-pyrimidine), 3.14 (m, 2H, OC-NH-CH_2), 1.74 (d, 3H, *J* = 1.0 Hz, CH_3-pyrimidine), 1.74 (m, 2H, OC-NH-CH_2-CH_2-CH_2-pyrimidine) ppm.

^{13}C NMR (500 MHz, DMSO-d_6) δ = 165.1, 164.8, 151.3, 142.0, 132.2, 125.6, 108.9, 45.9, 36.4, 29.1, 12,4 ppm.

FTIR (neat) ν_{max}/cm^{-1}: 3263 (H-N pyrimidine), 3097 (H-C=C pyrimidine), 2970, 2948 and 2927 (CH_3 pryimidine), 1687 and 1678 (C=O and C=C pyrimidine), 1647 (C=O amide).

HR-MS (m/z) found 260.1004, calc. 260.1011 $[M+Na]^+$.

Elemental analysis: Calculated (%) C 55.69, H 6.37, N 17.71; Found (%) C 55.56, H 6.41, N 17.82.

Melting point: 147-149 °C

2.6.8. Synthesis of 2-(((butylthio)carbonothiolyl)thio)propanoic acid (CTA)

The details of the procedures are as follows.[76] A 50% NaOH aqueous solution (8.0 g, containing 4.0 g, 100 mmol of NaOH) was added to a stirred mixture of butanethiol (10.7 mL, 100 mmol) and water (15 mL). CAUTION! Butanethiol is **extremely** smelly and **highly toxic**. It must be used in well-ventilated

fume hood, scrubbing exhaust gases with a sodium hypochlorite solution and surfactant mixture.[77, 78] All wastes from synthesis and work-up were similarly treated with sodium hypochlorite (bleach) prior to putting into labelled waste containers. Acetone (5 mL) was then added, and the resulting clear, colorless solution was stirred for 0.5 h then cooled to near-room temperature and treated with carbon disulfide (7.2 mL, 120 mmol) to give a clear orange solution. This was stirred for 0.5 h then cooled in an ice bath to an internal temperature of < 10 °C. 2-Bromopropanoic acid (9.3 mL, 103 mmol) was then added at a slow rate so the temperature did not exceed 30 °C. When the exothermic process had stopped, the ice bath was removed and water (15 mL) was added. The reaction was stirred at ambient temperature for 24 h then diluted with water (25 mL) and cooled in an ice bath while 10 M HCl (15 mL) was added at a rate which kept the temperature < 10 °C. A yellow oil separated and stirring of the mixture was continued at ice temperature until the oil solidified. The solid was collected by suction filtration, pressed and washed with cold water, and dried under reduced pressure to a state of semi-dryness. The lumps were crushed with a spatula; the now-granular solid was resuspended in cold water and stirred for 15 min then refiltered. The residue was washed with cold water and air-dried to afford a powdery yellow solid, which was recrystallized from hexane to give bright yellow crystals (17.2 g, 72%). ^{1}H NMR and ^{13}C NMR spectra are shown in Figure 2.25.

^{1}H NMR (400 MHz, $CDCl_3$) δ = 9.82 (br, 1H, COO*H*), 4.87 (q, *J* = 10.0 Hz, 1H, OC-C*H*-CH_3), 3.37 (t, *J* = 10.0 Hz, 2H, SC(=S)-CH_2), 1.69 (m, 2H, SC(=S)- CH_2-CH_2), 1.63 (d, *J* = 10.0 Hz, 3H, OC-CH-CH_3), 1.43 (m, 2H, C$H_2$$CH_3$), 0.93 (t, *J* = 10.0 Hz, 3H, CH_2CH_3) ppm.

^{13}C NMR (400 MHz, $CDCl_3$) δ = 177.4, 165.2, 47.7, 37.3, 30.1, 22.3, 16.8, 13.8 ppm.

FTIR (neat) ν_{max}/cm^{-1}: 3088 (acid), 2953 and 2926 (CH_3 pryimidine), 1721 and 1700 (C=O), 1042 and 822 (C=S). HR-MS (m/z) found 237.0082, calc. 237.0078 [M-H]$^{-}$.

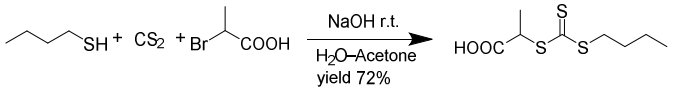

Scheme 2.3. Synthesis of 2-(((butylthio)carbonothiolyl)thio)propanoic acid (CTA).

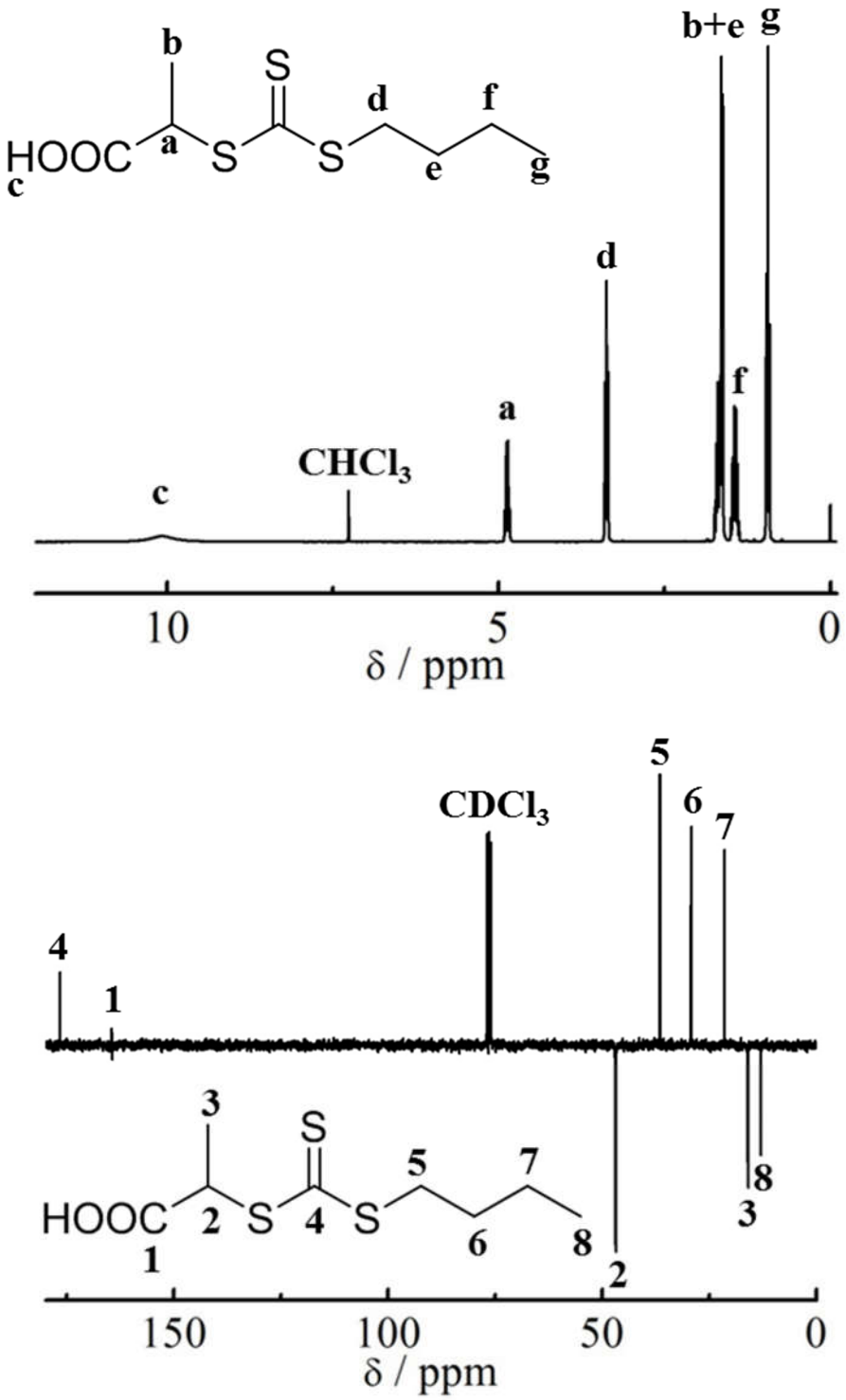

Figure 2.25. ^{1}H NMR and ^{13}C NMR spectra of 2-(((butylthio)carbonothiolyl)thio)propanoic acid (CTA) in $CDCl_3$.

2.6.9. Synthesis of poly(4-acryloylmorpholine) (PNAM) macro-CTA *via* RAFT polymerization

A 10 mL ampoule was charged with NAM (126 μL, 1.0 mmol), 2-(((butylthio)carbonothiolyl)thio)propanoic acid (2.4 mg, 0.01 mmol), VA-044 (0.32 mg, 0.001 mmol) and a mixture of 1,4-dioxane and water (0.5 mL, v:v 1:4).[62] The mixture was thoroughly degassed *via* 4 freeze-pump-thaw cycles, filled with nitrogen and then immersed in an oil bath at 70 °C for 2 h. The polymerization solution was precipitated three times from cold CH_3OH. The light yellow polymer was dried in a vacuum oven overnight at room temperature and analyzed by ^{1}H NMR spectroscopy and DMF SEC (Figures 2.3 and 2.4). The degree of polymerization (DP) of this PNAM macro-CTA, **P2.1**, was calculated to be 96 using ^{1}H NMR spectroscopy by comparing the integrated signals corresponding to the backbone signals (δ = 1.62 ppm) with those of the methyl group from the CTA (δ = 0.87 ppm).

2.6.10. Synthesis of $PNAM_{96}$-*b*-$PTAm_n$ and $PNAM_{96}$-*b*-$PAAm_m$ diblock copolymers

The typical procedures are as follows. For $PNAM_{96}$-*b*-$PTAm_{114}$, $PNAM_{96}$ (35 mg, 0.0025 mmol), TAm (71 mg, 0.30 mmol), and AIBN (0.04 mg, 0.00025 mmol) were dissolved in 0.5 mL DMSO. The mixture was thoroughly degassed *via* 4 freeze-pump-thaw cycles, filled with nitrogen and then immersed in an oil bath at 70 °C overnight. An aliquot of the crude product was taken and analyzed by ^{1}H NMR spectroscopy to calculate the conversion. The residual solution was precipitated three times from cold CH_3OH. The light yellow polymer was dried in a vacuum oven overnight at room temperature and analyzed by ^{1}H NMR spectroscopy and DMF SEC (Figures 2.3 and 2.4). See Table 2.1 for NMR and SEC characterization of polymers **P2.2**–**2.8**.

2.6.11. Self-assembly of PNAM-*b*-PTAm diblock copolymer in water

For the copolymer with moderate hydrophobic TAm blocks (**P2.4**, **P2.6** and **P2.7**), a vial was charged with 10 mg copolymer, 1 mL water and a stirrer bar. The vial was sealed and left at 70 °C overnight with

stirring and then cooled to room temperature to afford well-defined nanostructures. The micelle solutions were then diluted to 0.5 mg mL^{-1} with 18.2 MΩ·cm water at room temperature for TEM and DLS analyses. For the copolymer PNAM$_{96}$-*b*-PTAm$_{301}$ (**P2.5**) with a longer hydrophobic block, a solvent switch method was used to afford self-assembly. Specifically, the copolymer was dissolved in DMF (at 8 mg mL^{-1}) and stirred for 2 h. Then an excess of 18.2 MΩ·cm water was added *via* a syringe pump at a rate of 1 mL h^{-1}. The final volume ratio between water and organic solvent was 8:1. The solution was then dialyzed against 18.2 MΩ·cm water, incorporating at least 6 water changes, to afford self-assemblies at a concentration of *ca.* 1 mg mL^{-1}.

2.6.12. Addition of complementary copolymer PNAM-*b*-PAAm (P2.8) into PNAM-*b*-PTAm micellar solution

The diblock copolymer PNAM$_{96}$-*b*-PAAm$_{19}$ (**P2.8**) was dispersed in H_2O at 10 mg mL^{-1}. This was then added to the micellar solution of PNAM$_{96}$-*b*-PTAm$_n$ (0.5 mg mL^{-1}) dropwise with stirring. The molar ratios were calculated according to the M_n determined from ^{1}H NMR spectroscopic analyses and their mass concentration (see Section 2.6.13). The mixture was then sealed and allowed to stir at room temperature overnight. The solutions were then analyzed by DLS, TEM, SLS and SAXS analysis.

2.6.13. Calculation of the molar ratios of complementary copolymers

The degree of polymerization (DP) of PNAM$_{96}$-*b*-PAAm$_{19}$ (**P2.8**), PNAM$_{96}$-*b*-PTAm$_{114}$ (**P2.4**) and PNAM$_{96}$-*b*-PTAm$_{301}$ (**P2.5**) were obtained from ^{1}H NMR spectroscopic analysis. The number-average molecular weight M_n of the polymers can be calculated from the DP. The self-assemblies of PNAM$_{96}$-*b*-PTAm$_{114}$ (**M2.4**) or PNAM$_{96}$-*b*-PTAm$_{301}$ (**M2.5**) were prepared and the mass concentration is known as *c*. Thus, the molar concentration can be calculated. Then, the mass *m* of PNAM$_{96}$-*b*-PAAm$_{19}$ (**P2.8**) with the relative molar ratios *n* were calculated according to PNAM$_{96}$-*b*-PTAm$_{114}$ (**M2.4**) and PNAM$_{96}$-*b*-PTAm$_{301}$ (**M2.5**) mass concentration and the volume *v* using Equation 2.5.

$$m = \frac{ncvM_{n,\mathbf{P2.8}}}{M_{n,\mathbf{P2.4}}} \quad \text{(Equation 2.5)}$$

Therefore, the molar ratios $R_{\mathrm{A:T}}$ of complementary nucleobases A and T can also be calculated using the DPs of the AAm and TAm blocks as follows:

$$R_{\mathrm{A:T}} = n\frac{\mathrm{DP(A)}_{\mathbf{P2.8}}}{\mathrm{DP(T)}_{\mathbf{P2.4}}} \quad \text{(Equation 2.6)}$$

Where $\mathrm{DP(A)}_{\mathbf{P2.8}}$ is the degree of polymerization of the AAm block in polymer **P2.8**, and $\mathrm{DP(T)}_{\mathbf{P2.4}}$ is the degree of polymerization of the TAm block in polymer **P2.4**. Using molar ratios of complementary copolymers or nucleobases, the micellar size change both shows the same trend as shown in Figure 2.20.

2.7. References

1. L. Zhang and A. Eisenberg, *Science*, **1995**, *268*, 1728-1731.

2. Y.-Y. Won, H. T. Davis and F. S. Bates, *Science*, **1999**, *283*, 960-963.

3. Z. Li, E. Kesselman, Y. Talmon, M. A. Hillmyer and T. P. Lodge, *Science*, **2004**, *306*, 98-101.

4. H. Cui, Z. Chen, S. Zhong, K. L. Wooley and D. J. Pochan, *Science*, **2007**, *317*, 647-650.

5. X. Wang, G. Guerin, H. Wang, Y. Wang, I. Manners and M. A. Winnik, *Science*, **2007**, *317*, 644-647.

6. S. Jain and F. S. Bates, *Science*, **2003**, *300*, 460-464.

7. P. Yang, L. P. D. Ratcliffe and S. P. Armes, *Macromolecules*, **2013**, *46*, 8545-8556.

8. S. E. Mastroianni, J. P. Patterson, R. K. O'Reilly and T. H. Epps III, *Soft Matter*, **2013**, *9*, 10146-10154.

9. D. E. Discher and A. Eisenberg, *Science*, **2002**, *297*, 967-973.

10. D. A. Christian, A. Tian, W. G. Ellenbroek, I. Levental, K. Rajagopal, P. A. Janmey, A. J. Liu, T. Baumgart and D. E. Discher, *Nat. Mater.*, **2009**, *8*, 843-849.

11. J. R. Howse, R. A. L. Jones, G. Battaglia, R. E. Ducker, G. J. Leggett and A. J. Ryan, *Nat. Mater.*, **2009**, *8*, 507-511.

12. M. Massignani, C. LoPresti, A. Blanazs, J. Madsen, S. P. Armes, A. L. Lewis and G. Battaglia, *Small*, **2009**, *5*, 2424-2432.

13. J. N. Israelachvili, D. J. Mitchell and B. W. Ninham, *J. Chem. Soc., Faraday Trans. 2*, **1976**, *72*, 1525-1568.

14. M. Antonietti and S. Förster, *Adv. Mater.*, **2003**, *15*, 1323-1333.

15. Y. Geng, P. Dalhaimer, S. Cai, R. Tsai, M. Tewari, T. Minko and D. E. Discher, *Nat. Nanotechnol.*, **2007**, *2*, 249-255.

16. R. K. O'Reilly, C. J. Hawker and K. L. Wooley, *Chem. Soc. Rev.*, **2006**, *35*, 1068-1083.

17. A. Choucair and A. Eisenberg, *Soft Matter*, **2003**, *10*, 37-44.

18. Y. Zheng and H. T. Davis, *Langmuir*, **2000**, *16*, 6453-6459.

19. A. Blanazs, J. Madsen, G. Battaglia, A. J. Ryan and S. P. Armes, *J. Am. Chem. Soc.*, **2011**, *133*, 16581-16587.

20. N. J. Warren and S. P. Armes, *J. Am. Chem. Soc.*, **2014**, *136*, 10174-10185.

21. W. Cai, W. Wan, C. Hong, C. Huang and C. Pan, *Soft Matter*, **2010**, *6*, 5554-5561.

22. Y. Pei and A. B. Lowe, *Polym. Chem.*, **2014**, *5*, 2342-2351.

23. Y. Cai, K. B. Aubrecht and R. B. Grubbs, *J. Am. Chem. Soc.*, **2011**, *133*, 1058-1065.

24. A. O. Moughton, J. P. Patterson and R. K. O'Reilly, *Chem. Commun.*, **2011**, *47*, 355-357.

25. K. Wei, L. Su, G. Chen and M. Jiang, *Polymer*, **2011**, *52*, 3647-3654.

26. Y. Tao, K. Satoh and M. Kamigaito, *Macromol. Rapid Commun.*, **2011**, *32*, 226-232.

27. M. Akashi, H. Takada, Y. Inaki and K. Takemoto, *J. Polym. Sci., Polym. Chem. Ed.*, **1979**, *17*, 747-757.

28. Y. Kang, A. Lu, A. Ellington, M. C. Jewett and R. K. O'Reilly, *ACS Macro Lett.*, **2013**, *2*, 581-586.

29. A. Khan, D. M. Haddleton, M. J. Hannon, D. Kukulj and A. Marsh, *Macromolecules*, **1999**, *32*, 6560-6564.

30. C. R. South and M. Weck, *Macromolecules*, **2007**, *40*, 1386-1394.

31. P. K. Lo and H. F. Sleiman, *J. Am. Chem. Soc.*, **2009**, *131*, 4182-4183.

32. E. Stahl, T. G. Martin, F. Praetorius and H. Dietz, *Angew. Chem., Int. Ed.*, **2014**, *53*, 12735-12740.

33. P. W. K. Rothemund, *Nature*, **2006**, *440*, 297-302.

34. Z. Li, Y. Zhang, P. Fullhart and C. A. Mirkin, *Nano Lett.*, **2004**, *4*, 1055-1058.

35. Y. Dong, Z. Yang and D. Liu, *Acc. Chem. Res.*, **2014**, *47*, 1853-1860.

36. P. J. Milnes, M. L. McKee, J. Bath, L. Song, E. Stulz, A. J. Turberfield and R. K. O'Reilly, *Chem. Commun.*, **2012**, *48*, 5614-5616.

37. M. L. McKee, P. J. Milnes, J. Bath, E. Stulz, R. K. O'Reilly and A. J. Turberfield, *J. Am. Chem. Soc.*, **2012**, *134*, 1446-1449.

38. R. McHale and R. K. O'Reilly, *Macromolecules*, **2012**, *45*, 7665-7675.

39. F. Ilhan, T. H. Galow, M. Gray, G. Clavier and V. M. Rotello, *J. Am. Chem. Soc.*, **2000**, *122*, 5895-5896.

40. R. J. Thibault, P. J. Hotchkiss, M. Gray and V. M. Rotello, *J. Am. Chem. Soc.*, **2003**, *125*, 11249-11252.

41. H. S. Bazzi and H. F. Sleiman, *Macromolecules*, **2002**, *35*, 9617-9620.

42. H. J. Spijker, A. J. Dirks and J. C. M. van Hest, *J. Polym. Sci., Part A: Polym. Chem.*, **2006**, *44*, 4242-4250.

43. R. P. Sijbesma, F. H. Beijer, L. Brunsveld, B. J. B. Folmer, J. H. K. K. Hirschberg, R. F. M. Lange, J. K. L. Lowe and E. W. Meijer, *Science*, **1997**, *278*, 1601-1604.

44. R. McHale, J. P. Patterson, P. B. Zetterlund and R. K. O'Reilly, *Nat. Chem.*, **2012**, *4*, 491-497.

45. Y. Kang, A. Pitto-Barry, A. Maitland and R. K. O'Reilly, *Polym. Chem.*, **2015**, *6*, 4984-4992.

46. Y. Kang, A. Pitto-Barry, H. Willcock, W. Quan, N. Kirby, A. M. Sanchez and R. K. O'Reilly, *Polym. Chem.*, **2015**, *6*, 106-117.

47. Y. Tao, Y. Yang, D. Shi, M. Chen, C. Yang and X. Liu, *Polymer*, **2012**, *53*, 1551-1557.

48. R.-S. Lee, K.-Y. Peng, S.-W. Wang and Y.-Z. Li, *Polym. J.*, **2014**, *46*, 710-721.

49. H. Kuang, S. Wu, Z. Xie, F. Meng, X. Jing and Y. Huang, *Biomacromolecules*, **2012**, *13*, 3004-3012.

50. M. Garcia, K. Kempe, D. M. Haddleton, A. Khan and A. Marsh, *Polym. Chem.*, **2015**, *6*, 1944-1951.

51. T. Schnitzler and A. Herrmann, *Acc. Chem. Res.*, **2012**, *45*, 1419-1430.

52. T. G. Edwardson, K. M. Carneiro, C. K. McLaughlin, C. J. Serpell and H. F. Sleiman, *Nat. Chem.*, **2013**, *5*, 868-875.

53. T. R. Wilks, J. Bath, J. W. de Vries, J. E. Raymond, A. Herrmann, A. J. Turberfield and R. K. O'Reilly, *ACS Nano*, **2013**, *7*, 8561-8572.

54. F. E. Alemdaroglu, K. Ding, R. Berger and A. Herrmann, *Angew. Chem., Int. Ed.*, **2006**, *45*, 4206-4210.

55. M. Kwak, A. J. Musser, J. Lee and A. Herrmann, *Chem. Commun.*, **2010**, *46*, 4935-4937.

56. M.-P. Chien, A. M. Rush, M. P. Thompson and N. C. Gianneschi, *Angew. Chem., Int. Ed.*, **2010**, *49*, 5076-5080.

57. J.-F. Lutz, A. F. Thunemann and K. Rurack, *Macromolecules*, **2005**, *38*, 8124-8126.

58. H. J. Spijker, F. L. van Delft and J. C. M. van Hest, *Macromolecules*, **2007**, *40*, 12-18.

59. K. Zhang, M. Aiba, G. B. Fahs, A. G. Hudson, W. D. Chiang, R. B. Moore, M. Ueda and T. E. Long, *Polym. Chem.*, **2015**, *6*, 2434-2444.

60. Y. Inaki, *Prog. Polym. Sci.*, **1992**, *17*, 515-570.

61. J.-F. Lutz and H. G. Börner, *Prog. Polym. Sci.*, **2008**, *33*, 1-39.

62. G. Gody, T. Maschmeyer, P. B. Zetterlund and S. Perrier, *Nat. Commun.*, **2013**, *4*, 2505-2513.

63. L. Sun, N. Petzetakis, A. Pitto-Barry, T. L. Schiller, N. Kirby, D. J. Keddie, B. J. Boyd, R. K. O'Reilly and A. P. Dove, *Macromolecules*, **2013**, *46*, 9074-9082.

64. T. Nicolai, O. Colombani and C. Chassenieux, *Soft Matter*, **2010**, *6*, 3111-3118.

65. L. D. Blackman, D. B. Wright, M. P. Robin, M. I. Gibson and R. K. O'Reilly, *ACS Macro Lett.*, **2015**, *4*, 1210-1214.

66. R. Thomas, *Gene*, **1993**, *135*, 77-79.

67. J. P. Patterson, M. P. Robin, C. Chassenieux, O. Colombani and R. K. O'Reilly, *Chem. Soc. Rev.*, **2014**, *43*, 2412-2425.

68. D. B. Wright, J. P. Patterson, A. Pitto-Barry, P. Cotanda, C. Chassenieux, O. Colombani and R. K. O'Reilly, *Polym. Chem.*, **2015**, *6*, 2761-2768.

69. D. B. Wright, J. P. Patterson, A. Pitto-Barry, A. Lu, N. Kirby, N. C. Gianneschi, C. Chassenieux, O. Colombani and R. K. O'Reilly, *Macromolecules*, **2015**, *48*, 6516-6522.

70. D. B. Wright, J. P. Patterson, N. C. Gianneschi, C. Chassenieux, O. Colombani and R. K. O'Reilly, *Polym. Chem.*, **2016**, *7*, 1577-1583.

71. J. P. Patterson, A. M. Sanchez, N. Petzetakis, T. P. Smart, T. H. Epps III, I. Portman, N. R. Wilson and R. K. O'Reilly, *Soft Matter*, **2012**, *8*, 3322-3328.

72. P. V. Konarev, V. V. Volkov, A. V. Sokolova, M. H. J. Koch and D. I. Svergun, *J. Appl. Crystallogr.*, **2003**, *36*, 1277-1282.

73. S. Kline, *J. Appl. Crystallogr.*, **2006**, *39*, 895-900.

74. R. E. Kohman, C. Cha, S. C. Zimmerman and H. Kong, *Soft Matter*, **2010**, *6*, 2150-2152.

75. S. Racine, F. De Nanteuil, E. Serrano and J. Waser, *Angew. Chem., Int. Ed.*, **2014**, *53*, 8484-8487.

76. C. J. Ferguson, R. J. Hughes, D. Nguyen, B. T. T. Pham, R. G. Gilbert, A. K. Serelis, C. H. Such and B. S. Hawkett, *Macromolecules*, **2005**, *38*, 2191-2204.

77. F. M. Menger and A. R. Elrington, *J. Am. Chem. Soc.*, **1991**, *113*, 9621-9624.

78. F. M. Menger, and M. J. Rourk, *Langmuir*, **1999**, *15*, 309-313.

Chapter 3. Nanoparticles with a nucleobase-containing core showing pathway dependent and complementary chain selective morphological transitions

3.1. Declaration of authorship

The SLS data in this Chapter was analyzed by Dr. Joe Jones (University of Warwick) and the cryo-TEM images in this Chapter were obtained by Dr. Saskia Bakker (University of Warwick). HR Mass Spectra in this Chapter was analyzed by mass spectrometry group (University of Warwick).

3.2. Abstract

Specific, complementary hydrogen-bonding (H-bonding) interactions have been widely used to fabricate novel nanomaterials using DNAs or RNAs as building blocks. In contrast, nucleobase-containing synthetic polymers, a kind of mimic of DNAs or RNAs, normally have a carbon-carbon backbone and have seldom been employed based on their selective complementary interactions. Herein, we prepare a kind of nucleobase-containing nanoparticles, showing complementary chain-selective and pathway-dependent morphological transitions at room temperature in water. Non-complementary diblock copolymers could not induce efficient morphological transitions through only hydrophobic effects. The insertion of adenine-containing diblock copolymer into the micelle with a thymine-functionalized core gave rise to efficient transformation. Spheres, dumbbells and worms with distinct sizes could be selectively targeted by introducing adenine-containing copolymers of variable chain lengths. Both lengths of hydrophobic and hydrophilic blocks of added complementary copolymers could affect the morphological transitions. Meanwhile, the approach of adding the same complementary copolymers also influenced the transformation of nanoparticles. More importantly, worm-like nanoparticles with different lengths from 300 to over 1000 nm could be easily obtained through the stepwise introduction of complementary copolymers, suggesting successful controlled "living" growth through H-bonding interactions. The specific complementary interactions of synthetic polymers enable us to tailor *in-situ* the sizes and shapes of nanomaterials at room temperature in water.

3.3. Introduction

Nature provides a wealth of models for scientists to mimic.[1] For example, natural viruses can have distinct shapes such as spheres,[2] rods,[3] worms[4] and ellipsoids,[5] inspiring scientists to construct polymeric nanostructure mimics for systemic delivery. Normally, these nanoparticles are fabricated using weak intermolecular interactions, such as π-π stacking, hydrophobic or H-bonding interactions. Chemists now can prepare nanoparticles with various morphologies including spherical micelles,[6] cylindrical micelles,[7-10] bicontinuous structures,[11] lamellae[12, 13] and vesicles,[6, 14-17] among others.[6, 18]

Nanostructures with different morphologies can show distinct properties *in vivo*.[19, 20] For example, the Mao group reported a method for tuning plasmid DNA nanoparticles during the condensation of DNA with polymers containing random positive and negative charges.[20] This approach effectively enabled access to spherical, rod-like and worm-like micelles, demonstrating shape-dependent gene transfection efficiency. However, in order to achieve the morphological transition, they needed to dramatically alter the interfacial tension of polymeric nanoparticles by heating or introducing large volume ratios of cosolvent.[21-24]

Directional multiple hydrogen-bonding (H-bonding) interactions can result in strong, specific bindings within DNAs and RNAs. The Gianneschi group reported programmable shape-transformable micelles through complementary DNA interactions.[25] The controlled alteration of hydrophobic/hydrophilic weight fractions by specific DNA binding/unbinding enabled the formation of spherical and cylindrical nanoparticles reversibly. Specific complementary DNA interactions provide precise control over the morphologies of nanoparticles. Apart from the repulsive interactions among corona-forming chains, the degree of stretching of the core-forming blocks can also determine the stability of morphologies formed. The stretching of core chains of polymeric nanoparticles, to some extent, is difficult to tune due to the dense packing within the core. Compared with hydrophilic DNAs or RNAs, synthetic nucleobase-

containing polymers were recently highlighted to enable the specific complementary H-bonding interactions within the micelle core.[26, 27]

Nucleobase-containing synthetic polymers, unlike DNAs and RNAs, are a kind of nucleobase or nucleoside-functionalized polymer, the backbone of which consists of carbon-carbon, amide, thioether and so on.[26-35] These polymers can be prepared by controlled radical polymerization or sequential click reactions at a relatively large scale. By use of the pendant nucleobase functionalities, these polymers can be used to achieve templated polymerization,[30, 31, 33] fabricate DNA-like supramolecular aggregates,[29] and tune nanostructure morphologies and functionalities.[26-28, 32] However, complementary interactions among nucleobase-containing synthetic polymers, especially with respect to specific chain selectivity, have seldom been explored although they are the most prominent properties among DNAs and RNAs.

In the present study, we explored the interactions between thymine-containing micelles and complementary and non-complementary diblock copolymers. Our results suggest that morphological transitions can occur only when the polymers with the complementary nucleobase were added. The efficient transformation of initial micelles was caused by inserting complementary nucleobase polymers into the thymine-containing micelle core. Meanwhile, the observed morphological transitions show specific pathway dependence and complementary chain selectivity. Controlled living growth of worm-like micelles can be successfully achieved through the complementary nucleobase interactions. Thus, our study provides a straightforward approach to fabricating nanostructures with different sizes and shapes and represents a new development to create smart micelles with potential biomedical applications.

3.4. Results and discussion

3.4.1. Morphological transitions induced by complementary nucleobase interactions

Nucleobase-containing diblock copolymers poly(4-acryloylmorpholine)-*b*-poly(3-(adenine-9-yl)propyl acrylamide ($PNAM_{39}$-*b*-$PAAm_{20}$, **PA1**) and poly(4-acryloylmorpholine)-*b*-poly(3-(thymin-1-yl)propyl acrylamide ($PNAM_{39}$-*b*-$PTAm_{300}$, **PT1**), were prepared using reversible addition-fragmentation chain transfer (RAFT) polymerization as reported previously (Scheme 3.1, Table 3.1, Figures 3.1 and 3.2).[27] In contrast, methylated nucleobase-containing copolymers $\mathbf{PA^{Me}}$ (poly(4-acryloylmorpholine)-*b*-poly(3-(*N*6,*N*6-dimethyladenine-9-yl)propyl acrylamide), $PNAM_{39}$-*b*-$PMAAm_{20}$) and $\mathbf{PT^{Me}}$ (poly(4-acryloylmorpholine)-*b*-poly(3-(3-methylthymin-1-yl)propyl acrylamide, $PNAM_{39}$-*b*-$PMTAm_{300}$) were also synthesized and utilized to explore the specific effect of H-bonding interactions (Table 3.1).

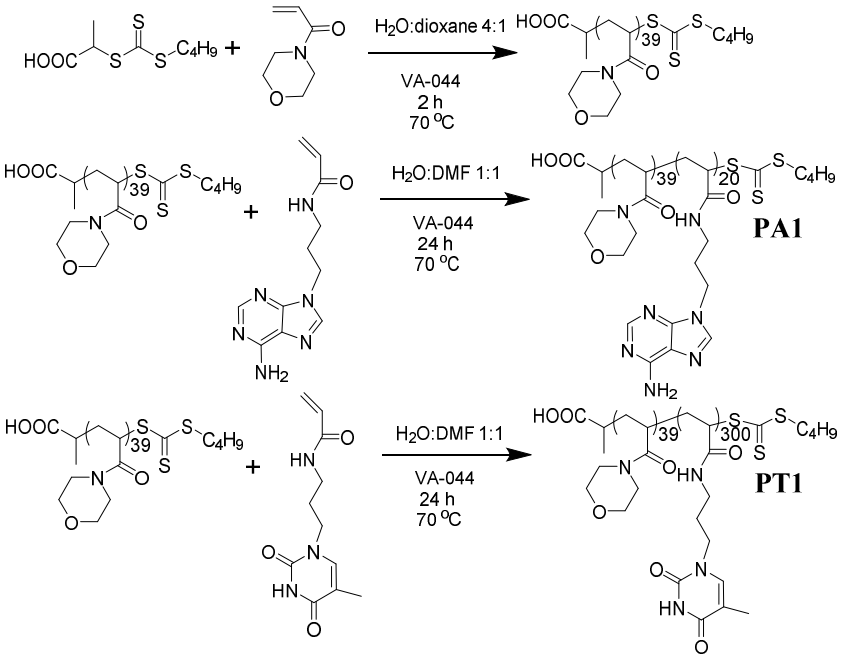

Scheme 3.1. Synthetic routes for $PNAM_{39}$, **PA1** ($PNAM_{39}$-*b*-$PAAm_{20}$) and **PT1** ($PNAM_{39}$-*b*-$PTAm_{300}$).

Table 3.1. Characterization of macroCTA and nucleobase-containing diblock copolymers.

Polymers	$M_{n,NMR}$[a] (kDa)	$M_{n,SEC}$[b] (kDa)	$Đ_M$[b]
$PNAM_{39}$	5.7	5.9	1.07
$PNAM_{295}$	41.9	35.0	1.11
$PNAM_{39}$-*b*-$PTAm_{300}$ **PT1**	76.9	58.5	1.33
$PNAM_{39}$-*b*-$PAAm_{20}$ **PA1**	10.7	12.6	1.07
$PNAM_{39}$-*b*-$PMAAm_{20}$ **PA^{Me}**	11.2	9.7	1.12
$PNAM_{39}$-*b*-$PTAm_{20}$ **PT2**	10.5	13.1	1.07
$PNAM_{39}$-*b*-PSt_{20} **PS**	7.8	8.0	1.09
$PNAM_{39}$-*b*-$PMTAm_{300}$ **PT^{Me}**	81.1	53.7	1.35
$PNAM_{39}$-*b*-$PAAm_{10}$ **PA2**	8.2	10.6	1.04
$PNAM_{39}$-*b*-$PAAm_{30}$ **PA3**	13.1	16.4	1.12
$PNAM_{96}$-*b*-$PAAm_{20}$ **PA4**[c]	18.6	19.9	1.08
$PNAM_{295}$-*b*-$PAAm_{20}$ **PA5**	47.0	36.8	1.17

[a]Determined by ^{1}H NMR spectroscopy (400 MHz) in deuterated DMSO. [b]Determined by DMF SEC, with poly(methyl methacrylate) (PMMA) standards. [c]Reported in Chapter 2 and our previous publication.[27]

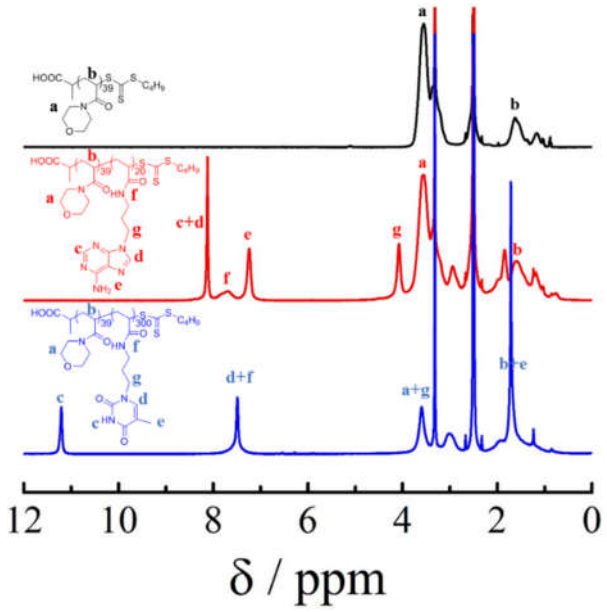

Figure 3.1. ^{1}H NMR spectra of $PNAM_{39}$, **PA1** ($PNAM_{39}$-*b*-$PAAm_{20}$) and **PT1** ($PNAM_{39}$-*b*-$PTAm_{300}$) by ^{1}H NMR spectroscopy (400 MHz) in DMSO-d_6.

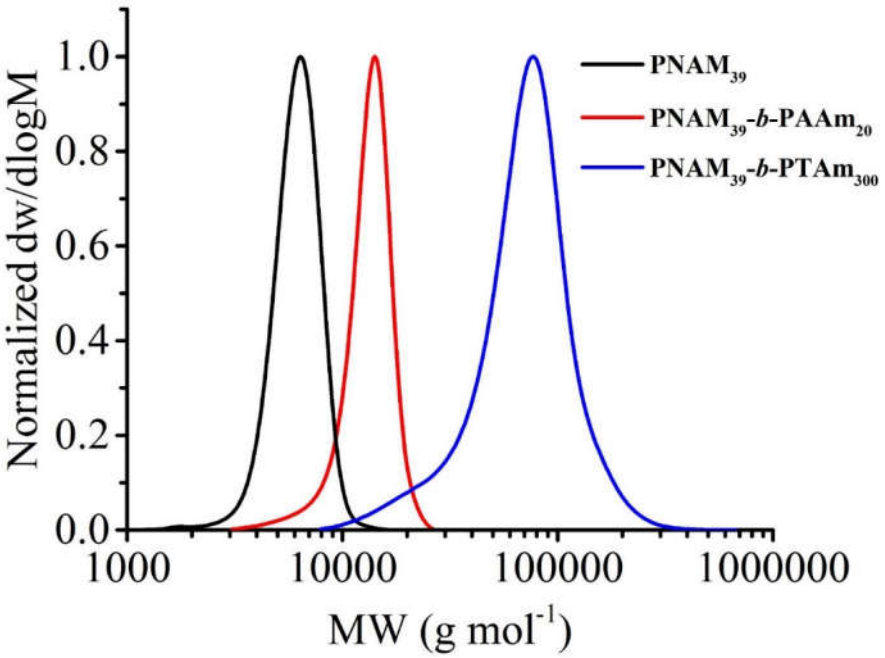

Figure 3.2. SEC traces of $PNAM_{39}$, **PA1** ($PNAM_{39}$-*b*-$PAAm_{20}$) and **PT1** ($PNAM_{39}$-*b*-$PTAm_{300}$) by DMF SEC, with poly(methyl methacrylate) (PMMA) standards.

The length of hydrophilic block is much shorter relative to the hydrophobic block, which significantly decreases the probability of unimer exchange from one micelle to another. Meanwhile, the disassembly of the formed mixed micelles was dramatically hindered in contrast to our previous work in Chapter 2.[27] Well-defined nanoparticles **MT1** consisting of **PT1** were formed through solvent switch from DMF to water (Scheme 3.2). TEM image showed that spherical micelles with number average diameter of 56 ± 7 nm were formed (Figure 3.3a). DLS analysis further confirmed that the micelles formed were monodisperse, with an average diameter of 78 nm that was in agreement with TEM (Figure 3.4).

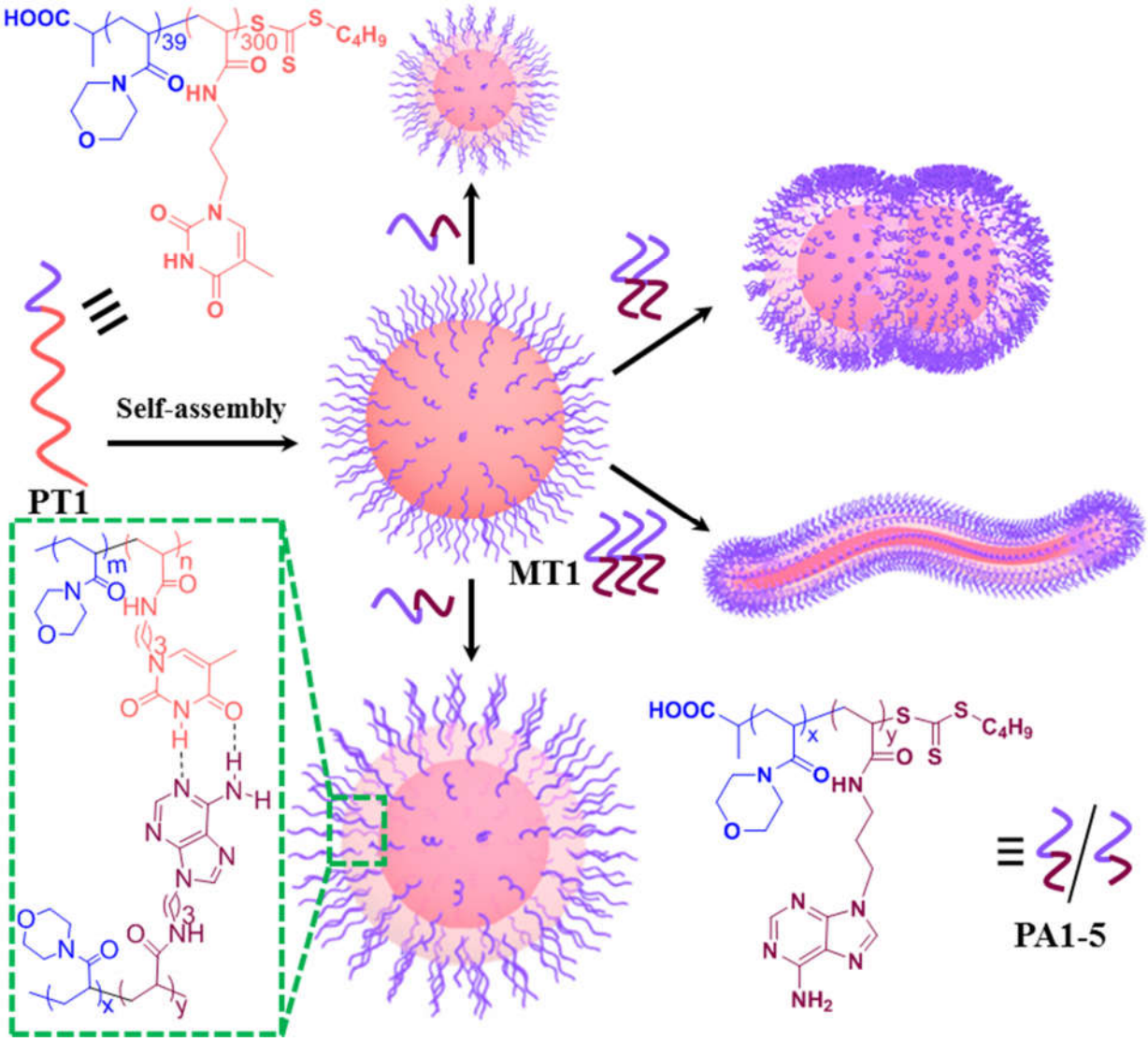

Scheme 3.2. Fabrication of thymine-containing core-functionalized micelles **MT1** and morphological transitions induced by adding distinct complementary nucleobase diblock copolymers **PA1-5**.

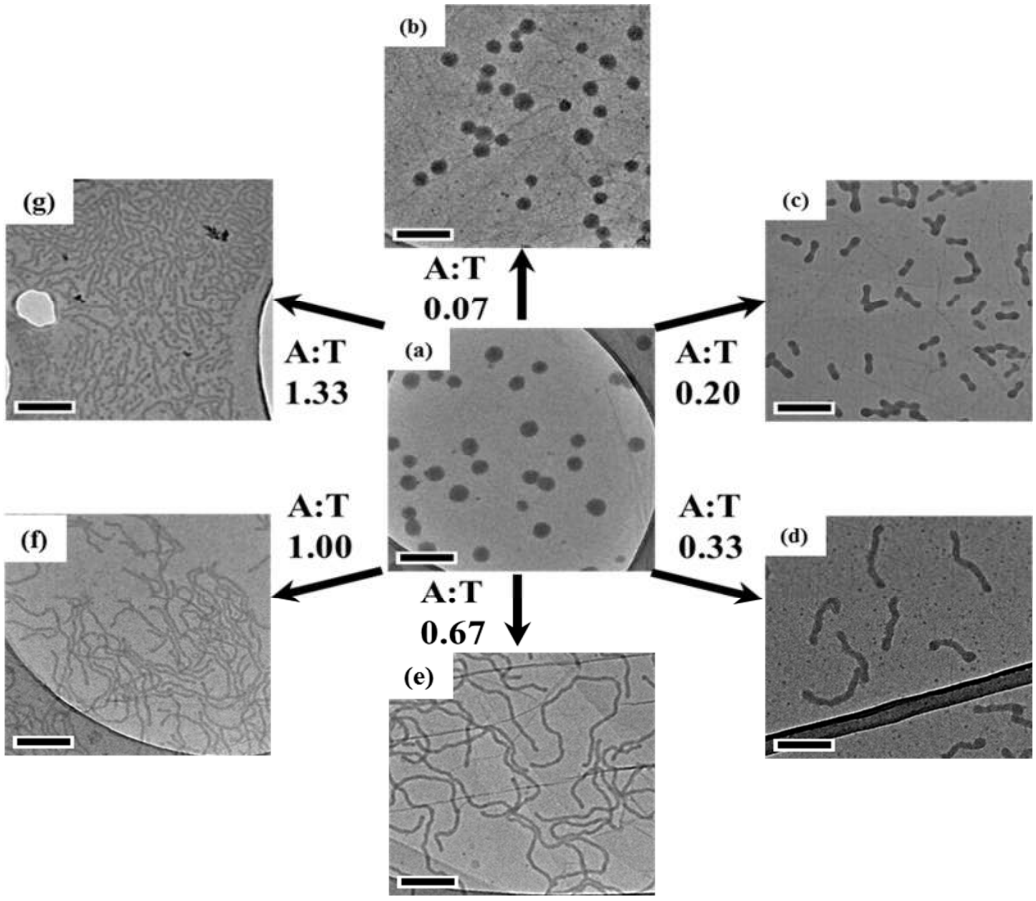

Figure 3.3. Micelles with different morphologies were prepared through mixing complementary **PA1** solution into the initial spherical micelle **MT1** under stirring at room temperature. Dry-state TEM images on graphene oxide of micelle **MT1** after adding **PA1** with variable molar ratios of **A:T**. (a) 0, (b) 0.07, (c) 0.20, (d) 0.33, (e) 0.67, (f) 1.00, (g) 1.33; scale bars = 200 nm.

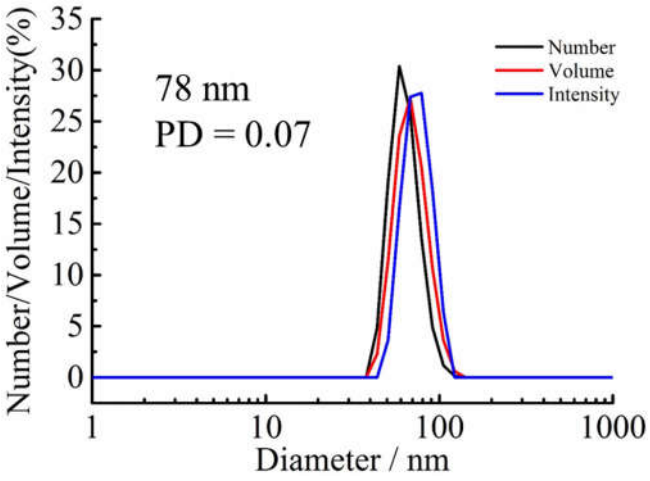

Figure 3.4. DLS analysis of self-assemblies **MT1** of $PNAM_{39}$-*b*-$PTAm_{300}$ **PT1** in water.

Following the formation of the micelle **MT1**, another diblock copolymer, poly(4-acryloylmorpholine)-*b*-poly(3-(adenine-9-yl)propyl acrylamide ($PNAM_{39}$-*b*-$PAAm_{20}$, **PA1**) with a complementary nucleobase block was introduced into the initial **MT1** solution (Scheme 3.2). Different molar equivalents of **PA1** solution were added to micelle **MT1** solutions and left to stir for at least 2 h at room temperature. The obtained samples were then imaged by TEM using graphene oxide (GO) grids without staining.[36] Slightly larger spherical micelles were observed when the molar ratio of **A:T** was 0.07 (Figure 3.3b). Interestingly, uniform dumbbell-like nanoparticles were formed with **A:T** molar ratio of 0.20 (Figure 3.3c). This nanostructure is reminiscent of the intermediate state of cell division, where the parent cell tends to divide into two daughter cells. When adding **PA1** with **A:T** molar ratio of 0.33, long worms with length over 200 nm were observed (Figure 3.3d). Figure 3.3e shows that much longer worms with length *ca.* 1000 nm were formed when mixing **PA1** with **A:T** molar ratio of 0.67. In contrast, short and thin worms were generated after adding **PA1** with **A:T** molar ratio of 1.00 and 1.33. Therefore, we observed the morphological change from spheres to dumbbells or worms when adding complementary diblock copolymers **PA1** with different molar ratios.

3.4.2. No morphological transitions induced by only hydrophobic effects

It is obvious that both hydrophobic effects and complementary H-bonding interactions between A and T play an important role in giving rise to the morphological transitions observed here. We also wondered whether hydrophobic effects alone could induce similar morphological transitions. Three different diblock copolymers, **PS** (poly(4-acryloylmorpholine)-*b*-polystyrene, $PNAM_{39}$-*b*-PSt_{20}), **PT2** ($PNAM_{39}$-*b*-$PTAm_{20}$) and $\mathbf{PA^{Me}}$ (poly(4-acryloylmorpholine)-*b*-poly(3-(*N*6,*N*6-dimethyladenine-9-yl)propyl acrylamide), $PNAM_{39}$-*b*-$PMAAm_{20}$) were synthesized (Figures 3.5 and 3.6) and added into the micellar solution **MT1**, respectively.

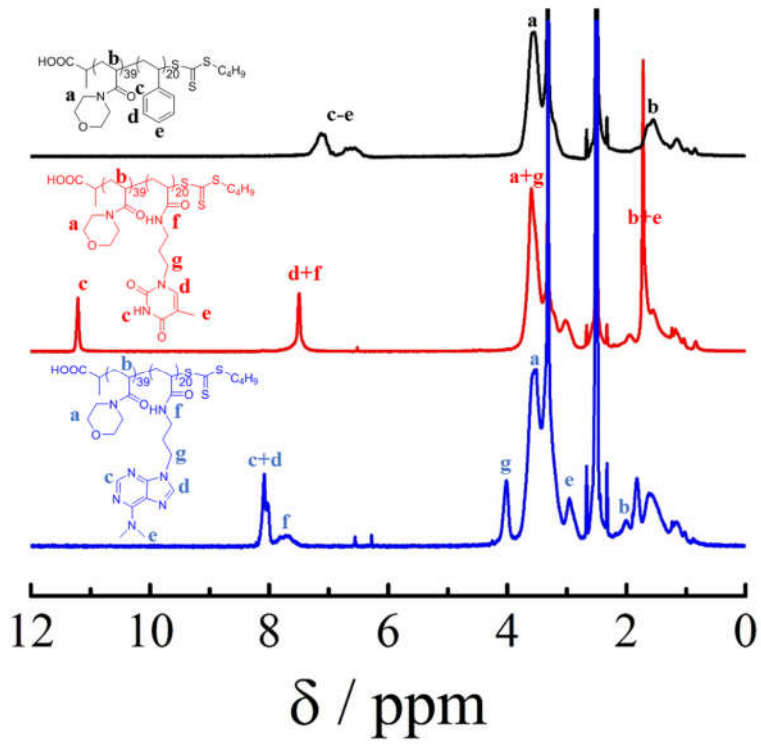

Figure 3.5. ^{1}H NMR spectra of **PS** (PNAM$_{39}$-*b*-PSt$_{20}$), **PT2** (PNAM$_{39}$-*b*-PTAm$_{20}$) and **PA^{Me}** (PNAM$_{39}$-*b*-PMAAm$_{20}$) by ^{1}H NMR spectroscopy (400 MHz) in deuterated DMSO.

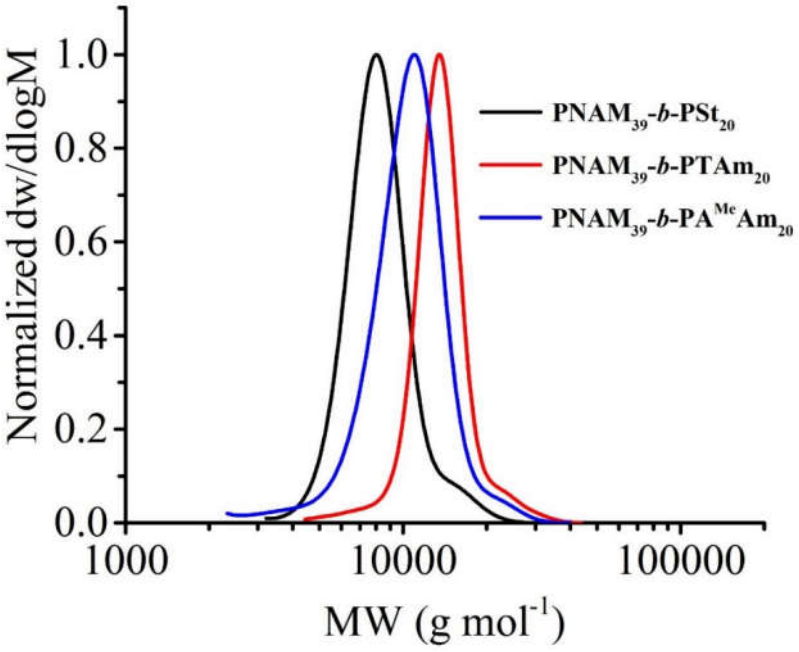

Figure 3.6. SEC traces of **PS** (PNAM$_{39}$-*b*-PSt$_{20}$), **PT2** (PNAM$_{39}$-*b*-PTAm$_{20}$) and **PA^{Me}** (PNAM$_{39}$-*b*-PMAAm$_{20}$) by DMF SEC, with poly(methyl methacrylate) (PMMA) standards.

No appreciable hydrodynamic diameter changes were observed by adding these non-complementary diblock copolymers as characterized by DLS analyses (Figure 3.7). As the added polymers **PS**, **PT2** and **PA^{Me}** can only form small aggregates (Figure 3.8), which scatter less light compared with the initial micelle **MT1**, leading to no obvious size change.

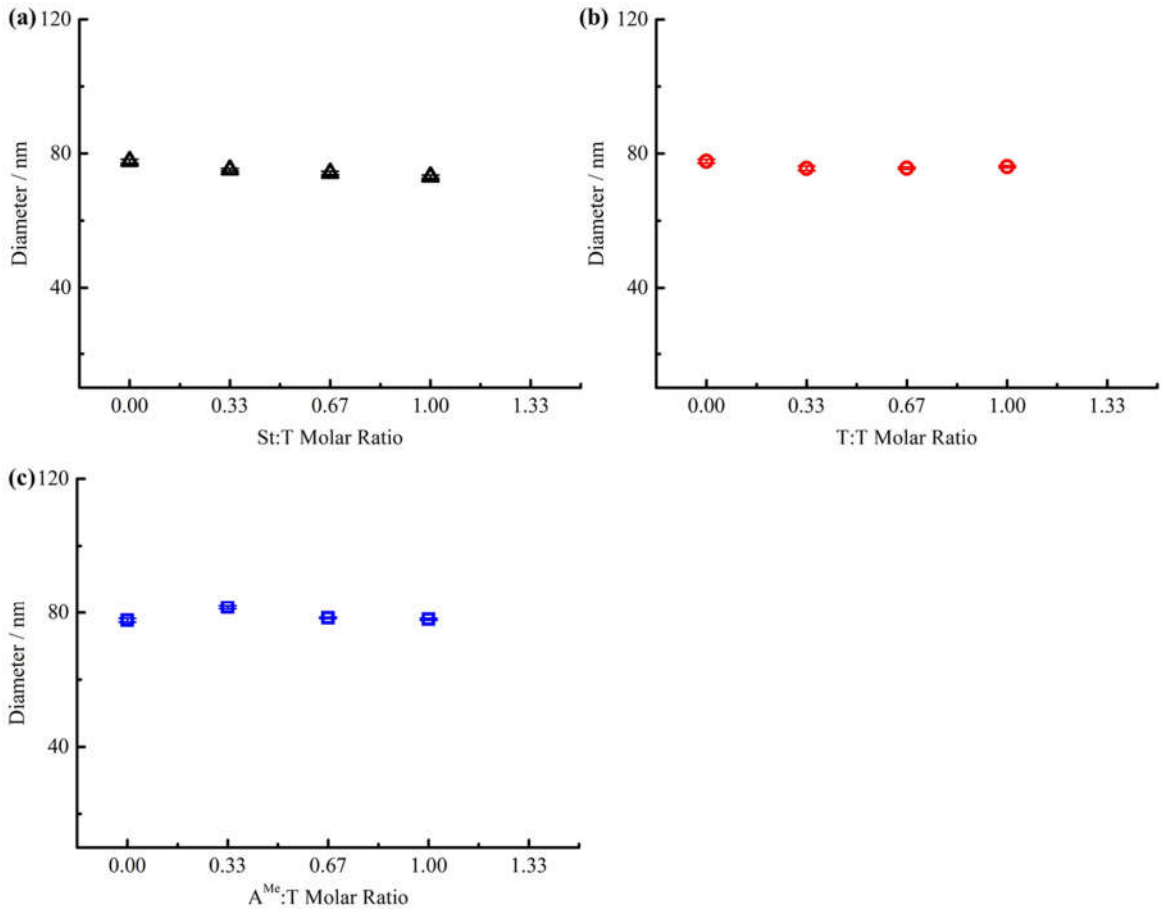

Figure 3.7. Variation of hydrodynamic diameter of the mixture of micelle with non-complementary copolymers as determined by DLS analyses. (a) Micelle **MT1** with **PS**; (b) micelle **MT1** with **PT2**; (c) micelle **MT1** with **PA^{Me}**.

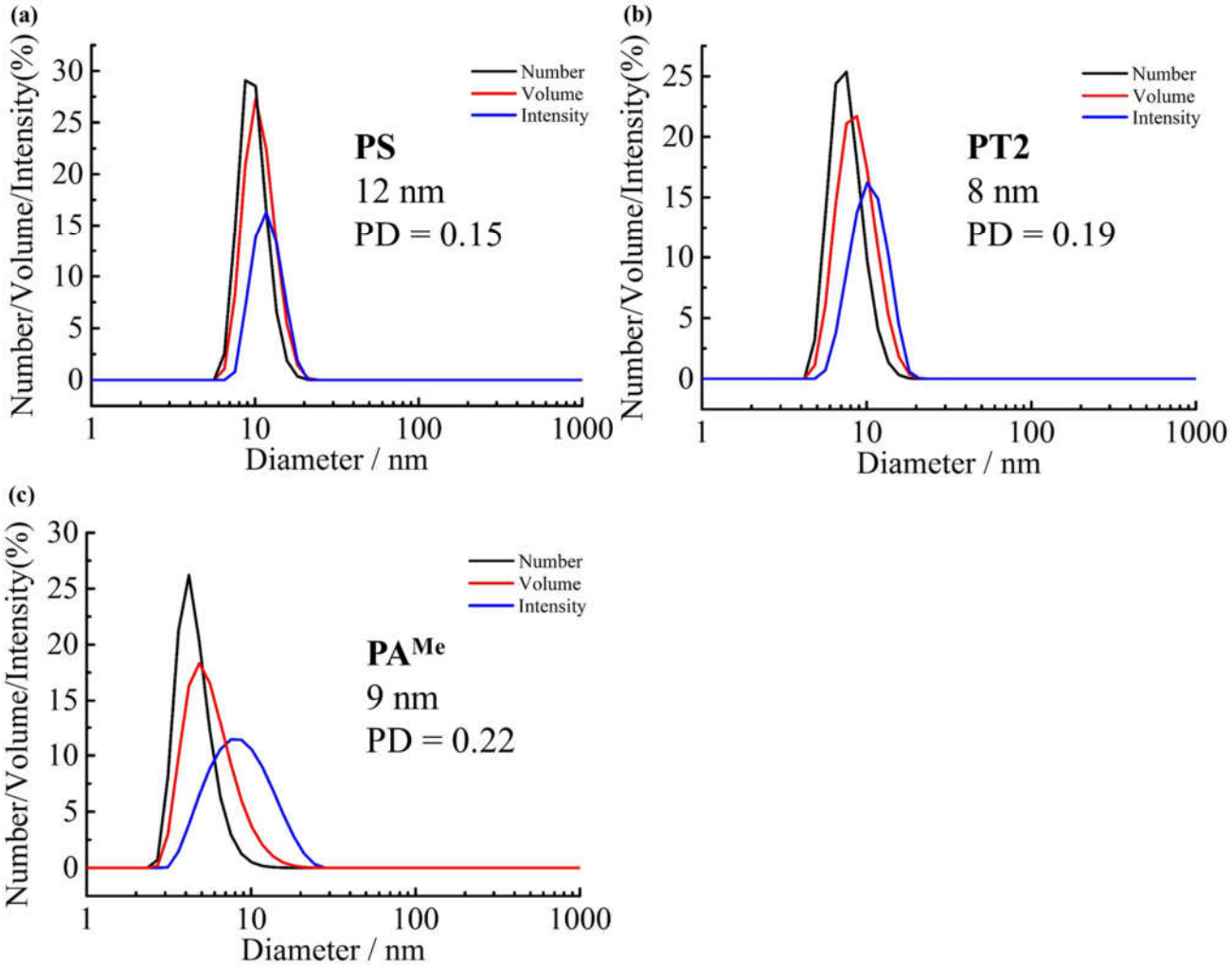

Figure 3.8. DLS analyses of small aggregated formed in water by (a) **PS**; (b) **PT2**; (c) **PA^{Me}**.

Meanwhile, the initial spherical micelles kept the same shape after adding non-complementary copolymers **PS**, **PT2** and **PA^{Me}** (Figure 3.9). Due to the small size of unstable **PT2** and **PA^{Me}** aggregates, which could not be imaged under TEM, well-defined spheres were observed when **T:T** and **A^{Me}:T** molar ratio was 1.00 (Figure 3.9b and 3.9c). In contrast, the mixtures of spherical **MT1** and worm-like micelles formed by **PS** in water were found when **MT1** and **PS** were mixed (Figure 3.9a and Figure 3.10).

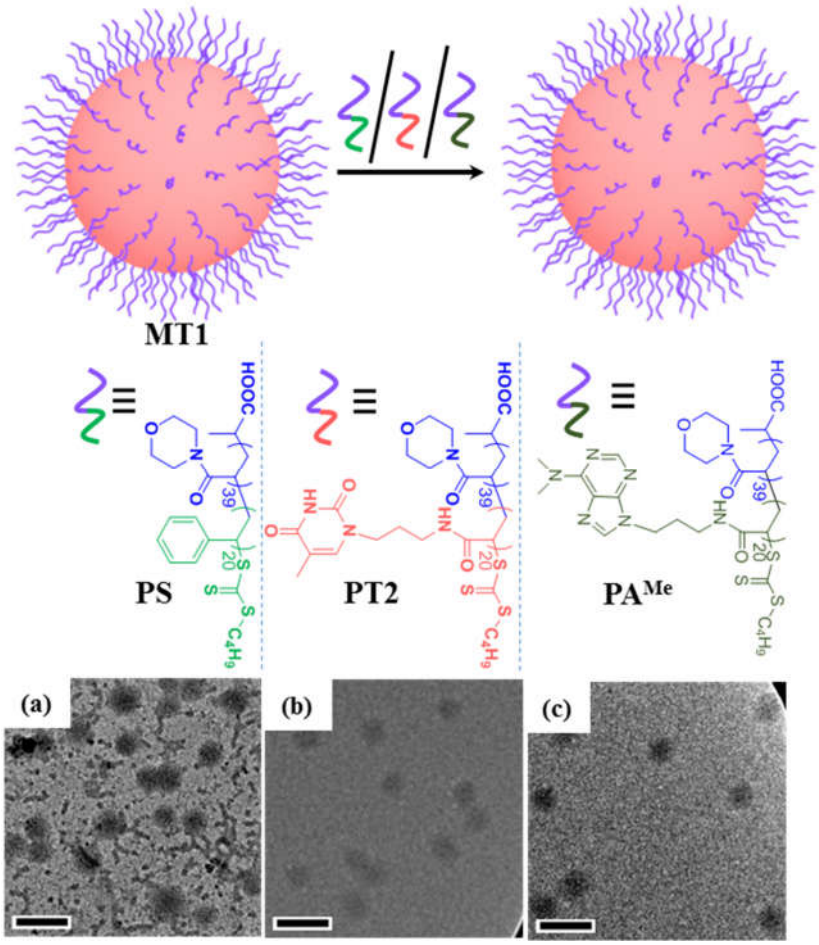

Figure 3.9. No morphological transitions were induced by non-complementary diblock copolymers through hydrophobic effects. Dry-state TEM images on graphene oxide of micelles **MT1** after adding **PS**, **PT2** and **PA^{Me}** with molar ratios of (a) **St:T** = 1.00; (b) **T:T** = 1.00; (c) **A^{Me}:T** = 1.00; scale bars = 200 nm.

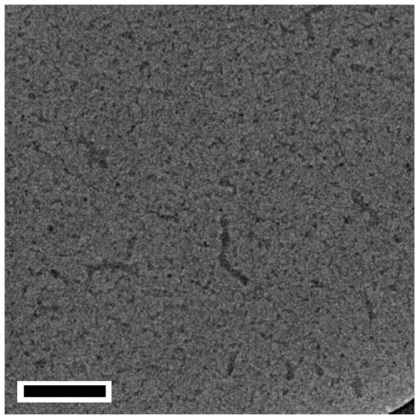

Figure 3.10. TEM images of **PS** aggregates formed in water; scale bar = 200 nm.

In addition, another micelle **MT^{Me}** was self-assembled from poly(4-acryloylmorpholine)-*b*-poly(3-(3-methylthymin-1-yl)propyl acrylamide (PNAM$_{39}$-*b*-PMTAm$_{300}$, **PT^{Me}**), in which the complementary H-bonding moieties were effectively blocked by methyl groups (Figures 3.11 and 3.12).

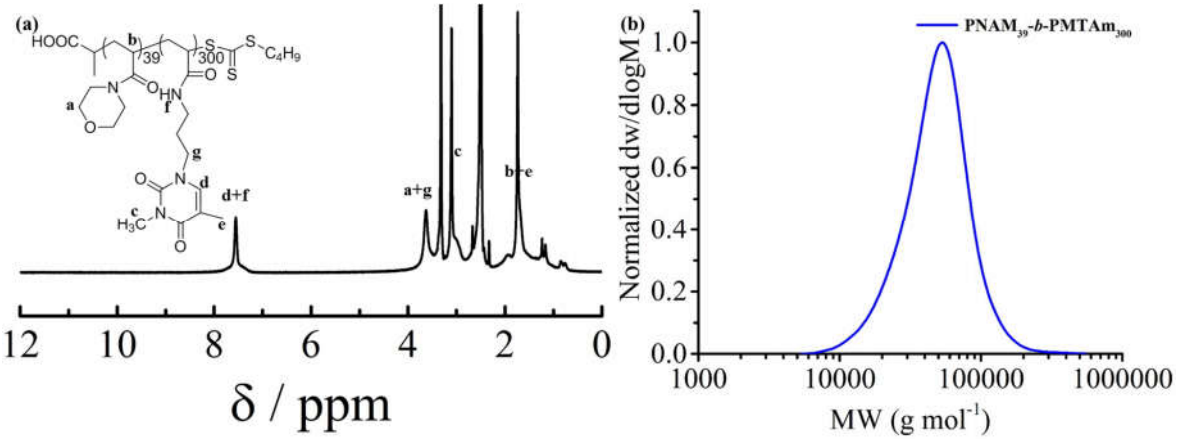

Figure 3.11. (a) ^{1}H NMR spectra of **PT^{Me}** (PNAM$_{39}$-*b*-PMTAm$_{300}$) by ^{1}H NMR spectroscopy (400 MHz) in deuterated DMSO; (b) SEC traces of **PT^{Me}** (PNAM$_{39}$-*b*-PMTAm$_{300}$) by DMF SEC, with poly(methyl methacrylate) (PMMA) standards.

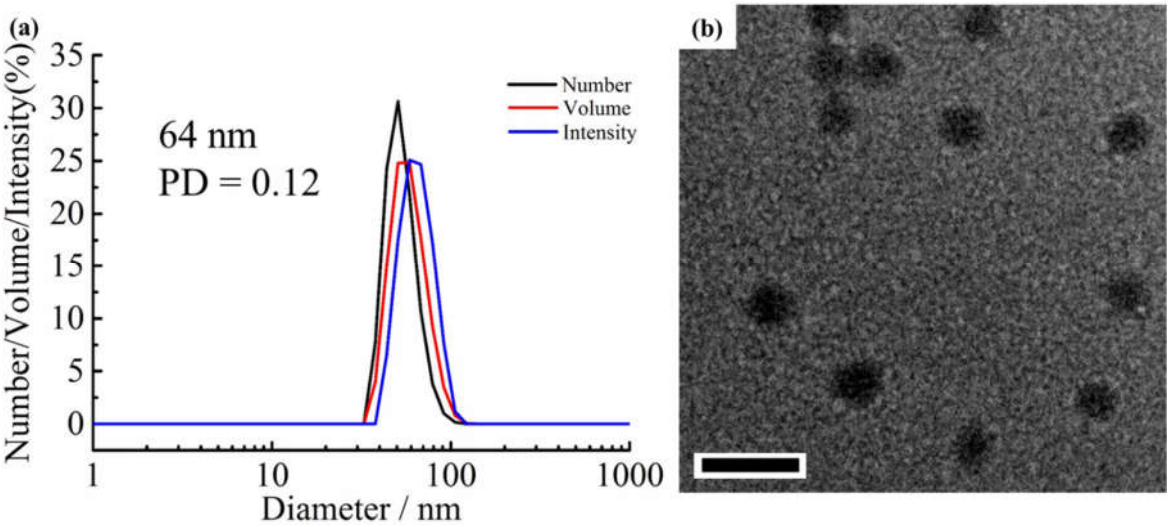

Figure 3.12. (a) DLS analysis of micelle **MT^{Me}** in water; (b) TEM images of micelle **MT^{Me}**; scale bar = 200 nm.

Likewise, TEM images and DLS analyses showed that no morphological transition was triggered by adding **PA1** once the micelle core was made of methylated thymine T^{Me} (Figure 3.13).

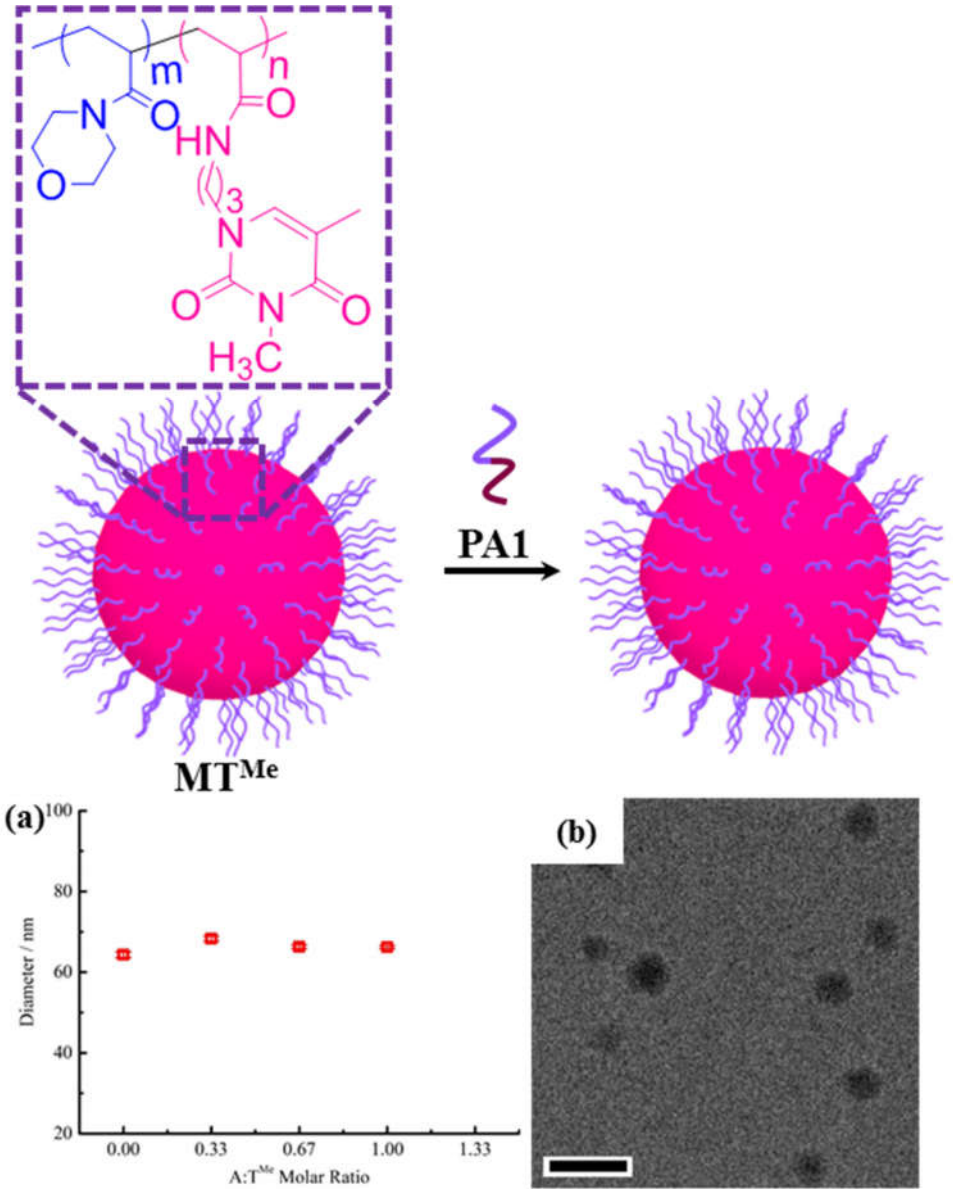

Figure 3.13. No morphological transitions were induced by non-complementary diblock copolymers through hydrophobic effects. (a) Variation of hydrodynamic diameter of the mixture of micelle $\mathbf{MT^{Me}}$ with non-complementary copolymers **PA1** as determined by DLS analyses; (b) dry-state TEM images of micelles $\mathbf{MT^{Me}}$ after adding **PA1** with molar ratios of $\mathbf{A{:}T^{Me}}$ = 1.00; scale bar = 200 nm.

These results strongly suggested that hydrophobic effects between added polymers and the initial micelle could not lead to morphological transitions. The micelle with a thymine-containing core shows a selective morphological transition only when triggered by specific polymers containing a complementary adenine block.

3.4.3. The mechanism of the morphological transitions

In order to explore the morphological transition mechanism, atomic force microscopy (AFM) was used to image the obtained nanoparticles. Compared with TEM analyses, AFM images can give the heights of nanoparticles, providing more useful information about the morphological change. Figure 3.14 shows that the micelle changes from spheres (with average height of 38 nm) to dumbbells (with average height of 23 nm) after adding **PA1** at a molar ratio of **A:T** 0.20 (Figure 3.14a and 3.14b). Worm-like micelles were formed with an average height of *ca.* 12 nm and a length of over 200 nm, when the molar ratio of **A:T** was 0.33.

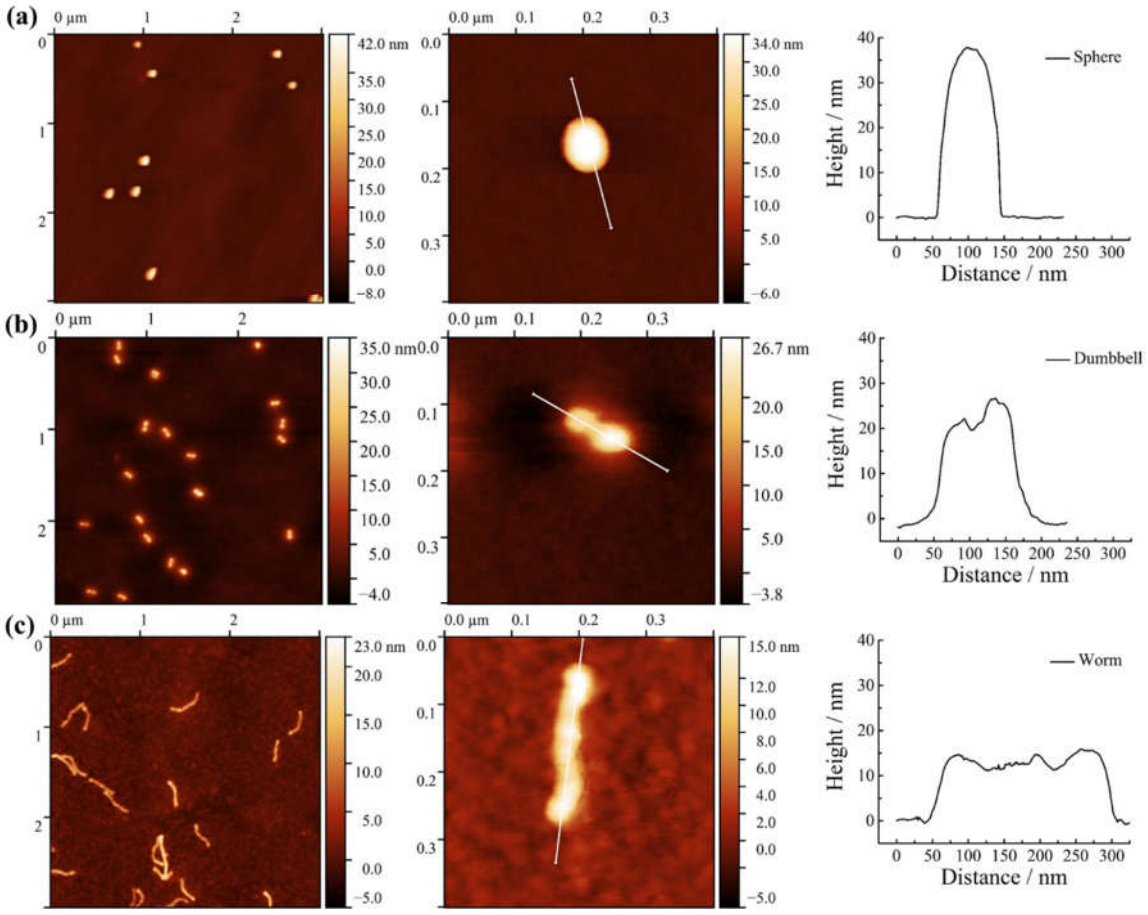

Figure 3.14. AFM analyses of **MT1** micelle after adding **PA1** with different molar ratios of **A:T**. (a) 0, (b) 0.07, (c) 0.20. Micelles with different morphologies were prepared through mixing complementary **PA1** solution into the initial spherical micelle **MT1** under stirring at room temperature. The micelle solutions (0.1 mg mL^{-1}) were drop cast on silicon surface for AFM imaging. The average height was obtained from the measurement of at least 10 micelles.

The morphological changes of block copolymer micelles have been widely studied, especially the transition from spherical micelles to worm-like micelles.[24] Most of these transitions are triggered by the change of core-medium interfacial tension. A spheres to worms transition may happen if the shell cannot effectively stabilize the interfacial tension. The morphological transition can normally be accounted for by one or a combination of the following two mechanisms. Mechanism 1: spherical micelles dissociate into unimers, and the unimers self-assemble again into worms; mechanism 2: core-core fusion of spherical micelles leads to the formation of worms. However, neither of these mechanisms may be able to explain the phenomena observed in our system. Firstly, the lack of heating and/or good solvent conditions in this

system significantly likely hindered the escape of a unimer from the initial micelle **MT1**.[37] Moreover, **MT1** is composed of a diblock copolymer with an exceedingly long hydrophobic block and a short hydrophilic block, which, to some extent, limits the dissociation of initial micelles into unimers. Secondly, the newly formed dumbbells only consist of two small spheres, which both have a height of *ca.* 23 nm. If the morphological transition was induced by the core-core fusion, two or more spheres would likely collide and fuse. Besides, the newly-formed fused micelles should have the similar height as the parent spheres, which have a height of *ca.* 38 nm. This result suggests the transition is not induced by the micelle core-core fusion. Based on the specific complementary H-bonding interactions between the added polymer **PA1** and the micelle **MT1**, we hypothesize that the morphological change observed for our system is a single micellar transformation. In this scenario, the added complementary copolymers inserted into the initial micellar core and increased the repulsion in both corona and core, leading to a morphological change.

Both TEM and AFM analyses provide direct information about the transformable properties of the micelle **MT1** through specific H-bonding interactions. However, both techniques may not necessarily be representative of the whole particle size distribution, as both assessments are restricted to a few hundred particles observed. In contrast, static light scattering (SLS) is a more statistically robust characterization technique, since the scattering is averaged over millions of particles. The monodispersities of both spheres and dumbells make it possible to analyse them using SLS (Figure 3.4 and 3.15). The initial spherical micelle **MT1** gave an average M_w of 63.4×10^6 Da, which is smaller than the one of dumbells, 68.7×10^6 Da (Table 3.2). A slight increase of molecular weight of dumbells further validates the insertion of the complementary **PA1** into **MT1** through complementary H-bonding interactions, which is in consistent to AFM characterization.

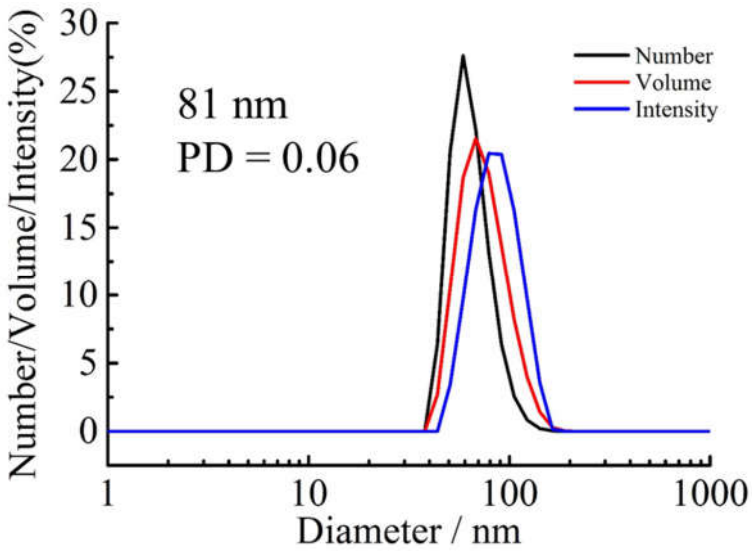

Figure 3.15. DLS analysis of **MT** micelles after adding **PA1** with the molar ratios of **A:T** = 0.20.

Table 3.2. Summary of SLS characterization of **MT1** and **MT1** with **PA1** (**A:T** = 0.20).

Sample	$\bar{M}_W/10^6\ Da$	$\langle R_G\rangle/10^{-9}m$	$\langle R_H\rangle/10^{-9}m$	$\langle R_G\rangle/\langle R_H\rangle$
MT1	63.4	30.8	38.2	0.81
MT1 with **PA1** (**A:T** = 0.20)	68.7	44.9	45.5	0.99

Notably, the phenomenon observed in our system is analogous to the living CDSA of crystalline copolymers. In the CDSA process, the newly added copolymers can only grow along the exposed lattice facet of the seeded micelle through energetically favourable crystallization. In contrast, the added complementary copolymers in our system can insert into the core of the seeded micelles through complementary H-bonding interactions. In order to further validate the programmable transition of this transformable micelle, we monitored the morphological changes in solution by using cryo-TEM. Considering both TEM and AFM images were obtained from dry-stated samples, they might contain artefacts during the sample preparation. Figure 3.16a illustrates that well-defined spherical micelles were obtained for the self-assembled micelle **MT1**. The intermediate state of the morphological transition,

dumbbell-like micelles were clearly observed when the initial spherical micelles were inserted with **PA1** (**A:T** = 0.20) (Figure 3.16b). Within the dumbbell-like micelles, more **PA1** was introduced to make in total **A:T** molar ratio 0.33. Indeed, Figure 3.16c indicated that well-defined long worms propagated from the dumbbell-like micelles. Based on the above results, we can confirm that the thymine-containing micelle can undergo a single micellar transition from spheres to dumbbells then to worms through inserting complementary copolymers.

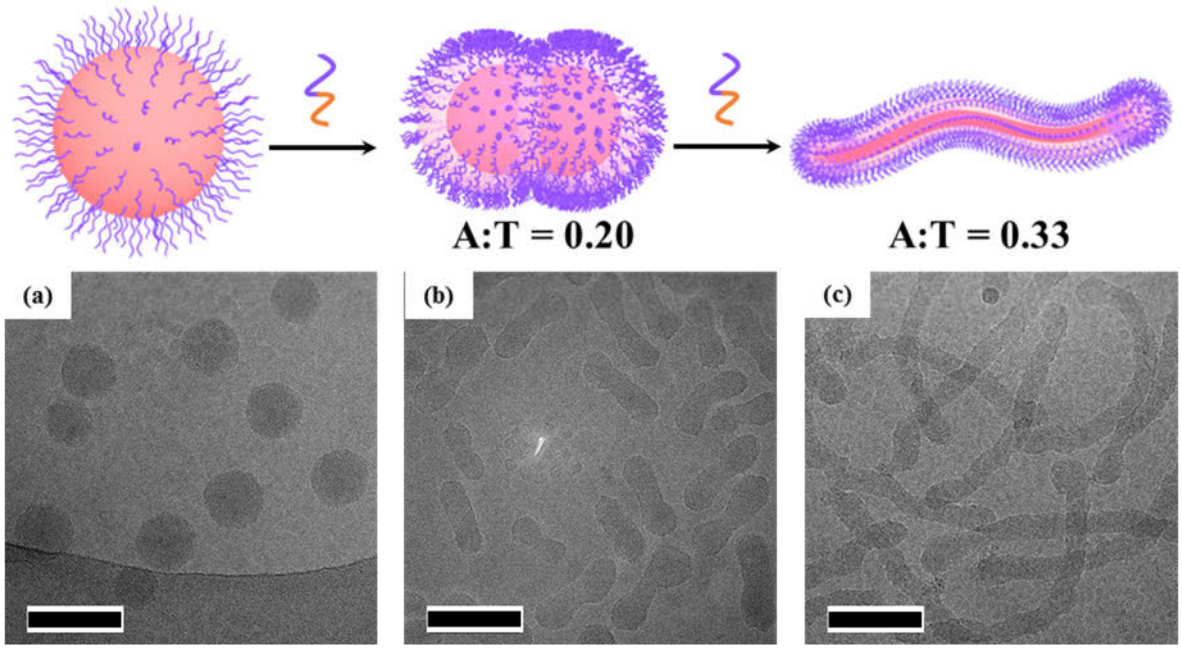

Figure 3.16. Morphological change from (a) spheres **MT1** to (b) dumbbells (**A:T** = 0.20) then to (c) worms (**A:T** = 0.33) by adding complementary copolymers validated by cryo-TEM imaging; scale bars = 100 nm.

3.4.4. Pathway-dependent morphological transitions

In the current system, the mixture of **PT1** and **PA1** can also self-assemble into micelles through a solvent switch method. **PT1** and **PA1** with different molar ratios of **A:T** (0.33, 0.67 and 1.00) were mixed in DMF and then water was slowly added. The formed micelle solutions were dialyzed and characterized by

TEM analyses. However, the shapes of formed micelles are all spherical and the sizes range from 49 ± 5 nm to 30 ± 5 nm (Figure 3.17).

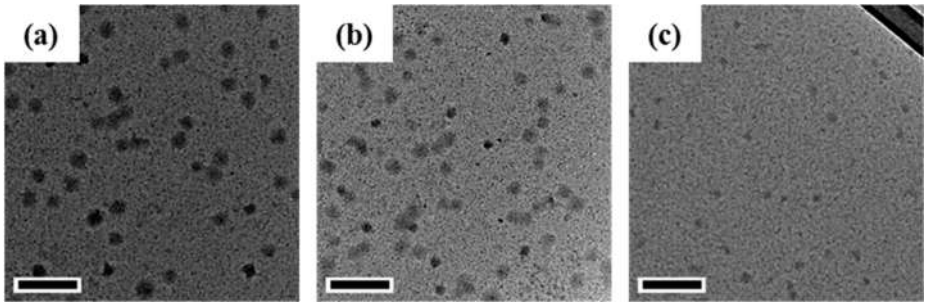

Figure 3.17. TEM images of micelles consisting of **PA1** and **PT1** prepared through a solvent switch method with different molar ratios of **A:T**. (a) 0.33; (b) 0.67; (c) 1.00; scale bars = 200 nm.

As reported before, 'frozen' nanoparticles remarkably rely on different preparation routes.[38] If exchange of polymer chains was kinetically trapped, the same polymers can form different aggregates by using different self-assembly routes. There is no obvious reorganization occurred when heating the micelle from 15 to 60 °C from DLS analyses, further confirming the formation of 'frozen' nanoparticles (Figure 3.18).

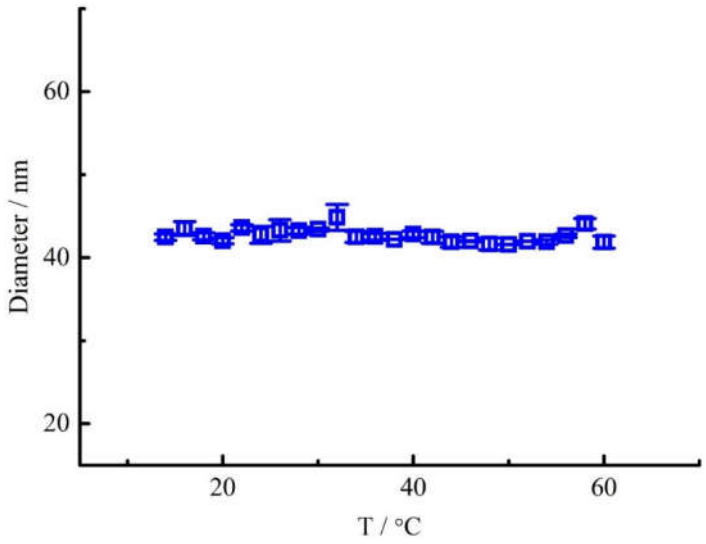

Figure 3.18. Variation of the hydrodynamic diameter of the micelle consisting of **PA1** and **PT1** (**A:T** = 1.00) with temperature as determined by DLS.

When directly adding different molar ratios of complementary copolymers into the initial micelle, morphological transitions from spheres to dumbbells or worms were observed. We propose that the slow addition of complementary copolymers might generate better-defined nanoparticles than by directly adding one to a solution of micelle to its complement. In this experiment, the complementary copolymer **PA1** solution was added into the initial micelle solution stepwise. Specifically, complementary copolymers **PA1** (0.07 molar ratio **A** relative to **T**) were added into the micelle **MT1** solution (0.5 mg mL^{-1}) and stirred for at least 2 h. Then, another equivalent of complementary copolymer **PA1** solution (0.07 molar ratio **A** relative to **T**) was added. After adding 5, 10 and 15 times in total, complementary copolymers **PA1** with 0.33, 0.67 and 1.00 molar ratios **A** relative to **T** were added into the initial micelle **MT1**. Interestingly, spherical micelles with gradually increasing sizes were obtained and no morphological transitions were observed when using this method. When adding complementary copolymers **PA1** with **A:T** molar ratio of 0.33, TEM image shows the average size of obtained nanoparticles was approximately 77 ± 13 nm (Figure 3.19a). Figure 3.19b and 3.19c shows that the sizes further increase to 94 ± 14 and 101 ± 16 nm respectively, after introducing complementary copolymers with 0.67 and 1.00 molar ratios **A** relative to **T** in total. Meanwhile, DLS analyses also indicated the sizes of the relevant micelles gradually increased from 77 nm to 112 nm by introducing complementary copolymers (Figure 3.19d).

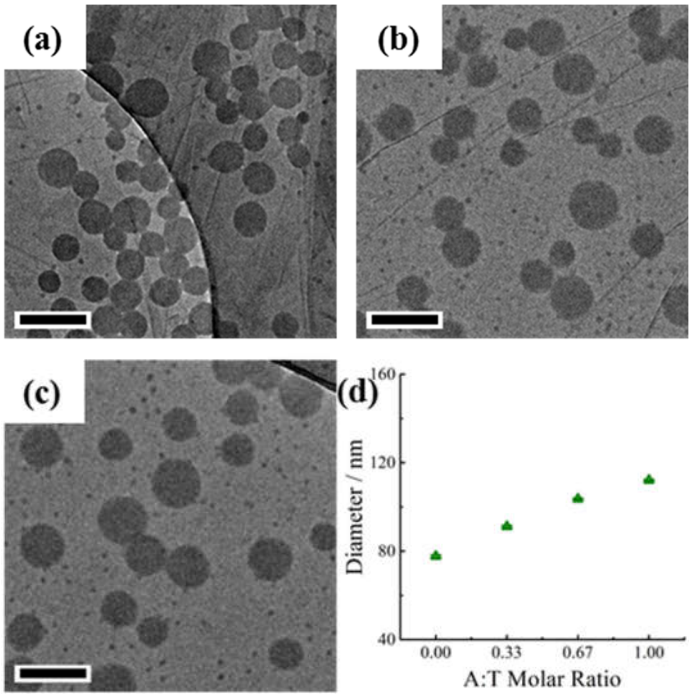

Figure 3.19. TEM images and DLS analyses of micelle **MT1** after stepwise addition of **PA1** with different molar ratios of **A:T**. Dry-state TEM images on graphene oxide of micelle **MT1** after adding **PA1** with different **A:T** molar ratios: (a) 0.33; (b) 0.67; (c) 1.00; scale bars = 200 nm. (d) Variation of hydrodynamic diameters of the mixtures of micelle **MT1** with complementary copolymers **PA1** by adding stepwise as determined by DLS analyses

Compared with the direct addition of different molar ratios of complementary copolymers, the immediate concentration of **PA1** after slow addition (with **A:T** molar ratio of 0.07) is lower. Similar to our previous publication,[27] **PA1**, when dispersed in water, can form small aggregates less than 10 nm (Figure 3.20a). In order to monitor the critical micelle concentration (CMC) of **PA1** in water, a series of **PA1** solutions at different concentration were measured by DLS. Below the CMC, the scattering light intensity detected from each concentration was similar to that obtained from water. Once the CMC was reached, the intensity of scattered light increased and the intersection between the 2 lines gave the CMC concentration of **PA1** *ca.* 0.09 mg mL^{-1} (Figure 3.20b). This value is higher than the concentration of **PA1** (0.07 mg mL^{-1}) mixed with **MT1** with **A:T** molar ratios of 0.07. Therefore, once complementary copolymer **PA1** with **A:T** molar ratios of 0.07 was added, the disassembled unimers could only insert into the micelle **MT1** and could not increase the interfacial repulsion enough to promote the morphological transition. In stark contrast, if

complementary copolymer **PA1** with **A:T** molar ratios over 0.20 was added, the quicker insertion of **PA1** can significantly fasten the change the interfacial tension to trigger the morphological transitions. With the slow addition of **PA1**, the gradually swelling micelle **MT1** core can accommodate more and more complementary copolymers without leading to the remarkable increase of interfacial tensions. Hence, larger and larger spheres were generated and no worms were formed.

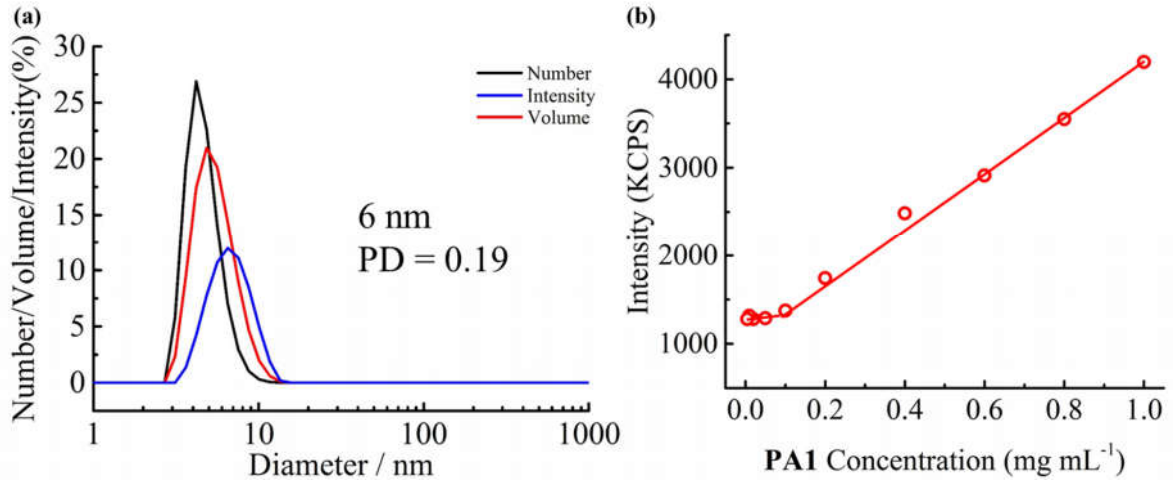

Figure 3.20. (a) DLS analyses of small aggregated formed in water by **PA1**; (b) A plot of the scattered light intensity obtained for various concentrations of **PA1** in water. The intersection of the two lines at *ca.* 0.09 mg mL^{-1} corresponds to the critical micelle concentration (CMC).

3.4.5. The effect of chain length on morphological transitions

The main factors that influence the morphological transitions in the current system are the core-chain stretching and corona chain repulsion caused by the inserted complementary copolymers. These factors can be effectively tuned by changing the lengths of the added complementary copolymers. The initial study was focused on the **PA1**, which has DPs of the hydrophobic and hydrophilic blocks about 40 and 20, respectively. In order to investigate the effect of hydrophobic block on morphological transitions, two diblock copolymers $PNAM_{39}$-*b*-$PAAm_{10}$ (**PA2**) and $PNAM_{39}$-*b*-$PAAm_{30}$ (**PA3**) with slightly shorter and longer PAAm blocks were prepared as shown in Figures 3.21 and 3.22.

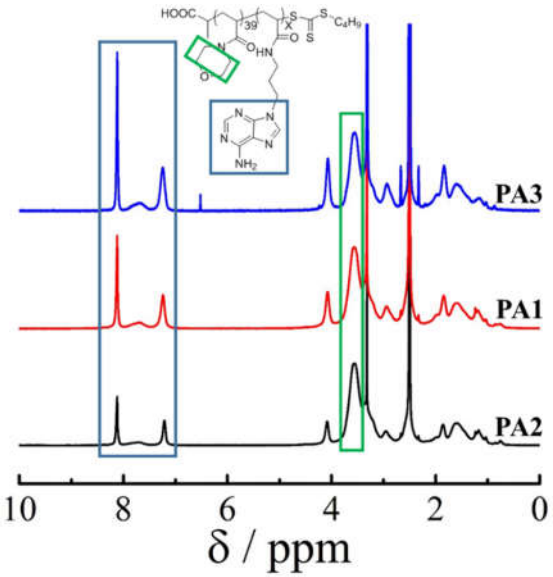

Figure 3.21. ^{1}H NMR spectra of **PA1** (PNAM$_{39}$-*b*-PAAm$_{20}$), **PA2** (PNAM$_{39}$-*b*-PAAm$_{10}$) and **PA3** (PNAM$_{39}$-*b*-PAAm$_{30}$) with different lengths of the hydrophobic block by ^{1}H NMR spectroscopy (400 MHz) in deuterated DMSO.

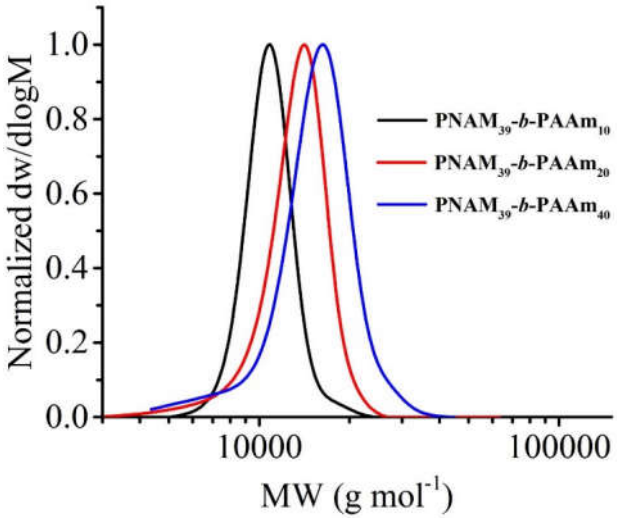

Figure 3.22. SEC traces of **PA1** (PNAM$_{39}$-*b*-PAAm$_{20}$), **PA2** (PNAM$_{39}$-*b*-PAAm$_{10}$) and **PA3** (PNAM$_{39}$-*b*-PAAm$_{30}$) with different lengths of the hydrophobic block by DMF SEC, with poly(methyl methacrylate) (PMMA) standards.

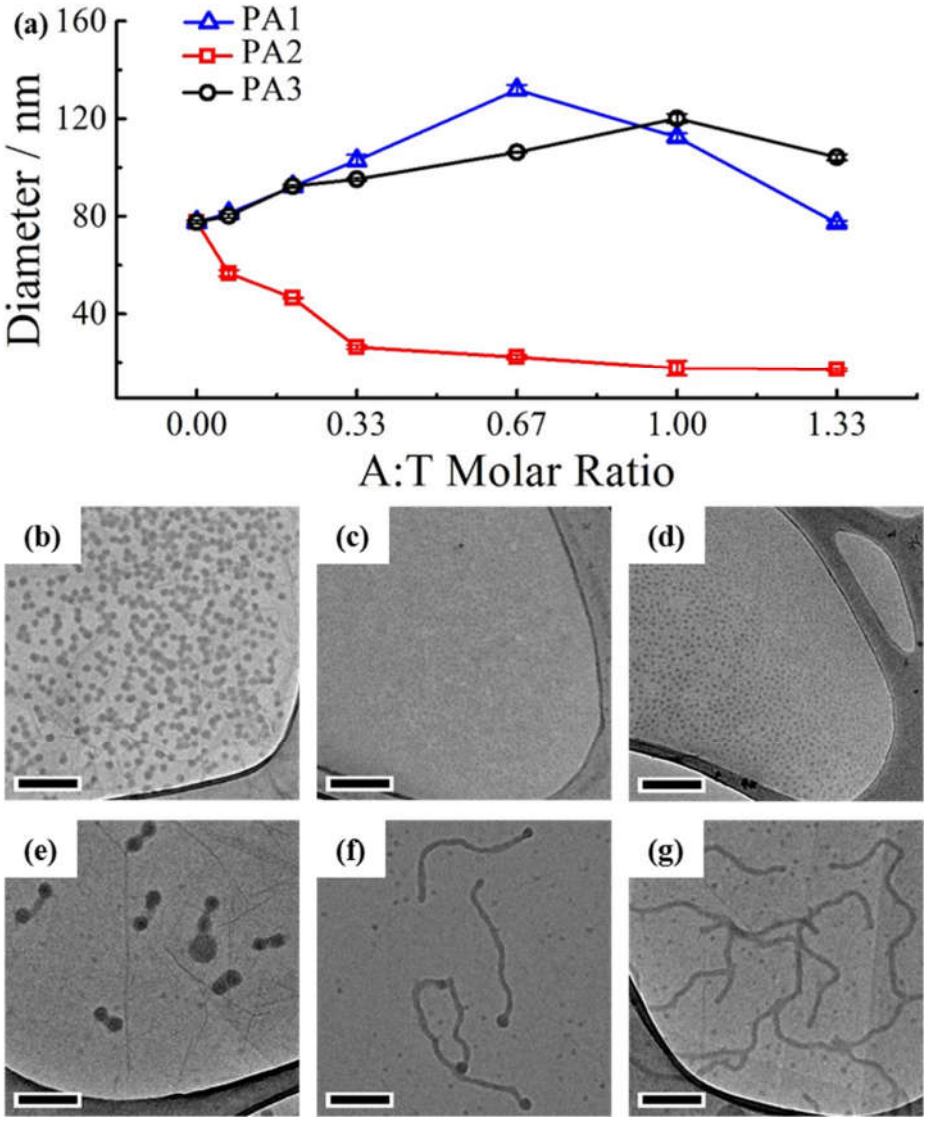

Figure 3.23. DLS analyses and TEM images of micelle **MT1** after adding complementary copolymers **PA2** and **PA3** with different hydrophobic chain lengths at different molar ratios of **A:T**. (a) Variation of hydrodynamic diameters of the mixtures of micelle **MT1** with complementary copolymers **PA1-3** as determined by DLS analyses. Dry-state TEM images on graphene oxide of micelle **MT1** after adding (b-d) **PA2** and (e-g) **PA3** with different **A:T** molar ratios: (b, e) 0.33; (c, f) 0.67; (d, g) 1.00; scale bars = 200 nm.

Intriguingly, when **PA2** was added into the initial micelle **MT1**, the sizes of the micelles gradually decreased as illustrated by Figure 3.23a. DLS analyses show a gradual decrease of the hydrodynamic diameters from 78 nm for **MT1** to 27 and 18 nm with **A:T** molar ratios 0.33 and 1.00, respectively. TEM images also confirmed that the sizes decreased with introducing more complementary copolymers and the shapes of all micelles were spherical in nature (Figure 3.23b-d). **PA2**, which has a shorter PAAm

block, likely has much weaker interactions with the core of micelle **MT1**. The size of the initial micelle probably decreased due to two main outcomes caused by the weaker interactions between **PA2** and **MT1**. The short hydrophobic block only slightly increased the core repulsion interactions, which was not enough to power the morphological transition to worms. In addition, the hydrophilic ratio is higher for the **PA2** with the same molar ratios of **A:T**, which increases the chain mobility. Therefore, increasingly smaller spherical micelles were formed as **PA2** was gradually introduced into the initial micelle **MT1**. In contrast, morphological transitions from spheres to worms were also observed when introducing **PA3** with a longer PAAm block into **MT1**. DLS analyses showed that the hydrodynamic diameters gradually increased (Figure 3.23a). As shown in Figure 3.23e-g, worms with different molar ratios of **A:T** by adding **PA3** were formed. Therefore, we can conclude that the minimum length of PAAm block is 20 to induce the morphological transition from spheres to worms.

In addition, the length of hydrophilic blocks also affects the corona chain repulsion caused by the inserted complementary copolymers. In order to explore the effect of corona chain repulsion on the morphological transitions of micelle **MT1**, two complementary copolymers $PNAM_{96}$-*b*-$PAAm_{20}$ (**PA4**) and $PNAM_{295}$-*b*-$PAAm_{20}$ (**PA5**) with longer hydrophilic blocks were introduced into the micelle **MT1** (Table 3.1 and Figures 3.24 and 3.25).

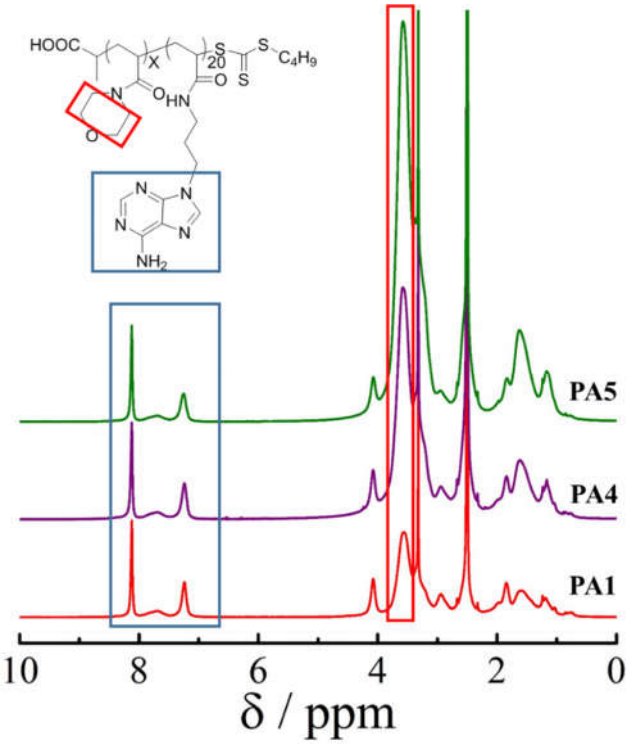

Figure 3.24. ^{1}H NMR spectra of **PA1** (PNAM$_{39}$-*b*-PAAm$_{20}$), **PA4** (PNAM$_{96}$-*b*-PAAm$_{20}$) and **PA5** (PNAM$_{295}$-*b*-PTAm$_{20}$) with different lengths of the hydrophobic block by ^{1}H NMR spectroscopy (400 MHz) in deuterated DMSO.

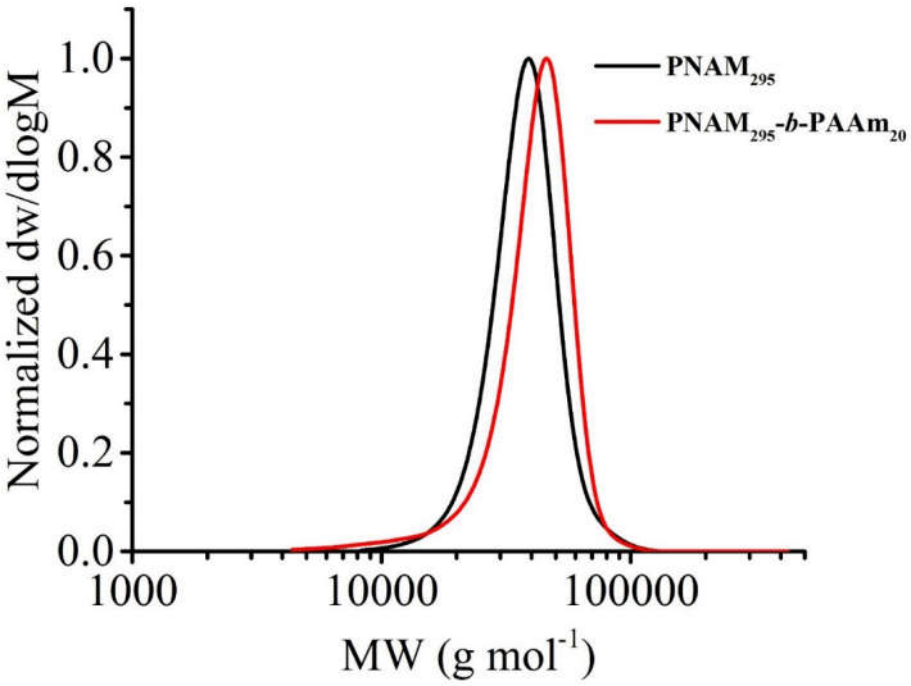

Figure 3.25. SEC traces of PNAM$_{295}$ and **PA5** (PNAM$_{295}$-*b*-PAAm$_{20}$) analyzed by DMF SEC, with poly(methyl methacrylate) (PMMA) standards.

Figure 3.26a suggests that the sizes of micelles increased initially when mixing complementary copolymers **PA4** or **PA5** with the initial micelle **MT1**. In contrast to **PA1**, the peaks were shifted for less complementary copolymers, *i.e.* the maximum hydrodynamic sizes are **A:T** molar ratios of 0.33 for **PA4** and 0.07 for **PA5**. The increased hydrophilic chain lengths dramatically enhanced the chain mobility when complementary chains were combined. TEM images show that worms were formed when **A:T** molar ratios for both polymers are 0.33 (Figure 3.26b and 3.26e). In contrast, much longer worms were obtained when the hydrophilic chain of complementary copolymers was shorter. Hence, we can effectively tune the lengths of worm-like micelles by adding different complementary copolymers into the same initial spherical micelles. Mixtures of worms and spheres or pure small spheres were observed when adding more complementary copolymers (Figure 3.26c-d and 3.26f-g). Meanwhile, the slow addition and direct addition of **PA3-5** gave rise to similar results of the morphological transitions, which might be caused by the larger core or corona repulsions due to the longer hydrophobic or hydrophilic chain lengths (Figures 3.27 and 3.28).

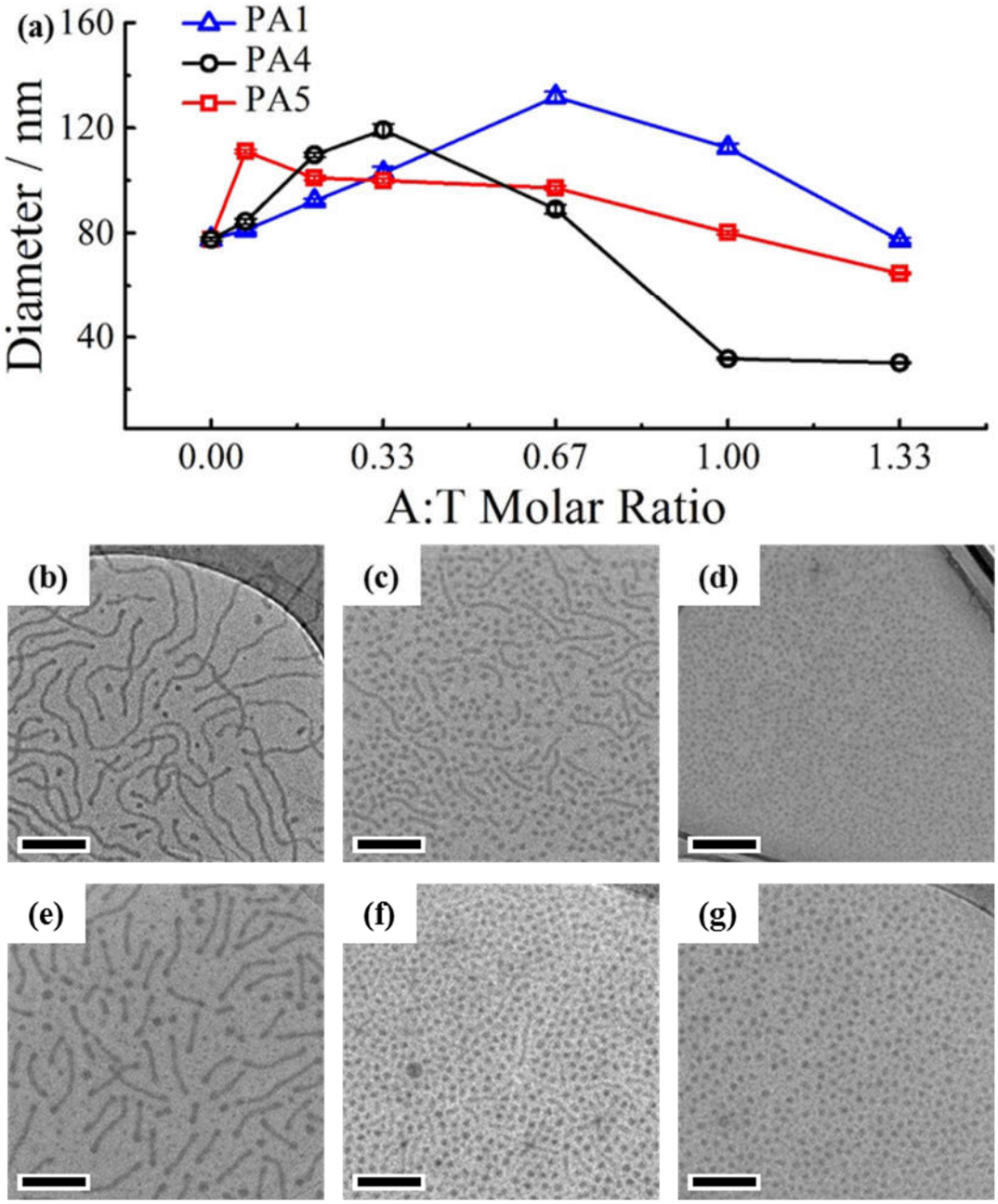

Figure 3.26. DLS analyses and TEM images of micelle **MT1** after adding complementary copolymers **PA4** and **PA5** with different hydrophilic chain lengths at different molar ratios of **A:T**. (a) Variation of hydrodynamic diameters of the mixtures of micelle **MT1** with complementary copolymers **PA4-5** as determined by DLS analyses. DLS analyses of **PA1** was also shown for comparison. Dry-state TEM images on graphene oxide of micelle **MT1** after adding (b-d) **PA4** and (e-g) **PA5** with different **A:T** molar ratios: (b, e) 0.33; (c, f) 0.67; (d, g) 1.00; scale bars = 200 nm.

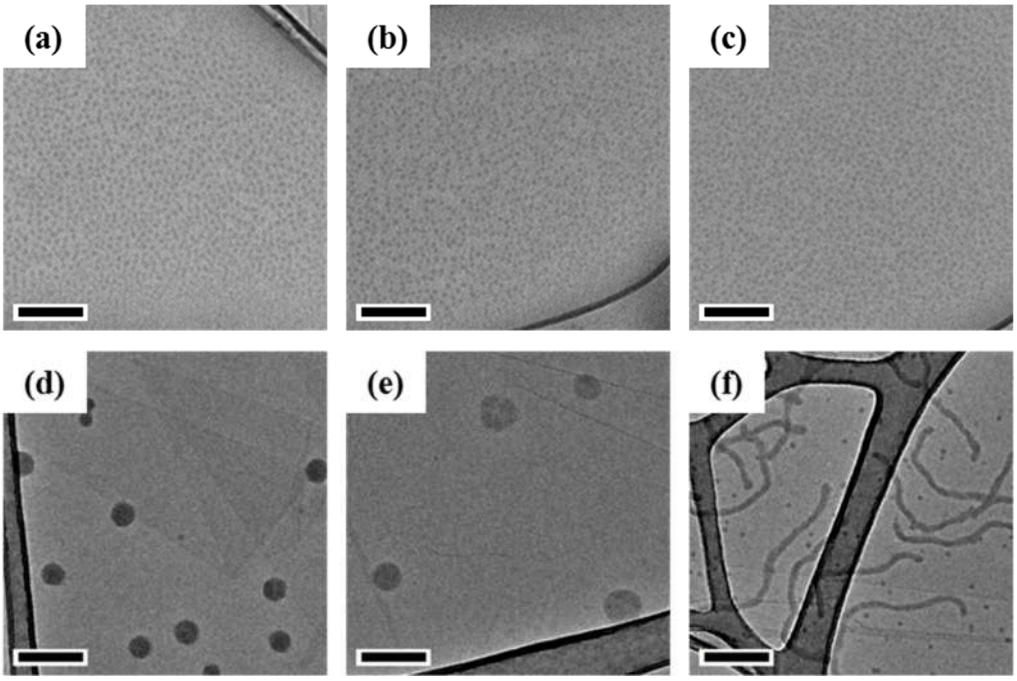

Figure 3.27. TEM images and DLS analyses of micelle **MT1** after stepwise adding (a-c) **PA2** and (d-f) **PA3** with different molar ratios of **A:T**: (a, d) 0.33; (b, e) 0.67; (c, f) 1.00; scale bars = 200 nm.

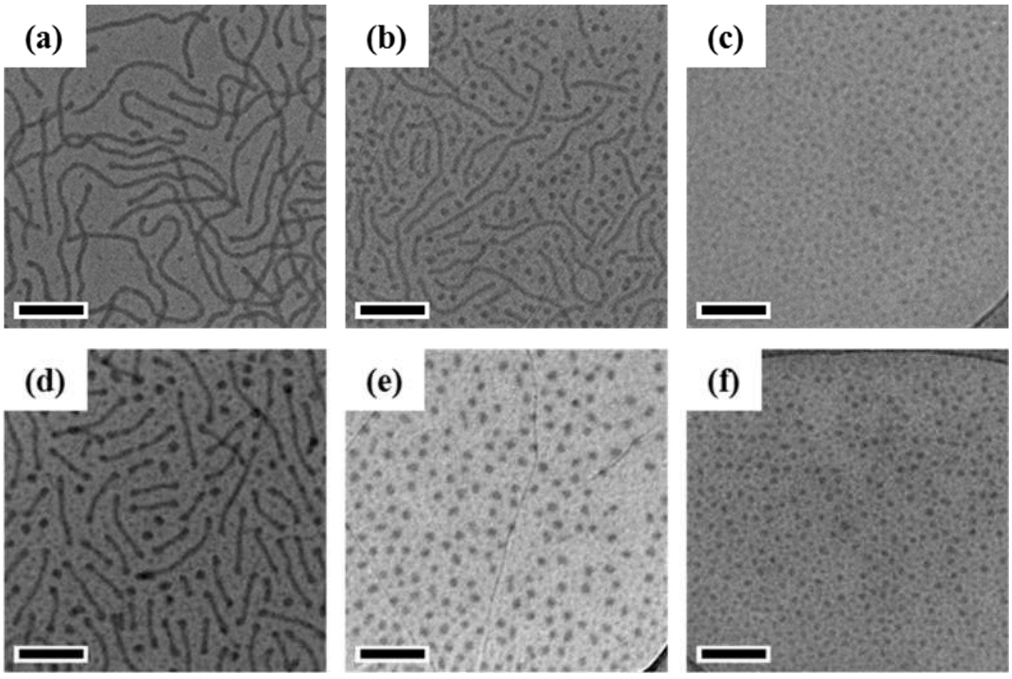

Figure 3.28. TEM images and DLS analyses of micelle **MT1** after stepwise adding (a-c) **PA4** and (d-f) **PA5** with different molar ratios of **A:T**: (a, d) 0.33; (b, e) 0.67; (c, f) 1.00; scale bars = 200 nm.

We are also interested in exploring whether the hydrophobic/hydrophilic ratio determines the morphological transitions. Intriguingly, no morphological transition was observed by adding **PA4** and **PA5** at a **A:T** molar ratio of 0.07 (Figure 3.29). Even if the volume ratio of the hydrophilic block in **PA5** of **A:T** molar ratio of 0.07 equals to that of 0.5 in **PA1**, still larger spherical micelles were obtained. The relatively subtle change in volume fraction was not sufficient in this case to outweigh the other factors. When **A:T** molar ratios are both 0.20 for **PA4** and **PA5**, worms were generated for both systems. Therefore, the most important factor that determined the morphological transition was the core-chain repulsion. On the other hand, the obtained stable morphologies were influenced by the core-corona volume ratios. The higher volume ratios of hydrophilic blocks in **PA4** and **PA5** compared with **PA1** gave rise to the formation of shorter worms.

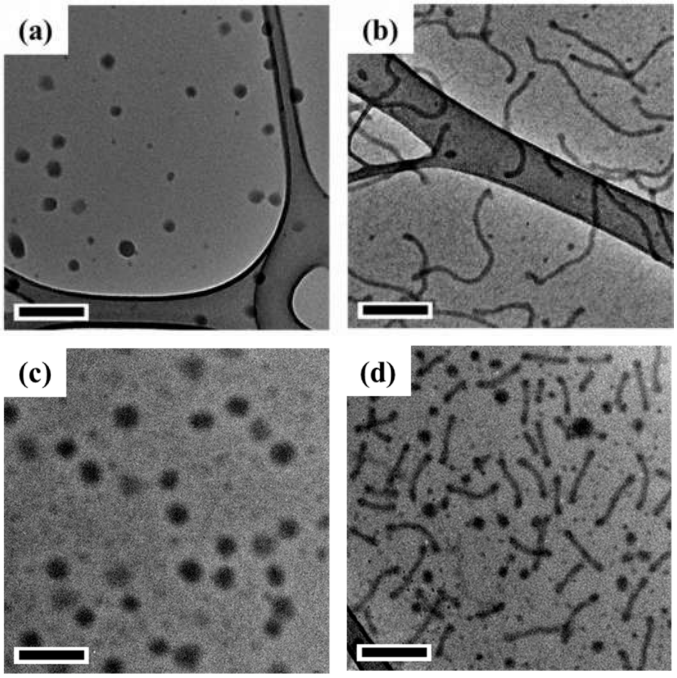

Figure 3.29. TEM images of micelle **MT1** after adding (a-b) **PA4** and (c-d) **PA5** consisting of different hydrophilic chain lengths with different **A:T** molar ratios: (a, c) 0.07; (b, d) 0.20; scale bar = 200 nm.

3.4.6. Controlled "living" growth mediated by complementary H-bonding interactions

Controlled "living" growth of anisotropic materials enables access to a wide range of complex hierarchial nanostructures. Recent advances in the solution crystallization of polymers such as poly(ferricenyldimethylsilane) (PFS), polylactide (PLA) and poly(ε-caprolactone) (PCL) block copolymers allow significant control over the formation of both 1D and 2D by crystallization-driven self-assembly (CDSA).[10, 39-41] To the best of our knowledge, successful "living" growth could only be achieved by CDSA using crystalline or semi-crystalline polymers. Indeed, no precise control over micellar growth using other intermolecular forces, such as H-bonding or supramolecular interactions, has been reported.

The complementary H-bonding interactions within the micelle core make it possible to efficiently grow worms in water. Short seeded worms were fabricated by directly adding **PA1** with **A:T** molar ratios of 0.33 into the micelle **MT1** (Figure 3.30a). Epitaxial growth was then achieved by adding **PA1** stepwise in water without cosolvent at room temperature. Figure 3.30b-d shows that longer and thinner worms were transformed from the seeded worms. The contour lengths of the worms extended to over 1000 nm from the initial 300 nm as shown in Figure 3.30e. In contrast, the widths of the worms decreased from 22 nm to about 14 nm. These results represent a novel method to precisely make worm-like micelles with different lengths and widths through specific H-bonding interactions.

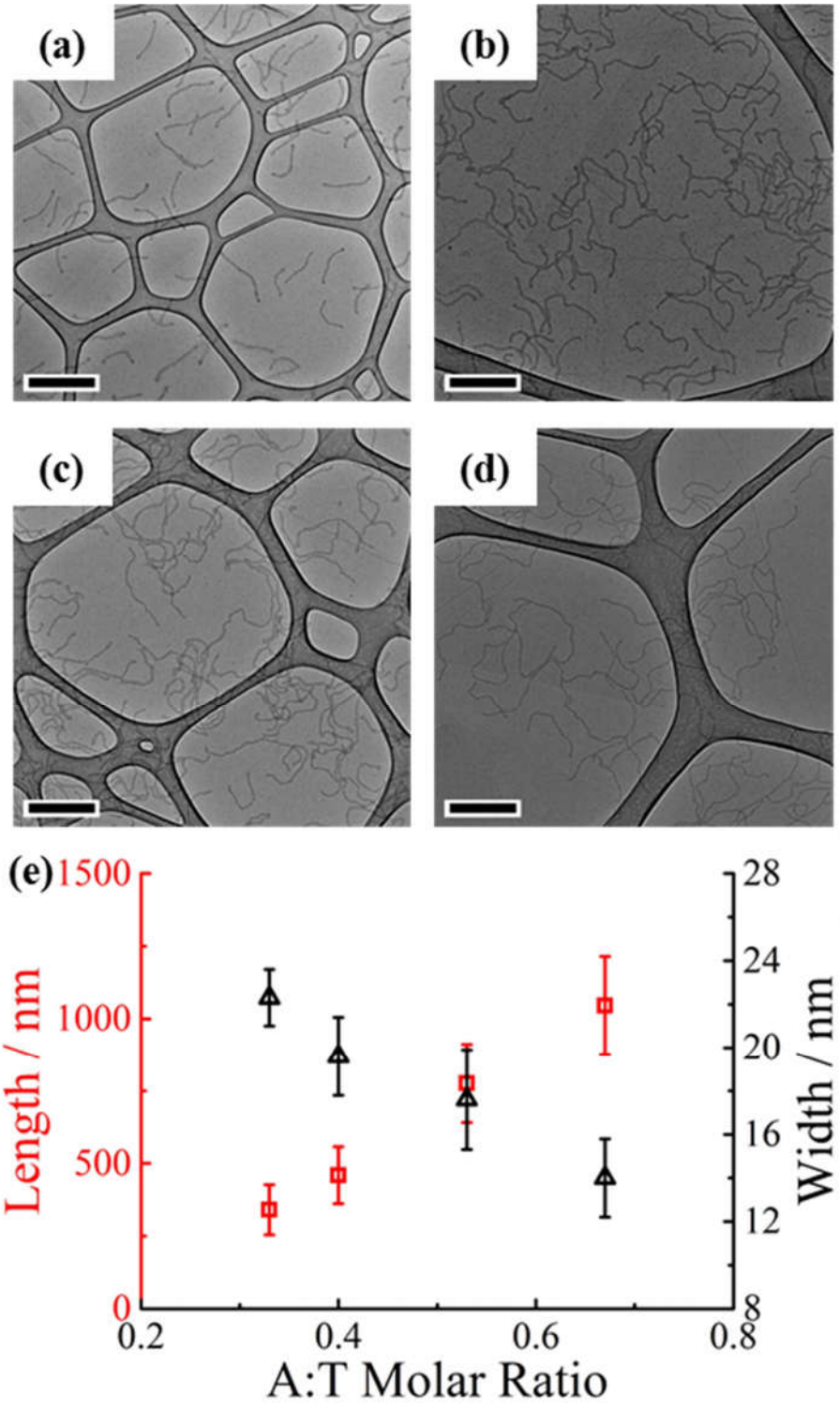

Figure 3.30. (a-d) Dry-state TEM images on graphene oxide of micelles after stepwise addition of **PA1** into the seeded micelle solution consisting of **MT1** micelle with **PA1** having **A:T** molar ratio of 0.33. **A:T** molar ratios in total: (a) 0.33; (b) 0.40; (c) 0.53; (d) 0.67; scale bars = 500 nm. (e) Analyses of contour lengths and widths of the worms in Figure 3.30a-d.

3.5. Conclusions

To summarize, spheres and worms of different sizes could be easily obtained through morphological transition of single initial spherical micelles. This kind of novel micelle contains a thymine core, which can undergo distinct morphological transitions depending on complementary adenine-containing diblock copolymers introduced. Hydrophobic effects alone could not effectively trigger the morphological transformations and only specific complementary H-bonding interactions were found to induce transitions. The morphological transitions from spheres to worms observed here follow a distinct mechanism, *i.e.* a single nanoparticle transformation, confirmed by AFM, SLS and cryo-TEM characterization. Meanwhile, morphological transitions observed also depend on the transformation pathway and show specific selectivity to the complementary chains introduced. More importantly, complementary H-bonding interactions within the micellar core enable us to precisely tune the lengths and widths of worm-like micelles. These important parameters of worms were difficult to be tailored by other approaches. We propose that this novel kind of living micelles allow us to precisely control these vital parameters of nanoparticles in aqueous media. In addition, we also anticipate that other supramolecular interactions can be introduced into the realm of controlled growth of living micelles.

3.6. Experimental section

3.6.1. Materials

2,2'-Azo-bis(isobutyronitrile) (AIBN) was obtained from Molekula and recrystallized from methanol. 2,2'-Azobis[2-(2-imidazolin-2-yl)propane]dihydrochloride (VA-044, Wako) was used without further purification. 4-Acryloylmorpholine (NAM) was bought from Aldrich and was purified by vacuum distillation. 2-(((butylthio)carbonothiolyl)thio)propanoic acid and $PNAM_{96}$-*b*-$PAAm_{20}$ (**PA4**) were synthesized as described previously and stored at 4 °C.[27] The p-silicon (100) wafers were purchased from Sigma-Aldrich and were cut into plates with a size of 10 mm × 10 mm for AFM imaging. Dialysis membranes (MWCO = 3.5 kDa) were purchased from Spectra/Por. DMF, DMSO and other chemicals were obtained from Fisher Chemicals and used without further purification. Dry solvents were obtained by passing over a column of activated alumina using an Innovative Technologies solvent purification system.

3.6.2. Instrumentation

^{1}H NMR spectra were recorded on a Bruker DPX-400 or HD500 spectrometer with DMSO-d_6 as the solvent. The chemical shifts of protons were relative to solvent residues (DMSO 2.50 ppm). Fourier transform infrared (FT-IR) spectra were obtained using a Perkin Elmer Spectrum 100 FT-IR. Scans from 550 to 4000 cm−1 were taken, and the spectra corrected for background absorbance. Size exclusion chromatography (SEC) data were obtained in HPLC grade DMF containing 5 mM NH_4BF_4 at 50 °C, with a flow rate of 1.0 mL min^{-1}, on a set of two PLgel 5 µm Mixed-D columns, and a guard column. SEC data were analyzed with Cirrus SEC software calibrated using poly(methyl methacrylate) (PMMA) standards. Preparative SEC was conducted using DMSO at 50 °C, with a flow rate of 0.5 mL min^{-1}.

Hydrodynamic diameters (D_h) and size distributions of the self-assemblies were determined by dynamic light scattering (DLS). The DLS instrumentation consisted of a Malvern Zetasizer NanoS instrument with a 4 mW He-Ne 633 nm laser module. Measurements were made at a detection angle of 173°, and Malvern DTS 7.03 software was used to analyze the data. D_h was calculated by fitting the apparent diffusion coefficient in the Stokes-Einstein equation $D_h = kT/(3\pi\eta D_{app})$, where k, T and η are the Boltzmann constant, the temperature and the viscosity of the solvent, respectively. Static light scattering (SLS) measurements were conducted with an ALV CGS3 (λ = 632 nm) at 25 °C. The data were collected from 50° to 130° with an interval of 5°.

TEM observations were performed on a JEOL 2100 electron microscope at an acceleration voltage of 200 kV. All TEM samples were prepared on graphene-oxide (GO)-coated lacey carbon grids (400 Mesh, Cu, Agar Scientific), to enable high contrast TEM images without any staining.[36] Generally, a drop of sample (10 µL) was pipetted on a grid and left for several minutes, then blotted away. TEM images were analyzed using the ImageJ software, and over 100 particles were counted for each sample to obtain number-average diameter D_n, length L_n and width W_n. AFM imaging and analysis were performed on an Asylum Research MFP3D-SA atomic force microscope in tapping mode. Samples for AFM analysis were prepared by drop casting 5 µL of solution (0.1 mg/mL) onto a freshly clean silicon wafer. The silicon wafer was washed with water and ethanol, then activated using plasma treatment to generate a hydrophilic surface.

3.6.3. Synthesis of 3-(*N*6, *N*6-dimethyladenine-9-yl)propyl acrylamide (MAAm)

To a suspension of *N*6, *N*6-dimethyladenine (0.16 g, 1.0 mmol) in dry DMF (5 mL), NaH (0.025 g, 1.05 mmol) was slowly added (Scheme 3.3). The mixture was stirred for 1 h until no gas was produced. The viscous mixture was immersed into an ice bath and 3-bromopropyl acrylamide freshly synthesized (0.23 g, 1.2 mmol) was added dropwise. The yellow viscous mixture was stirred overnight and the

resulting suspension was concentrated under vacuum. The obtained mixture was purified by column chromatography using a mixture of CH_2Cl_2 and CH_3OH as eluent and a gradient from 1:0 to 95:5 to give a white solid, MAAm (0.22 g, 80%). Assigned ^1H, ^{13}C NMR spectra are shown in Figure 3.31.

^1H NMR (500 MHz, DMSO-d_6) δ = 8.21 (s, 1H, purine *H*-2), 8.17 (s, 1H, purine *H*-8), 8.19 (t, *J* = 4.5 Hz, 1H, CON*H*), 6.20 (dd, *J* = 17.0 Hz, 10.0 Hz, 1H, CH_2=C*H*-CO), 6.07 (dd, *J* = 17.0 Hz, 2.0 Hz, 1H, C*H*$_2$=CH-CO), 5.59 (d, *J* = 10.0 Hz, 2.0 Hz, 1H, C*H*$_2$=CH-CO), 4.17 (t, 2H, *J* = 6.5 Hz, C*H*$_2$-purine) 3.45 (s, 6H, purine N-(C*H*$_3$)$_2$), 3.12 (q, 2H, *J* = 6.5 Hz, OC-NH-C*H*$_2$), 1.96 (m, 2H, *J* = 6.5 Hz, OC-NH-CH$_2$-C*H*$_2$-CH$_2$-purine) ppm.

^{13}C NMR (125 MHz, DMSO-d_6) δ = 165.1, 154.7, 152.2, 150.7, 140.2, 132.2, 125.6, 119.7, 41.4, 40.2, 36.3, 29.9 ppm.

FTIR (neat) ν_{max}/cm^{-1}: 3299 (H-N amide), 3109 and 3092 (H-C=C), 2975, 2956 and 2934 (CH$_3$-N), 1692 and 1625 (C=N purine), 1655 (C=O amide), 1569, 1548, 1484, 1454 and 1418 (C-N purine).

HR-MS (m/z) found 275.1616, calc. 275.1615 $[M+H]^+$.

Elemental analysis: Calculated (%) C 56.92, H 6.61, N 30.64; Found (%) C 56.86, H 6.88, N 30.65.

Melting point: 102-104 °C

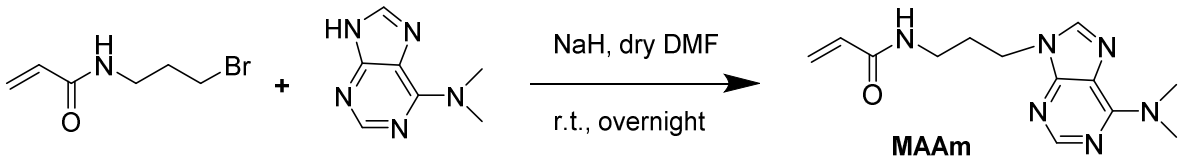

Scheme 3.3. The synthesis of 3-(*N*6, *N*6-dimethyladenine-9-yl)propyl acrylamide (MAAm).

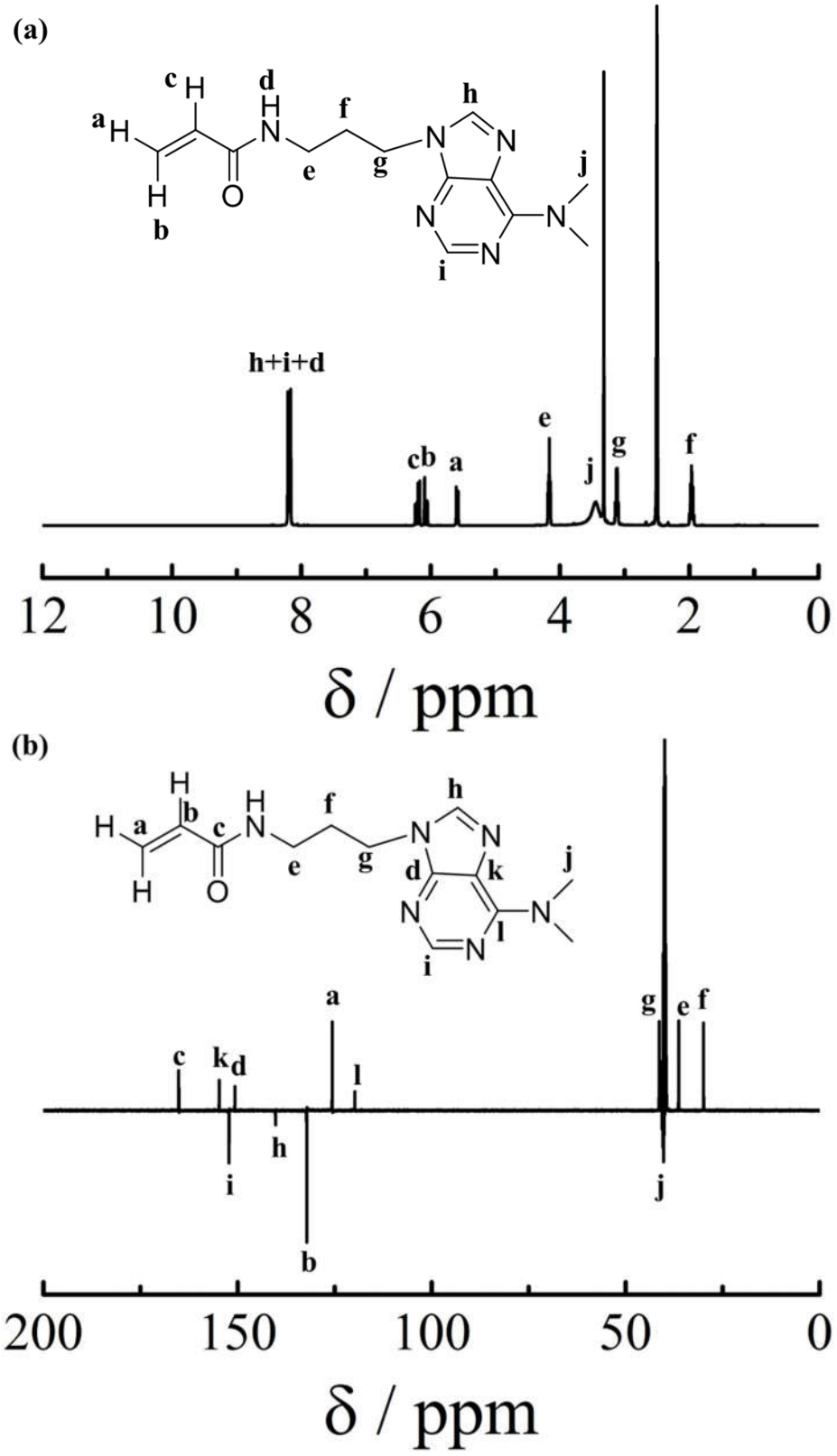

Figure 3.31. ^{1}H, ^{13}C NMR spectra of 3-(*N*6, *N*6-dimethyladenine-9-yl)propyl acrylamide (MAAm).

3.6.4. Synthesis of 3-(3-methylthymin-1-yl)propyl acrylamide (MTAm)

A mixture of 3-(thymin-1-yl)propyl acrylamide (TAm) (71 mg, 0.3 mmol), dry K_2CO_3 (66 mg, 0.48 mmol), iodomethane (75 µL) in anhydrous DMF (0.4 mL) was stirred at room temperature for 24 h, and then diluted with 20 mL ethyl acetate, washed with water (2 × 20 mL) and dried with anhydrous Na_2SO_4 (Scheme 3.4). The solvent was removed under vacuum. The mixture was further purified by column chromatography with a mixture of CH_2Cl_2/CH_3OH (95:5) to give a white solid (73 mg, 0.29 mmol, 97%). ^1H, ^{13}C NMR spectra are shown in Figure 3.32.

^1H NMR (500 MHz, DMSO-d_6) δ = 8.12 (t, J = 5.0 Hz, CON*H*), 7.59 (s, 1H, pyrimidine-H_6), 6.18 (dd, J = 17.5, 10.5 Hz, 1H, CH_2=C*H*-CO), 6.07 (dd, J = 17.5, 2.0 Hz, 1H, CH=CH_2-CO), 5.58 (dd, J = 10.5, 2.0 Hz, 1H, CH=CH_2-CO), 3.70 (t, 2H, J = 7.5 Hz, CH_2-pyrimidine), 3.17 (s, 3H, OC-NCH_3), 3.14 (m, 2H, OC-HN-CH_2), 1.80 (s, 3H, CH_3-pyrimidine), 1.76 (m, 2H, OC-NH-CH_2-CH_2-CH_2-pyrimidine) ppm.

^{13}C NMR (125 MHz, DMSO-d_6) δ = 165.1, 163.8, 151.5, 140.4, 132.2, 125.5, 107.9, 47.1, 36.3, 29.0, 28.0, 13.1 ppm.

FTIR (neat) ν_{max}/cm^{-1}: 3294 (H-N amide), 3066 (H-C=C), 2952 and 2937 (CH_3 pryimidine), 1693 and 1661 (C=O and C=C pyrimidine), 1637 (C=O amide).

HR-MS (m/z) found 274.1165, calc. 274.1162 $[M+Na]^+$.

Elemental analysis: Calculated (%) C 57.36, H 6.82, N 16.72; Found (%) C 57.45, H 6.89, N 16.71.

Melting point: 100-102 °C

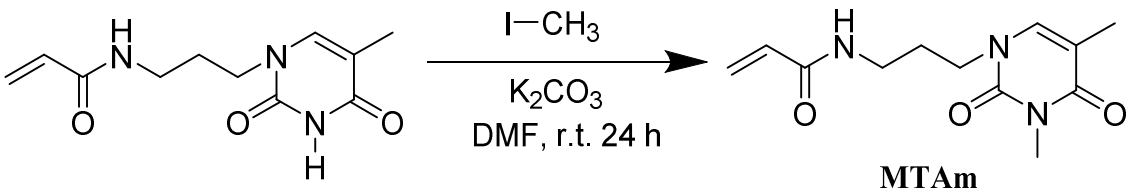

Scheme 3.4. Synthesis of 3-(3-methylthymin-1-yl)propyl acrylamide (MTAm).

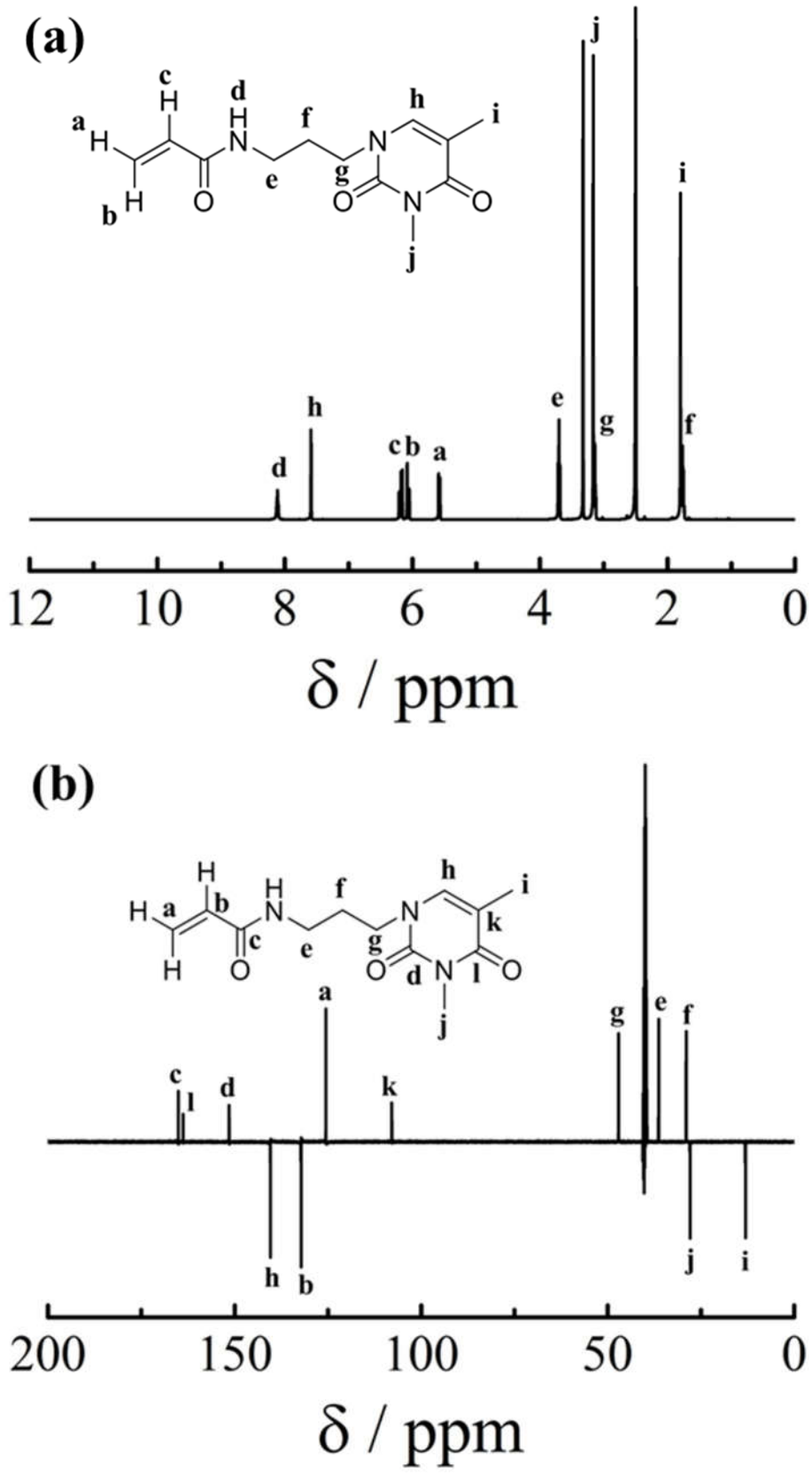

Figure 3.32. ^{1}H, ^{13}C NMR spectra of 3-(3-methylthymin-1-yl)propyl acrylamide (MTAm).

3.6.5. Synthesis of Poly(4-acryloylmorpholine) ($PNAM_{39}$ and $PNAM_{295}$) macro-CTA *via* RAFT polymerization.

The procedures are similar to our previous work.[27] The typical procedures are as follows. For $PNAM_{39}$, A 10 mL ampoule was charged with NAM (500 μL, 4.0 mmol), 2-(((butylthio)carbonothiolyl)thio)propanoic acid (23.8 mg, 0.1 mmol), VA-044 (1.3 mg, 0.004 mmol) and a mixture of 1,4-dioxane and water (2.0 mL, v:v 1:4). The mixture was thoroughly degassed *via* 4 freeze-pump-thaw cycles, filled with nitrogen and then immersed in an oil bath at 70 °C for 2 h. The polymerization solution was precipitated three times from cold CH_3OH. The light yellow polymer was dried in a vacuum oven overnight at room temperature and analyzed by ^1H NMR spectroscopy and DMF SEC. The degree of polymerization (DP) of this PNAM macro-CTA was calculated to be 39 using ^1H NMR spectroscopy by comparing the integrated signals corresponding to the backbone signals (δ = 1.62 ppm) with those of the methyl group from the CTA (δ = 0.87 ppm).

3.6.6. Synthesis of $PNAM_{39}$-*b*-$PTAm_n$, $PNAM_{39}$-*b*-$PMTAm_{300}$, $PNAM_x$-*b*-$PAAm_m$, $PNAM_{39}$-*b*-$PMAAm_{20}$ and $PNAM_{39}$-*b*-PSt_{20} diblock copolymers.

The typical procedures are as follows. For $PNAM_{39}$-*b*-$PTAm_{300}$, $PNAM_{39}$ (14 mg, 0.0025 mmol), TAm (178 mg, 0.75 mmol), and VA-044 (0.08 mg, 0.00025 mmol) were dissolved in a mixture of DMF and water (0.5 mL, v:v 1:1). The mixture was thoroughly degassed *via* 4 freeze-pump-thaw cycles, filled with nitrogen and then immersed in an oil bath at 70 °C overnight. An aliquot of the crude product was taken and analyzed by ^1H NMR spectroscopy to calculate the conversion. The degree of polymerization (DP) of obtained diblock copolymers was calculated using the conversion from ^1H NMR spectroscopy. The residual solution was then precipitated three times from cold CH_3OH. The light yellow polymer was dried in a vacuum oven overnight at room temperature and analyzed by ^1H NMR spectroscopy and DMF SEC. See Table 3.1 for NMR and SEC characterization of polymers used.

3.6.7. Self-Assembly of PNAM$_{39}$-*b*-PTAm$_{300}$ PT1, PNAM$_{39}$-*b*-PMTAm$_{300}$ PT^{Me} diblock copolymer in water

The typical procedures are as follows. Specifically, for the self-assembly of PNAM$_{39}$-*b*-PMTAm$_{300}$ **PT^{Me}**, the copolymer was dissolved in DMF (at 8 mg mL^{-1}) and stirred for 2 h at 70 °C. Then an excess of 18.2 MΩ·cm water was added *via* a syringe pump at a rate of 1 mL h^{-1}. The final volume ratio between water and organic solvent was about 8:1. The solution was then dialyzed against 18.2 MΩ·cm water, incorporating at least 6 water changes, to afford self-assemblies **MT^{Me}** at a concentration of *ca.* 1 mg mL^{-1}.

3.6.8. Addition of copolymers PNAM$_x$-*b*-PAAm$_y$, PNAM$_{39}$-*b*-PSt$_{20}$, PNAM$_{39}$-*b*-PTAm$_{20}$ or PNAM$_{39}$-*b*-PMAAm$_{20}$ into PNAM$_{39}$-*b*-PTAm$_{300}$ MT1 or PNAM$_{39}$-*b*-PMTAm$_{300}$ MT^{Me} micellar solution.

The typical procedures are as follows. The diblock copolymer PNAM$_{39}$-*b*-PAAm$_{20}$ **PA1** was dissolved in H_2O at 5 mg mL^{-1}. This was then added to the micellar solution of PNAM$_{39}$-*b*-PTAm$_{300}$ (0.5 mg mL^{-1}) with stirring to make the molar ratios of **A:T** 0.07, 0.20, 0.33, 0.67, 1.0, 1.33, respectively. The molar ratios were calculated according to the M_n determined from ^{1}H NMR spectroscopic analyses and their mass concentration. The mixture was then sealed and allowed to stir at room temperature for at least 2 h. The solutions were then characterized by DLS, TEM, and SLS analyses.

For the method of stepwise addition, complementary copolymers **PA1** solution (0.07 molar ratio **A** relative to **T**) was added into the micelle **MT1** solution (0.5 mg mL^{-1}). After 2 h stirring, another complementary copolymers **PA1** solution (0.07 molar ratio **A** relative to **T**) was added. Again and again, complementary copolymers **PA1** with 0.20, 0.33, 0.67, 1.00 and 1.33 molar ratios **A** relative to **T** was added into the initial micelle **MT1** and the solutions were characterized by DLS analyses. Small volume of solutions were taken out when the molar ratios of **A:T** are 0.20, 0.33, 0.67, 1.0, 1.33. The solutions were then imaged by TEM.

3.7. References

1. J. J. Green and J. H. Elisseeff, *Nature*, **2016**, *540*, 386-394.

2. C. S. Goldsmith and S. E. Miller, *Clin. Microbiol. Rev.*, **2009**, *22*, 552-563.

3. C. Sachse, J. Z. Chen, P.-D. Coureux, M. E. Stroupe, M. Fändrich and N. Grigorieff, *J Mol Biol*, **2007**, *371*, 812-835.

4. T. A. M. Bharat, T. Noda, J. D. Riches, V. Kraehling, L. Kolesnikova, S. Becker, Y. Kawaoka and J. A. G. Briggs, *Proc. Natl. Acad. Sci. U. S. A.*, **2012**, *109*, 4275-4280.

5. M. Häring, G. Vestergaard, R. Rachel, L. Chen, R. A. Garrett and D. Prangishvili, *Nature*, **2005**, *436*, 1101-1102.

6. L. Zhang and A. Eisenberg, *Science*, **1995**, *268*, 1728-1731.

7. Y.-Y. Won, H. T. Davis and F. S. Bates, *Science*, **1999**, *283*, 960-963.

8. Z. Li, E. Kesselman, Y. Talmon, M. A. Hillmyer and T. P. Lodge, *Science*, **2004**, *306*, 98-101.

9. H. Cui, Z. Chen, S. Zhong, K. L. Wooley and D. J. Pochan, *Science*, **2007**, *317*, 647-650.

10. X. Wang, G. Guerin, H. Wang, Y. Wang, I. Manners and M. A. Winnik, *Science*, **2007**, *317*, 644-647.

11. S. Jain and F. S. Bates, *Science*, **2003**, *300*, 460-464.

12. P. Yang, L. P. D. Ratcliffe and S. P. Armes, *Macromolecules*, **2013**, *46*, 8545-8556.

13. S. E. Mastroianni, J. P. Patterson, R. K. O'Reilly and T. H. Epps III, *Soft Matter*, **2013**, *9*, 10146-10154.

14. D. E. Discher and A. Eisenberg, *Science*, **2002**, *297*, 967-973.

15. D. A. Christian, A. Tian, W. G. Ellenbroek, I. Levental, K. Rajagopal, P. A. Janmey, A. J. Liu, T. Baumgart and D. E. Discher, *Nat. Mater.*, **2009**, *8*, 843-849.

16. J. R. Howse, R. A. L. Jones, G. Battaglia, R. E. Ducker, G. J. Leggett and A. J. Ryan, *Nat. Mater.*, **2009**, *8*, 507-511.

17. M. Massignani, C. LoPresti, A. Blanazs, J. Madsen, S. P. Armes, A. L. Lewis and G. Battaglia, *Small*, **2009**, *5*, 2424-2432.

18. L. Zhang and A. Eisenberg, *Macromolecules*, **1999**, *32*, 2239-2249.

19. Y. Geng, P. Dalhaimer, S. Cai, R. Tsai, M. Tewari, T. Minko and D. E. Discher, *Nat. Nanotechnol.*, **2007**, *2*, 249-255.

20. X. Jiang, W. Qu, D. Pan, Y. Ren, J. M. Williford, H. Cui, E. Luijten and H. Q. Mao, *Adv. Mater.*, **2013**, *25*, 227-232.

21. Y. Cai, K. B. Aubrecht and R. B. Grubbs, *J. Am. Chem. Soc.*, **2011**, *133*, 1058-1065.

22. A. O. Moughton, J. P. Patterson and R. K. O'Reilly, *Chem. Commun.*, **2011**, *47*, 355-357.

23. K. Wei, L. Su, G. Chen and M. Jiang, *Polymer*, **2011**, *52*, 3647-3654.

24. L. Wang, Y. Wang, H. Miao and D. Chen, *Soft Matter*, **2016**, *12*, 4891-4895.

25. M.-P. Chien, A. M. Rush, M. P. Thompson and N. C. Gianneschi, *Angew. Chem., Int. Ed.*, **2010**, *49*, 5076-5080.

26. Z. Hua, R. Keogh, Z. Li, T. R. Wilks, G. Chen and R. K. O'Reilly, *Macromolecules*, **2017**, *50*, 3662-3670.

27. Z. Hua, A. Pitto-Barry, Y. Kang, N. Kirby, T. R. Wilks and R. K. O'Reilly, *Polym. Chem.*, **2016**, *7*, 4254-4262.

28. F. Ilhan, T. H. Galow, M. Gray, G. Clavier and V. M. Rotello, *J. Am. Chem. Soc.*, **2000**, *122*, 5895-5896.

29. J.-F. Lutz, A. F. Thunemann and K. Rurack, *Macromolecules*, **2005**, *38*, 8124-8126.

30. C. R. South and M. Weck, *Macromolecules*, **2007**, *40*, 1386-1394.

31. P. K. Lo and H. F. Sleiman, *J. Am. Chem. Soc.*, **2009**, *131*, 4182-4183.

32. S. Cheng, M. Zhang, N. Dixit, R. B. Moore and T. E. Long, *Macromolecules*, **2012**, *45*, 805-812.

33. R. McHale, J. P. Patterson, P. B. Zetterlund and R. K. O'Reilly, *Nat. Chem.*, **2012**, *4*, 491-497.

34. W. Xi, S. Pattanayak, C. Wang, B. Fairbanks, T. Gong, J. Wagner, C. J. Kloxin and C. N. Bowman, *Angew. Chem., Int. Ed.*, **2015**, *54*, 14462-14467.

35. Z. Liu, B. Fairbanks, L. He, T. Liu, P. Shah, J. N. Cha, J. W. Stansbury and C. N. Bowman, *Chem. Commun.*, **2017**, *53*, 10156-10159.

36. J. P. Patterson, A. M. Sanchez, N. Petzetakis, T. P. Smart, T. H. Epps III, I. Portman, N. R. Wilson and R. K. O'Reilly, *Soft Matter*, **2012**, *8*, 3322-3328.

37. L. Sun, A. Pitto-Barry, N. Kirby, T. L. Schiller, A. M. Sanchez, M. A. Dyson, J. Sloan, N. R. Wilson, R. K. O'Reilly and A. P. Dove, *Nat. Commun.*, **2014**, *5*, 5746-5754.

38. T. Nicolai, O. Colombani and C. Chassenieux, *Soft Matter*, **2010**, *6*, 3111-3118.

39. A. Nazemi, C. E. Boott, D. J. Lunn, J. Gwyther, D. W. Hayward, R. M. Richardson, M. A. Winnik and I. Manners, *J. Am. Chem. Soc.*, **2016**, *138*, 4484-4493.

40. N. Petzetakis, A. P. Dove and R. K. O'Reilly, *Chem. Sci.* , **2011**, *2*, 955-960.

41. M. C. Arno, M. Inam, Z. Coe, G. Cambridge, L. J. Macdougall, R. Keogh, A. P. Dove and R. K. O'Reilly, *J. Am. Chem. Soc.*, **2017**, *139*, 16980-16985.

Chapter 4. Reversibly manipulating the surface chemistry of polymeric nanostructures *via* a ‘grafting to’ approach mediated by nucleobase interactions

4.1. Declaration of authorship

The syntheses of (2-aminoethyl)-α-D-mannopyranoside and 5-(3-bromo-4-(isopropylamino)-2,5-dioxo-2,5-dihydro-1H-pyrrol-1-yl)-2-cyanopentan-2-yl ethyl carbonotrithioate (CPET-ABM) in this Chapter were performed by Mr. Zhen Li (Fudan University, China) and Mr. Robert Keogh (University of Warwick), respectively. HR Mass Spectra in this Chapter was analyzed by mass spectrometry group (University of Warwick).

This work has been published in *Macromolecules*.

Hua, Z.; Keogh, R.; Li, Z.; Wilks, T. R.; Chen, G.; O'Reilly, R. K. Reversibly Manipulating the Surface Chemistry of Polymeric Nanostructures *via* a "Grafting To" Approach Mediated by Nucleobase Interactions. *Macromolecules* **2017**, *50*, 3662-3670.

4.2. Abstract

‘Grafting to’ polymeric nanostructures or surfaces is a simple and versatile approach to achieve functionalization. Herein, we describe the formation of mixed polymer-grafted nanoparticles through a supramolecular ‘grafting to’ method that exploits multiple hydrogen-bonding interactions between the thymine (T)-containing cores of preformed micelles and the complementary nucleobase, adenine (A), of added diblock copolymers. To demonstrate this new ‘grafting to’ approach, mixed-corona polymeric nanoparticles with different sizes were prepared by the addition of a series of complementary diblock copolymers containing thermo-responsive poly(*N*-isopropylacrylamide) (PNIPAM) to a preformed micelle with a different coronal forming block, poly(4-acryloylmorpholine) (PNAM). PNIPAM chains were distributed throughout the corona and facilitated a fast and fully reversible size change of the resulting mixed-corona micelles upon heating cycles. Through the introduction of an environmentally-sensitive fluorophore, the reversible changes in nanoparticle size and coronal composition could be easily probed. Furthermore, preparation of mixed-corona micelles also enabled protein ligands, such as D-mannose, to be concealed and displayed on the micelle surface. This supramolecular ‘grafting to’ approach provides a straightforward route to fabricate highly functionalized mixed polymeric nanostructures or surfaces with potential applications in targeted diagnosis or therapy and responsive surfaces.

4.3. Introduction

Hydrogen-bonding (H-bonding) mediated assemblies have for many decades been employed as surrogates to mimic the nanostructures formed as a result of nucleobase pairing within RNA and DNA.[1-9] Hydrogen bonds are normally weaker than covalent and ionic bonds, with an energy typically between 5 and 30 kJ mol^{-1}. Importantly, although a single hydrogen bond is weak, controlled display of multiple H-bonding groups can result in a strong, specific interaction. Synthetic chemists inspired by nature have widely utilized complementary H-bonding interactions to achieve templated polymerization,[10-14] mediate polymer tacticity[15] and tune nanoparticle morphologies.[16-18] Selective recognition of nucleobase functionalities has also provided a new route to modify and functionalize nucleobase- or DNA-containing nanomaterials.[19-23]

Mixed polymer-grafted nanostructures and surfaces, consisting of two distinct polymers in the outer layer, enable various applications such as smart wetting surfaces,[24, 25] controllable oil/water separation[26] and cancer diagnostics.[27] Generally, mixed-corona polymeric nanostructures are prepared using cooperative self-assembly of two distinct diblock copolymers in a common selective solvent, microphase separation can then occur due to differences in the properties of the two diblock copolymers.[28, 29] Alternatively, two 'grafting' strategies can be exploited to attach polymer chains to the surface of a nanostructure: (i) 'grafting from' and (ii) 'grafting to' approaches.[30] In the 'grafting from' approach, polymer chains are grown from initiator-functionalized nanostructures/surfaces, which can produce thick and very dense polymer layers.[31] However, stringent reaction conditions and complicated purification steps often limit potential applications. On the other hand, the relatively simple 'grafting to' strategy involves the attachment of prefabricated polymers *via* either physisorption[32] or covalent bond formation.[30, 33-36] Typically, the 'grafting to' strategy suffers from several limitations. For example, with increasing polymer molecular weight, the reaction efficiency between the polymer end-group and the reactive group on the

surface significantly decreases.[37] Furthermore, steric repulsion between polymer chains is expected to hinder the successful fabrication of novel polymeric materials due to relatively low grafting densities.

The 'grafting to' strategy also has some undoubted advantages. Tethered polymers can be thoroughly characterized prior to conjugation, which allows the fabrication of tailor-made nanostructures or surfaces.[38, 39] Furthermore, in contrast to the 'grafting from' approach, the 'grafting to' approach is experimentally very straightforward. The development of 'click' chemistry in the last decade, has led to a range of modular conjugation strategies which has breathed new life into 'grafting to' approaches.[40, 41] However, the relatively small and mostly buried reactive groups of long polymer chains often result in moderate grafting densities and often require high reactant concentrations.[42, 43]

Stimuli-responsive polymers represent a growing cadre of materials that support various applications such as responsive coatings and controlled release agents.[44] Many smart polymers have been developed to switch their various functions in response to an external stimulus such as pH, light, temperature.[45-50] Such switching behaviour has been utilized to turn on/off activity or the interaction of functional groups within the material. For example, switching of a cationic *N*, *N*-dimethyl-2-morpholinone (CD-Ring) film between attacking and defending against bacteria, has been achieved through a change in solution pH.[45] Furthermore, light-responsive azobenzene[46] and thermo-responsive PNIPAM[49, 50] have been utilized to reversibly conceal and expose ligands for biospecific cell adhesion or targeting.

Recent work in our group has highlighted the effect of complementary multiple H-bonding interactions within the core of self-assembled nanostructures on their self-assembly behavior.[17] Indeed, the utilization of specific complementary A-T interactions within the micelle cores enabled the progressive modulation of nanostructure morphologies. At high dilution (0.5 mg mL^{-1}), efficient complementary interactions allowed for control over nanostructure morphology. To expand on the utility and application of this discovery, we aimed to exploit the complementary interactions within the nanostructure cores to allow for the preparation of responsive mixed-corona micelles. Our previous work employed PNAM as the sole hydrophilic block, and thus generated micelles with a homogenous corona. In contrast, our new system

uses both hydrophilic PNAM and PNIPAM in two different diblock copolymers, thus forming a mixed corona. Mixed-corona micelles containing both thermoresponsive PNIPAM, which can reversibly manipulate the micelle surface functionality and a permanently hydrophilic, non-responsive PNAM, which can stabilize the nanoparticles above the characteristic cloud point of PNIPAM,[51] were prepared using a 'grafting to' approach. This approach allowed for the facile control of nanostructure size through the introduction of complementary diblock copolymers, poly(*N*-isopropylacrylamide)-*b*-poly(3-(adenine-9-yl)propyl acrylamide) (PNIPAM-*b*-PAAm) with different chain lengths, to preformed micelles with thymine functionalized cores. Interestingly, the thermo-responsive polymeric micelles exhibited behaviour consistent with single particle collapse/swelling and the transition was fully reversible. Introduction of an environmentally-sensitive fluorophore at the chain ends of the hydrophilic blocks, using a 'grafting to' approach allowed the hydrophobicity of the corona domain of the micelles to be probed at different temperatures. Having confirmed the reversible collapse/swelling of the thermo-responsive chains of the corona, it was then demonstrated that it was possible to selectively display or conceal a protein ligand using heat as a responsive trigger. This work demonstrates that a 'grafting to' approach, mediated by complementary nucleobase interactions, allows for the effective functionalization of polymeric nanostructures/surfaces and represents an efficient route to fabricate tailor-made nanomaterials.

4.4. Results and discussion

4.4.1. Synthesis of mixed-corona micelles through a supramolecular 'grafting to' approach

A diblock copolymer, **P4.1**, with a permanently hydrophilic domain and a thymine functionalized hydrophobic block was prepared by RAFT polymerization in Chapter 2. The self-assembly of this diblock copolymer was achieved *via* a solvent switch method as reported in Chapter 2,[17] to afford micelle **M4.1** (D_h = 69 nm, PD = 0.058) at *ca.* 1 mg mL^{-1}. The obtained micelle **M4.1** has a large core with a long thymine block length, providing the possibility for functionalizing the micelle through a 'grafting to' method.

In order to fabricate mixed-corona micelles, using a 'grafting to' approach a series of PNIPAM-*b*-PAAm diblock copolymers with various hydrophilic block lengths were also prepared *via* RAFT polymerization (Scheme 4.1). The obtained copolymers **P4.2-4.5** were characterized by ^{1}H NMR spectroscopy and SEC analyses (Table 4.1, Figures 4.1 and 4.2).

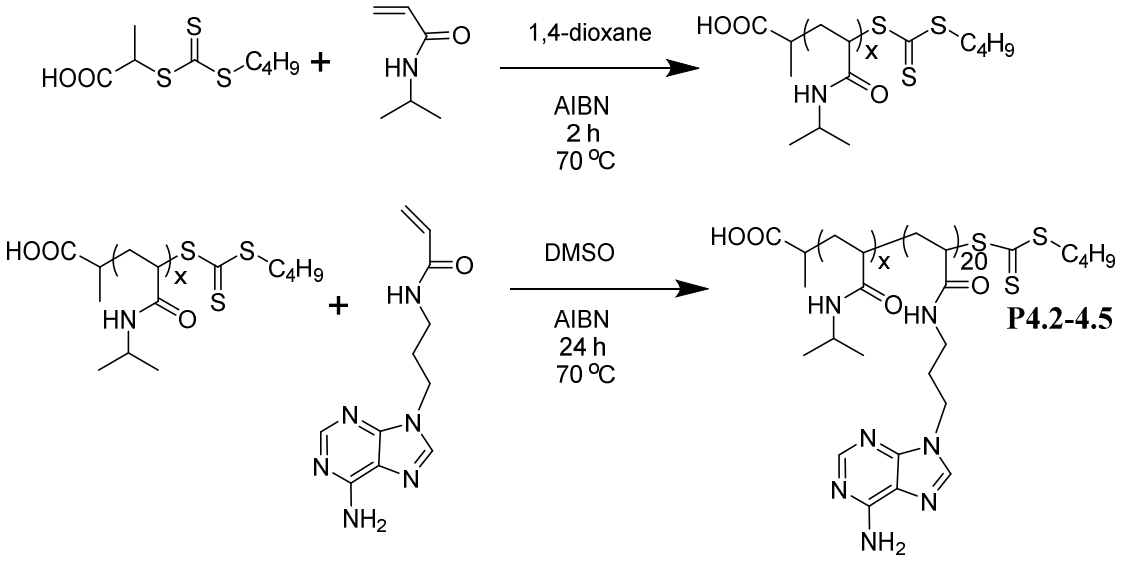

Scheme 4.1. Synthesis of PNIPAM$_x$-*b*-PAAm$_{20}$ **P4.2-4.5** with different DPs of PNIPAM.

Table 4.1. Characterization data of polymers **P4.1**-**4.10**.

Polymer	Structure	$M_{n,\,NMR}$[a] / kDa	$M_{n,\,SEC}$[b] / kDa	$Đ_M$[b]
P4.1	PNAM$_{96}$-*b*-PTAm$_{301}$	85.1	68.4	1.29
P4.2	PNIPAM$_{96}$-*b*-PAAm$_{20}$	15.5	17.8	1.05
P4.3	PNIPAM$_{176}$-*b*-PAAm$_{20}$	25.3	23.9	1.10
P4.4	PNIPAM$_{262}$-*b*-PAAm$_{20}$	35.3	34.1	1.13
P4.5	PNIPAM$_{438}$-*b*-PAAm$_{20}$	56.7	52.9	1.18
P4.6	PNIPAM$_{262}$	29.9	31.6	1.09
P4.7	PNAM$_{295}$-*b*-PAAm$_{20}$	47.0	36.8	1.17
P4.8	PNIPAM$_{237}$-*b*-PAAm$_{20}$[c]	33.0	32.8	1.17
P4.9	PNAM$_{244}$-*b*-PAAm$_{20}$[c]	40.5	33.0	1.25
P4.10	PNAM$_{98}$-*b*-PTAm$_{302}$[d]	85.8	64.2	1.32

[a]Determined by ^{1}H NMR spectroscopy (400 MHz) in deuterated DMSO. [b]Determined by DMF SEC, with poly(methyl methacrylate) (PMMA) standards. [c]Aminobromomaleimide-containing or [d]D-mannose-containing chain transfer agent (CTA) was used.

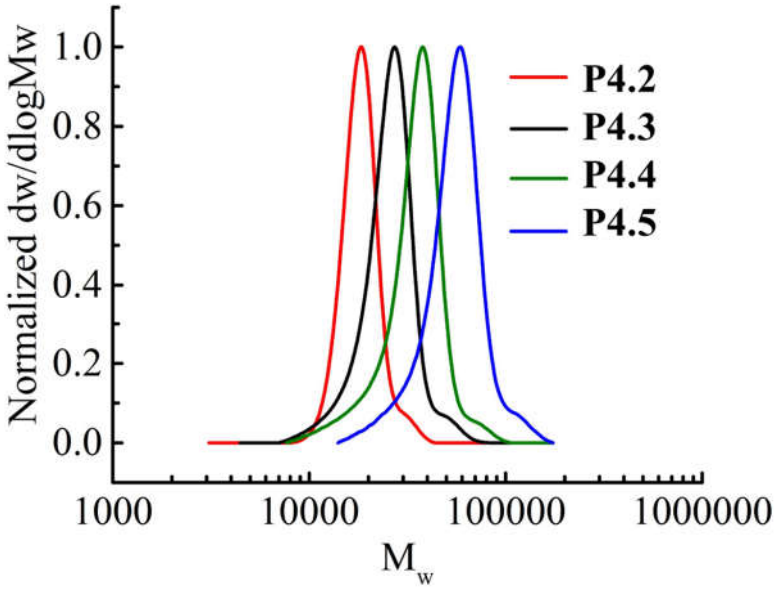

Figure 4.1. SEC traces (DMF + 5 mM NH_4BF_4 as eluent) of nucleobase-containing diblock copolymers **P4.2**-**P4.5**.

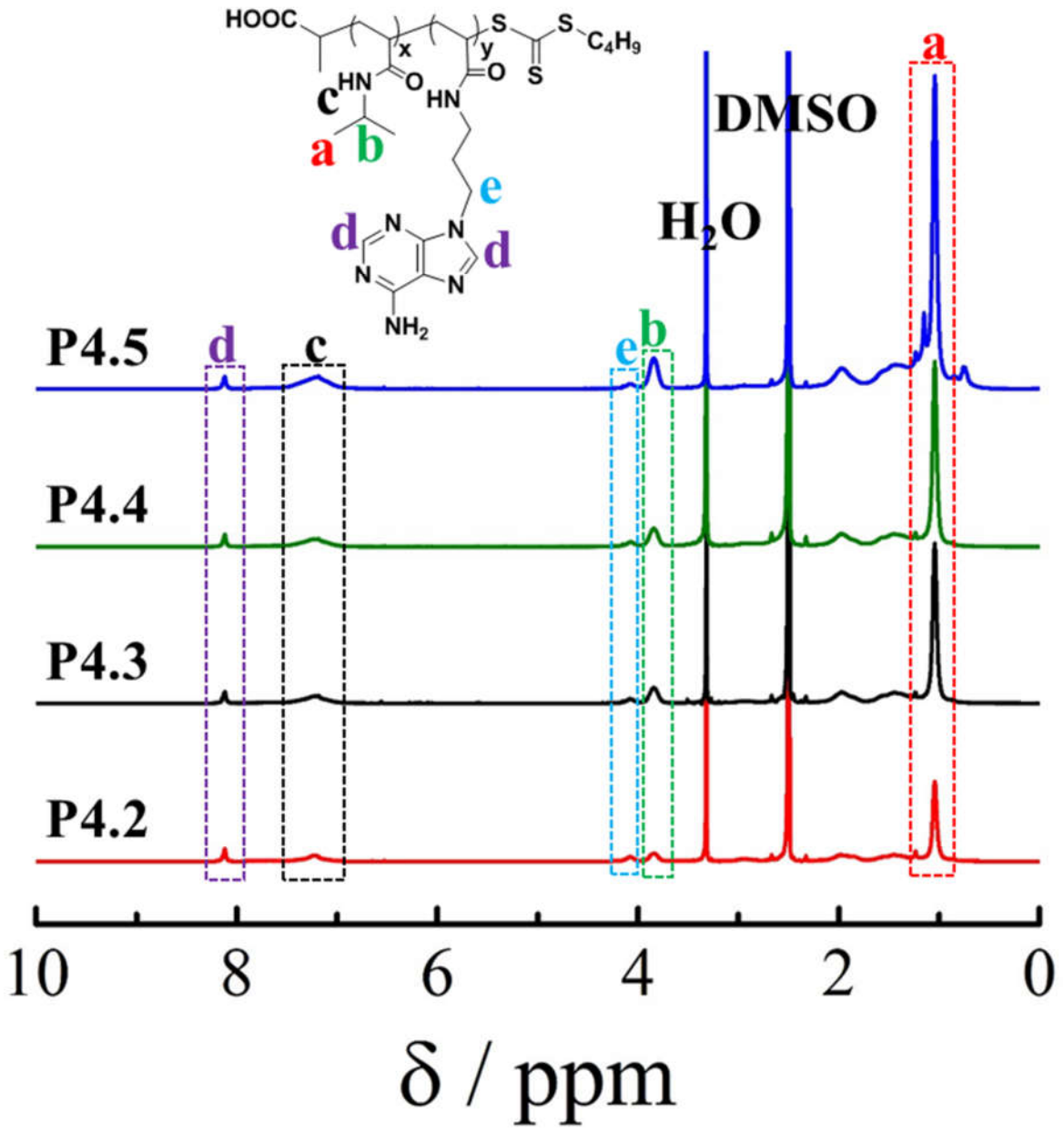

Figure 4.2. ^{1}H NMR (400 MHz) spectra of nucleobase-containing diblock copolymers **P4.2-4.5** in DMSO-d_6.

The DP of the complementary nucleobase PAAm block remains constant, whereas the length of the thermo-responsive PNIPAM block varies in the obtained copolymers **P4.2-4.5**. This is evident in Figure 4.2, as the peaks attributed to adenine do not change for **P4.2-4.5**. However, the peaks at 1.05 and 3.84 ppm from the isopropyl group in NIPAM showed a gradual increase as the DP of PNIPAM increases.

Subsequently, 1 molar eq. of complementary diblock copolymers **P4.2-4.5** in water was added to the micelle solution **M4.1** with stirring at room temperature for at least 2 h. In agreement with our previous work in Chapters 2 and 3, no morphology transition or disassembly occurred when only 1 molar eq. of complementary diblock copolymers was added to the preformed micelles.[17] Using this approach, well-defined mixed-corona micelles **M4.2-4.5** were formed through multiple H-bonding interactions between the thymine-containing micelle core of **M4.1** and the complementary adenine-containing diblock copolymer **P4.2-4.5** (Scheme 4.2, Figures 4.3).

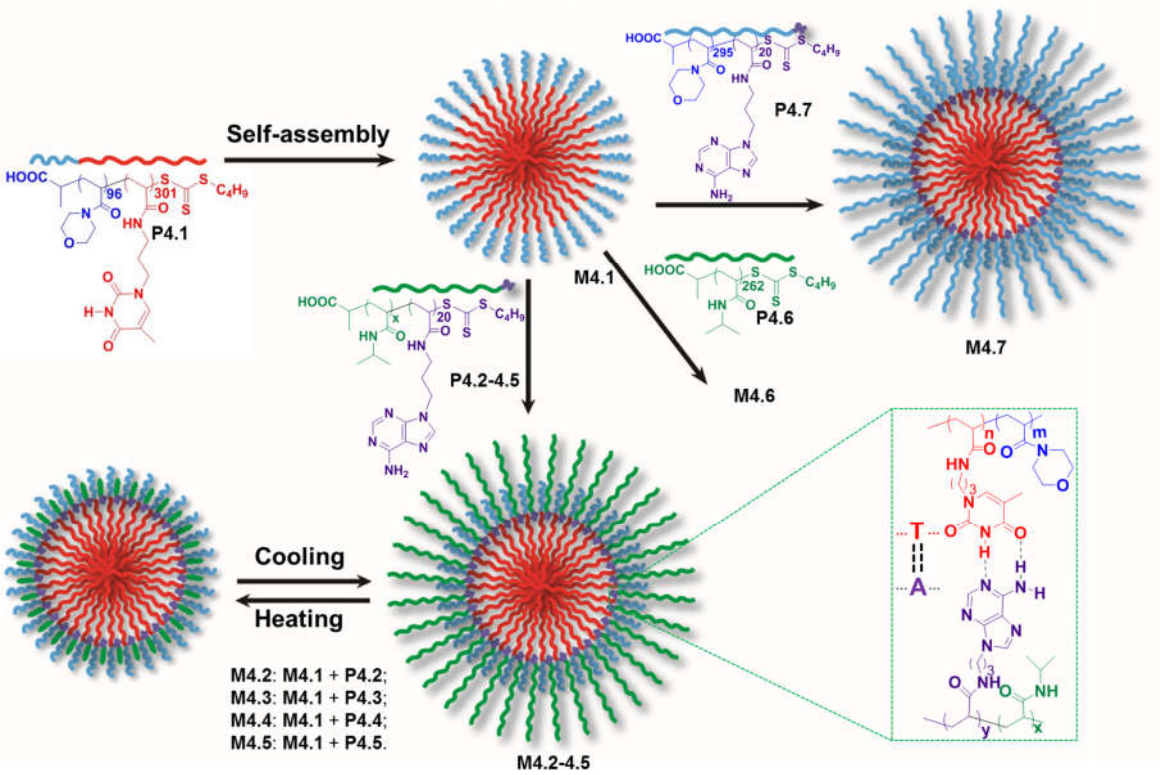

Scheme 4.2. Synthesis of mixed-corona polymeric nanostructures **M4.2**–**4.7** through a supramolecular 'grafting to' approach mediated by complementary nucleobase interactions.

DLS analysis indicated that the mixed micelles **M4.2-4.5** were monodisperse with narrow polydispersity. Meanwhile, they contained both a thermo-responsive PNIPAM and a permanently hydrophilic, non-

responsive PNAM to stabilize them at low temperatures. With increase of the length of the PNIPAM block, the obtained micelles showed increased hydrodynamic diameters accordingly (Figure 4.3a-d).

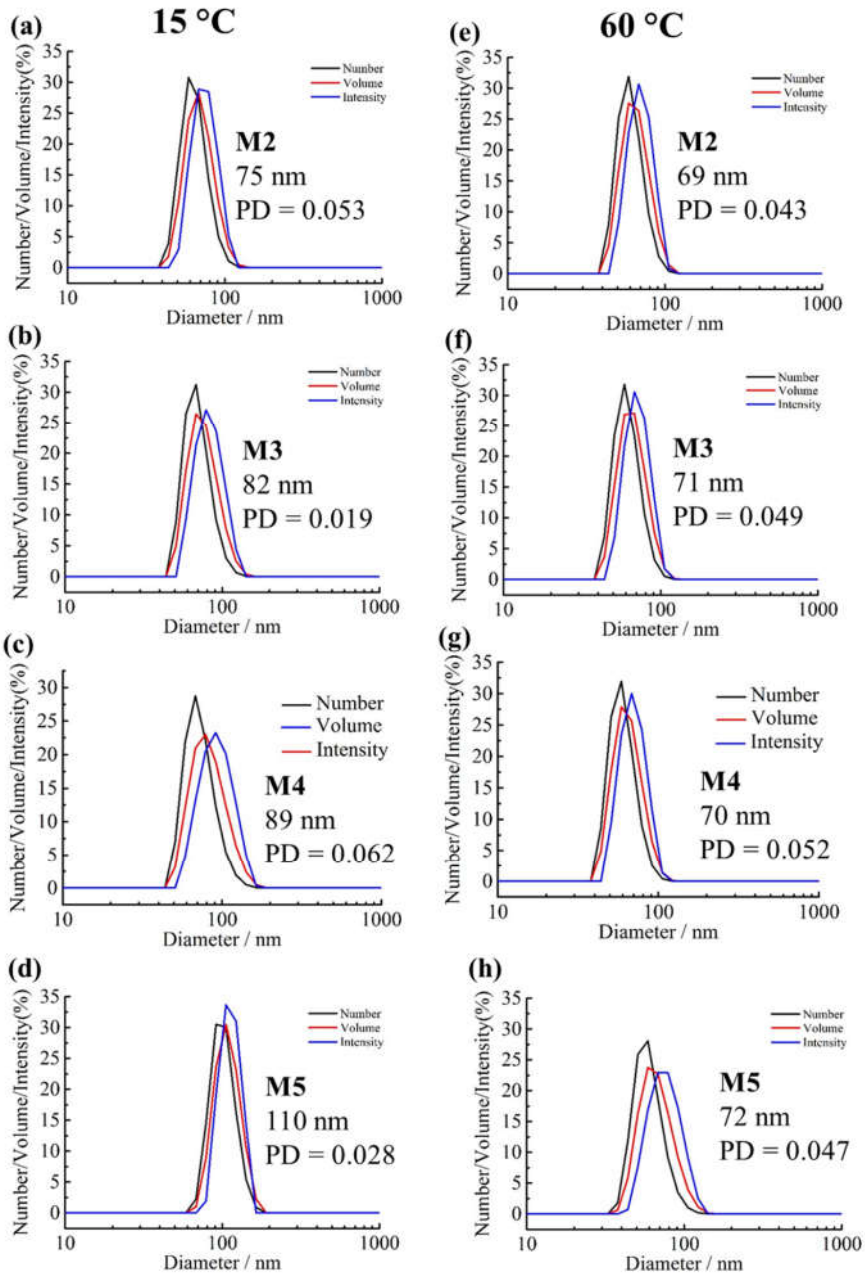

Figure 4.3. DLS analysis of the mixed-corona micelles in water (0.5 mg mL^{-1}). (a) **M4.2**; (b) **M4.3**; (c) **M4.4**; (d) **M4.5** at 15 °C and (e) **M4.2**; (f) **M4.3**; (g) **M4.4**; (h) **M4.5** at 60 °C.

Mixed-corona micelles generally inherit the solution properties of both the corona-forming blocks. Indeed, DLS analysis indicated that the PNIPAM chains in the mixed-corona micelles collapsed and no aggregation between self-assembled nanostructures was observed at 60 °C (Figure 4.3e-h).

Figure 4.4 shows the heating cycle for **M4.4** and the resulting hydrodynamic diameter of the mixed-corona micelles, which decreased from *ca.* 89 nm to *ca.* 70 nm upon heating from 15 °C to 60 °C. Meanwhile, the polydispersity values of the mixed-corona micelles were determined to lie in a range of 0.02 to 0.08 during this heating process.

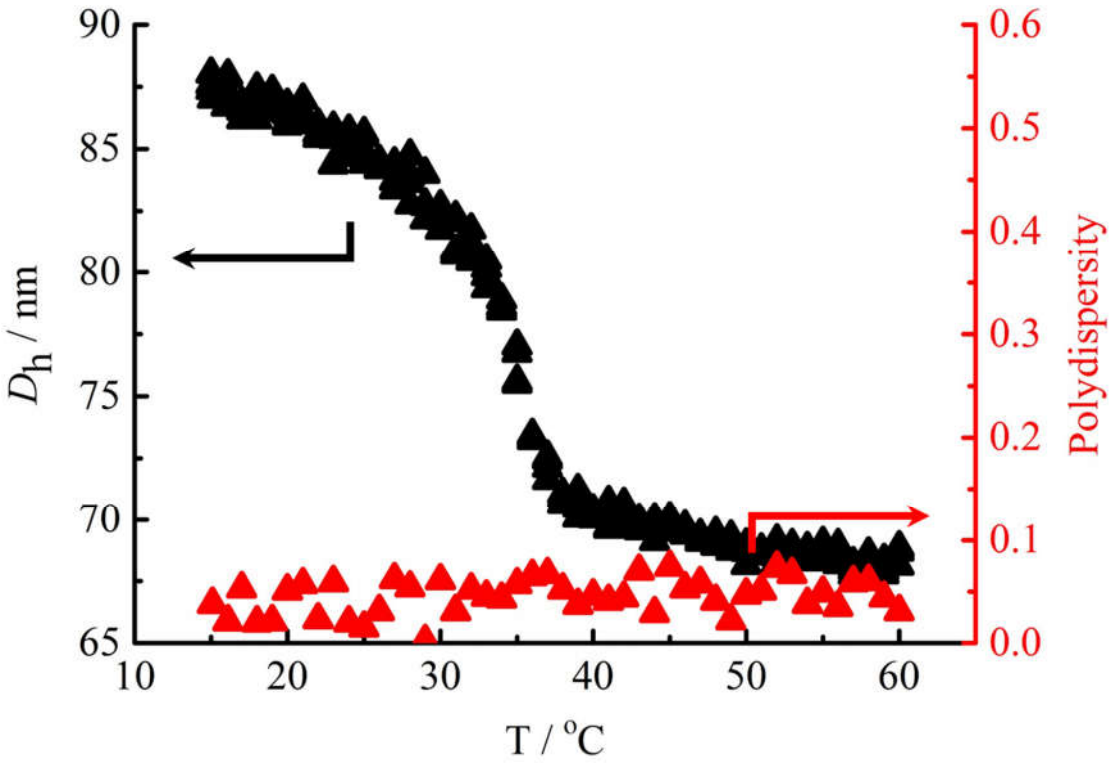

Figure 4.4. Variation of the hydrodynamic diameter (D_h) of the mixed-corona micelles **M4.4** (0.5 mg mL^{-1}) with temperature, as determined by DLS analysis.

Micelle **M4.4** solution was dried and stained with uranyl acetate at 20 and 60 °C for TEM imaging (Figure 4.5). TEM images further suggested that no aggregation was observed at 60 °C. Meanwhile, smaller spherical nanoparticles with diameter *ca.* 61 nm were observed at 60 °C compared with spherical

nanoparticles with diameter *ca.* 70 nm at 20 °C. This further suggests that these 'grafting to' mixed-corona micelle underwent intra-particle chain collapse without inter-particle aggregation.

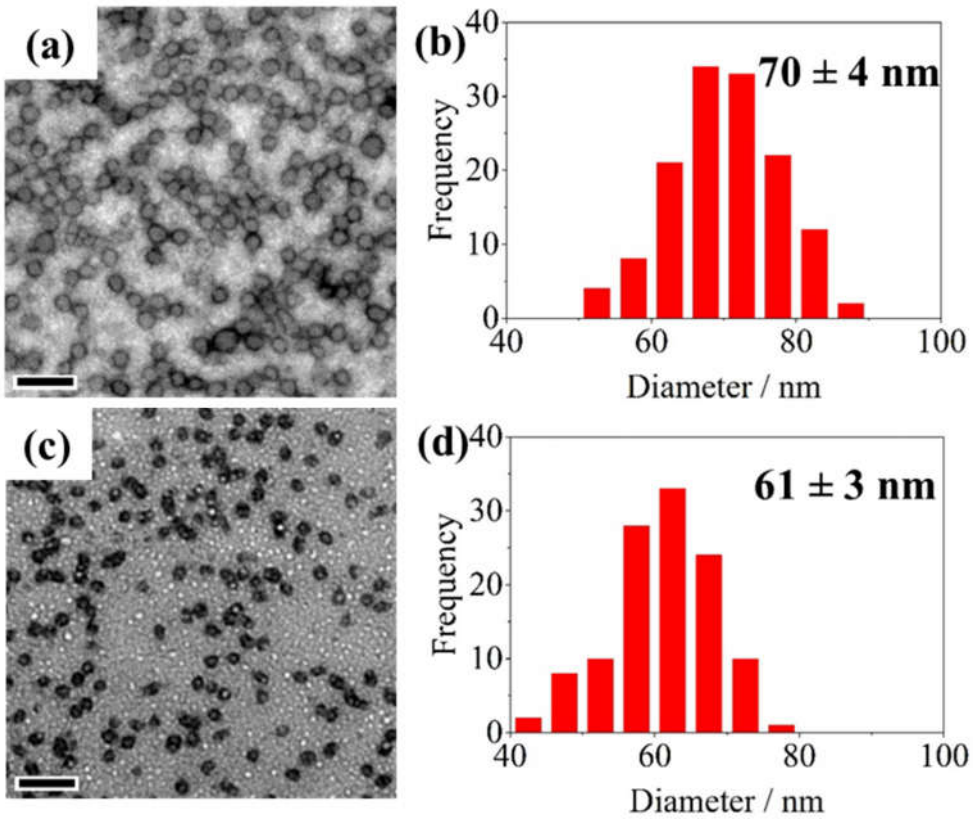

Figure 4.5. TEM images (stained with uranyl acetate) and histograms of number-average diameter distribution of **M4.4** at (a, b) 20 °C and (c, d) 60 °C; scale bar: 200 nm.

In stark contrast, upon addition of 1 molar eq. of PNIPAM **P4.6** which does not have a complementary nucleobase block to the preformed micelle **M4.1**, large aggregates and much higher dispersity values were observed by DLS for the resultant micelle, **M4.6**, above the cloud point of the PNIPAM block (Scheme 4.2, Figure 4.6). Therefore, the aggregation of unassembled **P4.6** led to the formation of large aggregates at high temperatures which is distinct from the intra-particle chain collapse of **M4.4** (Figure 4.4).

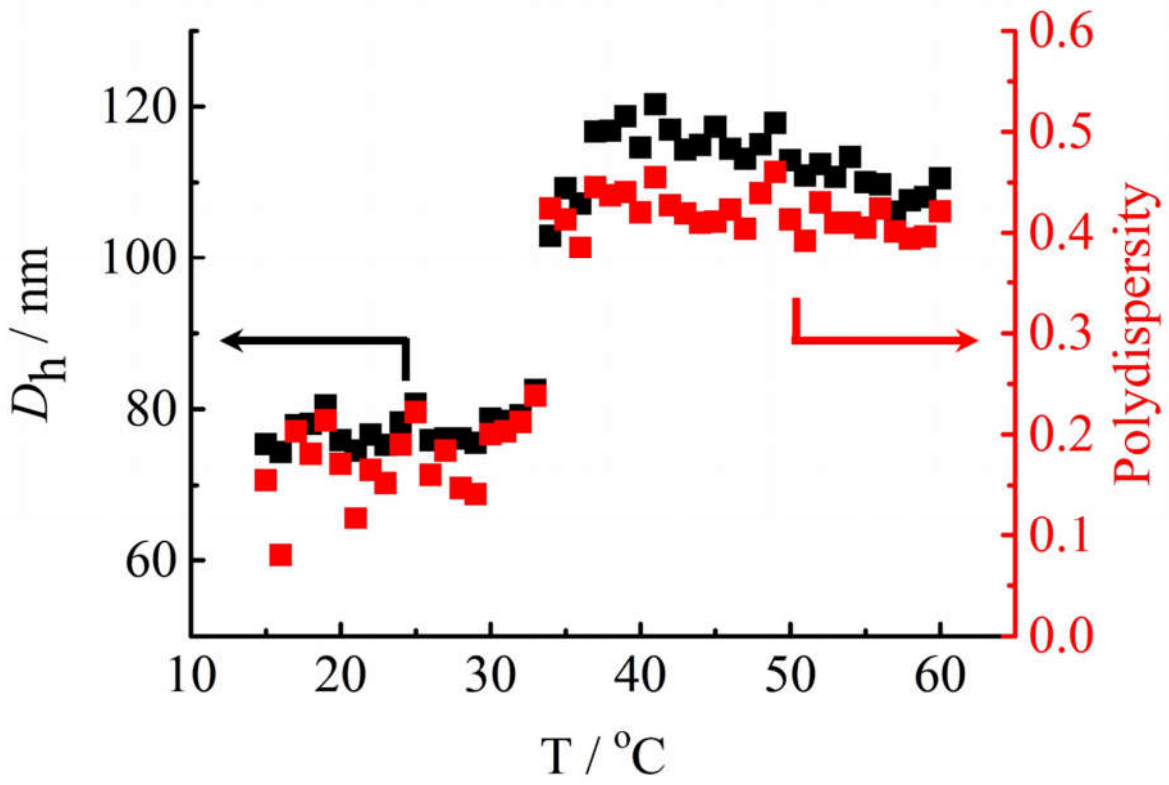

Figure 4.6. Variation of the hydrodynamic diameter (D_h) of the micelle **M4.6** (0.5 mg mL^{-1}) (which consisted of micelle **M4.1** and $PNIPAM_{262}$ **P4.6**).

Notably, complementary diblock copolymers **P4.2-4.5** with small anchoring groups avoided the formation of frozen aggregates and facilitated efficient incorporation of the complementary diblock copolymers. Static light scattering (SLS) analysis of micelle **M4.4** also indicated no appreciable change in the apparent molecular weight (M_w) by light scattering and aggregation number (N_{agg}) of the respective micelles at 15, 35 and 50 °C (Figure 4.7).[52]

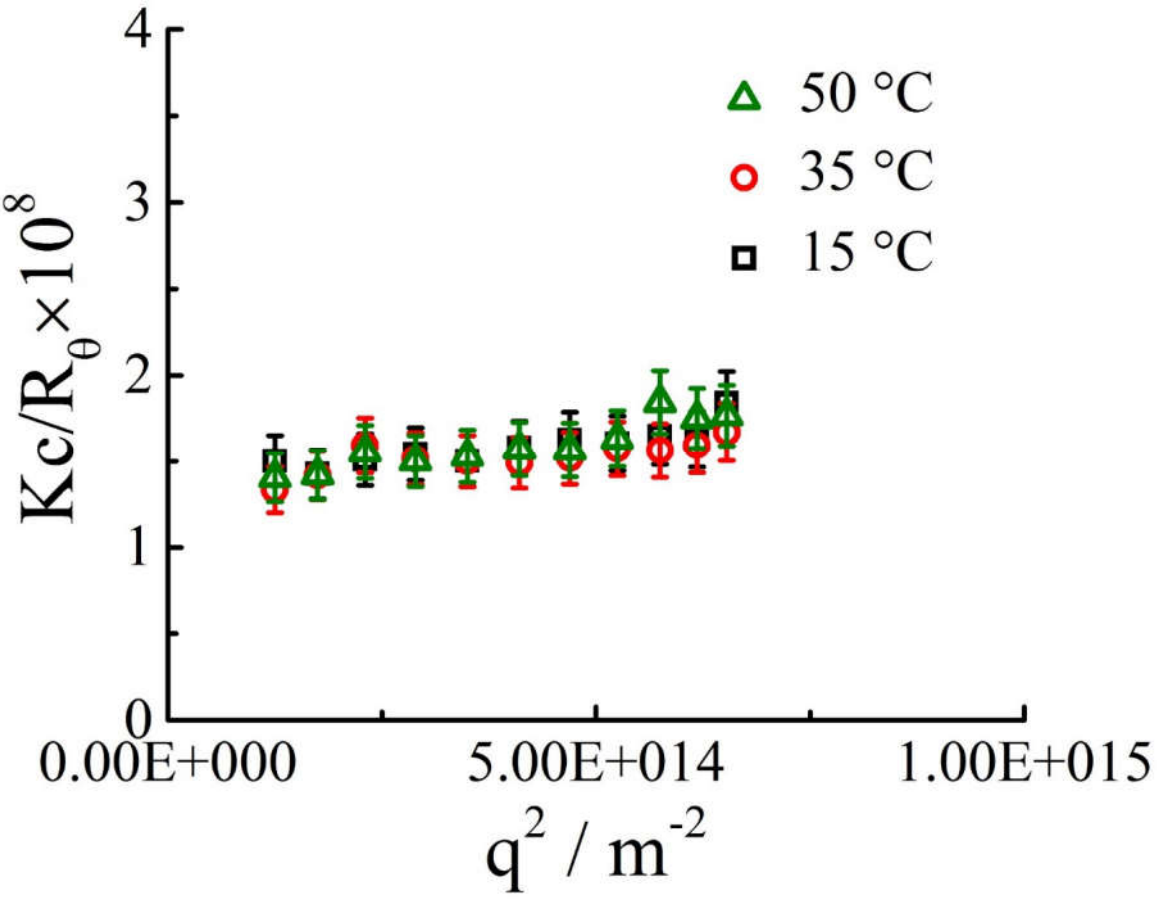

Figure 4.7. Plot of Kc/R_θ *vs* q^2 for the mixed-corona micelle **M4.4** (0.5 mg mL^{-1}) at 15, 35 and 50 °C with 10% error bars. Static light scattering (SLS) measurements were conducted from 50° to 150° with an interval of 10° against a toluene standard.

Based on these initial results, we proposed that the size change of the mixed-corona micelle upon heating was a result of PNIPAM collapse with retention of the micellar structure, rather than disassembly and reformation of the micellar aggregates (Scheme 4.2). As expected, the hydrophilic PNAM chains were still capable of stabilizing mixed-corona micelles even when the PNIPAM chains were fully collapsed at elevated temperatures.

Given that H-bonding interactions are known to be disrupted at elevated temperatures, we next investigated the effect of temperature on a PNAM corona micelles prepared by a 'grafting to' approach through the addition of a non-responsive diblock copolymer, **P4.7** ($PNAM_{295}$-*b*-$PAAm_{20}$) to the preformed micelle **M4.1** (Scheme 4.2). The resultant micelle **M4.7** was investigated by temperature dependant DLS and no appreciable size change was observed at elevated temperatures, which

demonstrated the stability of the H-bonding interactions in the micellar core up to 60 °C (Figure 4.8). This result also suggested that the size decrease observed in the mixed-corona micelles **M4.2-4.5** was solely caused by the intra-particle PNIPAM chain collapsing rather than the separation of complementary polymer chains at elevated temperatures.

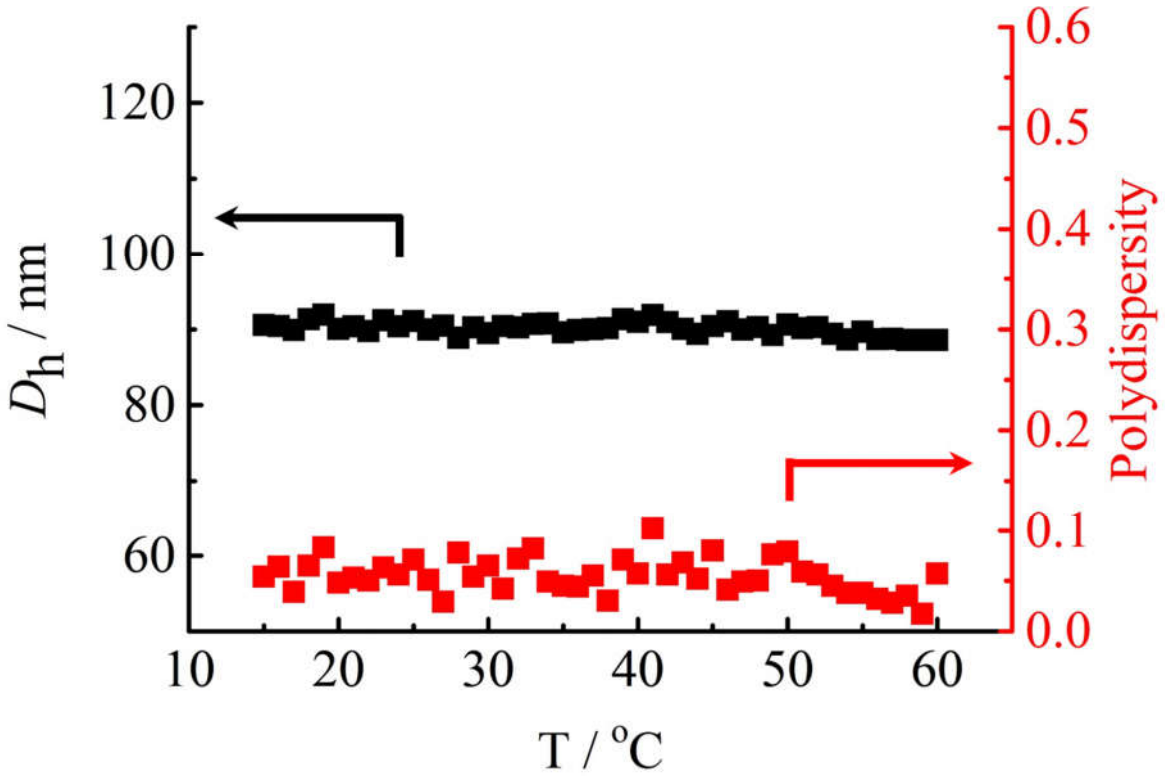

Figure 4.8. Variation of the hydrodynamic diameter (D_h) of **M4.7** (which consisted of micelle **M4.1** and $PNAM_{295}$-*b*-$PAAm_{20}$ **P4.7**) (0.5 mg mL^{-1}).

4.4.2. Reversible alteration of the sizes of mixed-corona nanoparticles

The size of a nanoparticle is an important parameter that affects the majority of applications but perhaps most notably their application in nanomedicine. In biomedical delivery applications, nanoparticle sizes greatly influence their circulation time, rate of clearance, selective tissue distribution and intracellular fate.[53] To circumvent the need for laborious syntheses to access nanoparticles of a particular size, the 'grafting to' strategy described here provides a facile method to prepare nanoparticles of controlled sizes. Indeed, we have demonstrated that a series of nanoparticles with different sizes (75 nm to 110 nm) could

be easily produced by adding complementary diblock copolymers with different chain lengths to a single preformed micelle (**M4.1** of a small size 69 nm). Moreover, the composition and properties of the newly-formed nanoparticles could be adjusted by changing the chemistry of the added complementary copolymers.

To demonstrate this approach, 1 molar eq. of complementary diblock copolymers **P4.2-4.5** were added to separate solutions of the preformed micelle **M4.1**. Hydrodynamic diameters of the resultant nanoparticles were observed to increase stepwise from *ca.* 69 nm for **M4.1** to *ca.* 75 nm for **M4.2**, then to *ca.* 110 nm for **M4.5.** We propose that this increase was due to the increase in PNIPAM chain length in the added complementary diblock copolymers. Upon heating of the mixed-corona micelle solutions, the PNIPAM chains appeared to gradually collapse until they reached their cloud point at 32 °C (Figure 4.9).

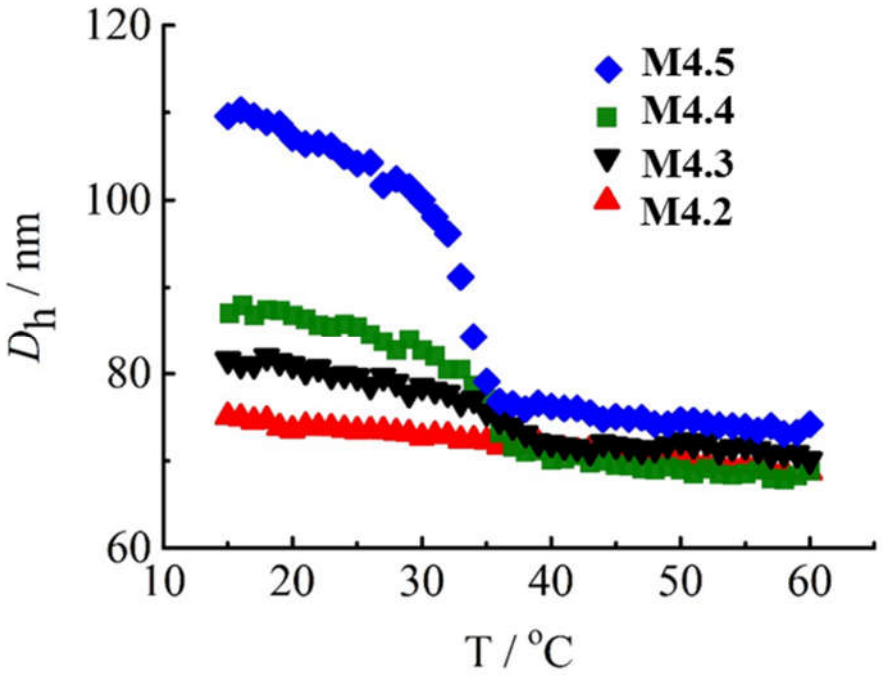

Figure 4.9. DLS analysis of the mixed-corona micelles **M4.2-4.5** (0.5 mg mL^{-1}) with different PNIPAM chain lengths heated from 15 to 60 °C.

Above 40 °C, there was no further size alteration observed by DLS analysis. It is notable that mixed-corona micelles **M4.2-4.5** all collapsed to micelles of similar sizes (70-74 nm in hydrodynamic diameter)

at 60 °C. We presumed that this was because the collapsed PNIPAM chains at elevated temperatures resided at the core-corona interface and therefore played a negligible role in determining the mixed-corona micelles' hydrodynamic diameter.

For thermo-responsive nanoparticles, fast and fully reversible switching behaviour is of great importance.[54-56] As shown in Figure 4.10, size switching of the mixed-corona micelles could be performed for at least five heating and cooling cycles, highlighting that this transition was fully reversible. More importantly, the transition could be achieved in just 2 minutes as determined by DLS analysis. We propose that the distribution of both thermo-responsive PNIPAM chains and non-responsive PNAM chains in the mixed micelle corona led to less chain entanglement and as a result a faster transition compared with micelles with sole PNIPAM as the corona.[54, 55] Therefore, the 'grafting to' mixed nature of the micelle coronas resulted in cooperative effects. The resulted mixed corona nanoparticles were more stabilized upon heating and the speed of the coronal collapse increased. The dispersity of the nanoparticles at both high and low temperatures remained below 0.1 throughout the 5 cycles. Hence, we propose that at low temperatures, the elongated PNIPAM chains served as the outer corona and stabilized the large mixed micelles. Then at high temperatures, the smaller mixed micelles remained stabilized by the hydrophilic PNAM chains, which were revealed as a result of the collapse of PNIPAM chains to the core-corona interface.

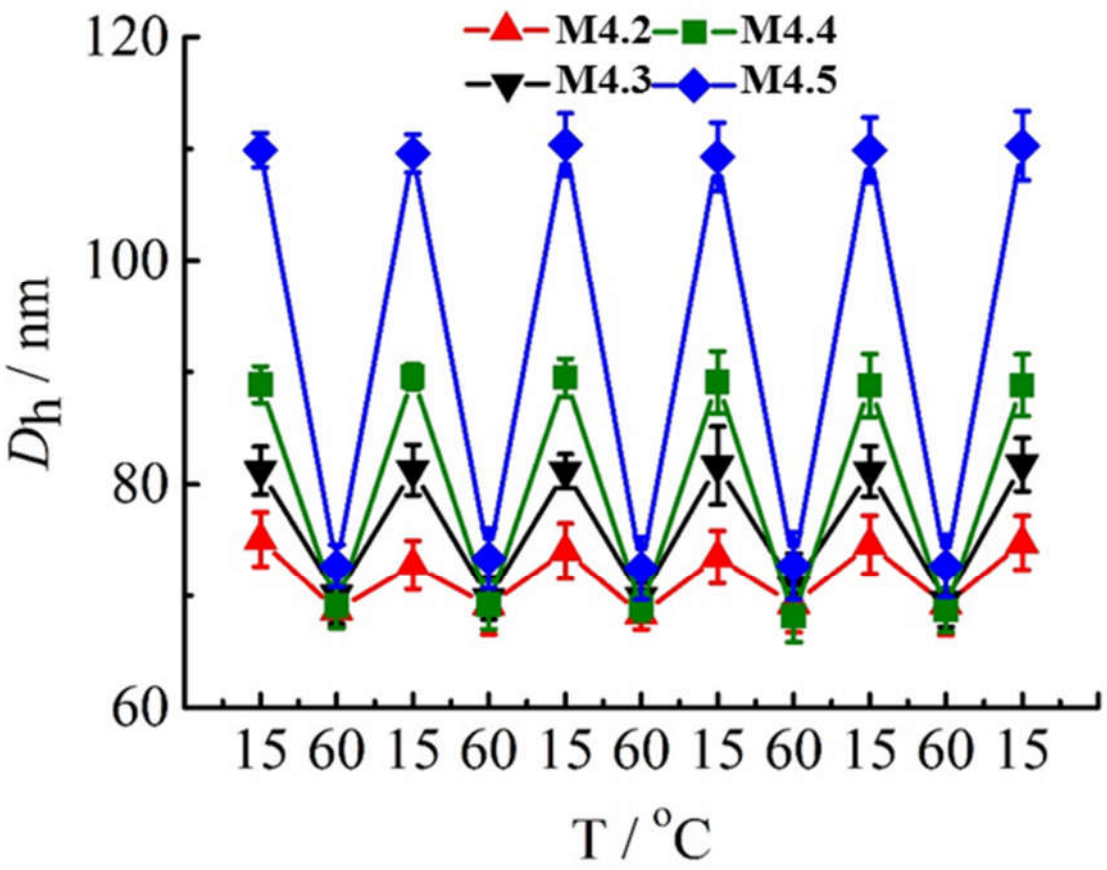

Figure 4.10. Reversible size change (D_h) of mixed-corona micelles **M4.2-4.5** (0.5 mg mL^{-1}) at both 15 and 60 °C. Error bars show size dispersity (PD).

4.4.3. Altering the coronas and surfaces of mixed-corona nanoparticles

Changes in the surface chemistry of nanostructures can be used to modulate hydrophilicity, cellular uptake and endocytosis.[49] However, it is difficult to probe a nanoparticle's surface chemistry and local environment. Recent work in our group has reported the development of aminobromomaleimide (ABM) and dithiolmalemide (DTM) fluorophores; [57, 58] a new class of highly emissive compounds which can be readily incorporated into micellar constructs without noticeable effects on the particle size or dynamics.[59, 60] Interestingly, these fluorophores show much lower emission in water compared with more hydrophobic environments and a concentration independent emission.[61] We therefore proposed that ABMs could be used as a probe to provide a fluorescence read-out of the hydrophobicity of the fluorophore's local environment.[62] In the present case, it was envisaged that ABMs could be used to reveal the hydration state

of the coronal domain of the mixed-corona micelles. ABMs can be incorporated into the R group of RAFT CTA in order to introduce into synthetic polymers effectively (Scheme 4.3). ^{1}H and ^{13}C NMR spectra confirmed the successful synthesis of the ABM-functionalized CTA (Figure 4.11).

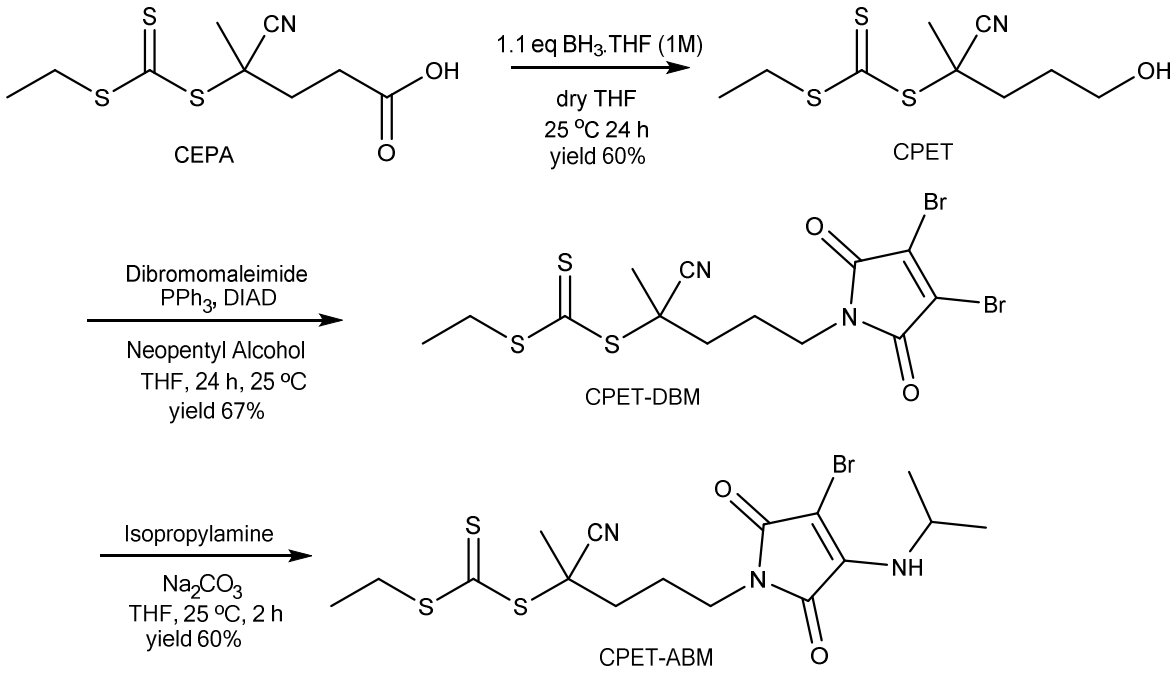

Scheme 4.3. Synthesis of an ABM functionalized RAFT agent (CPET-ABM).

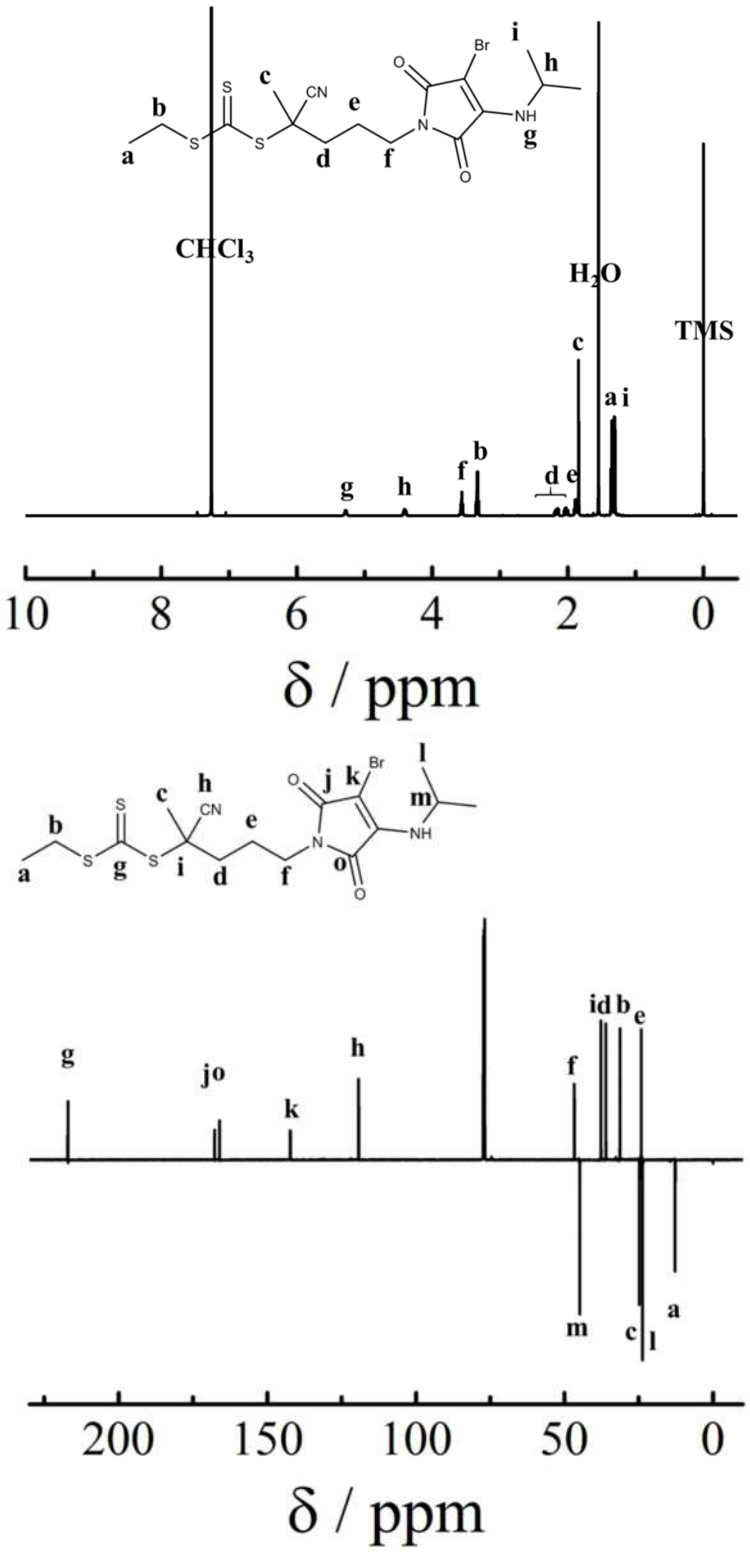

Figure 4.11. ^{1}H and ^{13}C NMR spectra of 5-(3-bromo-4-(isopropylamino)-2,5-dioxo-2,5-dihydro-1H-pyrrol-1-yl)-2-cyanopentan-2-yl ethyl carbonotrithioate (CPET-ABM) in $CDCl_3$.

Fluorescent diblock copolymer PNIPAM$_{237}$-*b*-PAAm$_{20}$ **P4.8** was synthesized (as described for **P4.2**-**4.5**) and added to preformed micelle **M4.1** to yield the mixed-corona micelle **M4.8** (Scheme 4.4 and Table 4.1). A clear fluorescence emission peak at 488 nm (λ_{ex} = 350 nm) was observed at 40 °C, (when the PNIPAM coronal chain was collapsed and hydrophobic in nature) which was attributed to the fluorescence emission of the ABM fluorophore in a hydrophobic environment (Figure 4.12). This fluorescence emission peak was no longer present at 25 °C as the elongated PNIPAM resulted in ABM being brought into a more hydrophilic environment, leading to fluorescence quenching. Note that the shoulder peak at 430 nm (in Figure 4.12) appeared as a result of scattering of the micelle solution.

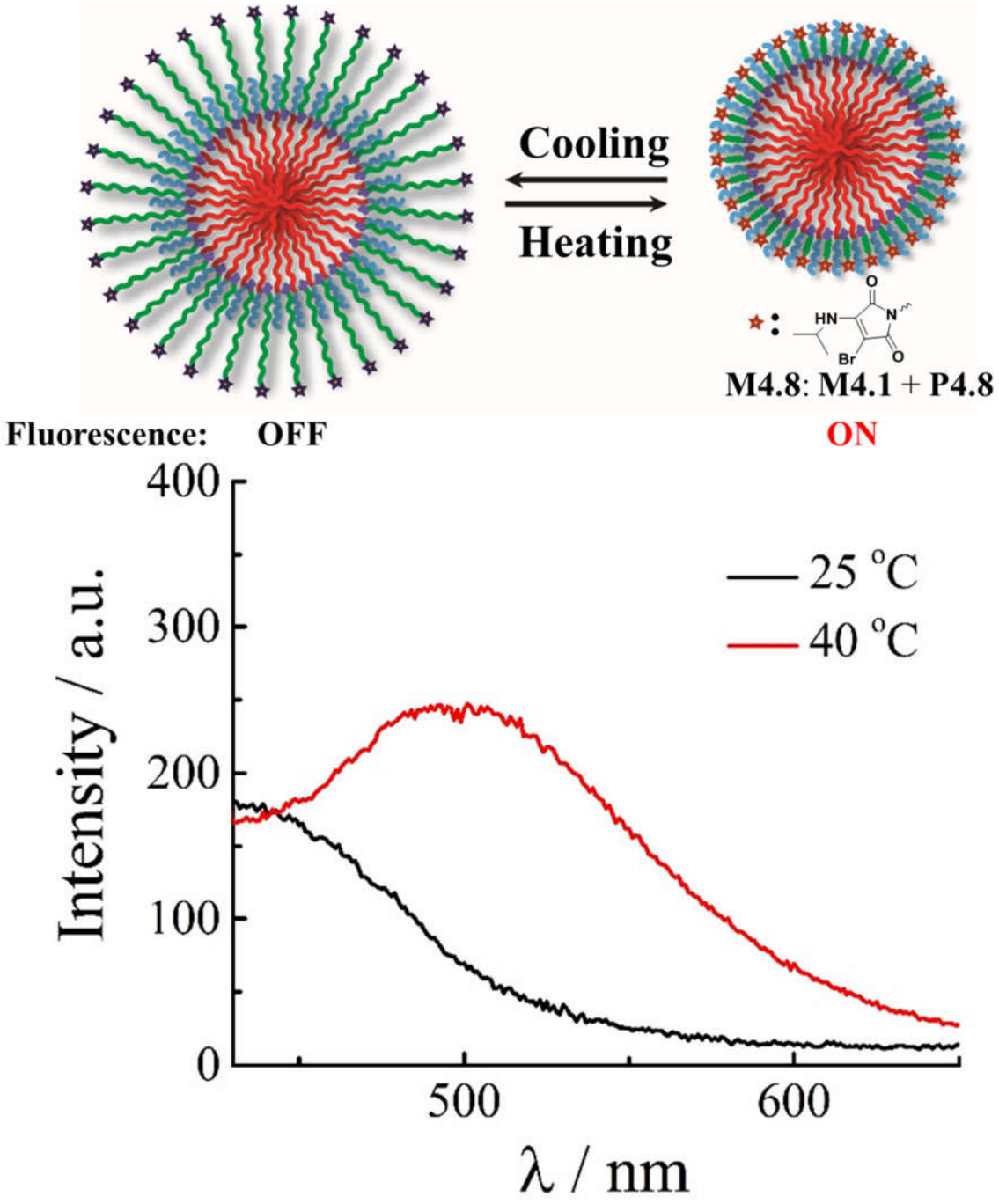

Figure 4.12. Demonstration of a reversible fluorescence ON/OFF switch using ABM-tagged mixed-corona nanoparticles and fluorescence spectra (λ_{ex} = 350 nm) of a mixed-corona micelle **M4.8** at 25 (black) and 40 °C (red).

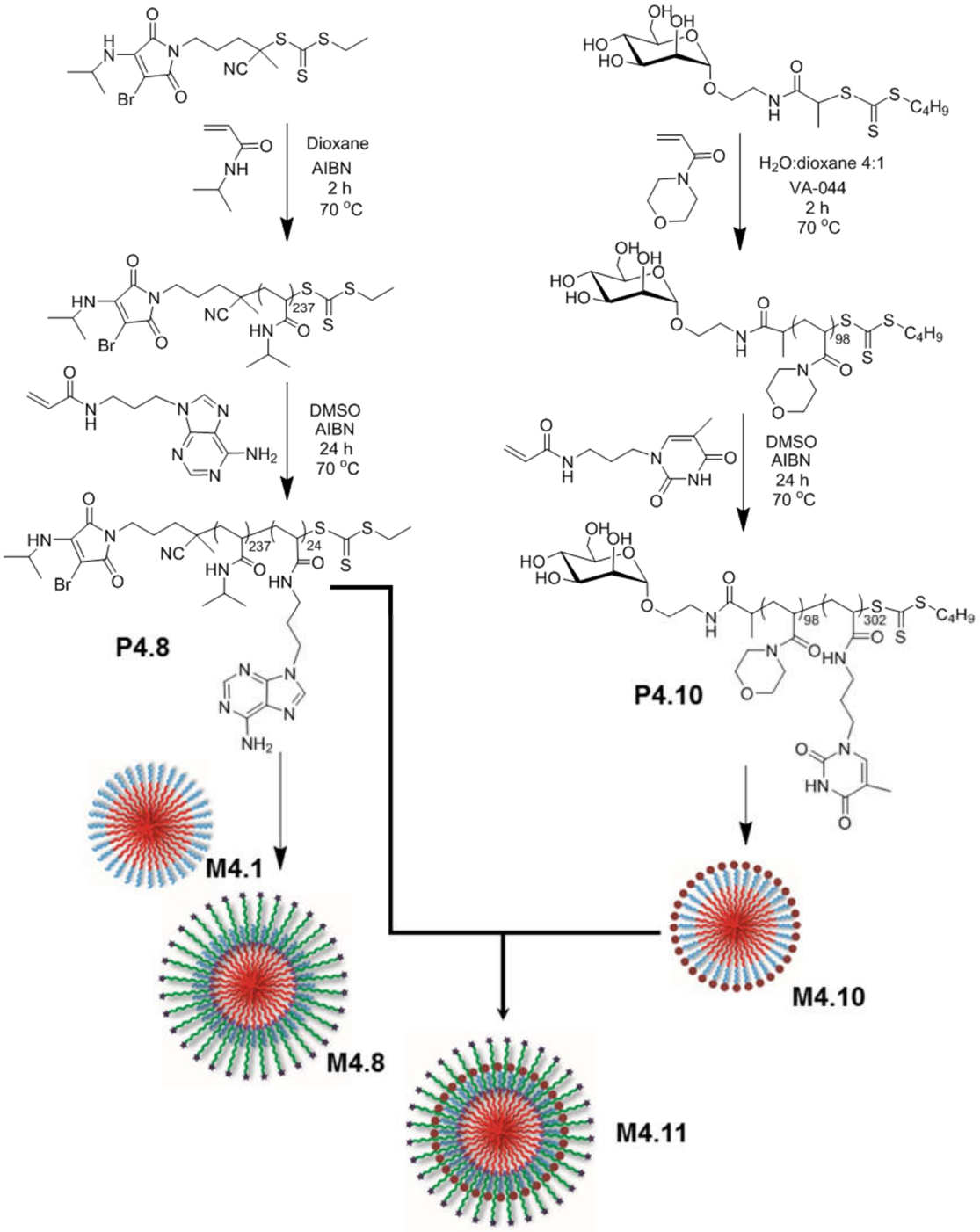

Scheme 4.4. Synthesis of ABM functionalized PNIPAM$_{237}$-*b*-PAAm$_{20}$ **P4.8** and subsequent addition to **M4.1** to afford mixed micelles **M4.8** and D-mannose functionalized PNAM$_{98}$-*b*-PTAm$_{302}$ **P4.10** and subsequent assembly to afford micelles **M4.10** and mixed micelles **M4.11**.

A control experiment using micelle **M4.4** (which did not contain the ABM functionality) displayed a slight decrease in the shoulder peak at 40 °C (Figure 4.13a), which can be rationalized by assuming that the collapsing nanostructures at 40 °C contributed to less scattering due to their smaller size. Moreover, the non-responsive corona micelle **M4.9** consisting of preformed micelle **M4.1** and ABM-functionalized $PNAM_{244}$-*b*-$PAAm_{20}$ **P4.9** exhibited no appreciable fluorescence change from 25 to 40 °C (Figure 4.13b). This is because the hydrophobicity of the coronal block does not change at elevated temperature and therefore the microenvironment of the fluorophore does not undergo any significant change. Similar fluorescence read-out to **M4.8** was observed for the mixed micelle consisting of micelle **M4.1** and ABM-attached $PNIPAM_{40}$-*b*-$PAAm_{20}$ (Figure 4.13c).

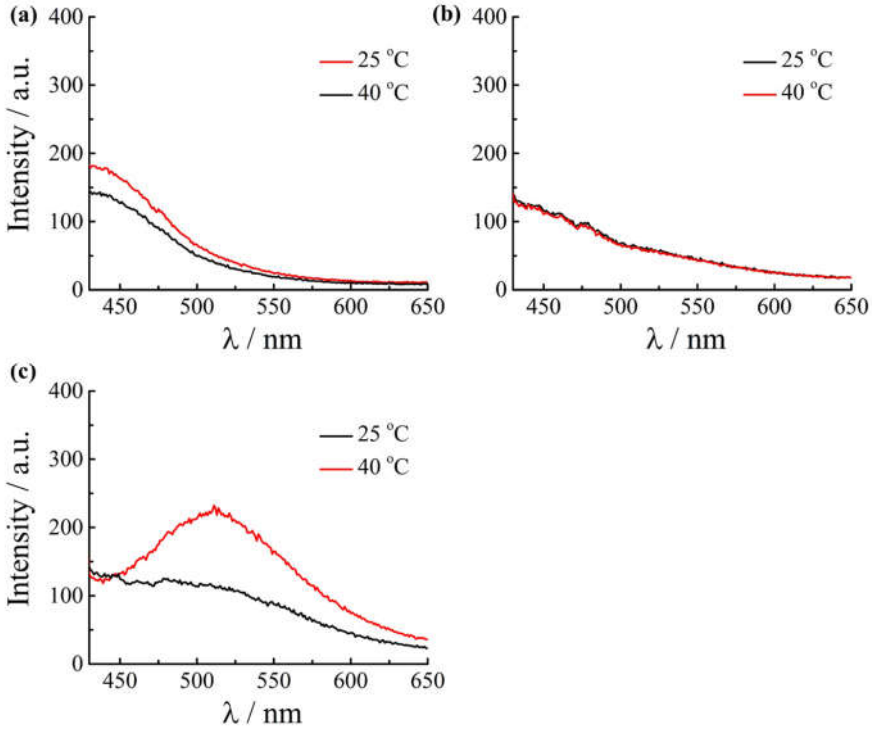

Figure 4.13. Fluorescence spectra of (a) micelle **M4.4** which does not contain the aminobromomalemide (ABM) probe; (b) the mixed-corona micelle **M4.9** which consisted of micelle **M4.1** and ABM-attached $PNAM_{244}$-*b*-$PAAm_{20}$ **P4.9** and (c) mixed micelle which consisted of micelle **M4.1** and ABM-attached $PNIPAM_{40}$-*b*-$PAAm_{20}$ at 25 and 40 °C.

The fluorescence read-out of ABMs is determined by the hydrophobic microenvironment in which the dye is located and is independent of PNIPAM length. We concluded that the fluorescence ON/OFF switch was triggered by changes in the microenvironment surrounding the ABM fluorophore upon collapse of the responsive block, this enabled a read-out of the surface state of the mixed corona micelles. Again, as suggested by DLS analysis and as shown in Figure 4.14, the temperature dependent fluorescence switch was fully reversible. At 40 °C, the intensity of the fluorescence emission peak at 488 nm did not decrease, even after 5 cycles of heating and cooling, which indicated that collapse and expansion of the PNIPAM did not lead to any loss of micelle structure and confirmed the integrity of the nucleobase interactions within the core domain during these heat-cool cycles.

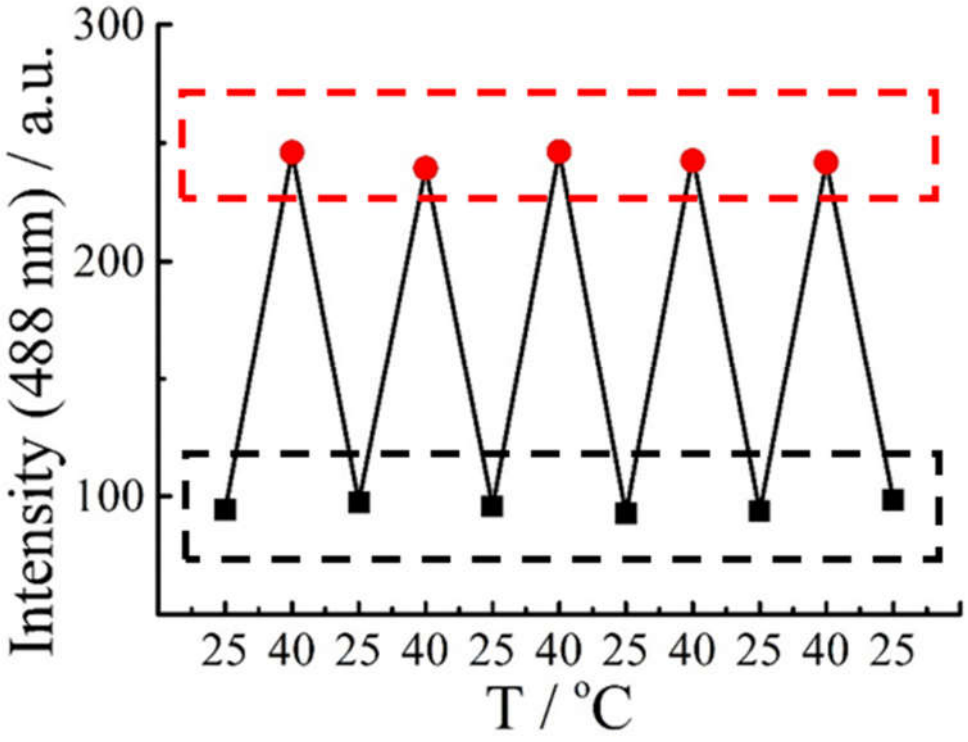

Figure 4.14. Reversible fluorescence emission intensity of **M4.8** at 488 nm at 25 °C and 40 °C for five consecutive heating and cooling cycles, λ_{ex} = 350 nm.

4.4.4. Controlling the ligand display by altering the surface of mixed-corona nanoparticle

We next explored the utility of this 'grafted to' system in controlling ligand display on the mixed micelle surface using changes in temperature. To achieve this we utilized concanavalin A (Con A), a tetrameric mannose-binding plant lectin, which can effectively bind to the ligand D-mannose with moderate binding constants.[63] This type of specific recognition between carbohydrates and proteins is involved in many complex cellular events, including cell adhesion, pathogen invasion and cancer metastasis to name but a few.[64] D-Mannose can be easily coupled to a RAFT CTA, as confirmed by NMR spectroscopy (Figure 4.15 and Scheme 4.5).

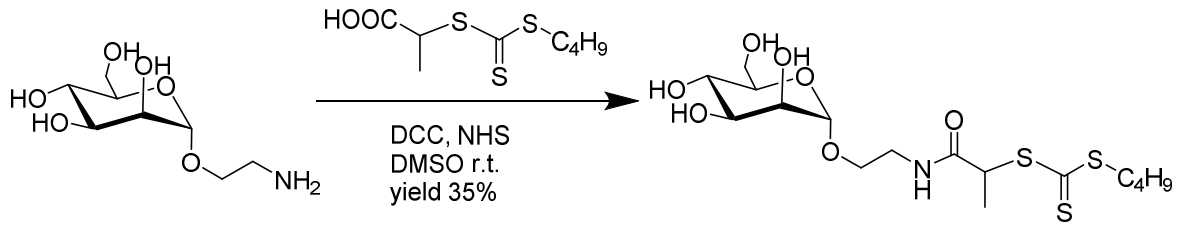

Scheme 4.5. Synthesis of the D-mannose containing RAFT CTA.

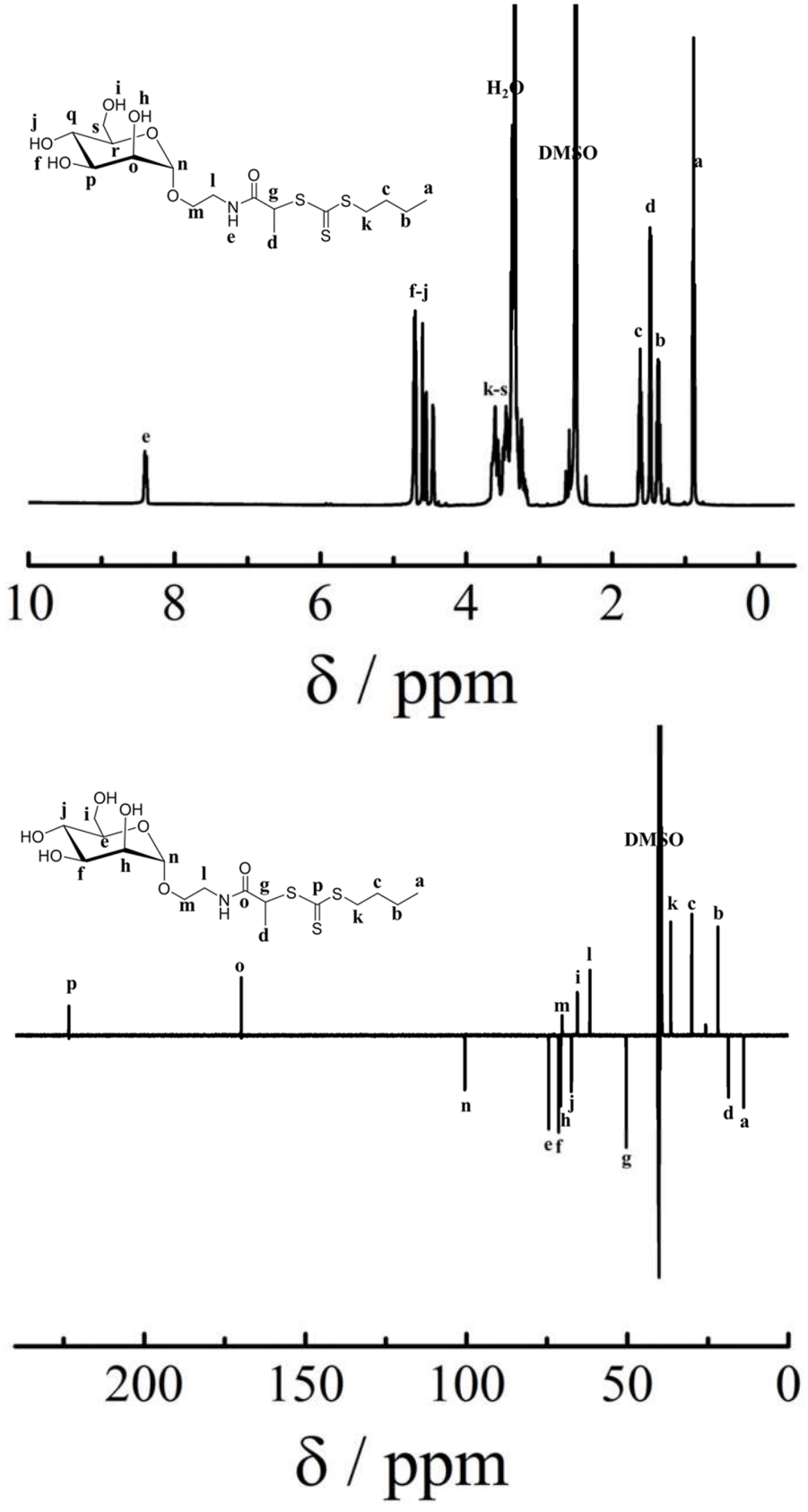

Figure 4.15. ^{1}H NMR and ^{13}C NMR spectra of D-mannose containing RAFT CTA in DMSO-d_6.

D-mannose functionalized PNAM$_{98}$-*b*-PTAm$_{302}$ **P4.10** was synthesized and self-assembled to form a non-responsive micelle **M4.10** as an experimental control (Scheme 4.4, Figure 4.16a). In addition, D-mannose containing mixed-corona micelles **M4.11** were prepared by adding diblock copolymer **P4.8** to preformed micelle **M4.10** (Scheme 4.4 and Figure 4.16b) as described for the previous mixed micellar systems. This afforded a micelle **M4.11** with a mixed-corona domain, which consisted of a responsive PNIPAM block bearing the ABM probe and a non-responsive PNAM block bearing the ligand. We proposed that the ligand could be selectively revealed and buried depending on the state of the responsive block (*i.e.* the temperature of the system).

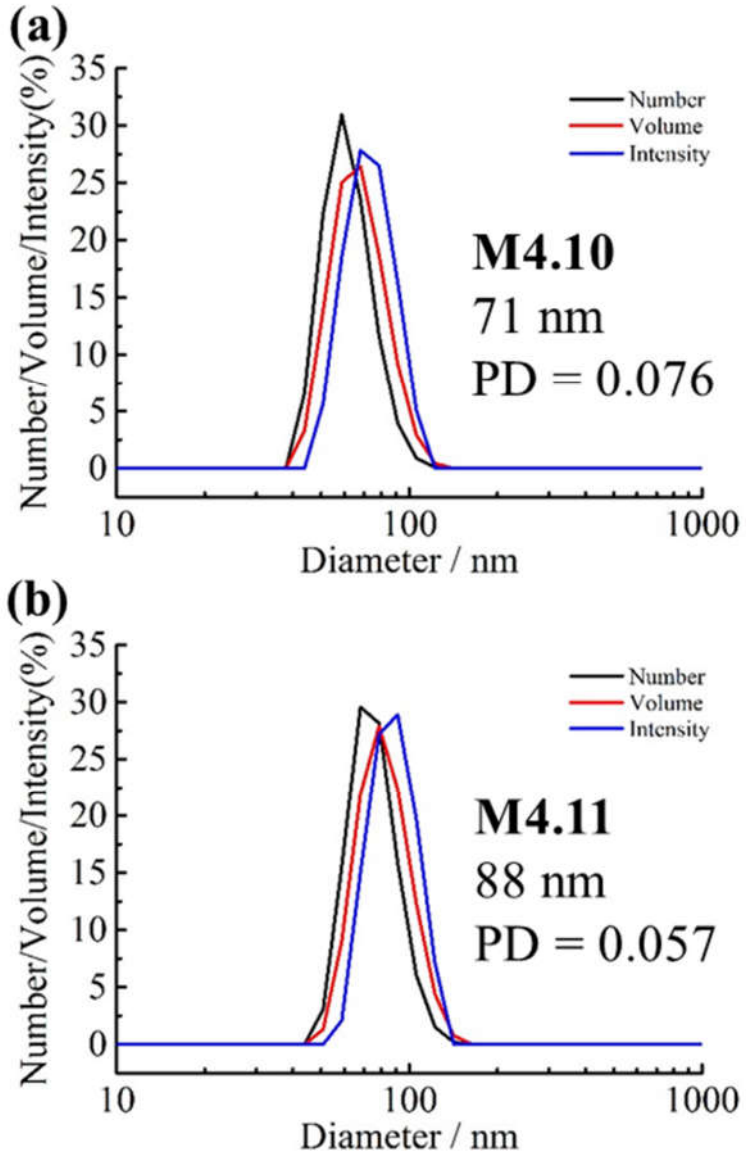

Figure 4.16. DLS analysis of (a) micelle **M4.10** and (b) mixed-corona micelle **M4.11** (0.5 mg mL^{-1}) in water at 15 °C.

To explore the temperature responsive reveal and concealment, a Con A agglutination assay was used to measure the extent of binding between Con A and **M4.11**.[65] Specifically, 50 µL of **M4.11** solution (0.38 mg mL^{-1}) was added into 300 µL of 5 mM Con A solution (the molar ratio of carbohydrate molecules to Con A is nearly 1:1). The mixture was shaken for 2 s before recording the absorbance change in time. At 25 °C, the D-mannose ligands were expected to be fully concealed by the extended PNIPAM chains and indeed no agglutination was observed at this temperature (Figure 4.17a). In contrast, at 40 °C the PNIPAM

chains were expected to collapse, revealing the ligands for binding with Con A and indeed at this temperature agglutination was observed. Notably, the binding between the ligand D-mannose with Con A is not reversible and the formed aggregates precipitated out after a few hours. No agglutination for Con A at 40 °C was observed. Further analysis of the ABM-tagged mixed-corona micelle **M4.11** using fluorescence spectroscopy confirmed the collapse of the PNIPAM above 40 °C, with the characteristic change in the emission spectrum of ABM again observed (Figure 4.17b).

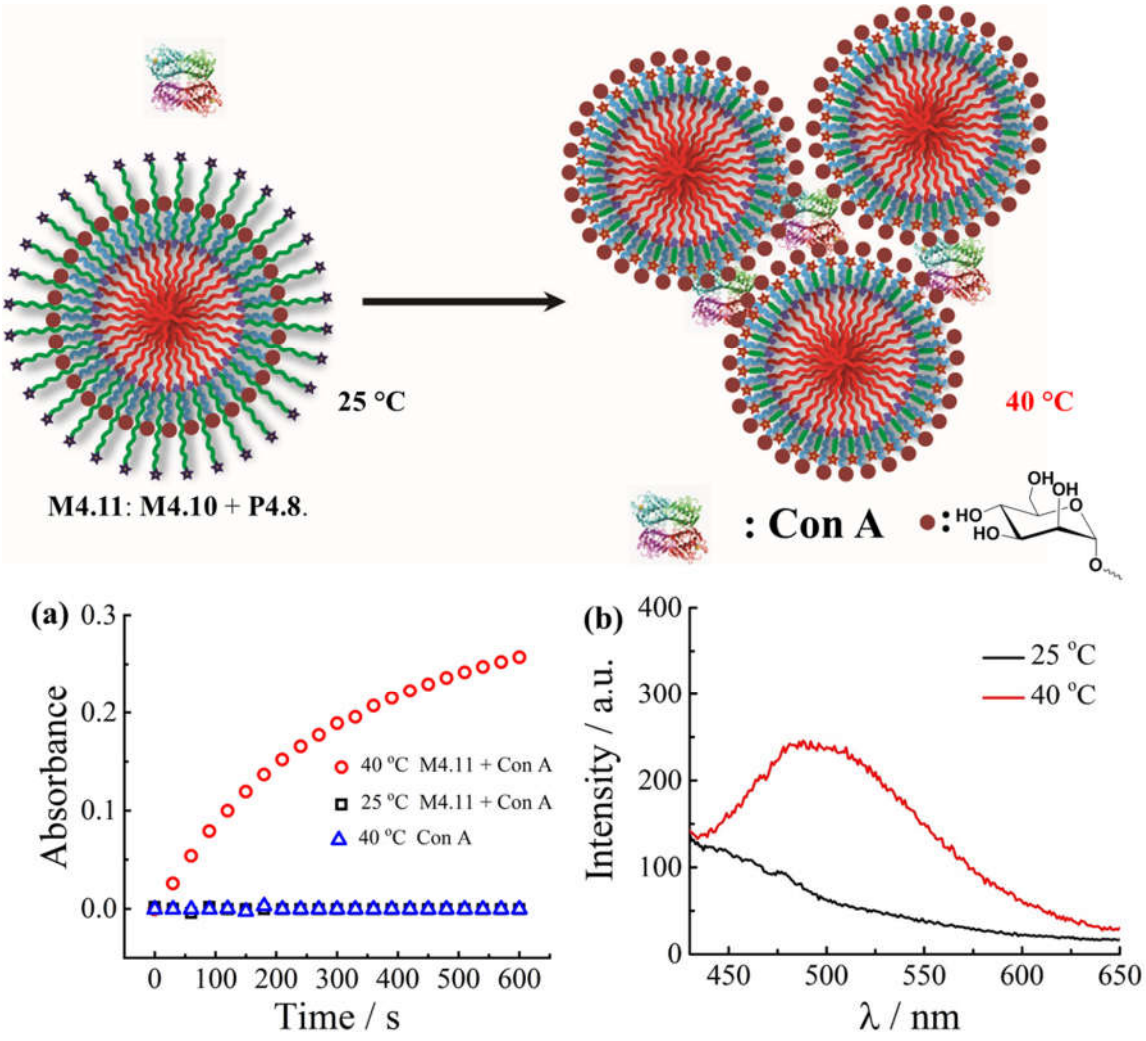

Figure 4.17. Controlled ligand display on the mixed-corona micelle surface. (a) Agglutination assay of mixed-corona micelle **M4.11** with Con A at 25 and 40 °C; Con A without M4.11 at 40 °C showing no agglutination; (b) Fluorescence spectra of **M4.11** at 25 and 40 °C, λ_{ex} = 350 nm.

4.5. Conclusions

In summary, a novel supramolecular 'grafting to' strategy, for the formation of well-defined mixed-corona micelles has been demonstrated. This strategy involved the exploitation of multiple complementary H-bonding interactions between thymine-containing micelle cores of preformed micelles and added adenine-containing diblock copolymers. Polymeric micelles with different sizes were easily prepared by changing the chain lengths of the added complementary diblock copolymers. Intra-particle chain collapse allowed micelle size and coronal state to be reversibly altered in response to an external stimulus – in this case temperature – and this could be coupled to the reversible display/concealment of ligands at the nanoparticle surface. Whilst in this work a temperature responsive block was utilized to showcase the viability of this approach for achieving the reversible presentation of functionality at the surface of a nanoparticle, other stimuli-responses could be easily utilized such as pH, light, etc. Indeed, through the synthesis of the appropriate complementary diblock copolymer, the incorporation of a diverse range of functionalities at the nanoparticles surface can be envisaged using this supramolecular 'grafting to' approach. This work provides a new route and platform to fabricate mixed polymer-grafted nanostructures and surfaces, which may find potential applications as smart materials for utilization in a range of areas such as nanomedicines.

4.6. Experimental section

4.6.1 Materials

2,2'-Azo-bis(isobutyronitrile) (AIBN) was obtained from Molekula and recrystallized from methanol. 2,2'-Azobis[2-(2-imidazolin-2-yl)propane]dihydrochloride (VA-044, Wako) was used without further purification. Concanavalin A (Con A) was used as purchased from Sigma-Aldrich. 4-Acryloylmorpholine (NAM) was bought from Sigma-Aldrich and was purified by vacuum distillation. *N*-isopropylacrylamide (NIPAM) was purchased from Sigma-Aldrich and recrystallized from a toluene-hexane mixture prior to use. 3-(Adenine-9-yl)propyl acrylamide (AAm), 3-(thymin-1-yl)propyl acrylamide (TAm), 2-(((butylthio)carbonothiolyl)thio)propanoic acid and micelle **M4.1** were synthesized as described previously[17] and stored at 4 °C. DMF, DMSO and other chemicals were obtained from Fisher Chemicals and used without further purification. Dry solvents were obtained by passing over a column of activated alumina using an Innovative Technologies solvent purification system. Dialysis membranes (MWCO = 3.5 kDa) were purchased from Spectra/Por.

4.6.2 Instrumentation

^{1}H NMR and ^{13}C NMR spectra were recorded on a Bruker DPX-300, DPX-400 or HD500 spectrometer with DMSO-d_6 or $CDCl_3$ as the solvent. The chemical shifts of protons were reported relative to tetramethylsilane (TMS) at δ = 0 ppm when using $CDCl_3$ or solvent residues (DMSO 2.50 ppm). UV-vis spectra were recorded on a Perkin-Elmer Lambda 35 UV-vis instrument. Turbidimetry assays were performed as described in a previous publication.[65] Fluorescence spectra were recorded using an Agilent Cary Eclipse Fluorescence spectrophotometer. The samples were incubated at the relevant temperatures for at least 2 minutes and then measured immediately. High resolution mass spectrometry (HR-MS) was conducted on a Bruker UHR-Q-TOF MaXis with electrospray ionization (ESI). Size exclusion chromatography (SEC) data were obtained in HPLC grade DMF containing 5 mM NH_4BF_4 at 50 °C, with

a flow rate of 1.0 mL min^{-1}, on a set of two PLgel 5 μm Mixed-D columns, and a guard column. SEC data was analyzed with Cirrus SEC software calibrated using poly(methyl methacrylate) (PMMA) standards. Hydrodynamic diameters (D_h) and size distributions of the self-assemblies were determined by dynamic light scattering (DLS). The DLS instrumentation consisted of a Malvern Zetasizer NanoS instrument with a 4 mW He-Ne 633 nm laser module. Measurements were made at a detection angle of 173°, and Malvern DTS 7.03 software was used to analyze the data. D_h was calculated by fitting the apparent diffusion coefficient in the Stokes-Einstein equation $D_h = kT/(3\pi\eta D_{app})$, where k, T and η are the Boltzmann constant, the temperature and the viscosity of the solvent, respectively. As the measured sample is a solution of monodispersed spherical micelles, D_h coincides to the real hydrodynamic diameter as D_{app} is equal to the translational diffusion coefficient (D_t). For thermo-responsive size change, all measurements were run at least three times with a minimum of 10 runs per measurement for every temperature point. For reversible size change, the samples were incubated at the relevant temperature for 2 minutes before measurement. Static light scattering (SLS) measurements were conducted with an ALV CGS3 (λ = 632 nm) at different temperatures. The data were collected from 50° to 150° with an interval of 10° against a toluene standard. The self-assembled solutions were filtered through 0.45 μm nylon filters prior to analysis.

TEM observations were performed on a JEOL 2000FX electron microscope at an acceleration voltage of 200 kV. TEM samples were prepared by drop deposition of an aqueous solution onto a copper grid coated with Formvar. Generally, a drop of sample (10 μL) was pipetted on a grid and left for several minutes, then blotted away. Uranyl acetate (UA, 1%) was used for the staining of TEM samples. TEM images were analyzed using the ImageJ software package, and over 100 particles were counted for each sample to obtain number-average diameter D_n (for spherical micelles).

4.6.3 Synthesis of 2-cyano-5-hydroxypentan-2-yl ethyl carbonotrithioate (CPET)

To a flame-dried round bottom flask, 4-cyano-4-(((ethylthio)carbonothioyl)thio)pentanoic acid (CEPA) (10 g, 38 mmol) was added followed by the addition of dry tetrahydrofuran (250 mL) with the resulting solution cooled to -78 °C. 1 M Borane tetrahydrofuran complex solution (40 mL, 39.9 mmol) was subsequently added dropwise over 30 min. The reaction mixture was left to stir for 1 h, after which the cooling bath was removed and the reaction stirred overnight at ambient temperature under a nitrogen atmosphere. After 24 h of stirring, methanol (100 mL) was added in five portions and stirred for 10 min after each addition until no further bubbling was observed. After removal of tetrahydrofuran and methanol under vacuum, the organic residue was dissolved in diethyl ether (250 mL) and washed with saturated $NaHCO_3$ solution (3 × 250 mL) and then with brine (250 mL). Further extraction using diethyl ether from the collected aqueous layers was carried out. The combined organic layers were dried over anhydrous $MgSO_4$, filtered and evaporated to dryness. Purification was carried out using silica gel flash column chromatography (petroleum ether 40/60:ethyl acetate = 1:1) affording 2-cyano-5-hydroxypentan-2-yl ethyl carbonotrithioate (CPET) as an orange-red oil (5.64 g, 22.6 mmol, 60%).

^{1}H NMR (500 MHz, $CDCl_3$): δ = 3.72 (t, J_{H-H} = 6.0 Hz, 2H), 3.34 (q, J_{H-H} = 7.5 Hz, 2H), 2.4-2.0 (m, 2H), 1.89 (s, 3H), 1.88-1.78 (m, 2H), 1.35 (t, J_{H-H} = 7.5 Hz, 3H) ppm.

^{13}C NMR (125 MHz, $CDCl_3$): δ = 217.4, 119.5, 61.7, 46.9, 35.7, 31.3, 27.9, 24.9, 12.8 ppm. HR-MS (m/z) found 272.0216, calc. 272.0208 $[M+Na]^+$.

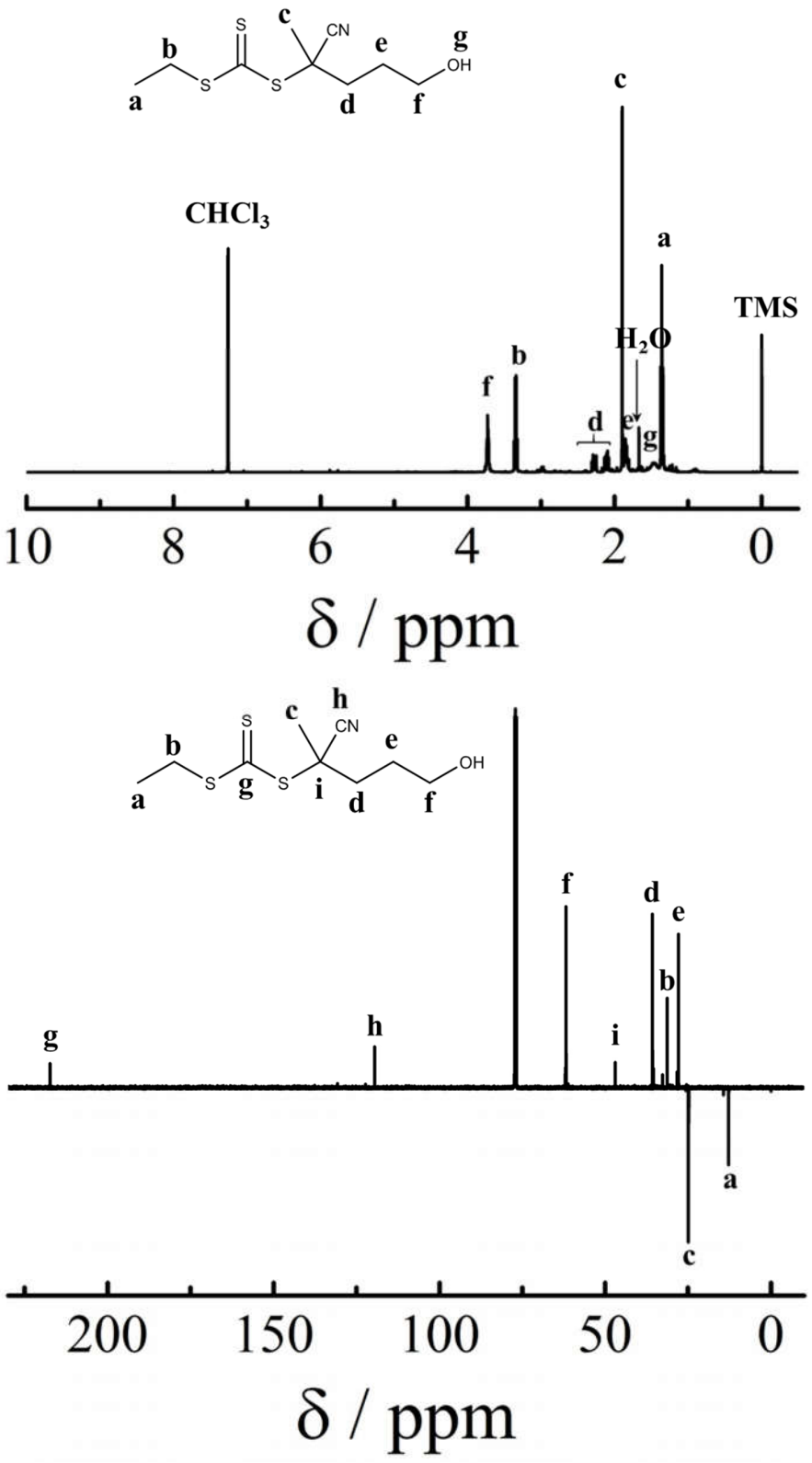

Figure 4.18. ^{1}H and ^{13}C NMR spectra of 2-cyano-5-hydroxypentan-2-yl ethyl carbonotrithioate (CPET) in $CDCl_3$.

4.6.4. Synthesis of 2-cyano-5-(3,4-dibromo-2,5-dioxo-2,5-dihydro-1H-pyrrol-1-yl)pentan-2-yl ethyl carbonotrithioate (CPET-DBM)

To a flame-dried round bottom flask, triphenylphosphine (5.67 g, 21.6 mmol) was added followed by the addition of dry tetrahydrofuran (150 mL) and the resulting solution cooled to -78 °C. Diisopropyl azodicarboxylate (DIAD) (4.26 mL, 21.6 mmol) was added dropwise over 2-3 min. Reaction mixture was stirred for 5 min after which 2-cyano-5-hydroxypentan-2-yl ethyl carbonotrithioate (CPET) (5.39 g, 21.6 mmol) dissolved in dry tetrahydrofuran (25 mL) was added using air sensitive techniques and stirred for 5 min. Neopentyl alcohol (0.95 g, 10.8 mmol) was added and the reaction mixture left to stir for 10 min. Dibromomaleimide (5.51 g, 21.6 mmol) was then added to the reaction mixture. The resulting suspension was allowed to remain at -78 °C for 10 min before the cooling bath was removed and the reaction was stirred overnight at ambient temperature under a nitrogen atmosphere. After removal of tetrahydrofuran under vacuum, purification was carried out using silica gel flash column chromatography (dichloromethane:petroleum ether 40/60 = 3:1) affording 2-cyano-5-(3,4-dibromo-2,5-dioxo-2,5-dihydro-1H-pyrrol-1-yl)pentan-2-yl ethyl carbonotrithioate (CPET-DBM) as an orange red oil (7.01 g, 14.4 mmol, 67%).

^{1}H NMR (300 MHz, $CDCl_3$): δ = 3.68 (t, $J_{H\text{-}H}$ = 6.9 Hz, 2H), 3.33 (q, $J_{H\text{-}H}$ = 7.5 Hz, 2H), 2.3-2.0 (m, 2H), 1.92 (m, 2H), 1.84 (s, 3H), 1.35 (t, $J_{H\text{-}H}$ = 7.5 Hz, 3H) ppm.

^{13}C NMR (75 MHz, $CDCl_3$): δ = 217.0, 163.8, 129.5, 119.1, 46.5, 38.8, 35.8, 31.4, 24.8, 24.0, 12.7 ppm.

HR-MS (m/z) found 506.8476, calc. 506.8476 $[M+Na]^+$.

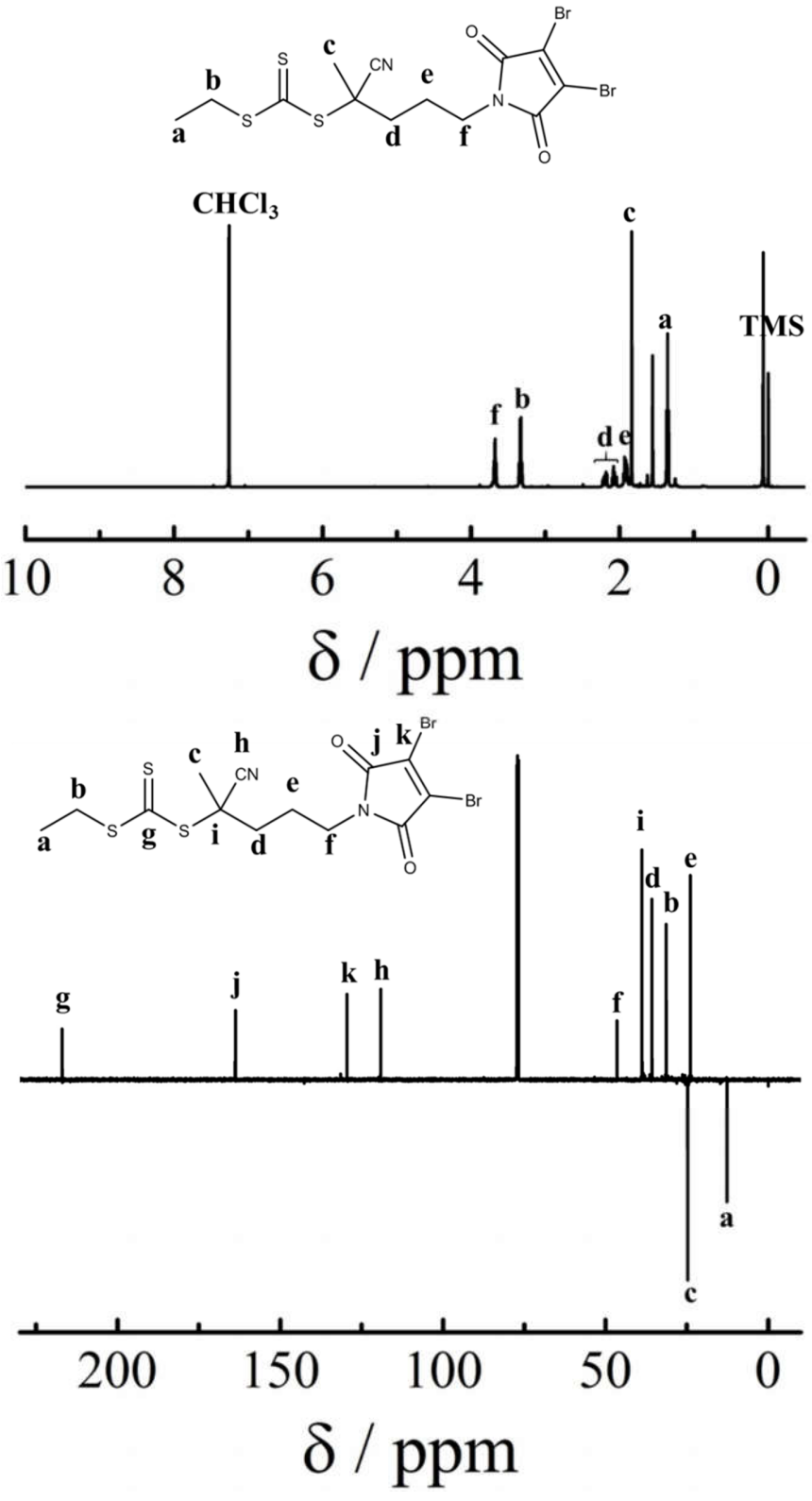

Figure 4.19. ^{1}H and ^{13}C NMR spectra of 2-cyano-5-(3,4-dibromo-2,5-dioxo-2,5-dihydro-1H-pyrrol-1-yl)pentan-2-yl ethyl carbonotrithioate (CPET-DBM) in $CDCl_3$.

4.6.5. Synthesis of 5-(3-bromo-4-(isopropylamino)-2,5-dioxo-2,5-dihydro-1H-pyrrol-1-yl)-2-cyanopentan-2-yl ethyl carbonotrithioate (CPET-ABM)

To a suspension of Na_2CO_3 (3.72 g, 35.1 mmol) and 2-cyano-5-(3,4-dibromo-2,5-dioxo-2,5-dihydro-1H-pyrrol-1-yl)pentan-2-yl ethyl carbonotrithioate (CPET-DBM) (6.83 g, 14 mmol) in tetrahydrofuran (150 mL), isopropylamine (3.02 mL, 35.1 mmol) was added. The reaction mixture was stirred at room temperature with the conversion of CPET-DBM monitored by thin layer chromatography. After 1 hour, tetrahydrofuran was removed under vacuum and the organic residue dissolved in dichloromethane (250 mL) and washed with deionized water (3 × 250 mL). Organic layer was dried over anhydrous $MgSO_4$, filtered and evaporated to dryness. Purification was carried out using silica gel flash column chromatography (dichloromethane:petroleum ether 40/60 = 9:1) affording 5-(3-bromo-4-(isopropylamino)-2,5-dioxo-2,5-dihydro-1H-pyrrol-1-yl)-2-cyanopentan-2-yl ethyl carbonotrithioate (CPET-ABM) as an orange red oil (3.92 g, 8.44 mmol, 60%).

^1H and ^{13}C NMR spectra are shown in Figure 4.11.

^1H NMR (500 MHz, $CDCl_3$): δ = 5.28 (d, J_{H-H} = 8.7 Hz, 1H), 4.41 (m, J_{H-H} = 6.6 and 8.7 Hz, 1H), 3.56 (t, J_{H-H} = 6.6 Hz, 2H), 3.33 (q, J_{H-H} = 7.5 Hz, 2H), 2.25-1.95 (m, 2H), 1.95-1.7 (m, 2H), 1.84 (s, 3H), 1.4-1.25 (m, 9H) ppm.

^{13}C NMR (125 MHz, $CDCl_3$): δ = 217.1, 167.7, 166.0, 142.2, 119.2, 46.6, 44.8, 37.7, 36.0, 31.3, 24.8, 24.1, 23.7, 12.7 ppm.

HR-MS (m/z) found 485.9948, calc. 485.9950 $[M+Na]^+$.

4.6.6. Synthesis of D-mannose containing RAFT CTA

The synthetic route to prepare the D-mannose containing RAFT CTA is shown in Scheme 4.5. (2-aminoethyl)-α-D-mannopyranoside was prepared as reported previously.[66] It was used for the synthesis of D-mannose containing CTA as follows. Dicyclohexylcarbodiimide (DCC) (49.5 mg, 0.24 mmol) was slowly added to a solution of 2-(((butylthio)carbonothiolyl)thio)propanoic acid (CTA) (47.6 mg, 0.2

mmol) and *N*-hydroxylsuccinimide (NHS) (27.6 mg, 0.24 mmol) in CH_2Cl_2, cooled to 0 °C with an ice bath. The solution was stirred for 2 h then filtered. To the filtrate was added (2-aminoethyl)-α-D-mannopyranoside (44 mg, 0.2 mmol). The reaction solution was further stirred overnight. The reaction solution was concentrated under vacuum and the residue was further purified by column chromatography using a mixture of CH_2Cl_2 and CH_3OH as eluent and a gradient from 1:0 to 93:7 to give a yellow solid (31 mg, 0.07 mmol, 35%).

^1H and ^{13}C NMR spectra are shown in Figure 4.15.

^1H NMR (500 MHz, DMSO-d_6) δ = 8.40 (m, 1H), 4.40-4.74 (m, 5H), 3.17-3.66 (m, 13H), 1.62 (m, 2H), 1.48 (d, J = 7.0 Hz, 3H), 1.37 (m, 2H), 0.89 (t, J = 7.0 Hz, 3H) ppm.

^{13}C NMR (125 MHz, DMSO-d_6) δ = 223.4, 169.9, 100.4, 74.4, 71.4, 70.7, 70.3, 67.4, 65.5, 61.7, 50.4, 36.5, 30.1, 21.9, 18.7, 13.9 ppm.

HR-MS (m/z) found 466.0996, calc. 466.0998 $[M+Na]^+$.

4.6.7. Synthesis of poly(*N*-isopropylacrylamide) (PNIPAM) macro-CTA *via* RAFT polymerization

The typical procedure was as follows; a 10 mL ampoule was charged with NIPAM (339.5 mg, 3.0 mmol), 2-(((butylthio)carbonothiolyl)thio)propanoic acid (2.4 mg, 0.01 mmol), AIBN (0.16 mg, 0.001 mmol) and 1,4-dioxane (0.68 mL). The mixture was thoroughly degassed *via* 4 freeze-pump-thaw cycles, filled with nitrogen and then immersed in an oil bath at 70 °C for 2 h. The conversion was determined by ^1H NMR spectroscopy. The polymerization solution was then precipitated three times from cold diethyl ether. The light yellow polymer was dried in a vacuum oven overnight at room temperature and analyzed by ^1H NMR spectroscopy and DMF SEC.

4.6.8. Synthesis of $PNIPAM_x$-*b*-$PAAm_y$ diblock copolymers

The typical procedure was as follows; for $PNIPAM_{262}$-*b*-$PAAm_{20}$; $PNIPAM_{262}$ (75 mg, 0.0025 mmol), AAm (15.4 mg, 0.0625 mmol), and AIBN (0.04 mg, 0.00025 mmol) were dissolved in DMSO (0.3 mL).

The mixture was thoroughly degassed *via* 4 freeze-pump-thaw cycles, filled with nitrogen and then immersed in an oil bath at 70 °C overnight. An aliquot of the crude product was taken and analyzed by ^{1}H NMR spectroscopy to calculate the conversion. The residual solution was precipitated three times from cold CH_3OH. The light yellow polymer was dried in a vacuum oven overnight at room temperature and analyzed by ^{1}H NMR spectroscopy and DMF SEC.

4.6.9. Self-assembly of PNAM$_{98}$-*b*-PTAm$_{302}$ P4.10 diblock copolymer in water

The copolymer PNAM$_{98}$-*b*-PTAm$_{302}$ **P4.10** was synthesized using a D-mannose containing CTA. For the self-assembly of **P4.10**, a solvent switch method was used. Specifically, the copolymer was dissolved in DMF (at 8 mg mL^{-1}) and stirred for 2 h. Then an excess of 18.2 MΩ·cm water was added *via* a syringe pump at a rate of 1 mL h^{-1}. The final volume ratio between water and organic solvent was 8:1. The solution was then dialyzed against 18.2 MΩ·cm water (MWCO = 3.5 kDa), incorporating at least 6 water changes, to afford self-assemblies (M10) at a concentration of *ca.* 1 mg mL^{-1}.

4.6.10. Preparation of mixed-corona micelles containing PNIPAM-*b*-PAAm and PNAM-*b*-PTAm

Diblock copolymers PNIPAM$_x$-*b*-PAAm$_y$ **P4.2-4.9** were dissolved in H_2O at 10 mg mL^{-1}. This was then added to the micellar solution of **M4.1** or **M4.10** (0.5 mg mL^{-1}) dropwise with stirring. The molar ratios were calculated according to the M_n determined from ^{1}H NMR spectroscopic analysis and the polymer mass concentration. The mixture was then sealed and allowed to stir at room temperature for at least 2 h. The solutions were then analyzed by DLS, TEM and SLS.

4.7. References

1. G. M. Peters and J. T. Davis, *Chem. Soc. Rev.*, **2016**, *45*, 3188-3206.

2. E. Krieg, M. M. Bastings, P. Besenius and B. Rybtchinski, *Chem. Rev.*, **2016**, *116*, 2414-2477.

3. R. McHale and R. K. O'Reilly, *Macromolecules*, **2012**, *45*, 7665-7675.

4. B. D. Mather, M. B. Baker, F. L. Beyer, M. D. Green, M. A. G. Berg and T. E. Long, *Macromolecules*, **2007**, *40*, 4396-4398.

5. K. Zhang, S. J. Talley, Y. P. Yu, R. B. Moore, M. Murayama and T. E. Long, *Chem. Commun.*, **2016**, *52*, 7564-7567.

6. J.-F. Lutz, A. F. Thunemann and K. Rurack, *Macromolecules*, **2005**, *38*, 8124-8126.

7. H. J. Spijker, F. L. van Delft and J. C. M. van Hest, *Macromolecules*, **2007**, *40*, 12-18.

8. K. Zhang, M. Aiba, G. B. Fahs, A. G. Hudson, W. D. Chiang, R. B. Moore, M. Ueda and T. E. Long, *Polym. Chem.*, **2015**, *6*, 2434-2444.

9. J. Romulus and M. Weck, *Macromol. Rapid Commun.*, **2013**, *34*, 1518-1523.

10. A. Khan, D. M. Haddleton, M. J. Hannon, D. Kukulj and A. Marsh, *Macromolecules*, **1999**, *32*, 6560-6564.

11. C. R. South and M. Weck, *Macromolecules*, **2007**, *40*, 1386-1394.

12. P. K. Lo and H. F. Sleiman, *J. Am. Chem. Soc.*, **2009**, *131*, 4182-4183.

13. R. McHale, J. P. Patterson, P. B. Zetterlund and R. K. O'Reilly, *Nat. Chem.*, **2012**, *4*, 491-497.

14. P. J. Milnes, M. L. McKee, J. Bath, L. Song, E. Stulz, A. J. Turberfield and R. K. O'Reilly, *Chem. Commun.*, **2012**, *48*, 5614-5616.

15. Y. Tao, K. Satoh and M. Kamigaito, *Macromol. Rapid Commun.*, **2011**, *32*, 226-232.

16. Y. Kang, A. Pitto-Barry, M. S. Rolph, Z. Hua, I. Hands-Portman, N. Kirby and R. K. O'Reilly, *Polym. Chem.*, **2016**, *7*, 2836-2846.

17. Z. Hua, A. Pitto-Barry, Y. Kang, N. Kirby, T. R. Wilks and R. K. O'Reilly, *Polym. Chem.*, **2016**, *7*, 4254-4262.

18. F. Ilhan, T. H. Galow, M. Gray, G. Clavier and V. M. Rotello, *J. Am. Chem. Soc.*, **2000**, *122*, 5895-5896.

19. Z. Li, Y. Zhang, P. Fullhart and C. A. Mirkin, *Nano Lett.*, **2004**, *4*, 1055-1058.

20. P. W. K. Rothemund, *Nature*, **2006**, *440*, 297-302.

21. E. Stahl, T. G. Martin, F. Praetorius and H. Dietz, *Angew. Chem., Int. Ed.*, **2014**, *53*, 12735-12740.

22. R. J. Thibault, P. J. Hotchkiss, M. Gray and V. M. Rotello, *J. Am. Chem. Soc.*, **2003**, *125*, 11249-11252.

23. T. R. Wilks, J. Bath, J. W. de Vries, J. E. Raymond, A. Herrmann, A. J. Turberfield and R. K. O'Reilly, *ACS Nano*, **2013**, *7*, 8561-8572.

24. L. Ionov and S. Minko, *ACS Appl. Mater. Interfaces*, **2012**, *4*, 483-489.

25. S. Minko, M. Muller, D. Usov, A. Scholl, C. Froeck and M. Stamm, *Phys. Rev. Lett.*, **2002**, *88*, 035502.

26. L. Zhang, Z. Zhang and P. Wang, *NPG Asia Mater.*, **2012**, *4*, e8.

27. J. Song, J. Zhou and H. Duan, *J. Am. Chem. Soc.*, **2012**, *134*, 13458-13469.

28. Z. Zhang, C. Zhou, H. Dong and D. Chen, *Angew. Chem., Int. Ed.*, **2016**, *55*, 6182-6186.

29. B. Zhao and L. Zhu, *Macromolecules*, **2009**, *42*, 9369-9383.

30. R. Barbey, L. Lavanant, D. Paripovic, N. Schuwer, C. Sugnaux, S. Tugulu and H.-A. Klok, *Chem. Rev.*, **2009**, *109*, 5437–5527.

31. R. R. Patil, S. Turgman-Cohen, J. Šrogl, D. Kiserow and J. Genzer, *ACS Macro Lett.*, **2015**, *4*, 251-254.

32. P. Brandani and P. Stroeve, *Macromolecules*, **2003**, *36*, 9492-9501.

33. A. S. Goldmann, L. Barner, M. Kaupp, A. P. Vogt and C. Barner-Kowollik, *Prog. Polym. Sci.*, **2012**, *37*, 975-984.

34. K. Ohno, Y. Ma, Y. Huang, C. Mori, Y. Yahata, Y. Tsujii, T. Maschmeyer, J. Moraes and S. Perrier, *Macromolecules*, **2011**, *44*, 8944-8953.

35. A. Olivier, F. Meyer, J.-M. Raquez, P. Damman and P. Dubois, *Prog. Polym. Sci.*, **2012**, *37*, 157-181.

36. C. M. Hui, J. Pietrasik, M. Schmitt, C. Mahoney, J. Choi, M. R. Bockstaller and K. Matyjaszewski, *Chem Mater*, **2014**, *26*, 745-762.

37. A. C. Balazs, C. Singh, E. Zhulina, S.-S. Chern, Y. Lyatskaya and G. Pickett, *Prog. Surf. Sci.*, **1997**, *55*, 181-269.

38. J. Zhao, H. Lai, H. Lu, C. Barner-Kowollik, M. H. Stenzel and P. Xiao, *Biomacromolecules*, **2016**, *17*, 2946-2955.

39. N. Zhan, G. Palui, J. P. Merkl and H. Mattoussi, *J. Am. Chem. Soc.*, **2016**, *138*, 3190-3201.

40. L. Nebhani and C. Barner-Kowollik, *Adv. Mater.*, **2009**, *21*, 3442-3468.

41. A. M. Laradji, C. D. McNitt, N. S. Yadavalli, V. V. Popik and S. Minko, *Macromolecules*, **2016**, *49*, 7625-7631.

42. A. Papra, N. Gadegaard and N. B. Larsen, *Langmuir*, **2001**, *17*, 1457-1460.

43. R. M. Hensarling, V. A. Doughty, J. W. Chan and D. L. Patton, *J. Am. Chem. Soc.*, **2009**, *131*, 14673–14675.

44. P. Theato, B. S. Sumerlin, R. K. O'Reilly and T. H. Epps III, *Chem. Soc. Rev.*, **2013**, *42*, 7055-7056.

45. Z. Cao, L. Mi, J. Mendiola, J. R. Ella-Menye, L. Zhang, H. Xue and S. Jiang, *Angew. Chem., Int. Ed.*, **2012**, *51*, 2602-2605.

46. D. Liu, Y. Xie, H. Shao and X. Jiang, *Angew. Chem., Int. Ed.*, **2009**, *48*, 4406-4408.

47. S. Desseaux and H. A. Klok, *Biomacromolecules*, **2014**, *15*, 3859-3865.

48. H. A. Zayas, A. Lu, D. Valade, F. Amir, Z. Jia, R. K. O'Reilly and M. J. Monteiro, *ACS Macro Lett.*, **2013**, *2*, 327-331.

49. F. Mastrotto, P. Caliceti, V. Amendola, S. Bersani, J. P. Magnusson, M. Meneghetti, G. Mantovani, C. Alexander and S. Salmaso, *Chem. Commun.*, **2011**, *47*, 9846-9848.

50. S. Won, S.-J. Richards, M. Walker and M. I. Gibson, *Nanoscale Horiz.*, **2017**, *2*, 106-109.

51. C. Wu and X. Wang, *Phys. Rev. Lett.*, **1998**, *80*, 4092-4094.

52. J. P. Patterson, M. P. Robin, C. Chassenieux, O. Colombani and R. K. O'Reilly, *Chem. Soc. Rev.*, **2014**, *43*, 2412-2425.

53. M. Elsabahy and K. L. Wooley, *Chem. Soc. Rev.*, **2012**, *41*, 2545–2561.

54. A. O. Moughton, J. P. Patterson and R. K. O'Reilly, *Chem. Commun.*, **2011**, *47*, 355-357.

55. K. Wei, L. Su, G. Chen and M. Jiang, *Polymer*, **2011**, *52*, 3647-3654.

56. L. D. Blackman, D. B. Wright, M. P. Robin, M. I. Gibson and R. K. O'Reilly, *ACS Macro Lett.*, **2015**, *4*, 1210-1214.

57. A. B. Mabire, M. P. Robin, W. D. Quan, H. Willcock, V. G. Stavros and R. K. O'Reilly, *Chem. Commun.*, **2015**, *51*, 9733-9736.

58. M. P. Robin, P. Wilson, A. B. Mabire, J. K. Kiviaho, J. E. Raymond, D. M. Haddleton and R. K. O'Reilly, *J. Am. Chem. Soc.*, **2013**, *135*, 2875-2878.

59. M. P. Robin, A. B. Mabire, J. C. Damborsky, E. S. Thom, U. H. Winzer-Serhan, J. E. Raymond and R. K. O'Reilly, *J. Am. Chem. Soc.*, **2013**, *135*, 9518-9524.

60. M. P. Robin and R. K. O'Reilly, *Polym Int*, **2015**, *64*, 174-182.

61. M. P. Robin, J. E. Raymond and R. K. O'Reilly, *Mater. Horiz.*, **2015**, *2*, 54-59.

62. A. B. Mabire, Q. Brouard, A. Pitto-Barry, R. J. Williams, H. Willcock, N. Kirby, E. Chapman and R. K. O'Reilly, *Polym. Chem.*, **2016**, *7*, 5943-5948.

63. C. W. Cairo, J. E. Gestwicki, M. Kanai and L. L. Kiessling, *J. Am. Chem. Soc.*, **2002**, *124*, 1615-1619.

64. H. Lis and N. Sharon, *Chem. Rev.*, **1998**, *98*, 637−674.

65. Z. Li, L. Sun, Y. Zhang, A. P. Dove, R. K. O'Reilly and G. Chen, *ACS Macro Lett.*, **2016**, *5*, 1059-1064.

66. A. L. Martin, B. Li and E. R. Gillies, *J. Am. Chem. Soc.*, **2008**, *131*, 734–741.

Chapter 5. Entrapment and rigidification of adenine by a photocrosslinked thymine network leads to fluorescent polymer nanoparticles

5.1. Declaration of authorship

The SAXS data in this Chapter was collected by Dr. Steven Huband (University of Warwick) and analyzed by Mr. Robert Keogh (University of Warwick). HR Mass Spectra in this Chapter was analyzed by mass spectrometry group (University of Warwick).

This work has been published in *Chemistry of Materials*.

Hua, Z.; Wilks, T. R.; Keogh, R.; Herwig, G.; Stavros, V. G.; O'Reilly, R. K. Entrapment and Rigidification of Adenine by a Photo-Cross-Linked Thymine Network Leads to Fluorescent Polymer Nanoparticles. *Chem. Mater.* **2018**, *30*, 1408-1416.

5.2. Abstract

Fluorescence emission from non-conjugated polymer dots has attracted increasing interest recently given their potential applications in bioimaging and delivery. Such materials do not contain conventional fluorophores but instead contain sub-fluorophore groups whose photoluminescence can be enhanced upon immobilization through the crosslink-enhanced emission effect (CEE). In this Chapter, photocrosslinking of nucleobase-containing polymer micelles was observed to result in fluorescent polymer nanoparticles. By varying the micelle assembly conditions, it was possible to probe the origins of this behavior. A number of factors were investigated including the effect of omitting one of the nucleobases, blocking hydrogen-bonding interactions, detaching the nucleobase from the polymer backbone and changing the degree of core crosslinking. Spectroscopic investigations were also carried out to further characterize the fluorescent nanoparticles. These data revealed that no new small molecule fluorophores were created during crosslinking and that a dense, hydrogen-bonded network of photodimerized thymine with entrapped adenine was required for fluorescence to arise. We conclude that rigidification and immobilization of adenine in this way leads to the enhancement of an already extant fluorescence pathway, and suggests that synergistic covalent and supramolecular entrapment of profluorophores may provide a general strategy for the production of novel fluorescent polymer nanoparticles.

5.3. Introduction

Highly specific hydrogen-bonding (H-bonding) interactions between complementary nucleobases form the basis of nature's ability to encode genetic information in the DNA double helix and enable the essential biological functions of transcription, translation and replication. Inspired by this selective recognition, synthetic chemists have widely utilized complementary H-bonding interactions to achieve templated polymerization/synthesis,[1-6] fabricate DNA-like supramolecular aggregates,[7] and tune nanostructure morphologies and functionalities.[8-12]

Thymine, one of the natural nucleobases, can undergo photodimerization under UV irradiation to generate a cyclobutane pyrimidine,[13, 14] and this has been exploited by various groups, for example in the fabrication of adhesive materials[15] and the formation of core-crosslinked polymer nanoparticles.[16] Photodimerization is an attractive crosslinking method as it is non-toxic, tunable, controllable remotely and does not yield any byproducts.[17] Our laboratory has recently reported the synthesis of a new class of nucleobase-containing nanoparticles based on diblock copolymers containing adenine (A) or thymine (T).[6, 9, 10, 18, 19] Polymers with relatively long nucleobase blocks self-assemble in water to give micelles with an A or T core. When a diblock copolymer with the complementary nucleobase is added, it is absorbed, driven by A:T base pairing in the micelle core. This behavior can be exploited to various ends. For example, varying the A:T ratio and polymer block lengths resulted in highly tunable switching of the micelle size and shape, as mentioned in Chapters 2 and 3.[9] In Chapter 4, we have shown that by attaching different hydrophilic blocks to the A- and T-containing polymers it is possible to create micelles with a mixed polymer corona, and to straightforwardly introduce different functional groups (such as protein ligands) with a high degree of control over loading density.[10] However, the above systems are not stable to dilution or to changes in solvent since the micelles are held together solely by supramolecular interactions in the core.

Inspired by the work described above, it is highly desired to explore whether photodimerization of T could be used as a straightforward method for the core crosslinking of nucleobase-containing micelles. Interestingly, our initial experiments revealed that at high crosslinking densities the A:T-containing nanoparticles became fluorescent. This was not unprecedented – recent work by Yang and coworkers has shown that the rigidification of polymer nanoparticles can result in the generation of fluorescence from non-fluorescent components, which they have termed the crosslink-enhanced emission effect (CEE).[20] In these systems, it is hypothesized that fluorescence behavior results from the formation of clusters of electron rich heteroatoms such as nitrogen,[21, 22] oxygen[23] or sulfur,[24] however the exact mechanism of the CEE is not yet fully understood.

Fluorescent polymer nanoparticles (sometimes termed polymer dots, or Pdots) are of interest because they may have better toxicity and biodistribution profiles than traditional quantum dots (Qdots), making applications in medical diagnostics and drug delivery more feasible.[20] Pdots based on non-conjugated polymers (NCPdots) are a particular target because they are usually easier to synthesize than conjugated Pdots. However, it has not proved straightforward to synthesize NCPdots in a controllable and reproducible manner. This is because the majority of systems use poorly-defined starting materials (for example modified natural polymers, which have high batch-to-batch variability). Many methods for the production of NCPdots (such as hydrothermal synthesis) also do not lend themselves to systematic studies of the origins of fluorescence by the CEE because the chemical structure of the final products is not known and is difficult to determine.[20] We hypothesized that our A:T based system could represent a solution to both of these problems as it is assembled from well-defined starting materials and the composition can be carefully controlled by altering a number of different parameters, including polymer side chain functionality, A:T ratios, crosslinking density and solvent. We therefore set out to further investigate our NCPdot system, with the hope that an increased understanding of the origins of the CEE will aid in the development and application of this interesting new class of materials.

5.4. Results and discussion

5.4.1. Synthesis of nucleobase-containing fluorescent nanoparticles

Two diblock copolymers with short nucleobase core forming blocks, poly(4-acryloylmorpholine)-*b*-poly(3-(adenine-9-yl)propyl acrylamide (PNAM-*b*-PAAm) and poly(4-acryloylmorpholine)-*b*-poly(3-(thymin-1-yl)propyl acrylamide (PNAM-*b*-PTAm), were prepared *via* RAFT polymerization as reported previously.[9] Due to the chain transfer agent used for polymer synthesis, each polymer chain contained both an acid functional group and a trithiocarbonate end group. The trithiocarbonate group has been demonstrated to degrade under UV irradiation,[25] so it was removed from all the polymers used in this study using a previously reported method,[26] in order to prevent complications arising during later photocrosslinking experiments (Table 5.1, Scheme 5.1 and Figures 5.1-5.2). Meanwhile, hydrolysable nucleobase-containing diblock copolymers, poly(4-acryloylmorpholine)-*b*-poly(3-(adenine-9-yl)propyl acrylate (PNAM-*b*-PAAc, **PA***) and poly(4-acryloylmorpholine)-*b*-poly(3-(thymin-1-yl)propyl acrylate (PNAM-*b*-PTAc, **PT***), were also synthesized (Table 5.1).

Table 5.1. Summary of the SEC data (using DMF as an eluent) of nucleobase-containing diblock copolymers (**PA**, **PT**, **PT^{Me}**, **PA*** and **PT***) after end group removal.

Polymer	M_n[a] / kDa	$Đ_M$[a]
PNAM$_{96}$-*b*-PAAm$_{19}$ (**PA**)	19.6	1.08
PNAM$_{96}$-*b*-PTAm$_{18}$ (**PT**)	21.1	1.11
PNAM$_{96}$-*b*-PMTAm$_{19}$ (**PT^{Me}**)	19.4	1.08
PNAM$_{96}$-*b*-PAAc$_{20}$ (**PA***)	20.0	1.20
PNAM$_{96}$-*b*-PTAc$_{19}$ (**PT***)	19.4	1.16

[a]Determined by DMF SEC, with poly(methyl methacrylate) (PMMA) standards.

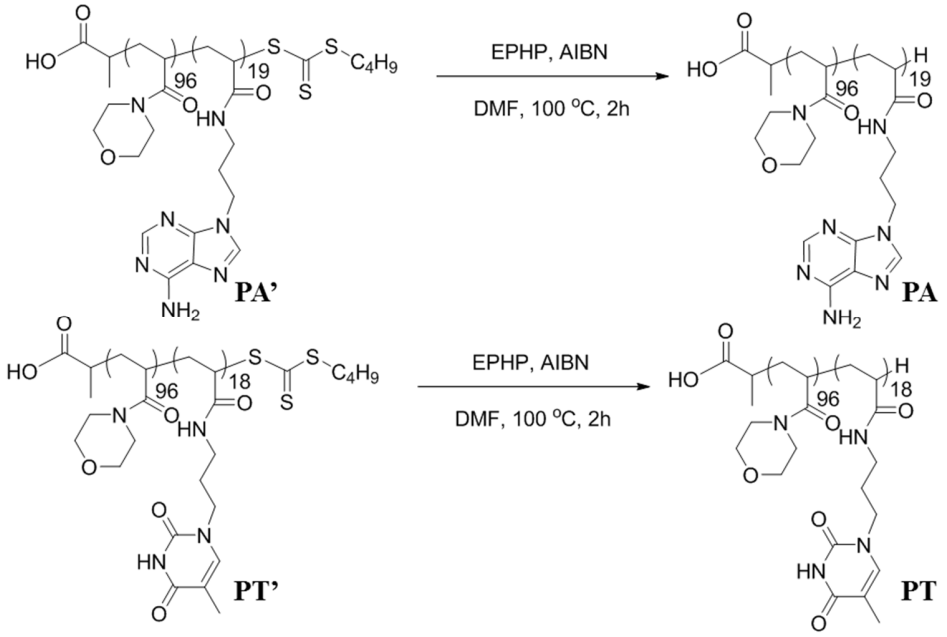

Scheme 5.1. End group removal of $PNAM_{96}$-*b*-$PAAm_{19}$ (**PA'**) and $PNAM_{96}$-*b*-$PTAm_{18}$ (**PT'**).

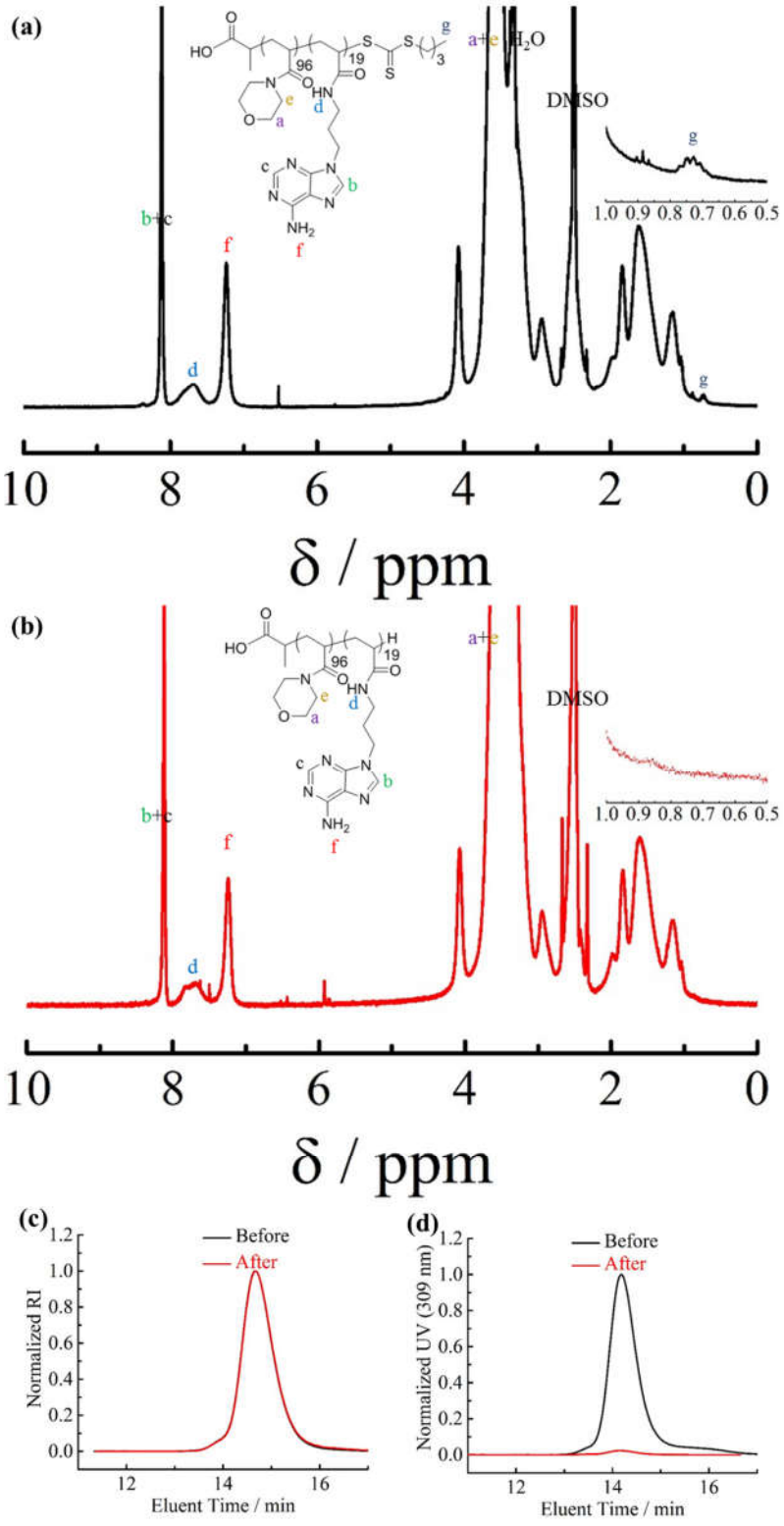

Figure 5.1. ^{1}H NMR spectra of PNAM$_{96}$-*b*-PAAm$_{19}$ (**PA**) (a) before and (b) after end group removal and DMF SEC traces of PNAM$_{96}$-*b*-PAAm$_{19}$ (**PA**) before and after end group removal (c) RI and (d) UV response at 309 nm.

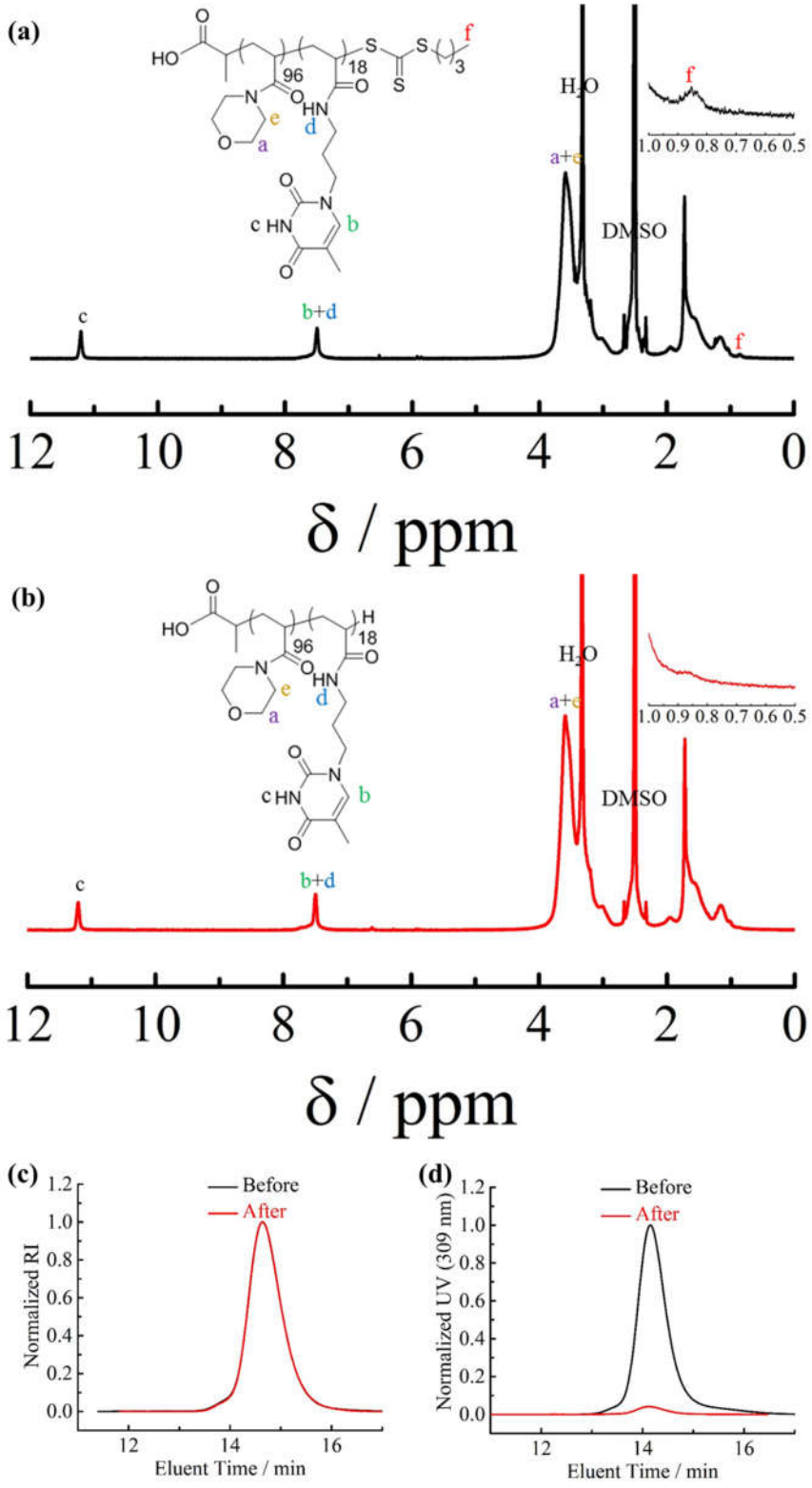

Figure 5.2. ^{1}H NMR spectra of PNAM$_{96}$-*b*-PTAm$_{18}$ (**PT**) (a) before and (b) after end group removal and DMF SEC traces of PNAM$_{96}$-*b*-PTAm$_{18}$ (**PT**) before and after end group removal (c) RI and (d) UV response at 309 nm.

The resulting diblock copolymers, $PNAM_{96}$-*b*-$PAAm_{19}$ (**PA**; with a hydrophobic adenine block) and $PNAM_{96}$-*b*-$PTAm_{18}$ (**PT**; with a hydrophobic thymine block) were mixed in a 1:1 molar ratio and self-assembled by direct dissolution in water at 10 mg mL^{-1} to give micelles **M(A:T)**, which were characterized by dynamic and static light scattering (DLS and SLS) (Scheme 5.2 and Figures 5.3-5.4). Well-defined nanoparticles with hydrodynamic diameter (D_h) of 19 nm were obtained and partial Zimm plot gave $M_w = 3.03 \times 10^5$ g mol^{-1} and an average aggregation number $N_{agg} = 15$ for **M(A:T)**.

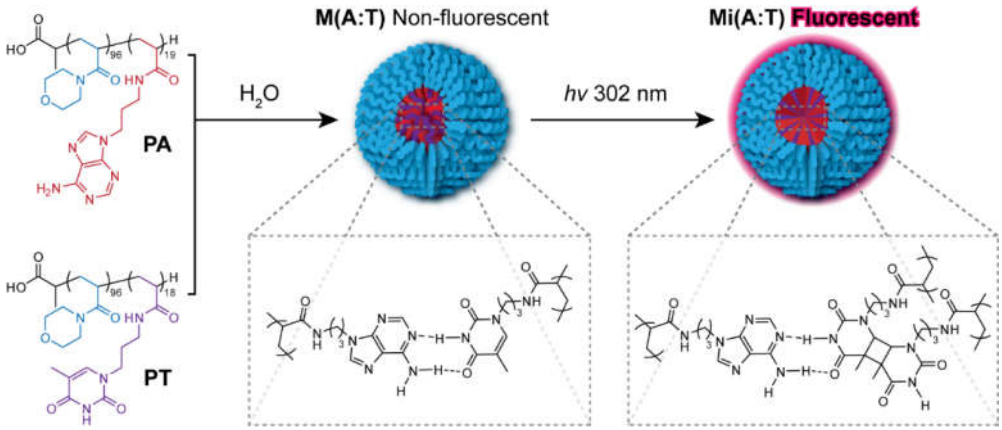

Scheme 5.2. Synthesis of fluorescent nanoparticles by self-assembly and photocrosslinking of nucleobase-containing polymers. **PA** and **PT** were mixed in a 1:1 molar ratio and dissolved in water, to give micelles **M(A:T)** with complementary A:T base pairing in the core. Irradiation with UV light for 12 hours induced photodimerization of T and yielded fluorescent nanoparticles **Mi(A:T)**.

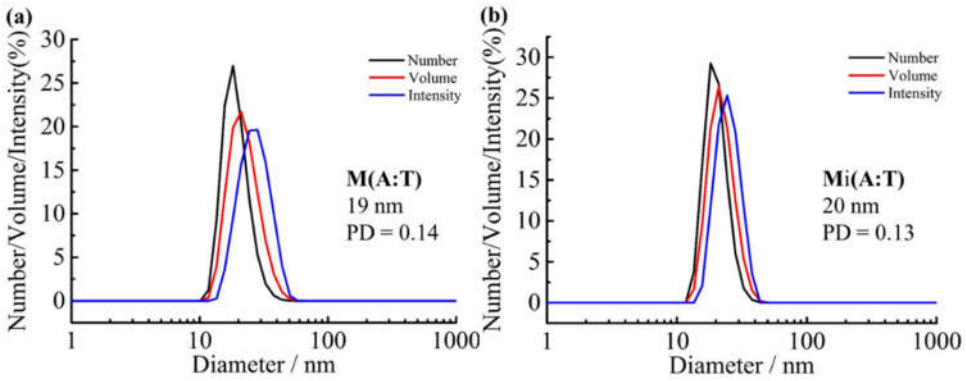

Figure 5.3. DLS analyses of (a) noncrosslinked micelle **M(A:T)** and (b) crosslinked micelle **Mi(A:T)** containing a complementary nucleobase core of A and T.

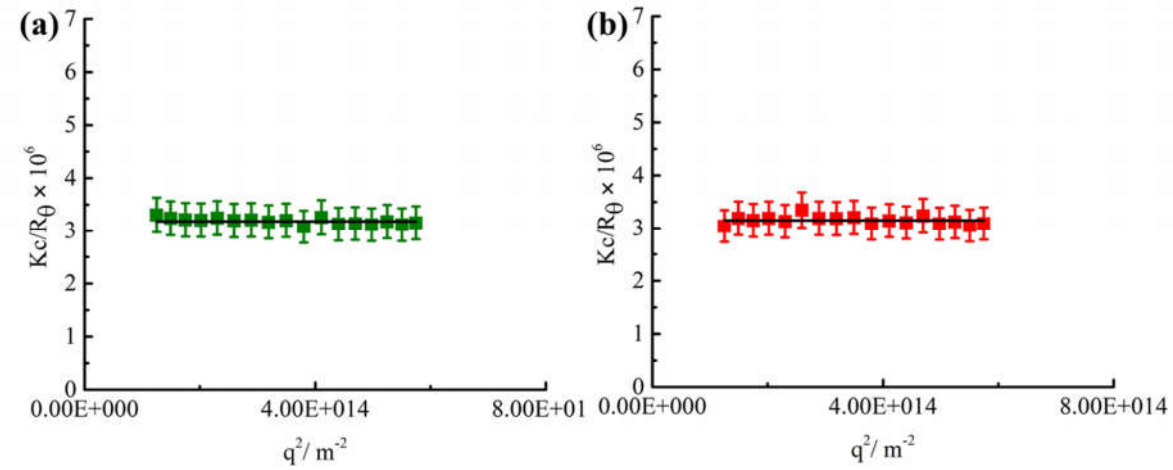

Figure 5.4. SLS plot of the Rayleigh ratio *vs* q^2 for (a) noncrosslinked micelle **M(A:T)** and (b) crosslinked micelle **Mi(A:T)** in water with 10% error bars. This plot gave $M_w = 3.03 \times 10^5$ g mol^{-1} and an average aggregation number $N_{agg} = 15$ for **M(A:T)** and $M_w = 3.18 \times 10^5$ g mol^{-1} and $N_{agg} = 16$ for **Mi(A:T)**.

We attempted characterization by transmission electron microscopy (TEM), but the particles disassembled upon drying to give a polymer film. **M(A:T)** were then irradiated with UV light at 302 nm for 12 h (*ca.* 170 J cm^{-2}) to form nanoparticles **Mi(A:T)** as shown in Scheme 5.2. TEM indicated that well-defined spherical micelles with a number-average diameter of 13 ± 2 nm were obtained (Figure 5.5a). DLS, SLS and small-angle X-ray scattering (SAXS) analyses showed that no significant change in particle dispersity or size occurred upon irradiation (Figures 5.3-5.4, 5.5b and 5.6). Atomic force microscopy (AFM) studies also confirmed the formation of well-defined nanoparticles (Figure 5.7). Interestingly, **Mi(A:T)** were observed to fluoresce under UV light (Figure 5.5c). We decided to investigate the causes of this fluorescence behavior by exploiting the tunability of the micelle system.

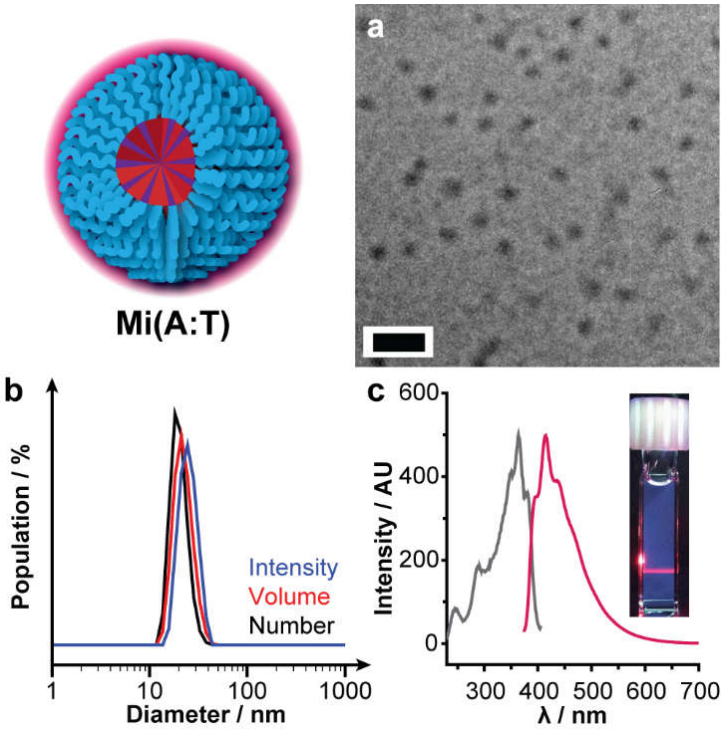

Figure 5.5. Characterization of the crosslinked nanoparticles **Mi(A:T)**: a) TEM on graphene oxide[27] (scale bar = 50 nm); b) DLS analyses by scattered light intensity (blue), particle volume (red) and particle number (black); c) Fluorescence excitation (λ_{em} = 415 nm) and emission (λ_{ex} = 365 nm) spectra (inset **Mi(A:T)** solution under UV lamp (365 nm) with a red laser flux in the horizontal direction).

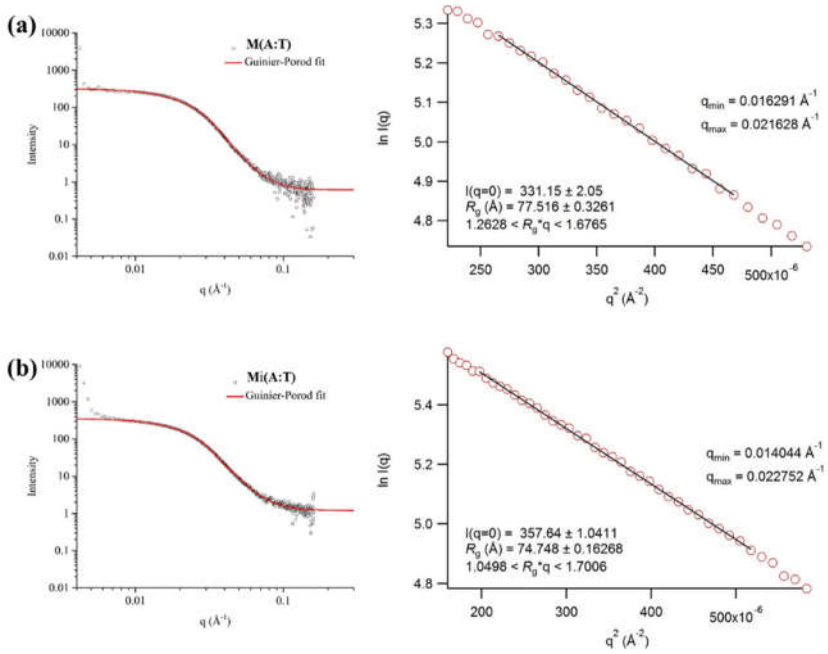

Figure 5.6. SAXS raw profiles, Guinier-Porod fits (left) and Guinier fits (right) for mixed micelles (a) **M(A:T)** and (b) **Mi(A:T)**.

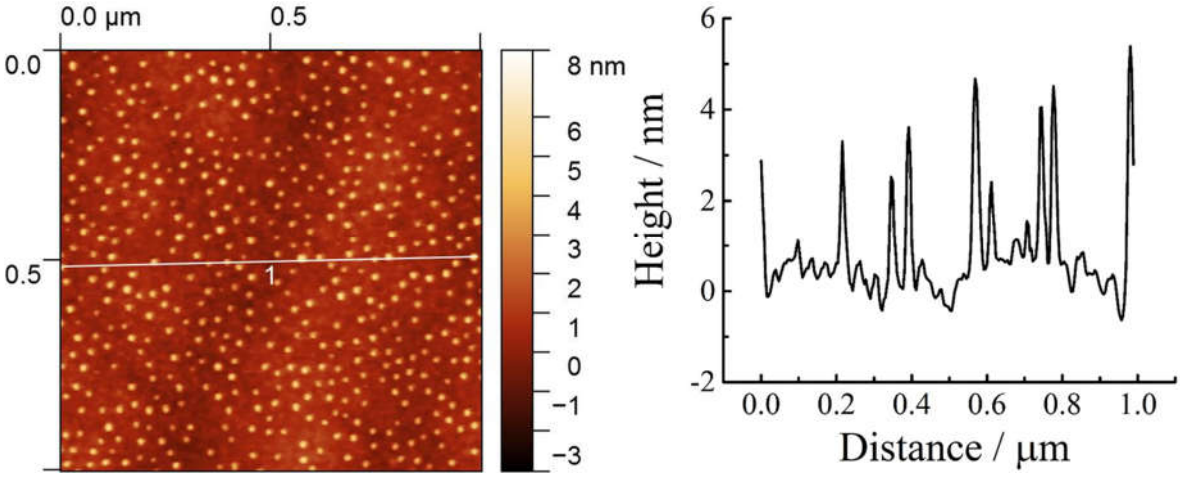

Figure 5.7. AFM image and the corresponding height profile of **Mi(A:T)** along the line labelled 1.

5.4.2. Effect of H-bonding on the fluorescence behavior

We began by exploring whether H-bonding was required for the fluorescence behavior to arise. **PA** and **PT** were self-assembled separately to give micelles **MA** and **MT** respectively, using an identical procedure to that described above for **M(A:T)**. TEM and light scattering analyses confirmed the formation of well-defined micelles (Figure 5.8), neither of which exhibited significant fluorescence. Irradiation of these micelles gave **MiA** and **MiT**, with no significant changes in particle size or dispersity detected (Figure 5.8). Again, neither of these was found to exhibit significant fluorescence (Figure 5.9), supporting the conclusion that A:T H-bonding was indeed important in the generation of fluorescence in this system.

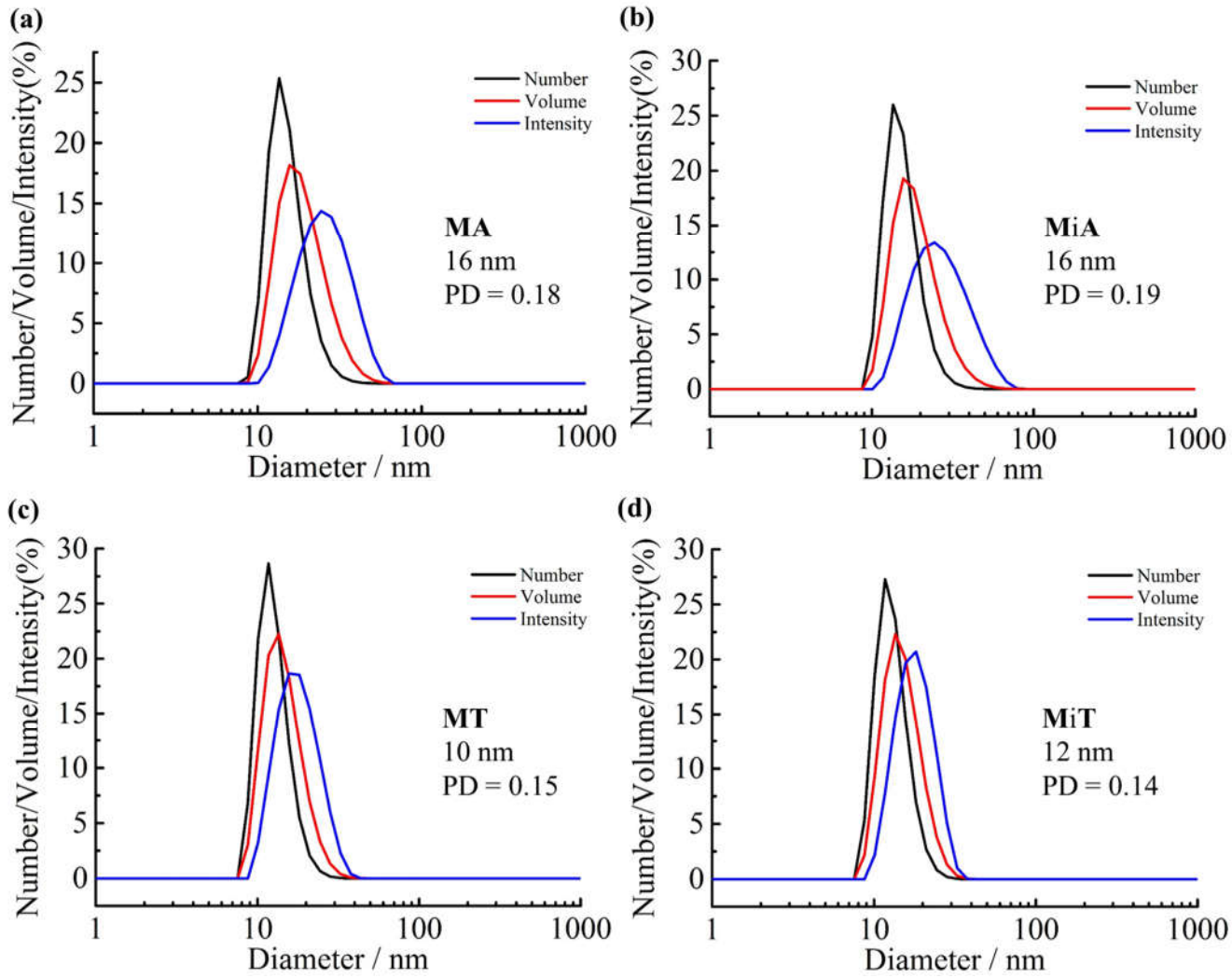

Figure 5.8. DLS analyses for nucleobase-containing nanoparticles (a) **M(A)**, (b) **Mi(A)**, (c) **M(T)** and (d) **Mi(T)**.

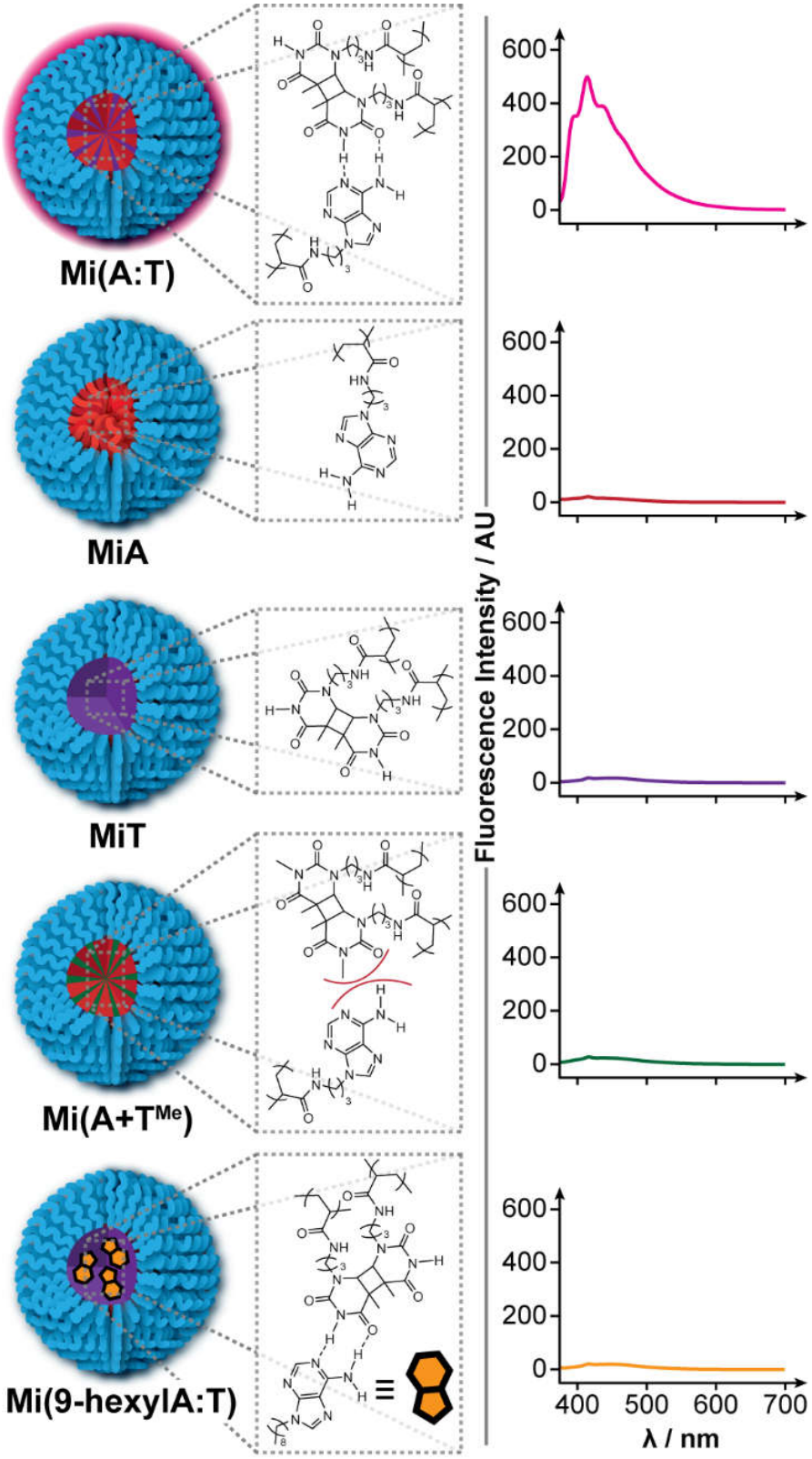

Figure 5.9. Cartoons showing the core compositions of irradiated micelles **Mi(A:T)**, **MiA**, **MiT**, **Mi(A+T^{Me})** and **Mi(9-hexylA:T)**, and (right) fluorescence emission spectra (λ_{ex} = 365 nm) for these particles, showing that no significant fluorescence was observed as a result of the absence or interruption of H-bonding, or detachment of A from the polymer backbone.

We also investigated an analogue to **Mi(A:T)** in which H-bonding had been disrupted. This was achieved by synthesizing a new monomer in which the T residue had been methylated, and polymerized as described above to give a methylated version of **PT**, termed **PT^{Me}**. **PT^{Me}** was mixed in a 1:1 molar ratio with **PA** and self-assembled into micelles **M(A+T^{Me})**, then irradiated to produce **Mi(A+T^{Me})**. Well-defined particles were observed to form (Figures 5.10-5.11) and neither sample displayed significant fluorescence (Figure 5.9), so it was concluded that A:T H-bonding was essential for this behavior to arise.

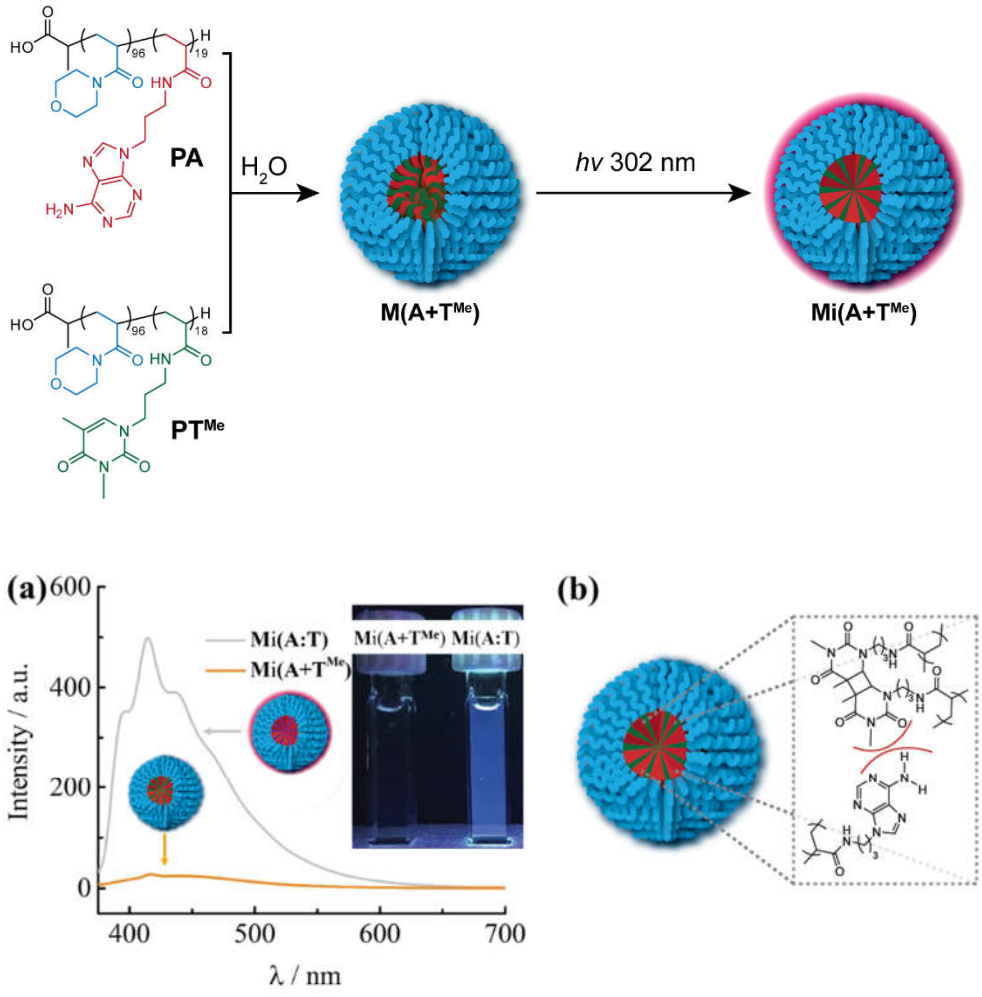

Figure 5.10. (a) Fluorescence spectra (λ_{ex} = 365 nm) of solutions (0.5 mg mL^{-1}) of **Mi(A:T)** and **Mi(A+T^{Me})**; the insets show the photos of **Mi(A:T)** and **Mi(A+T^{Me})** solutions under UV lamp (365 nm); (b) Illustration of the interruption of H-bonding in the core of micelle **Mi(A+T^{Me})** due to thymine methylation.

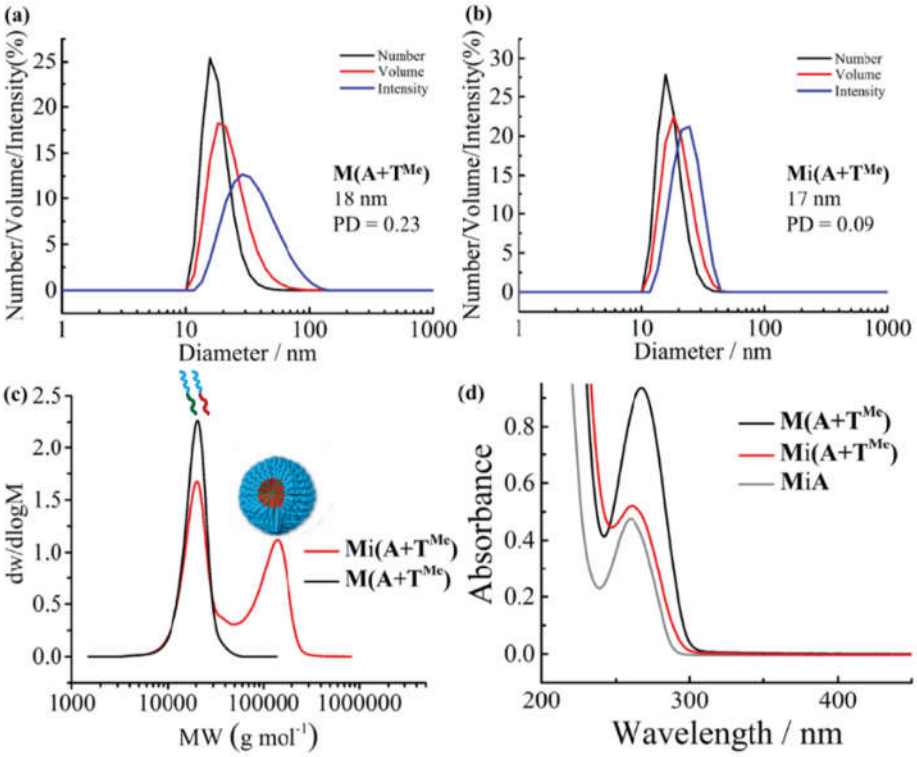

Figure 5.11. DLS and DMF SEC analyses of noncrosslinked micelle **M(A+T^{Me})** and crosslinked micelle **Mi(A+T^{Me})** containing nucleobase core which is incapable of H-bonding consisting of adenine (A) and methylated thymine (T^{Me}). DLS analyses of (a) **M(A+T^{Me})** and (b) **Mi(A+T^{Me})**; DMF SEC analyses of (c) **M(A+T^{Me})** and **Mi(A+T^{Me})**; (d) UV-vis spectra of solutions of **M(A+T^{Me})** and **Mi(A+T^{Me})** (0.1 mg mL^{-1}) and **MiA** (0.05 mg mL^{1}) after 12 h irradiation at 302 nm, illustrating high photodimerization (over 80%) of T^{Me}.

5.4.3. Importance of crosslinking on the fluorescence property

Next, we set out to confirm that the nanoparticles had indeed been crosslinked by the irradiation process, by transferring them into DMF, a good solvent for both polymer blocks. Uncrosslinked micelles were expected to disassemble into the component polymers under these conditions, whereas crosslinked nanoparticles were anticipated to survive largely intact. **MA**, **MT**, **M(A:T)**, **MiA**, **MiT** and **Mi(A:T)** were all transferred from water to DMF and analyzed by size exclusion chromatography (SEC, eluting with DMF) (Figure 5.12).

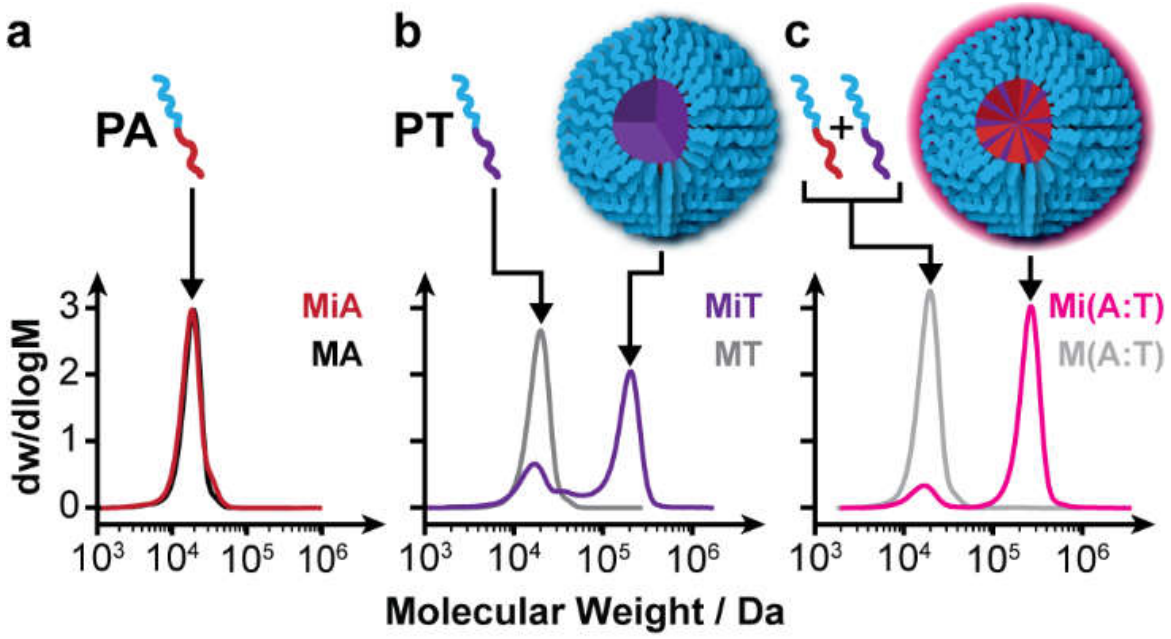

Figure 5.12. SEC traces using DMF as solvent of (a) **MA** and **MiA**; (b) **MT** and **MiT**; (c) **M(A:T)** and **Mi(A:T)**. In cases where T was present in the core, a new peak at around 250 kDa appeared, attributed to the crosslinked nanoparticles, which could not disassemble even in a good solvent.

All uncrosslinked micelles (**MA**, **MT** and **M(A:T))** were found to exhibit a single peak, the mass of which was consistent with the constituent free polymers (**PA** and/or **PT**), see Figure 5.12 (black/gray traces). The irradiated micelles **MiA**, which contained no thymine groups and were therefore not expected to crosslink under UV light, also eluted as a single peak with the same mass as **MA** (Figure 5.12a, red traces). In contrast, **MiT** and **Mi(A:T)** exhibited a new peak at around 250 kDa, which was attributed to crosslinked nanoparticles that were incapable of disassembly in DMF (Figure 5.12b and c, purple and pink traces respectively). Based on these data, it was concluded that the nanoparticles were indeed highly crosslinked, and the lack of any significant fluorescence for **MiT** confirmed that crosslinking was necessary but not sufficient for fluorescence to arise.

5.4.4. Requirement for polymer immobilization to the observed fluorescence

To test whether immobilization of A on a polymer backbone was necessary for fluorescence behavior, we assembled **PT** in the presence of 1 molar equivalent of 9-hexyladenine (9-hexylA) to form micelles **M(9-hexylA:T)**, which were subsequently irradiated to give nanoparticles **Mi(9-hexylA:T)** (Figures 5.9, 5.13 and 5.14). Interestingly, this system was not fluorescent, so we concluded that immobilization of A by attachment to a polymer backbone was also essential for the CEE to occur. This further suggested that rigidification of the polymer nanoparticle was key in the generation of fluorescence.

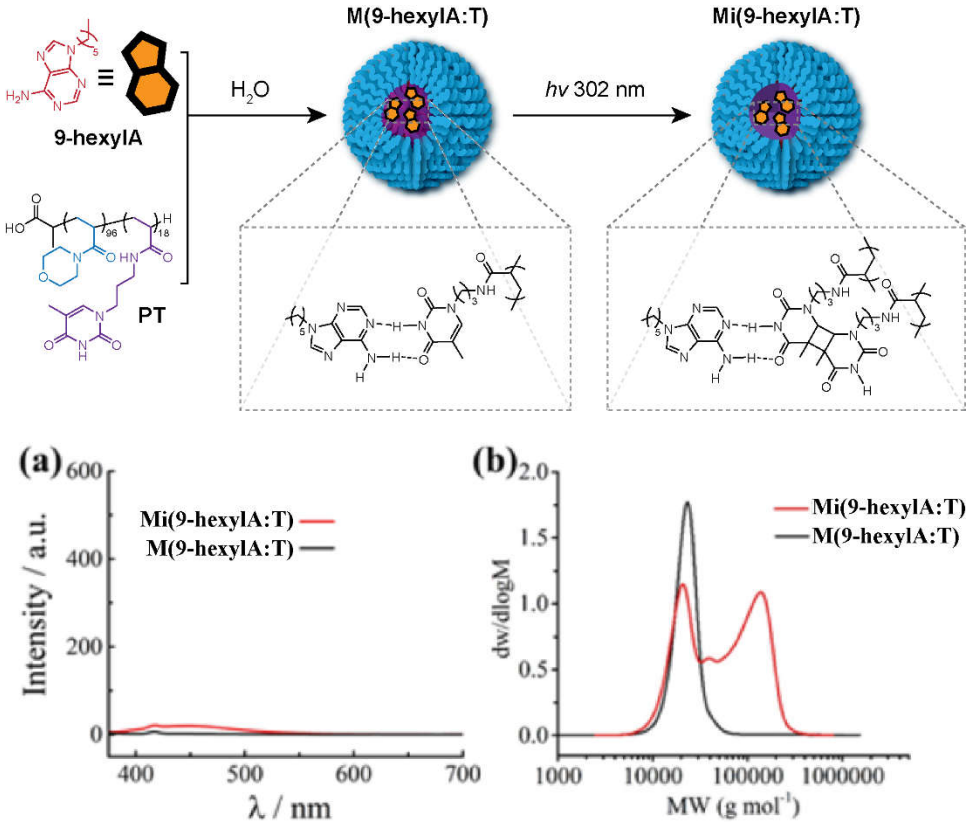

Figure 5.13. The crosslinked micelle **Mi(9-hexylA:T)** from micelle **M(9-hexyl-A:T)** consisting of **PT** and small molecule 9-hexyladenine (9-hexylA). (a) Fluorescence spectra of **M(9-hexyl-A:T)** and **Mi(9-hexyl-A:T)**; (b) DMF SEC analyses of **M(9-hexyl-A:T)** and **Mi(9-hexyl-A:T)**.

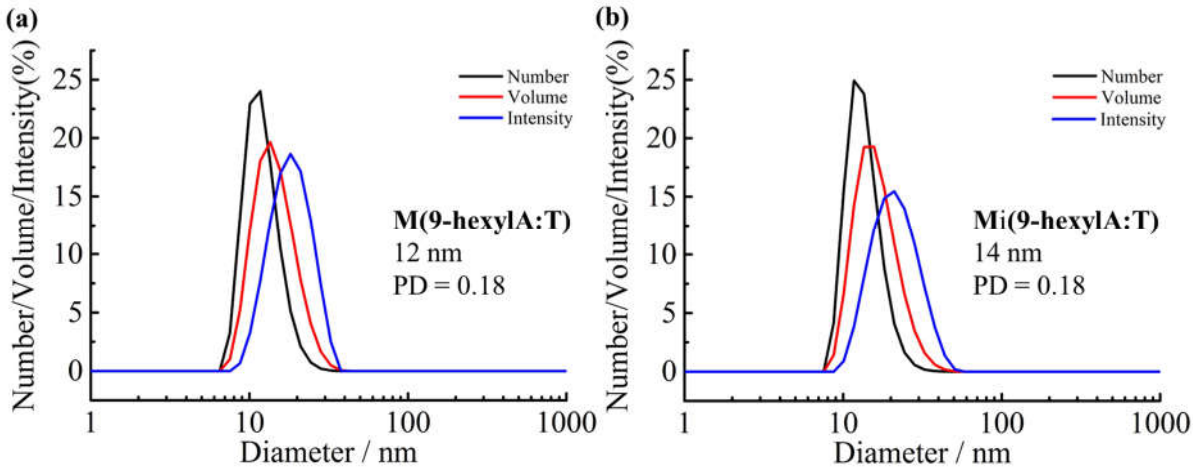

Figure 5.14. DLS analyses for nucleobase-containing nanoparticles **M(9-hexylA:T)** and **Mi(9-hexylA:T)**.

5.4.5. Probing the crosslinking process

We studied the crosslinking process using UV and fluorescence spectroscopy in order to gain further insights into the generation of fluorescence in our system. **MA**, **MT** and **M(A:T)** were each irradiated for a total of twelve hours, with aliquots removed at regular time intervals for analysis by UV-vis and fluorescence spectroscopy (at 0.1 mg mL^{-1}). As expected, a gradual decrease in absorbance at 272 nm, was observed for **MiT** and **Mi(A:T)**, which was attributed to the photodimerization of thymine (Figure 5.15a).

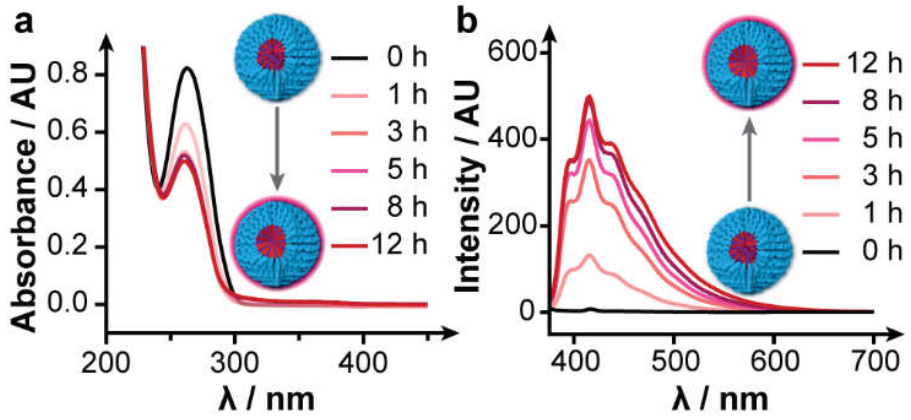

Figure 5.15. UV-vis absorption (a) and fluorescence emission (b, λ_{ex} = 365 nm) spectra of **M(A:T)** after different irradiation times to form **Mi(A:T)**, showing the decrease in absorbance at 272 nm due to crosslinking of the T groups and the appearance of the characteristic fluorescence peak for the crosslinked nanoparticles.

As no obvious alterations were observed in the spectra of **MiA** after UV irradiation (Figure 5.16), we could quantify the thymine photodimerization degree using the decrease in absorbance at 272 nm during UV irradiation. The crosslinking of thymine in both **MiT** and **Mi(A:T)** appeared to be very efficient (Figure 5.17) with around 90% photodimerization achieved after 12 h irradiation, which was consistent with the SEC results described above. Fluorescence spectroscopy of the irradiated solution of **M(A:T)** revealed an increase in fluorescence over the course of the crosslinking experiment as expected (Figure 5.15b).

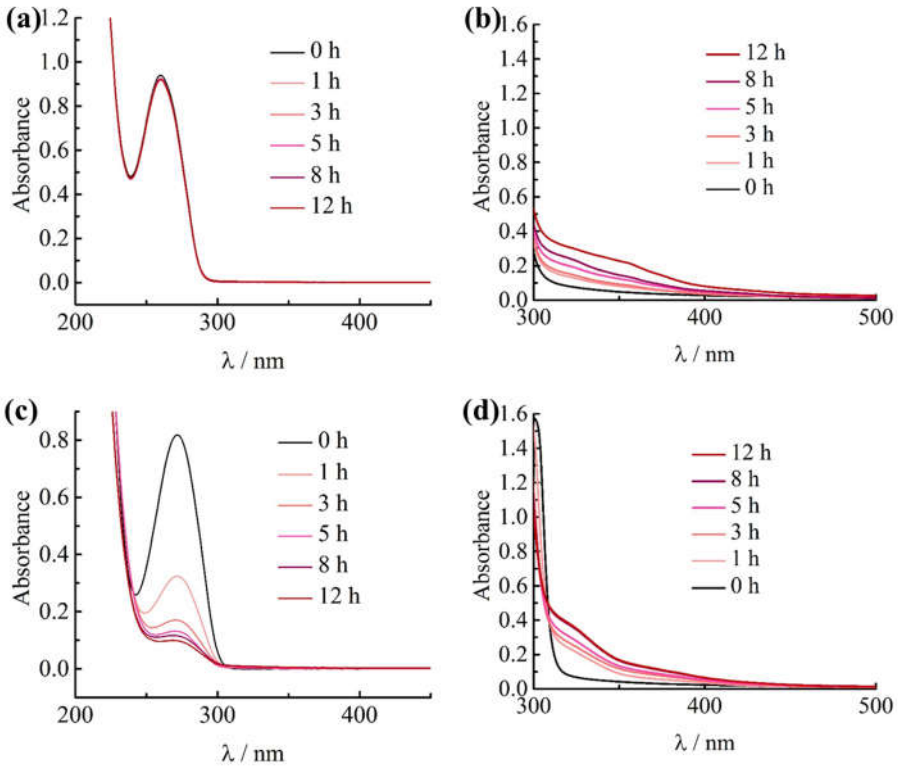

Figure 5.16. UV-vis spectra of micelles (a, b) **MiA**; (c, d) **MiT** containing an individual nucleobase core A or T at different concentrations ((a, c) 0.1 mg mL^{-1} and (b, d) 9.5 mg mL^{-1}) with different irradiation times.

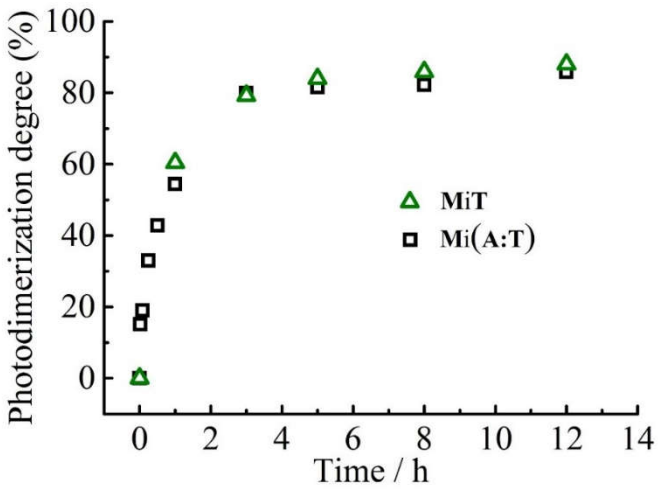

Figure 5.17. Calculated photodimerization degree of thymine in micelles **MiT** and **Mi(A:T)** using the drop in absorbance at 272 nm in UV-vis analyses with different irradiation times.

By combining the UV-vis and fluorescence measurements for irradiation of **M(A:T)**, it was possible to plot fluorescence intensity *versus* degree of crosslinking (Figure 5.18). Interestingly, this revealed a non-linear relationship: at a critical point (around 3h irradiation time, or approximately 80% thymine photodimerization) a notable increase in fluorescence was observed. This suggested that a certain minimum degree of crosslinking was required in order for the CEE to emerge and cause fluorescence.

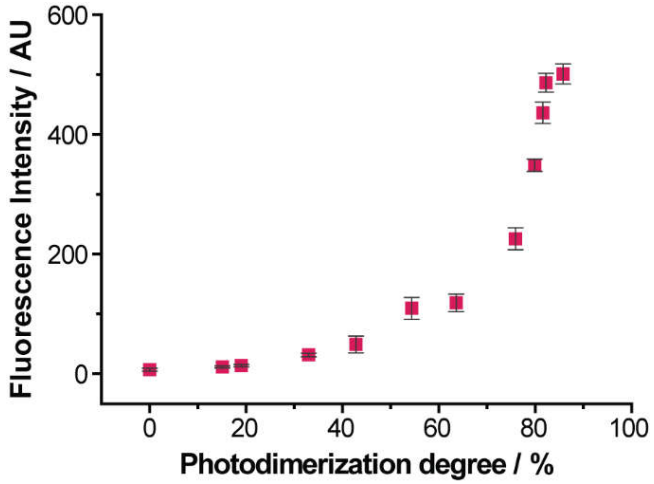

Figure 5.18. Plot of fluorescence intensity of Mi(A:T) at 415 nm versus photodimerization degree showing the non-linear relationship. Error bars are the standard deviation from three experimental replicates.

During the UV-vis experiments we observed a small tail above 300 nm in the UV-vis absorption spectrum, which developed at prolonged irradiation times. However, due to the relatively low concentration, no recognizable features could be determined. Irradiation of **M(A:T)** at a much higher concentration (9.5 mg mL^{-1}) was therefore investigated. Three peaks at 346, 362 and 380 nm were initially observed after 3 h of UV irradiation followed by a smooth increase in intensity (Figure 5.19). When both **M(A:T)** and **Mi(A:T)** were excited at 305 nm, **M(A:T)** showed no obvious emission and **Mi(A:T)** had decreased emission but with the same triple peaks (Figure 5.20a). This result supported the observed fluorescence emission originated from the species with the peak absorbance at 365 nm. Notably, the same features were not observed during irradiation of **MA** or **MT**, suggesting that the interaction between complementary nucleobases in the crosslinked core played an important part in generating them. In agreement with the fluorescence spectroscopy results above, a plot of UV absorbance at 362 nm *versus* photodimerization degree displayed a non-linear relationship (Figure 5.20b). This further supported the conclusion that a certain critical amount of crosslinking was required to induce fluorescence.

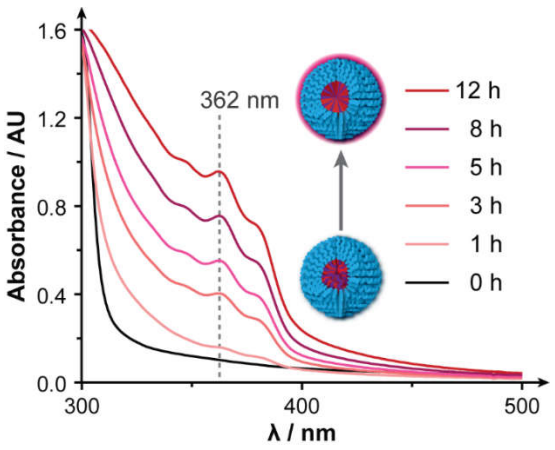

Figure 5.19. UV-vis absorption spectrum of **M(A:T)** after different irradiation times to form **Mi(A:T)** at a higher concentration of 9.5 mg mL^{-1} showing the appearance of vibronic features with a principal peak at 362 nm.

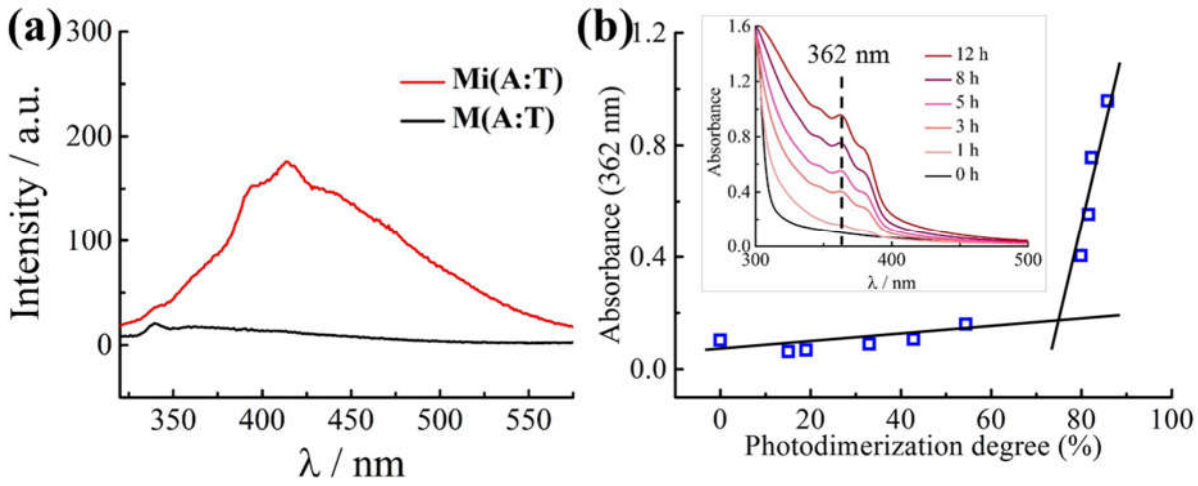

Figure 5.20. Analysis of the observed fluorescence of **Mi(A:T)**. (a) Fluorescence spectra (λ_{ex} = 305 nm) of solutions (0.5 mg mL^{-1}) of **M(A:T)** and **Mi(A:T)**; (b) variation of the UV absorbance (at 362 nm) of **Mi(A:T)** (9.5 mg mL^{-1}) with the photodimerization degree of thymine as determined by UV-vis analyses; the inset shows UV-vis spectra of solutions of **Mi(A:T)** after different irradiation times.

5.4.6. Characterization of fluorescence pathways

In order to provide further information about the nature of the fluorophore created in **Mi(A:T)**, solution-state time-correlated single-photon counting (TCSPC) was conducted to determine the fluorescence lifetimes of the constructs (Figure 5.21 and Table 5.2). For samples which contained adenine – **Mi(A:T)**, **MiA** and **M(A:T)** – TCSPC measured at λ_{em} = 415 nm showed almost identical emission decay profiles once the significant difference in the signal to noise ratio between **Mi(A:T)** and the other two samples was taken into account. Moreover, all three adenine-containing samples shared the same two longer lifetime components (τ_2 = ~4 ns and τ_3 = ~11 ns; see Table 5.2 for details).

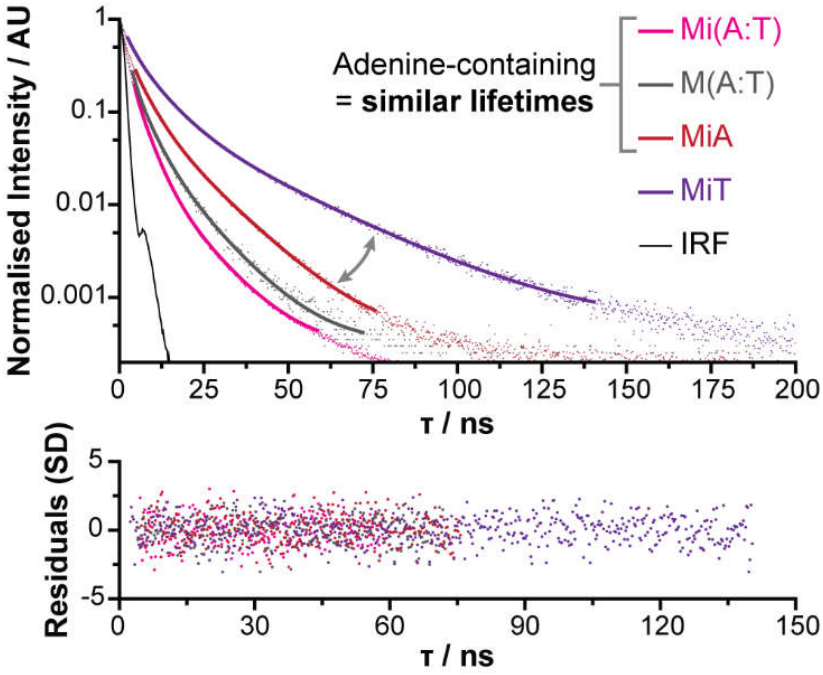

Figure 5.21. Normalized TCSPC fluorescence lifetime decay spectra with residuals for **MiA**, **MiT**, **M(A:T)** and **Mi(A:T)** in water at 0.5 mg mL^{-1}, showing the similarity between the adenine-containing samples. The instrument response function (IRF, black) is also shown for comparison.

Table 5.2. Emission lifetime for **MiA**, **MiT**, **M(A:T)** and **Mi(A:T)** solutions (λ_{ex} = 369 nm, λ_{em} = 415 nm).

Sample	A_1	$\tau_1(ns)$	A_2	$\tau_2(ns)$	A_3	$\tau_3(ns)$	$\tau_{av,I}(ns)$	$\tau_{av,A}(ns)$
MiA	0.01	0.9	0.41	4.5	0.58	12.7	11.0	9.2
MiT	0.09	2.8	0.49	7.8	0.42	24.8	19.9	14.5
M(A:T)	0.09	1.5	0.51	4.2	0.40	10.9	6.7	4.6
Mi(A:T)	0.04	1.0	0.63	3.6	0.33	10.5	5.7	4.0

However, whilst the aforementioned lifetimes were in agreement, there were marked differences in the fluorescence quantum yields (QY). The relative QY of **Mi(A:T)** was 7.9% (Table 5.3) (comparable to that of quantum carbon dots[28]), which was 80-fold higher than that of **M(A:T)** and 40-fold higher than that of **MiA**. These results suggested that rather than creating a new fluorophore, crosslinking resulted in the promotion of an already extant

emissive pathway. Without crosslinking, the initially populated state (with a lifetime shorter than the TCSPC instrument response) was able to decay *via* alternative, non-emissive, pathways to the ground state. Crosslinking resulted in a higher fraction of the initially populated state passing into the emissive pathway, likely promoted by π–π stacking,[29, 30] and hence increased fluorescence.

Table 5.3. Relative quantum yields for **MA**, **MiA**, **MT**, **MiT**, **M(A:T)** and **Mi(A:T)** solutions with respect to quinine sulfate dihydrate.[31]

Micelles	QY (%)
MA	< 0.1
MiA	0.2
MT	< 0.1
MiT	0.4
M(A:T)	< 0.1
Mi(A:T)	7.9

5.4.7. Degradation studies of the fluorescent nanoparticles

In order to rule out the possibility that the observed fluorescence was due to the formation of new molecular species (other than the thymine dimer) during irradiation, an additional crosslinked mixed micelle **Mi(A*:T*)** was prepared (Figure 5.22). This micelle was analogous to **Mi(A:T)** (and showed similar fluorescence properties, see Figure 5.22c) but it contained a hydrolyzable ester rather than a stable amide linkage between the nucleobase and polymer backbone, to allow for nanoparticle disassembly. The acrylate-containing nanoparticles **Mi(A*:T*)**, were hydrolyzed in 1 M HCl aqueous solution at room temperature for 7 days to form **MiH(A*:T*)** and then the polymer and small molecules were separated by dialysis. SEC and NMR analyses of the high molecular weight product confirmed successful cleavage of the

nucleobase functionalities and the presence of poly(4-acryloylmorpholine)-*b*-poly(acrylic acid) (PNAM-*b*-PAA) (Figure 5.22 and Figure 5.23).

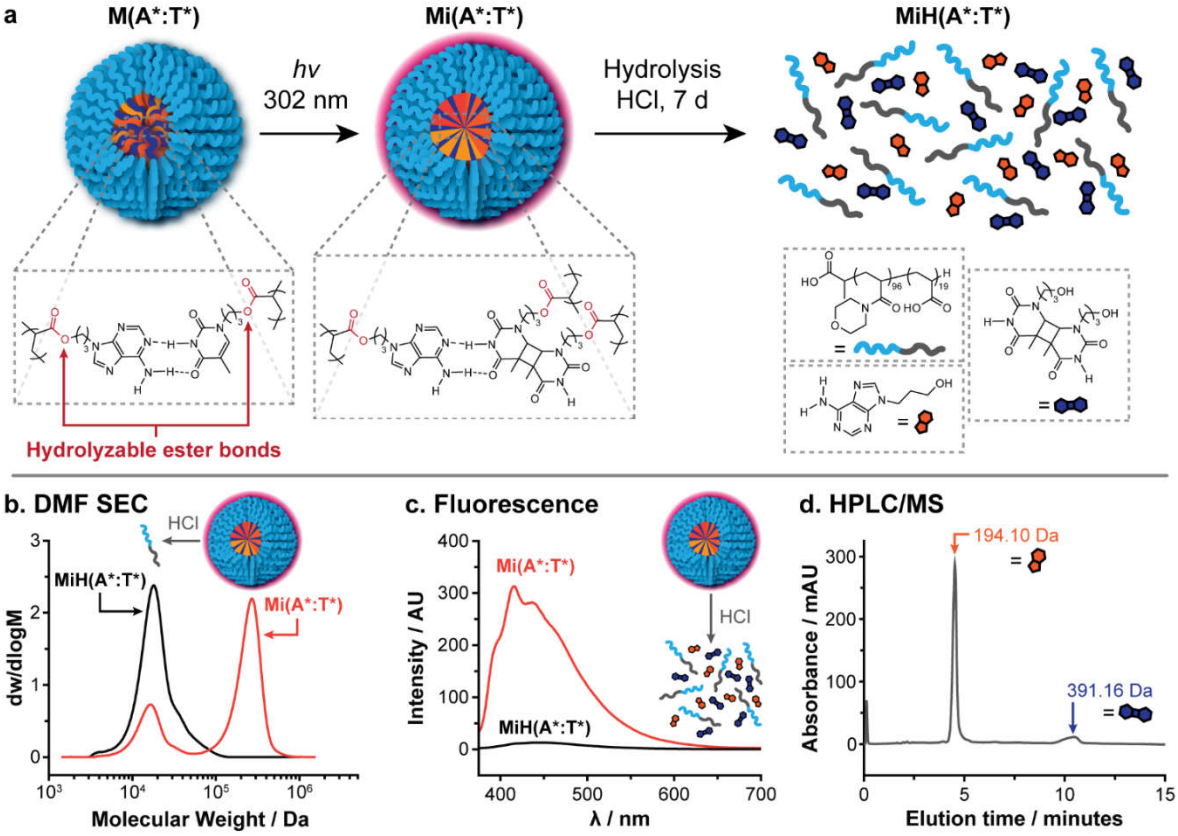

Figure 5.22. Synthesis and characterization of the hydrolyzable nanoparticle **Mi(A*:T*):** a) cartoon illustrating the crosslinking and subsequent disassembly of **Mi(A*:T*)** by hydrolysis to give **MiH(A*:T*)**; b) DMF SEC analysis of **Mi(A*:T*)** showing the persistent high molecular weight peak attributed to the crosslinked nanoparticle (orange trace) – following hydrolysis to produce **MiH(A*:T*)** (black trace) this peak disappeared and the trace indicated only the presence of free polymer; c) Fluorescence emission spectra (λ_{ex} = 365 nm) of **Mi(A*:T*)** and **MiH(A*:T*)** showing the loss of fluorescence upon hydrolysis; d) HPLC chromatogram showing the two low molecular weight species isolated upon hydrolysis of **Mi(A*:T*)** – MS analyses (shown above each peak) confirmed these to be the expected products.

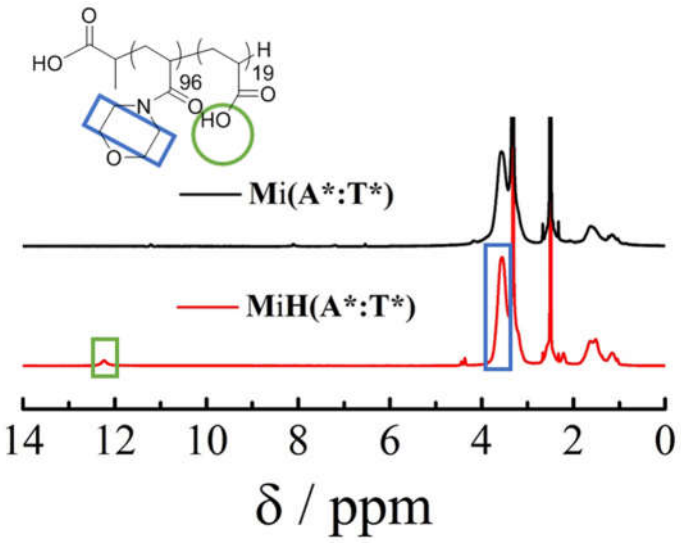

Figure 5.23. ^{1}H NMR spectra of **Mi(A*:T*)** and separated $PNAM_{96}$-*b*-PAA_{19} from **MiH(A*:T*)**.

A loss of fluorescence of the solution of **MiH(A*:T*)** was observed compared to the parent micelle **Mi(A*:T*)**, as shown in Figure 5.22c. The small molecules were analyzed by HPLC which revealed the presence of 2 species (Figure 5.22d), neither of which were fluorescent. The species at 4.5 min had a strong UV peak absorption at 260 nm which was confirmed by MS to be attributable to adenine moieties and the second species at longer retention time was attributed to the thymine dimer (Figure 5.22d). As a control reaction the stable acrylamide crosslinked micelle, **Mi(A:T)**, was reacted under the same conditions and no obvious hydrolysis (as determined by SEC) or loss in fluorescence occurred (Figure 5.24).

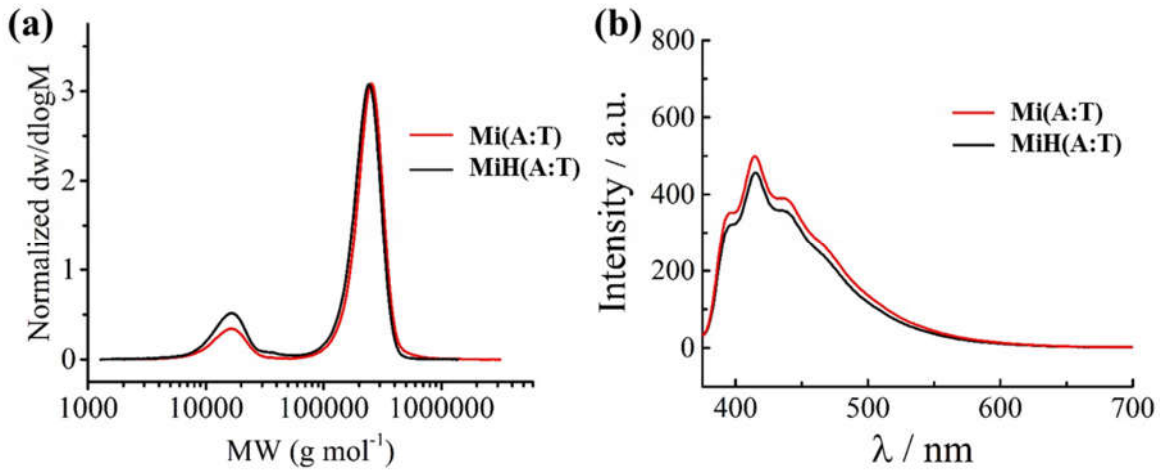

Figure 5.24. The hydrolysis of micelle **Mi(A:T)** into **MiH(A:T)** showed no obvious change under the same conditions as **Mi(A*:T*)**. (a) SEC traces of **MiH(A:T)** using DMF as solvent; (b) fluorescence spectra (λ_{ex} = 365 nm) of **MiH(A:T)** (0.5 mg mL^{-1}).

5.4.8. Robustness of fluorescent properties to changes in temperature, solvent and pH

We were also interested in exploring the response of **Mi(A:T)** to changes in temperature, solvent and pH. The fluorescence of both **M(A:T)** and **Mi(A:T)** was unchanged after heating at 60 °C overnight, indicating stable fluorescent properties (Figure 5.25). Luminogens based on aggregation-induced emission are traditionally formed *via* the solvophobic effect and are therefore not very robust towards such changes;[32] we speculated that our highly crosslinked nanoparticles may be more resistant. **Mi(A:T)** was dissolved in a series of solvents of different polarities (Figure 5.26a). Complete quenching of the fluorescence was not observed in any of the solvents tested but there was a variation in emission intensity, which correlated with the differing abilities of the solvents to solvate/swell the micelle core and disrupt A:T interactions.

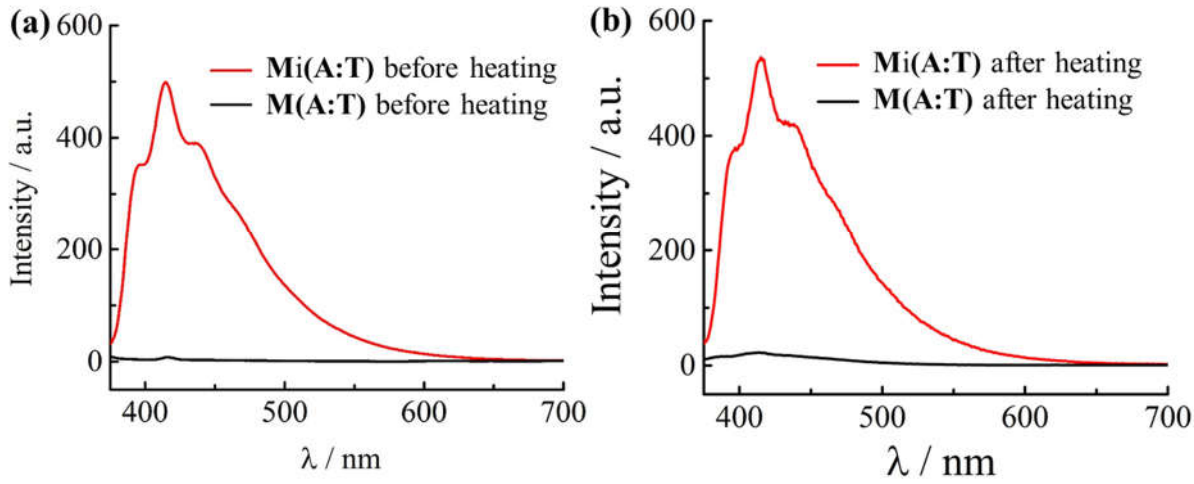

Figure 5.25. Fluorescence spectra (λ_{ex} = 365 nm) of micelles **M(A:T)** and **Mi(A:T)** after heating at 60 °C overnight.

To further test this hypothesis, we examined the drop in fluorescence when nanoparticles with lower crosslink densities were dissolved in DMF and DMSO (Figure 5.27). A greater percentage drop in fluorescence was observed at lower crosslink densities, which we attributed to the increased ability of the solvents to penetrate into the core and disrupt the fluorophore. Finally, we investigated the effect of changing the solution pH. **Mi(A:T)** solution was freeze dried and then was dissolved in PBS buffers (100 mM) at different pH and the fluorescence intensity measured (Figure 5.26b). Almost no change in intensity was recorded across the pH range used, with the exception of pH 2, which we speculated may be due to protonation of adenine.[33] Meanwhile, no impact on fluorescence was observed with a range of NaCl concentrations present, underscoring the system's potential for biomedical applications (Figure 5.28).

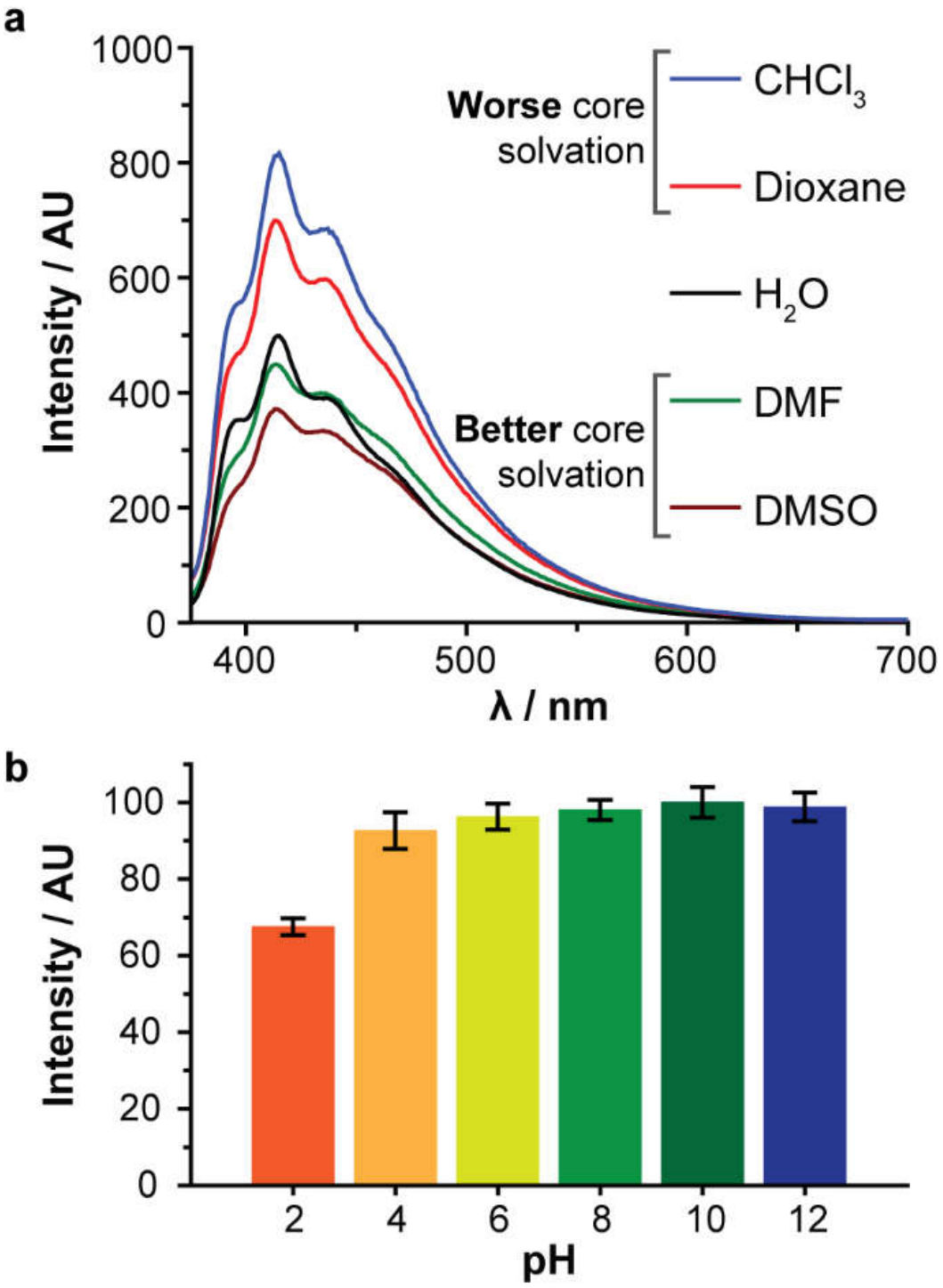

Figure 5.26. Effect of solvent conditions on **Mi(A:T)** fluorescence: a) Fluorescence emission spectra (λ_{ex} = 365 nm) for **Mi(A:T)** dispersed in different solvents; b) Dependence of fluorescence emission intensity at 415 nm (λ_{ex} = 365 nm) on aqueous solution pH for **Mi(A:T)** – data were scaled so that the emission intensity at pH 10 was 100 AU.

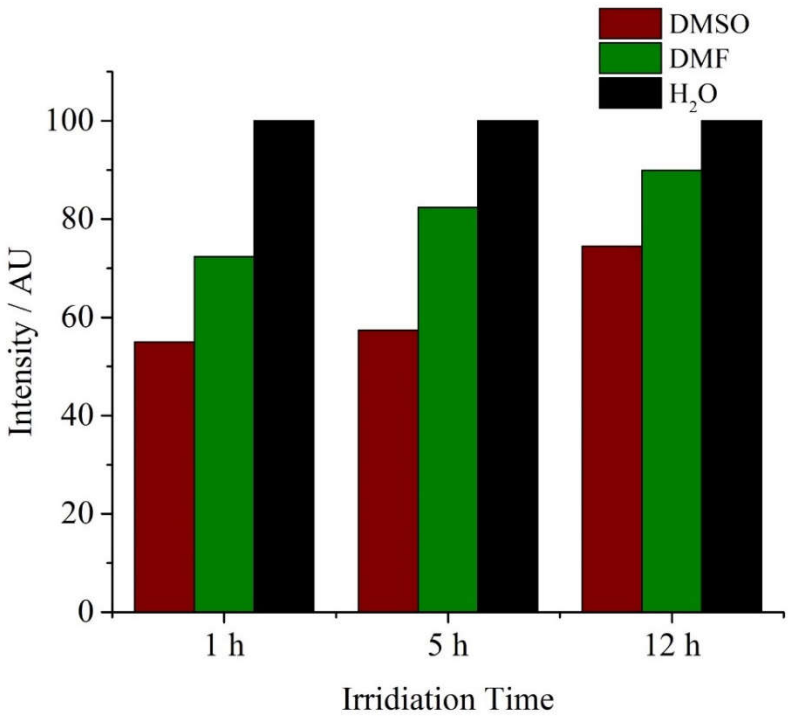

Figure 5.27. Dependence of fluorescence emission intensity at 415 nm (λ_{ex} = 365 nm) on different solvents for **Mi(A:T)** with irradiation times, *i.e.* different crosslink densities – data were scaled so that the emission intensity in water was 100 AU.

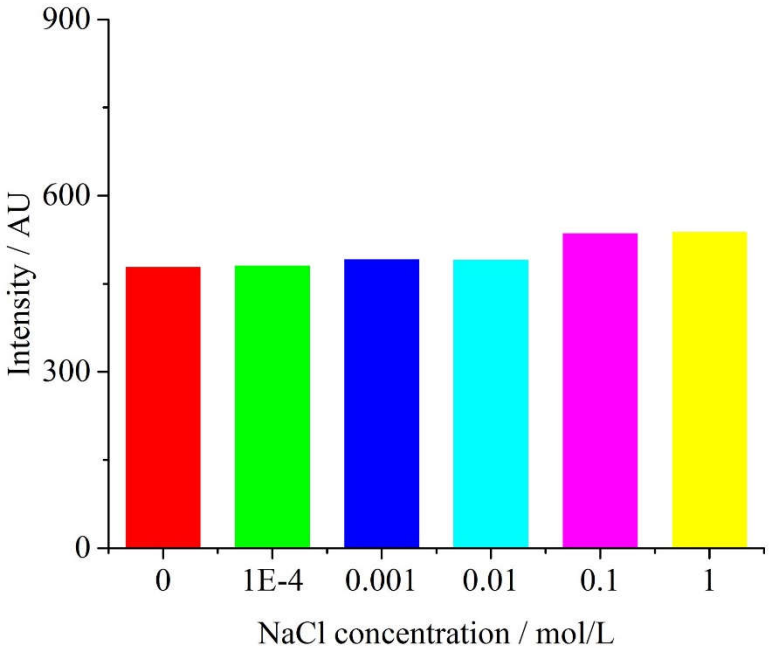

Figure 5.28. Dependence of fluorescence emission intensity at 415 nm (λ_{ex} = 365 nm) on aqueous solution with different NaCl concentrations for **Mi(A:T)**.

5.5. Conclusions

Based on the data presented in this Chapter, we propose that the fluorescence of the **Mi(A:T)** nanoparticles arises because of the entrapment and rigidification of adenine by the photocrosslinked thymine network. Under these conditions, adenine units are forced into a particular configuration that favours the population of an emissive decay pathway. Based on literature reports on the excited state dynamics of oligonucleotides,[29, 30] it seems reasonable to suggest that π–π stacking drives this process. This interpretation is supported by the observation that any change to the system that results in a less ordered and tightly packed nanoparticle core – interruption of H-bonding, absence of crosslinking, detachment of the nucleobase from the polymer backbone – results in fluorescence effectively being switched off. We could find no evidence, either through TCSPC or degradation studies, that any new molecular species are formed during the crosslinking process, which provides further support for the conclusion that fluorescence is induced by aggregation of usually non-fluorescent components. The hypothesis that rigidification is responsible for fluorescence is supported by the distinct vibronic bands in the UV-vis absorption and fluorescence spectra of **Mi(A:T)** (Figure 5.5c and Figure 5.19), which are characteristic of the formation of rigid structures.[34]

Taken together, these data confirm the formation of a new class of NCPdot based on synergistic chemical crosslinking and selective H-bonding. By assembling the NCPdots out of well-defined polymer components, it was possible to selectively change the make-up of the nanoparticles in order to identify the underlying fluorescence mechanism. We propose that this could provide a general strategy for understanding the mechanisms underpinning the CEE.

NCPdots that possess core-shell structures could offer a number of advantages over classical fluorescent organic dyes. Most notably, the corona/shell can provide an effective physical shield from complicated exterior environments, resulting in more stable fluorescence – our investigations into the effects of temperature, different solvents and pHs provide a tentative

first proof of this concept. We also anticipate that it may be possible to generalize our strategy to create a diverse array of new NCPdots by combining selective supramolecular interactions with chemical crosslinking.

5.6. Experimental section

5.6.1. Materials

2-(((butylthio)carbonothiolyl)thio)propanoic acid, 3-bromopropyl acrylate, 3-benzoylthymine, 9-hexyladenine, $PNAM_{96}$, $PNAM_{96}$-*b*-$PAAm_{19}$ (**PA**) and $PNAM_{96}$-*b*-$PTAm_{18}$ (**PT**) were synthesized as described previously and stored at 4 °C.[9, 35, 36] 2,2'-Azo-bis(isobutyronitrile) (AIBN) was obtained from Molekula and recrystallized from methanol. 2,2'-Azobis[2-(2-imidazolin-2-yl)propane]dihydrochloride (VA-044, Wako), 1-Ethylpiperidine hypophosphite (EPHP, Sigma-Aldrich) were used without further purification. 4-Acryloylmorpholine (NAM) was bought from Aldrich and was purified by vacuum distillation. The p-silicon (100) wafers were purchased from Sigma-Aldrich and were cut into plates with a size of 10 mm × 10 mm for AFM imaging. Dialysis membranes (MWCO = 3.5 kDa) were purchased from Spectra/Por. DMF, DMSO and other chemicals were obtained from Fisher Chemicals and used without further purification. Dry solvents were obtained by passing them over a column of activated alumina using an Innovative Technologies solvent purification system.

5.6.2 Instrumentation

^{1}H NMR and ^{13}C NMR spectra were recorded on a Bruker DPX-400 or HD500 spectrometer with DMSO-d_6 or DMF-d_7 as the solvent. The chemical shifts of protons were relative to solvent residues (DMF 8.01 ppm and DMSO 2.50 ppm). Fourier transform infrared (FT-IR) spectra were obtained using a Perkin Elmer Spectrum 100 FT-IR. Scans from 550 to 4000 cm^{-1} were taken, and the spectra corrected for background absorbance. For the UV irradiation of the samples, a UVP-1000 crosslinker chamber, equipped with 5 × 8 watt UV dual bipin discharge type tubes that emit within the midrange of the UV spectrum with the maximum intensity at 302 nm was used. UV-vis spectra were recorded on a Perkin-Elmer Lambda 35 UV-vis instrument. Fluorescence spectra were recorded using an Agilent Cary Eclipse fluorescence

spectrophotometer. For fluorescence in different pH, salt concentrations and solvents, micellar solution was freeze dried and then was dissolved in relevant solvents and the fluorescence intensity was measured. Time correlated single photon counting (TCSPC) was employed to obtain all fluorescence lifetime spectra, using an Edinburgh Instruments FLS920 spectrometer and 375 nm solid state ps diode laser source (PicoQuant) in matched quartz 3.5 mL cells (Starna Cell). Instrument response functions (IRF) were determined from scatter signal solution of Ludox HS-40 colloidal silica (0.01% particles in water wt/wt). High resolution mass spectrometry (HR-MS) was conducted on a Bruker UHR-Q-TOF MaXis with electrospray ionization (ESI). HPLC was carried out using XBridgeTM OST C18 (2.5 μm) 50 × 4.6 mm column. The HPLC system was an Agilent 1260 infinity series stack equipped with an Agilent 1260 binary pump, mixer and degasser. Samples were injected using an Agilent 1260 autosampler and detection was achieved using an Agilent 1260 variable wavelength detector, connected in series. UV detection was monitored at λ = 260 nm and the mobile phase used was 100% v/v water. Size exclusion chromatography (SEC) data were obtained in HPLC grade DMF containing 5 mM NH_4BF_4 at 50 °C, with a flow rate of 1.0 mL min^{-1}, on a set of two PLgel 5 μm Mixed-D columns, and a guard column. SEC data were analyzed with Cirrus SEC software calibrated using poly(methyl methacrylate) (PMMA) standards. Preparative SEC was conducted using DMSO at 50 °C, with a flow rate of 0.5 mL min^{-1}.

Hydrodynamic diameters (D_h) and size distributions of the self-assemblies were determined by dynamic light scattering (DLS). The DLS instrumentation consisted of a Malvern Zetasizer NanoS instrument with a 4 mW He-Ne 633 nm laser module. Measurements were made at a detection angle of 173°, and Malvern DTS 7.03 software was used to analyze the data. D_h was calculated by fitting the apparent diffusion coefficient in the Stokes-Einstein equation $D_h = kT/(3\pi\eta D_{app})$, where k, T and η are the Boltzmann constant, the temperature and the viscosity of the solvent, respectively. As the measured sample is a solution of monodispersed spherical

micelles, D_h coincides to the real hydrodynamic diameter as D_{app} is equal to the translational diffusion coefficient (D_t). Static light scattering (SLS) measurements were conducted with an ALV CGS3 (λ = 632 nm) at 25 °C. The data were collected from 50° to 130° with an interval of 5°. The self-assembled solutions were filtered through 0.45 μm nylon filters prior to analysis. Small-angle X-ray scattering (SAXS) experiments were performed using Xeuss 2.0 facility. The samples in solutions were run using 1.5 mm diameter quartz capillaries. All patterns were normalized to a fixed transmitted flux using a quantitative beam stop detector. The two-dimensional SAXS images were converted into one-dimensional SAXS profile ($I(q)$ *versus* q) by circular averaging, where $I(q)$ is the scattering intensity.

TEM observations were performed on a JEOL 2000FX electron microscope at an acceleration voltage of 200 kV. All TEM samples were prepared on graphene oxide (GO)-coated lacey carbon grids (400 Mesh, Cu, Agar Scientific), to enable high contrast TEM images without any staining.[27] Generally, a drop of sample (10 μL) was pipetted on a grid and left for several minutes, then blotted away. TEM images were analyzed using the ImageJ software, and over 100 particles were counted for each sample to obtain number-average diameter D_n. AFM imaging and analysis were performed on an Asylum Research MFP3D-SA atomic force microscope in tapping mode. Samples for AFM analysis were prepared by drop casting 5 μL of solution (0.1 mg mL^{-1}) onto a freshly clean silicon wafer. The silicon wafer was washed with water and ethanol, then activated using plasma treatment to generate a hydrophilic surface.

5.6.3. Synthesis of 3-(adenine-9-yl)propyl acrylate (AAc)

To a suspension of adenine (3.0 g, 24.2 mmol) in dry DMF (100 mL), NaH (0.85 g, 35.4 mmol) was slowly added (Scheme 5.3). The mixture was stirred for 1 h until no gas was produced. The viscous mixture was immersed into an ice bath and 3-bromopropyl acrylate freshly synthesized (5.4 g, 28.2 mmol) was added dropwise. The yellow viscous mixture was stirred overnight and the resulting suspension was concentrated under vacuum. The solid was washed

with CH_2Cl_2 several times and then concentrated. The mixture was further purified by column chromatography using a mixture of CH_2Cl_2 and CH_3OH as eluent and a gradient from 1:0 to 95:5 to give a white solid, AAc (0.55 g, 9%). ^1H, ^{13}C NMR spectra are shown in Figure 5.29.

^1H NMR (500 MHz, DMSO-d_6) δ = 8.14 (s, 1H, purine *H*-2), 8.12 (s, 1H, purine *H*-8), 7.18 (s, 2H, NH_2), 6.25 (d, J = 17.0 Hz, 1H, CH_2=CH-CO), 6.08 (dd, J = 17.0 Hz, 10.0 Hz, 1H, CH_2=C*H*-CO), 5.91 (d, J = 10.0 Hz, 1H, CH_2=CH-CO), 4.25 (t, 2H, J =6.5 Hz, CH_2-purine), 4.10 (t, 2H, J =6.0 Hz, OC-O-CH_2), 2.19 (m, 2H, J =6.5 Hz, OC-O-CH_2-CH_2-CH_2-purine) ppm.

^{13}C NMR (100 MHz, DMSO-d_6) δ = 165.8, 156.4, 152.8, 150.1, 141.3, 132.0, 128.6, 119.2, 62.1, 40.7, 28.9 ppm.

FTIR (neat) ν_{max}/cm^{-1}: 3346 and 3274 (H-N purine), 3111 (H-C=C), 1720 (C=O), 1668 and 1632 (C=N purine), 1575, 1516, 1474 and 1447 (C-N purine).

HR-MS (m/z) found 270.0961, calc. 270.0962 $[M+Na]^+$.

Elemental analysis: Calculated (%) C 53.43, H 5.30, N 28.32; Found (%) C 53.46, H 5.16, N 28.15.

Melting point: 131-133 °C

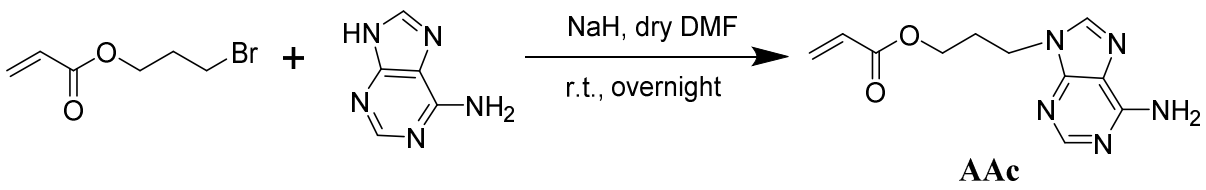

Scheme 5.3. Synthesis of 3-(adenine-9-yl)propyl acrylate (AAc).

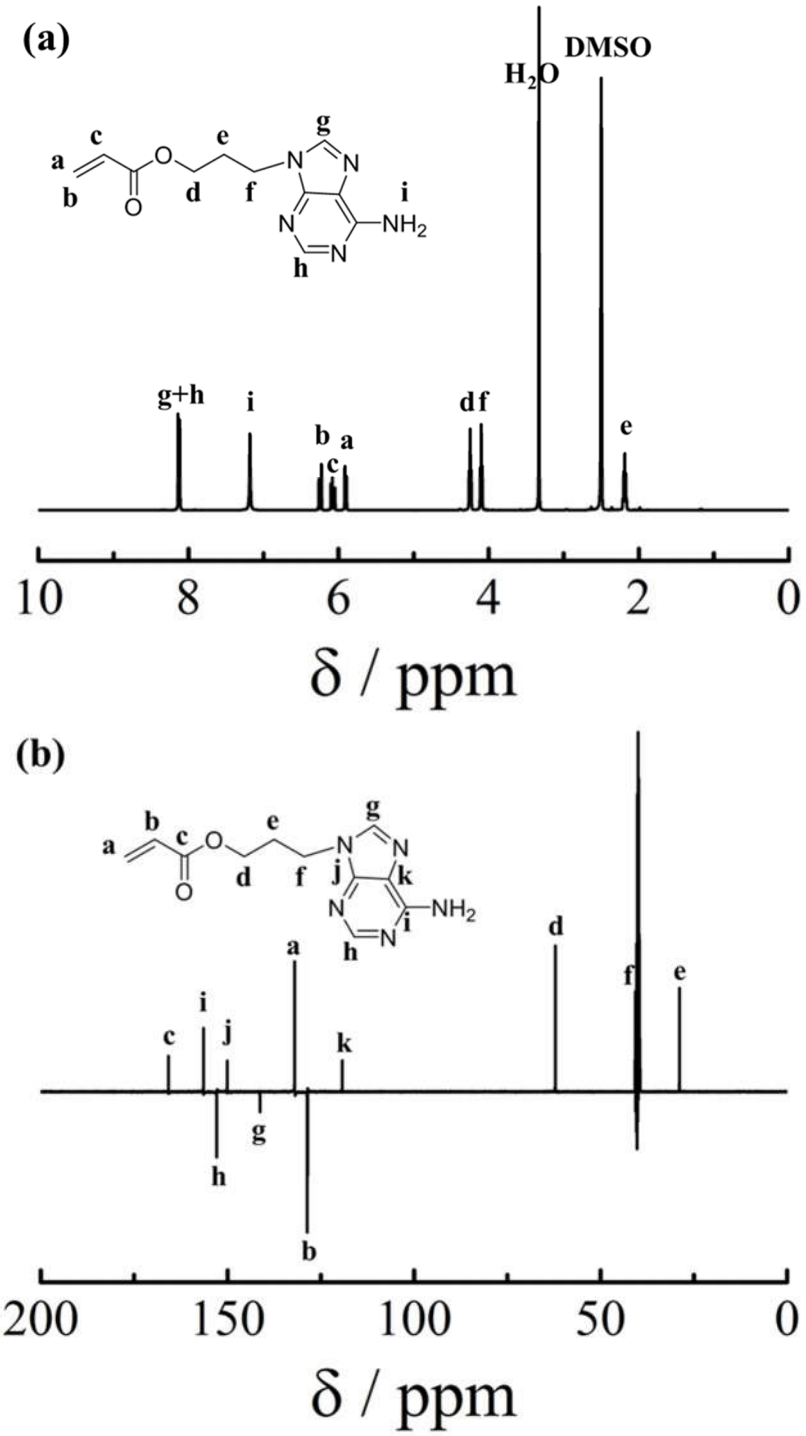

Figure 5.29. ^{1}H NMR and ^{13}C NMR spectra of 3-(adenine-9-yl)propyl acrylate (AAc) in DMSO-d_6.

5.6.4. Synthesis of 3-(3-benzoylthymin-1-yl)propyl acrylate

To the solution of 3-benzoylthymine (4.6 g, 20.0 mmol) in dry DMF (100 mL), NaH (0.50 g, 21.0 mmol) was slowly added (Scheme 5.4). The mixture was stirred for 1 h until no gas was produced. The viscous mixture was immersed in an ice bath and 3-bromopropyl acrylate freshly synthesized (4.6 g, 24.0 mmol) was added dropwise. The yellow, viscous mixture was stirred overnight. The resulting solution was concentrated under vacuum. The residue was partitioned with EtOAc and water. The aqueous layer was extracted three times with EtOAc and the combined organic layers were dried over anhydrous $MgSO_4$. The solvent was removed under vacuum. The mixture was further purified by column chromatography using EtOAc as eluent to give a viscous liquid (4.2 g, 61%).

^{1}H NMR (400 MHz, DMSO-d_6) δ = 7.93 (d, J = 7.2 Hz, 2H, benzene-*H*1,*H*5), 7.80 (s, 1H, pyrimidine-*H*6), 7.78 (t, J = 7.6 Hz, 1H, benzene-*H*3), 7.59 (t, J = 7.6 Hz, 2H, benzene-*H*2, *H*4), 6.32 (dd, J = 17.2 Hz, 1.6 Hz, 1H, CH_2=CH-CO), 6.14 (dd, J = 17.2 Hz, 10.4 Hz, 1H, CH_2=C*H*-CO), 5.94 (dd, J = 10.4 Hz, 1.6 Hz, 1H, CH_2=CH-CO), 4.18 (t, 2H, J = 7.0 Hz, OC-O-CH_2), 3.93 (t, 2H, J = 7.0 Hz, CH_2-pyrimidine), 2.02 (m, 2H, J = 6.4 Hz, OC-O-CH_2-CH_2-CH_2-pyrimidine), 1.83 (s, 3H, CH_3-pyrimidine) ppm.

^{13}C NMR (100 MHz, DMSO-d_6) δ = 170.2, 165.8, 163.4, 149.9, 143.0, 135.9, 132.1, 131.7, 130.9, 130.0, 128.6, 109.0, 62.3, 46.0, 27.8, 12.3 ppm.

5.6.5. Synthesis of 3-(thymin-1-yl)propyl acrylate (TAc)

(3-Benzoylthymin-1-yl)propyl acrylate (3.0 g, 8.8 mmol) was dissolved in a mixture of TFA/DCM (3:1) (20 mL) (Scheme 5.4). The reaction solution was stirred at room temperature overnight. After completion of the reaction, solvent was removed under vacuum. The residue was purified by column chromatography with a gradient of $CHCl_3$/CH_3OH from 1:0 to 95:5 to

give a viscous liquid. Ethanol (20 mL) was then added to give a white solid (1.70 g, 74%). ^{1}H, ^{13}C NMR spectra are shown in Figure 5.30.

^{1}H NMR (500 MHz, DMSO-d_6) δ = 11.21 (s, 1H, pyrimidine-*H*3), 7.52 (s, 1H, pyrimidine-*H*6), 6.30 (d, J = 16.5 Hz, 1H, CH_2=CH-CO), 6.11 (dd, J = 16.5 Hz, 10.0 Hz, 1H, C*H*=CH$_2$-CO), 5.93 (d, J = 10.0 Hz, 1H, CH_2=CH-CO), 4.12 (t, 2H, J = 6.0 Hz, OC-O-CH_2), 3.73 (t, 2H, J = 6.5 Hz, CH_2-pyrimidine), 1.95 (m, 2H, J = 6.5 Hz, OC-O-CH$_2$-CH_2-CH$_2$-pyrimidine), 1.73 (s, 3H, CH_3-pyrimidine) ppm.

^{13}C NMR (125 MHz, DMSO-d_6) δ = 165.8, 164.8, 151.4, 141.9, 132.0, 128.6, 109.0, 62.3, 45.3, 27.9, 12,4 ppm.

FTIR (neat) ν_{max}/cm^{-1}: 3328 (H-N pyrimidine), 3041 (H-C=C pyrimidine), 2971, 2951 and 2932 (CH$_3$ pryimidine), 1719 (C=O), 1680 and 1650 (C=O and C=C pyrimidine).

HR-MS (m/z) found 261.0840, calc. 261.0846 [M+Na]$^{+}$.

Elemental analysis: Calculated (%) C 55.46, H 5.92, N 11.76; Found (%) C 55.27, H 5.89, N 11.68.

Melting point: 107-109 °C

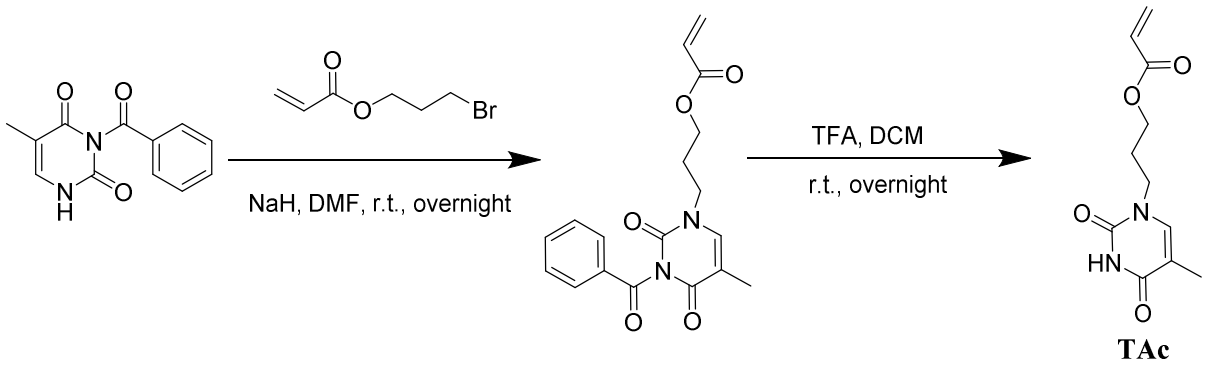

Scheme 5.4. Synthesis of 3-(thymin-1-yl)propyl acrylate (TAc).

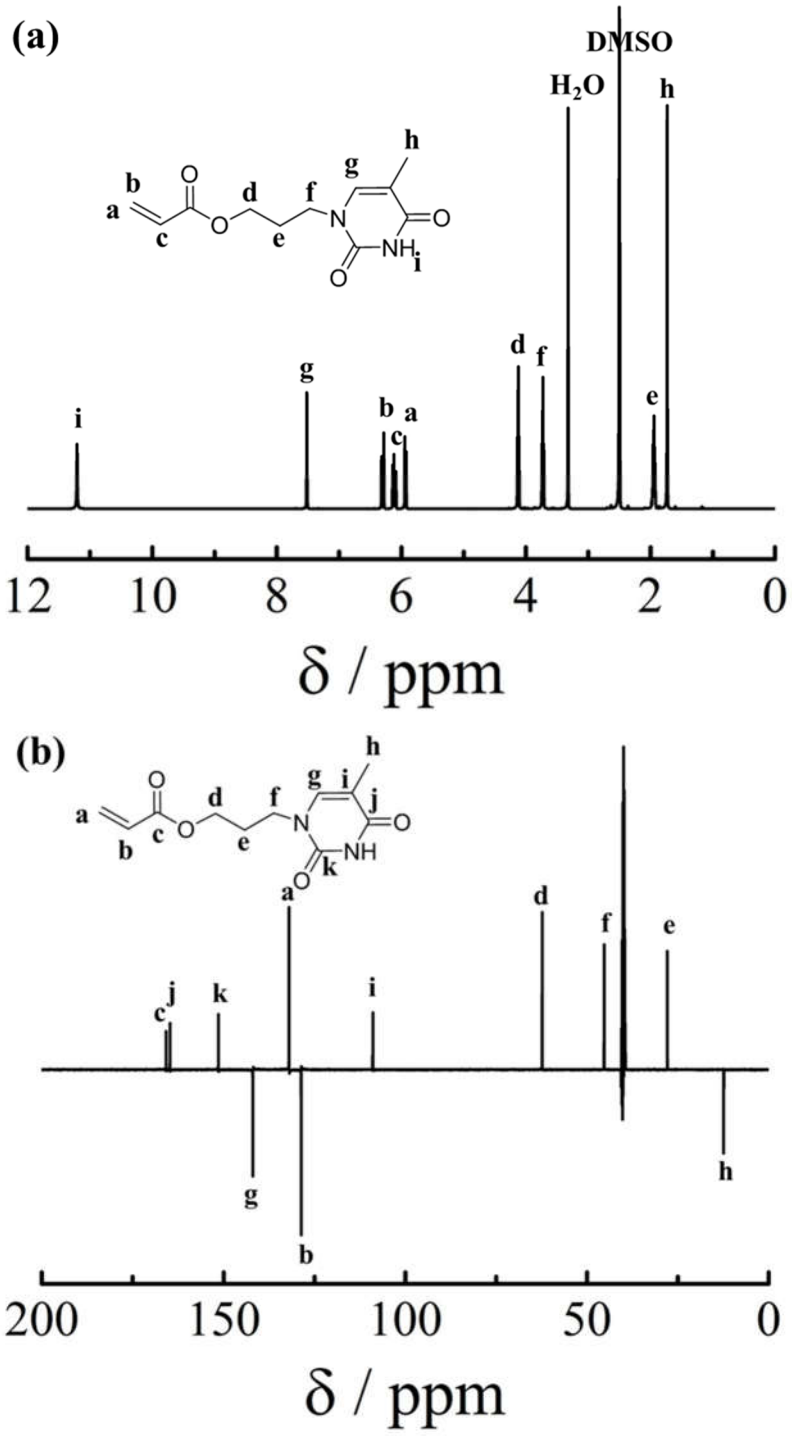

Figure 5.30. ^{1}H NMR and ^{13}C NMR spectra of 3-(thymin-1-yl)propyl acrylate (TAc) in DMSO-d_6.

5.6.6. Synthesis of PNAM$_{96}$-*b*-PMTAm$_{19}$ (PT^{Me}'), PNAM$_{96}$-*b*-PAAc$_{20}$ (PA*') and PNAM$_{96}$-*b*-PTAc$_{19}$ (PT*') diblock copolymers

The typical procedure was as follows. For PNAM$_{96}$-*b*-PMTAm$_{19}$ (**PT^{Me}'**), PNAM$_{96}$ (69 mg, 0.005 mmol), MTAm (25 mg, 0.1 mmol), and AIBN (0.08 mg, 0.0005 mmol) were dissolved in DMSO (0.3 mL). The mixture was thoroughly degassed *via* 4 freeze-pump-thaw cycles, filled with nitrogen and then immersed in an oil bath at 70 °C overnight. An aliquot of the crude product was taken and analyzed by ^{1}H NMR spectroscopy to calculate the conversion. The residual solution was precipitated three times from cold CH_3OH. The light yellow polymer was dried in a vacuum oven overnight at room temperature and analyzed by ^{1}H NMR spectroscopy and DMF SEC.

5.6.7. End group removal of PNAM$_{96}$-*b*-PAAm$_{19}$ (PA'), PNAM$_{96}$-*b*-PTAm$_{18}$ (PT'), PNAM$_{96}$-*b*-PMTAm$_{19}$ (PT^{Me}'), PNAM$_{96}$-*b*-PAAc$_{20}$ (PA*') and PNAM$_{96}$-*b*-PTAc$_{19}$ (PT*') diblock copolymers

The typical procedure was as follows. PNAM$_{96}$-b-PAAm$_{19}$ (**PA'**) (100 mg, 0.0052 mmol), EPHP (9.4 mg, 0.052 mmol), and AIBN (0.28 mg, 0.0017 mmol) were dissolved in DMF (2.0 mL) (Scheme 5.1). The mixture was thoroughly degassed *via* 4 freeze-pump-thaw cycles, filled with nitrogen and then immersed in an oil bath at 100 °C for 2 h. The solution was precipitated three times from cold CH_3OH. The diblock copolymer was further purified by dialysis against 18.2 MΩ·cm water (MWCO = 3.5 kDa), incorporating at least 6 water changes and followed by lyophilization to yield a white solid. The obtained white polymer **PA** was further analyzed by ^{1}H NMR spectroscopy and DMF SEC (Figures 5.1 and Table 5.1).

5.6.8. Self-assembly and UV irradiation of micelles MA, MT, M(A:T), M(A+T^{Me}), M(A*:T*) and M (9-hexylA:T)

The typical procedure was as follows. For **M(A:T)**, diblock copolymers **PA** (10 mg, 0.00052 mmol) and **PT** (10 mg, 0.00052 mmol) were dissolved in H_2O (2.0 mL). The obtained

solution was kept stirring for at least 2 h at room temperature prior to use. The self-assembled solution was then transferred to an NMR tube for UV irradiation using a UVP-1000 crosslinker chamber.

5.6.9. Hydrolysis of micelles Mi(A:T) and Mi(A*:T*)

The typical procedure was as follows. **Mi(A*:T*)** (10 mg) was dissolved using 1 M HCl aqueous solution (1 mL) and was kept stirring at room temperature for 7 days. Then 1 M $NaHCO_3$ aqueous solution was added to tune the pH to 7. The mixture was passed through a neutral Al_2O_3 column and the solvent was removed under vacuum and the obtained white solid was characterized using DMF SEC and fluorescence spectrophotometer. In order to further analyze the hydrolyzed products in **MiH(A*:T*)**, the solution was dialyzed (MWCO = 3.5 kDa). The dialyzate was freeze-dried and analyzed by HPLC and HR-MS.

5.7. References

1. C. R. South and M. Weck, *Macromolecules*, **2007**, *40*, 1386-1394.

2. P. K. Lo and H. F. Sleiman, *J. Am. Chem. Soc.*, **2009**, *131*, 4182-4183.

3. K. Gorska and N. Winssinger, *Angew. Chem., Int. Ed.*, **2013**, *52*, 6820-6843.

4. R. K. O'Reilly, A. J. Turberfield and T. R. Wilks, *Acc. Chem. Res.*, **2017**, *50*, 2496-2509.

5. R. McHale and R. K. O'Reilly, *Macromolecules*, **2012**, *45*, 7665-7675.

6. R. McHale, J. P. Patterson, P. B. Zetterlund and R. K. O'Reilly, *Nat. Chem.*, **2012**, *4*, 491-497.

7. J.-F. Lutz, A. F. Thunemann and K. Rurack, *Macromolecules*, **2005**, *38*, 8124-8126.

8. F. Ilhan, T. H. Galow, M. Gray, G. Clavier and V. M. Rotello, *J. Am. Chem. Soc.*, **2000**, *122*, 5895-5896.

9. Z. Hua, A. Pitto-Barry, Y. Kang, N. Kirby, T. R. Wilks and R. K. O'Reilly, *Polym. Chem.*, **2016**, *7*, 4254-4262.

10. Z. Hua, R. Keogh, Z. Li, T. R. Wilks, G. Chen and R. K. O'Reilly, *Macromolecules*, **2017**, *50*, 3662-3670.

11. M.-P. Chien, A. M. Rush, M. P. Thompson and N. C. Gianneschi, *Angew. Chem., Int. Ed.*, **2010**, *49*, 5076-5080.

12. S. Cheng, M. Zhang, N. Dixit, R. B. Moore and T. E. Long, *Macromolecules*, **2012**, *45*, 805-812.

13. R. Beukers and W. Berends, *Biochim. Biophys. Acta*, **1960**, *41*, 550-551.

14. C. Rauer, J. J. Nogueira, P. Marquetand and L. Gonzalez, *J. Am. Chem. Soc.*, **2016**, *138*, 15911-15916.

15. N. Ishikawa, M. Furutani and K. Arimitsu, *ACS Macro Lett.*, **2015**, *4*, 741-744.

16. K. Saito, L. R. Ingalls, J. Lee and J. C. Warner, *Chem. Commun.*, **2007**, *0*, 2503-2505.

17. P. Johnston, C. Braybrook and K. Saito, *Chem. Sci.*, **2012**, *3*, 2301.

18. Y. Kang, A. Pitto-Barry, M. S. Rolph, Z. Hua, I. Hands-Portman, N. Kirby and R. K. O'Reilly, *Polym. Chem.*, **2016**, *7*, 2836-2846.

19. D. Fong, Z. Hua, T. R. Wilks, R. K. O'Reilly and A. Adronov, *J. Polym. Sci., Part A: Polym. Chem.*, **2017**, *55*, 2611-2617.

20. S. Zhu, Y. Song, J. Shao, X. Zhao and B. Yang, *Angew. Chem. Int. Ed.*, **2015**, *54*, 14626-14637.

21. B. Sun, B. Zhao, D. Wang, Y. Wang, Q. Tang, S. Zhu, B. Yang and H. Sun, *Nanoscale*, **2016**, *8*, 9837-9841.

22. M. Sun, C. Y. Hong and C. Y. Pan, *J. Am. Chem. Soc.*, **2012**, *134*, 20581-20584.

23. Y. Gong, Y. Tan, J. Mei, Y. Zhang, W. Yuan, Y. Zhang, J. Sun and B. Z. Tang, *Sci. China: Chem.*, **2013**, *56*, 1178-1182.

24. W. Li, X. Wu, Z. Zhao, A. Qin, R. Hu and B. Z. Tang, *Macromolecules*, **2015**, *48*, 7747-7754.

25. H. Wang, Q. Li, J. Dai, F. Du, H. Zheng and R. Bai, *Macromolecules*, **2013**, *46*, 2576-2582.

26. Y. K. Chong, G. Moad, E. Rizzardo and S. H. Thang, *Macromolecules*, **2007**, *40*, 4446-4455.

27. J. P. Patterson, A. M. Sanchez, N. Petzetakis, T. P. Smart, T. H. Epps III, I. Portman, N. R. Wilson and R. K. O'Reilly, *Soft Matter*, **2012**, *8*, 3322-3328.

28. Y.-P. Sun, B. Zhou, Y. Lin, W. Wang, K. A. S. Fernando, P. Pathak, M. J. Meziani, B. A. Harruff, X. Wang, H. Wang, P. G. Luo, H. Yang, M. E. Kose, B. Chen, L. M. Veca and S.-Y. Xie, *J. Am. Chem. Soc.*, **2006**, *128*, 7756-7757.

29. C. E. Crespo-Hernandez, B. Cohen and B. Kohler, *Nature*, **2005**, *436*, 1141-1144.

30. C. Su, C. T. Middleton and B. Kohler, *J. Phys. Chem. B.*, **2012**, *116*, 10266-10274.

31. C. Wurth, M. Grabolle, J. Pauli, M. Spieles and U. Resch-Genger, *Nat. Protoc.*, **2013**, *8*, 1535-1550.

32. R. Hu, N. L. Leung and B. Z. Tang, *Chem. Soc. Rev.*, **2014**, *43*, 4494-4562.

33. Y. Boulard, J. A. H. Cognet, J. Gabarro-Arpa, M. Le Bret, L. C. Sowers and G. V. Fazakerley, *Nucleic Acids Res.*, **1992**, *20*, 1933-1941.

34. H. A. M. Ardona, T. S. Kale, A. Ertel and J. D. Tovar, *Langmuir*, **2017**, *33*, 7435-7445.

35. Y. Kang, A. Pitto-Barry, A. Maitland and R. K. O'Reilly, *Polym. Chem.*, **2015**, *6*, 4984-4992.

36. T. R. Barlow, J. C. Brendel and S. Perrier, *Macromolecules*, **2016**, *49*, 6203-6212.

Chapter 6. Conclusions and outlook

6.1. Conclusions

In this thesis, the synthesis, self-assembly behaviors and their potential applications of synthetic nucleobase-containing acrylamide polymers have been studied.

In Chapters 2 and 3, the nucleobase-containing acrylamide monomers were successfully synthesized and polymerized using RAFT polymerization. Polymers with high DPs (over 300) of nucleobase and low dispersity could be achieved using these highly reactive monomers. These nucleobase-containing amphiphiles were easily self-assembled into well-defined nanoparticles with a thymine core through either a direct dissolution or a solvent switch method. These novel micelles were observed to selectively respond to copolymers containing a complementary nucleobase block. Interestingly, worm-like nanoparticles with different lengths from 300 nm to 1 μm could be easily obtained through the stepwise introduction of complementary copolymers, suggesting controlled living growth mediated through H-bonding interactions. It was validated that complementary H-bonding interactions in synthetic polymers could provide a new stimulus to access and tailor nanostructure sizes and morphologies.

In Chapter 4, a supramolecular 'grafting to' approach was developed to prepare mixed corona micelles based on the knowledge gained from Chapters 2 and 3. The complementary H-bonding interactions between the added adenine-containing copolymer and the initial micelle with a thymine core enabled the formation of mixed-corona polymeric nanoparticles. A series of complementary adenine-containing diblock copolymers containing thermo-responsive PNIPAM were introduced into the mixed corona micelle. This novel mixed micelle was elucidated to undergo a fast and full reversible size change upon heating through collapsing and swelling of PNIPAM chains. Through attaching an environmentally sensitive fluorophore and protein ligands at both polymer ends, the change of fluorescence intensity and reversible reveal and concealment of protein ligands could be easily attained by heating and cooling. This supramolecular 'grafting to' strategy could efficiently avoid the low grafting density observed

among conventional ‘grafting to’ methods, showing great potential in fabricating mixed polymer-modified functional nanostructures and surfaces.

In Chapter 5, photocrosslinking of nucleobase-containing polymer micelles was observed to result in fluorescent polymer nanoparticles. These novel fluorescent nanoparticles did not contain conventional fluorophores and the observed photoluminescence was significantly enhanced through the crosslink-enhanced emission effect (CEE). A number of factors were investigated including the effect of omitting one of the nucleobases, blocking hydrogen-bonding interactions, detaching the nucleobase from the polymer backbone and changing the degree of core crosslinking. It was revealed that no new small molecule fluorophores were created and that a dense, hydrogen-bonded network of photodimerized thymine with entrapped adenine was required for fluorescence to arise. This kind of new non-conjugated fluorescent nanoparticles, which was based on synergistic chemical crosslinking and selective H-bonding, was observed to be robust under a series of experimental conditions such as organic solvents, heating and salts.

6.2. Outlook

Compared with nucleic acids such as DNAs or RNAs, synthetic nucleobase-containing polymers are much easier to synthesize, modify and scale-up. In this thesis, we have synthesized a series of nucleobase-containing polymers even with high DPs over 300, and fabricated responsive nanoparticles with complementary nucleobases in aqueous solutions. Synthetic nucleobase-containing polymers show great possibility and are promising to replace nucleic acids for many potential applications in DNA nanotechnology, materials science and biological science, to name but a few. However, there are still several limitations and unsatisfied aspects to be resolved in order to achieve more widespread applications of synthetic nucleobase polymers.

The solubility of nucleobase-containing monomers and polymers reported before are limited in water. More water soluble nucleobase-containing monomers and polymers are highly desired, which might make it possible to attain the complementary interactions with DNAs or RNAs. By using nucleosides or introducing a charge group between nucleobase and vinyl group might provide a feasible route to prepare fully water-soluble nucleobase-containing polymers. In addition, acrylamide-type monomers are more favourable to achieve complementary H-bonding interactions in contrast to (meth)acrylates, methacrylamides and styrene-type monomers, considering its more flexible backbone and lower T_g. These new polymers are expected to interact with either nucleic acids or complementary polymers to build more advanced and complex nanostructures.

With the development of sequence-controlled polymers, the established methodology can be easily copied to the synthesis of nucleobase-containing polymers. These sequence-controlled polymers are more robust than nucleic acids under non-physiological conditions. Meanwhile, vital functions such as transcription, replication and translation for nucleic acids might be successfully accomplished using these mimics. Template polymerization can also be expected

to give daughter polymers with specific lengths and monomer sequences. Besides, all nucleic acids currently utilized in DNA nanotechnology and materials science might be substituted by synthetic nucleobase-containing polymers.

Moreover, nucleobase-containing polymers with more complex architectures are also expected to be prepared in the near future. Although linear nucleic acids are dominant in nature, synthetic mimics are not limited to the simple architectures. Various architectural polymers can be easily synthesized, including multi-arm star polymers, hyperbranched polymers, dendrimers and bottlebrush polymers. Replacing the common monomers in these polymers with nucleobase monomers will definitely bring more attractive and interesting properties, not only from the specific structures but also from the highly functional moieties.

More researchers are encouraged to enter the tiny nucleobase-containing polymer community, not only polymer chemists but also organic chemists. In future, we hope that synthetic nucleobase-containing polymers can replace nucleic acids. Information can be efficiently encoded into these sequence-controlled nucleobase-containing polymers and they can also achieve the essential biological functions of transcription, translation and replication. More importantly, these synthetic mimics can overcome some disadvantages of DNAs and RNAs such as hydrolysis. These synthetic nucleobase-containing polymers are expected to have more widespread applications in biological chemistry, materials science, biomedicines and so on.